

Department of Electronic and Electrical Engineering

**Design and Analysis of LVDC Offshore
Microgrids for Improving Electric
Infrastructure of Multi-use Platforms**

by

Walid Mohamady Hassan Nassar

BSc, MSc

A thesis presented in fulfilment of the requirements for the
degree of Doctor of Philosophy

2021

This thesis is the result of the author's original research. It has been composed by the author and has not been previously submitted for examination which has led to the award of any degree.

The copyright of this thesis belongs to the author under the terms of the United Kingdom Copyright Acts as qualified by University of Strathclyde Regulation 3.50. Due acknowledgement must always be made of the use of any material contained in, or derived from, this thesis.

Signed: *W. Mohamady*

Date: 19/07/2021

Acknowledgements

“Alhamdulillah Rab Allameen”, all praise is to Allah for His blessing and guidance throughout my PhD journey and the whole of my life.

I would like to express my deep gratefulness to my supervisor Prof. Olimpo Anaya-Lara for his guidance, constructive comments, encouragement, and support during my research. In addition to his intellectual support, Olimpo is a really good friend to me who always asking about my personal life and my family to ensure everybody is ok. Many thanks to Prof. Olimpo for his support during the hard time of the Covid pandemic. I would like, also, to thank Dr. David McMillan for his guidance and useful feedback.

A very special thanks to Dr. Khaled Ahmed for his continuous support and priceless advices throughout my PhD study. Also, many thanks to Dr. Mohamed Atef for his advice during my study.

Many thanks to Dr. Abdelnaser Abdelaal for giving me hope and ambition to achieve my postgraduate study.

Many thanks to Mr. Ross Mackay, Ibrahim Abdellah, Shakira Lamidi and Nurudeen Olaotan Odeskina for their help in proofreading the thesis.

Thanks to all staff of the EEE department, student business department, financial department and every member of staff of the University of Strathclyde who helped and advised me during my research.

Gratitude, thankfulness and love to my wife, Fatma, my daughters, Habiba and Bisan and my son, Mohamed.

Walid Mohamady

July 2021

Dedication

A special feeling of gratitude to my loving parents, Mohamady and Nasima, great mercy and forgiveness to their souls, who always supported me in life and whose words of encouragement and push for success ring in my ears., my brother, Ayman, my sisters, Shalabia, Wafa'a, Iman, Shar, my father-in-law, Abdel-Raouf, my sister-in-law, Fifi and my brother-in-law, Fathy for their prayers and encouragement that give me the power and strength to finish my PhD.

Table of Content

Acknowledgements	3
Dedication	4
Table of Content	5
Abstract	10
List of Symbols	i
List of Abbreviations	iv
List of Tables and Figures	v
Chapter 1 Introduction	1
1.1 Renewable energy current situation	1
1.2 Offshore multi-use platform	2
1.3 Prominence and potential impact of MUPs	4
1.4 Challenges and research gaps of MUPs	5
1.4.1 Wind/tidal turbine failure	5
1.4.2 Power quality issues	6
1.4.3 Circulating current problem	7
1.4.4 The complexity of the system controller	7
1.5 Research question	8
1.6 Motivation and objectives	8
1.7 Research output	9
1.7.1 Contribution to conference	9
1.7.2 Contribution to journal	10
1.8 Thesis structure	10
Chapter 2 Multi-use Platforms (MUPs)	13
2.1 Background	13
2.2 Potential offshore energy resources	13

2.2.1	Wind and tidal energy	14
□	Wind energy	14
□	Tidal energy	17
2.2.2	Floating solar photovoltaic farms	18
2.2.3	Other marine energies	21
□	Wave energy	21
□	Ocean thermal energy	21
□	Marine biomass energy	22
2.3	Offshore MUP structures	22
2.3.1	Co-located systems	23
2.3.2	Combined structures	23
2.3.3	Island structure	25
2.4	Evaluation of offshore multi-use platforms	29
2.5	Offshore MUP design methodology	29
2.6	Offshore MUP grid configuration	31
2.7	Offshore MUP grid control	34
2.8	Summary	35
Chapter 3 Optimal Sizing of Renewable Energy Resources		37
3.1	Background	37
3.1.1	Optimal sizing of hybrid power systems	37
3.1.2	Optimal number of parallel converters for efficiency maximization	40
3.2	Optimal sizing methodology	42
3.3	Proposed system description	44
3.4	Optimisation modelling of energy resources	45
3.4.1	Optimization model of wind/tidal turbine	45
3.4.2	Optimization model of a solar module	47
3.4.3	Storage unit optimization model	47
3.5	Data description, a case study at the North Sea	49
3.5.1	Electrical load data profile	50
3.5.2	Wind/tidal speed data profile	51
3.5.3	Solar irradiation data profile	53
3.5.4	Energy and storage systems considered for the case study	53
3.6	Optimization objectives and constraints	54
3.6.1	Optimization objectives	54

3.6.2	Optimisation constraints and design variables	55
3.7	Optimization model and results	56
3.7.1	Cost-reliability method proposed for optimal sizing of energy resources	59
3.7.2	Verification of cost-reliability method using Matlab tool (Linprog)	61
3.8	DC conversion efficiency maximisation	64
3.9	Summary	69
Chapter 4	Parallel DC-DC Power Converters	70
4.1	DC-DC power converter topology	70
4.1.1	Boost converter steady-state analysis	73
4.2	Parallel converters control in an islanded DC microgrid	80
4.2.1	Droop control	80
4.2.2	Active load sharing control techniques	84
4.3	Circulating current among parallel-connected converters	89
4.3.1	Circulating current between two parallel converters	90
4.3.2	Circulating current among three parallel converters	91
4.3.3	Circulating current among n-parallel converters	94
4.4	Investigation of circulating current among parallel-connected converters	96
4.4.1	Simulation results	97
4.5	Summary	107
Chapter 5	A New Adaptive IACS Controller for Circulating Current Minimization	109
5.1	Background	109
5.2	System configuration	110
5.3	The proposed control scheme	111
5.3.1	Steepest Descent Method (SDM)	112
5.4	System modelling	116
5.4.1	Single DC-DC converter model	116
5.4.2	Model of a boost converter with IACS	119
5.4.3	Model of n-parallel connected converters with IACS	121
5.5	Stability analysis	126
5.5.1	Stability analysis of a single boost converter	127
5.5.2	Stability analysis of n-parallel converters	128

5.5.3	Stability analysis of the current control loop in IACS	129
5.5.4	Selection of the adaptive gain λ	130
5.6	Simulation results	130
5.6.1	Simulation results of the conventional and proposed controllers	131
5.6.2	Simulation results of the proposed IACS and droop controllers	132
5.6.3	Simulation results of the proposed IACS with fast fluctuations applied	134
5.7	Summary	137
 Chapter 6 A New Coordinated Controller for Offshore LVDC Microgrid Control		
	138	
6.1	Background	138
6.2	Offshore LVDC microgrid configuration	139
6.3	Control of offshore LVDC microgrid	140
6.3.1	The proposed coordinated controller	141
6.4	Mathematical dynamic models and control loops of system components	142
6.4.1	Dynamic model of wind/tidal turbine with MPPT controller	143
6.4.2	Dynamic model of a solar array with MPPT controller	153
6.4.3	Dynamic model of bi-directional buck-boost converter with control loops	154
6.5	Overall model of floating energy unit and stability analysis	162
6.6	Simulation results	166
6.6.1	Part I: Single floating energy unit	167
6.6.2	Part II: Dynamic performance of 2-floating energy units	173
6.6.3	Part III: 3- parallel energy units within an islanded offshore DC microgrid	176
6.7	Summary	182
 Chapter 7 Conclusions and Future Works		183
7.1	General conclusion	183
7.2	Suggestions for future research	185
7.3	Author's contribution	185
 References		187
 Appendices		199
Appendix A	The Ocean of Tomorrow Projects	199

Appendix B	Energy Systems Datasheets, Converters Costs and Matlab Codes of Chapter 3	201
Appendix C	System simulation parameters of Chapter 6	214

Abstract

Hybrid and interconnected energy sources are becoming the norm for the low carbon energy sector. This implies parallel connection of different sources to a common platform, as it is seen in wind farm connection, self-contained microgrids, offshore Multi-Use Platforms (MUPs), etc. MUPs and their associated marine activities draw the attention of many countries worldwide to exploit resources of the oceans which cover over 68% of the surface of the earth. This helps to cut greenhouse gas emissions and also facilitate provision of food in a sustainable way. There are many challenges relating to developing the microgrid of the MUPs. These include space limitation, high costs of system components, installations related issues, unavailability of backup options, critical loads concerns such as aquaculture or isolated communities, power quality issues and turbine failure.

To tackle the aforementioned problems, this research focuses on improving the electric infrastructure of MUPs by considering Direct Current (DC) systems for the offshore microgrid of these platforms. Integrating various energy resources, such as wind, tidal and solar, in a floating structure is proposed under this research. A new graphical concept for the optimal sizing of the MUPs' microgrid is proposed which is verified by the Matlab/Linprog tool. In addition, a new methodology is proposed to determine the optimal number of parallel DC-DC converters connected to wind/tidal turbines for conversion efficiency maximization, and for increasing turbines' reliability and availability. A case study for an MUP at the North Sea is discussed to demonstrate the validity of the proposed optimal sizing concept and the proposed methodology for efficiency maximisation. A new adaptive Instantaneous Average Current Sharing (IACS) controller is proposed for minimizing the circulating current among parallel DC-DC converters. A generalized model of n -parallel-connected DC-DC converters with the improved IACS controller is derived for stability analysis purposes. A New coordinated controller is proposed for the Low Voltage Direct Current (LVDC) microgrid of the MUPs with n -parallel floating structures. A Model of a floating structure is derived which comprises wind and tidal turbines, solar array and energy storage, with boost and bidirectional converters.

The outcomes of this research show that wind/tidal turbine failures could be reduced while increasing the turbines' efficiency and availability by determining the optimal number of parallel DC-DC converters connected to the turbine. Based on the new developed technique of determining optimal number of parallel converters instead of a single rated converter, the annual average efficiency of a wind turbine would be increased from 57 to 75 % under the case study considered in this research. Also, the novel adaptive IACS controller reduced the circulating current among parallel-connected DC-DC converters faster than the conventional controller. In addition, the load voltage is accurately regulated to the nominal value with applying this novel controller, while a steady error is recorded for the load voltage with applying the conventional IACS controller. Modeling and stability analysis were conducted for the DC wind/tidal turbines, which has never been done in the literature, showed that the turbine-based surface-mounted permanent magnet synchronous generator is stable, but two conditions should be fulfilled for a turbine-based interior-mounted permanent magnet synchronous generator to ensure turbine stability. Lastly, based on the modelling and stability analysis held for the LVDC microgrid of the MUPs, the new idea of considering DC system for MUPs is a viable solution that ensures stable and more efficient operation.

List of Symbols

f_s	Switching frequency
T_s	Switching period
v_s	Applied voltage on a switch
C	Converter capacitor
L	Converter inductance
D	Converter duty cycle
V_{i1}, V_{i2}	Converter-1 and converter-2 input voltages
V_{conv-1}, V_{conv-2}	Converter-1 and converter-2 output voltages
i_1, i_2	Converter-1 and converter-2 output currents
R_1, R_2	Converter-1 and converter-2 line impedances
I_{c12}	Circulating current passing from converter-1 to converter-2
R_{load}	Load resistance
v_{conv-i}	Output voltage of converter ith where i equals 1 to n
v_{load}	Load voltage
v_{avg}	Average output voltage of parallel-connected converters
$V_{nominal}$	Nominal load voltage
V_{ref-i}	Reference voltage after adaptation
K_c	Gain of inner capacitor current feedback loop
K	Outer current loop gain
I_{ci}	Capacitor current for ith converter
$f(k)$	Cost function of steepest descent algorithm
λ	Adaptive gain which controls convergence speed of f(k)
i_{li}	Inductor current of ith boost converter
v_{ci}	Capacitor voltage of ith boost converter
V_{ii}	Converter input voltage of ith boost converter
K_f	Gain of voltage feedforward loop
G_c	Transfer function of voltage loop PI-controller
k_{pv}	Proportional gain of voltage PI-controller
k_{iv}	Integral gain of voltage PI-controller
i_{dis}	Disturbance current
k_{pc}	Current controller proportional gain
k_{ic}	Current controller integral gain

Note *The following group of symbols with ‘w’ in the superscript or subscript refers to the symbols of a wind turbine, PMSG and boost converter. The same group of symbols with ‘T’ instead of ‘w’ refers to a tidal turbine with its PMSG and its boost converter.*

P_{wm}	Mechanical output power of a wind turbine (w)
ρ^w	Air density (kg/m ³)
A^w	Rotor swept area of wind turbine (m^2)
C_p^w	Power coefficient of wind turbine
β^w	Pitch angle of wind turbine (°)
v_w	Wind speed associated to a wind turbine (m/s)
λ^w	Tip speed ratio of wind turbine
R^w	Rotor radius of wind turbine (m)
T_m^w, T_e^w	Mechanical and Electromagnetic torque of wind turbine (N.m)
J_m^w	Shaft inertia of wind turbine (kg.m ²)
B_m^w	Viscous friction of wind turbine (N.m.s)
ω_m^w, ω_r^w	Mechanical and electrical rotor speed of wind turbine (rad/s)
P_p^w	Number of pole pairs of wind turbine
v_{ds}^w, v_{qs}^w	Stator voltages of PMSG in dq -frame of wind turbine (V)
i_{ds}^w, i_{qs}^w	Stator currents of PMSG in dq -frame of wind turbine (A)
R_s^w	Stator winding resistance of wind turbine (Ω)
ψ_r^w	Maximum flux linkage created by permanent magnets of wind turbine (Wb).
\hat{v}_o	Voltage of local DC-bus
\hat{v}_g^w	Input voltage of boost converter connected to wind turbine
\hat{d}_w	Duty cycle of boost converter connected to wind turbine
V_o	Local bus voltage at steady state
G_s^w	Transfer function of PI-speed controller of wind turbine
G_c^w	Transfer function of PI-current controller of wind turbine
k_s^w	Proportional gain of speed controller of wind turbine
k_c^w	Proportional gain of current controller of wind turbine
T_s^w	Integral gain of speed controller of wind turbine
T_c^w	Integral gain of current controller of wind turbine

Note *The following group of symbols with 'PV' in the superscript or subscript for a PV array and its boost converter*

R_s^{PV}	Structural resistance of PV cell (Ω)
R_p^{PV}	Parallel resistance for modelling leakage current of p - n junction in a PV cell (Ω)
i_g^{PV}	Current generated by light for a PV cell (A)
G^{PV}	solar irradiance (w/m^2)
G_r^{PV}	Standard irradiance at standard test condition (w/m^2)
T^{PV}	Real cell temperature (Celsius)
T_r^{PV}	Temperature at standard test condition (Celsius)
I_{sc}^{PV}	Short circuit current at standard test condition (A)

K_{sc}^{PV}	Short circuit current temperature coefficient provided by manufacturer.
i_m^{PV}	Output current of a solar PV module (A)
v_m^{PV}	Output voltage of a solar PV module (V)
M_s	Number of series-connected PV cells per module
q	Electron charge (1.602e-19 C)
k	Boltzmann's constant (1.38e-23 J/K)
a	Diode ideality factor
I_0	diode reverse current saturation
N_s	Number of series-connected modules per array
N_p	Number of parallel-connected modules per array
i_{ary}^{PV}	Output current of PV array
v_{ary}^{PV}	Output voltage of PV array
$i_{d_ary}^{PV}$	Diode current considering equivalent circuit of PV array
R_{ary}^{PV}	Norton equivalent resistance of PV array
$i_{s_ary}^{PV}$	Norton equivalent current source of PV array
\hat{v}_g^{PV}	Input voltage of boost converter connected to solar PV array
Note	<i>The following group of symbols with 'B' in the superscript or subscript for a battery system with its bidirectional converter.</i>
v_{batt}	Battery terminal voltage
i_{batt}	Battery current
\hat{v}_{ref}^B	Reference voltage to battery system
\hat{v}_g^B	Low voltage side of bi-directional converter connected to a battery system
G_v^B	Transfer function of PI-voltage controller of bi-directional converter connected to a battery system
k_v^B	Proportional gain of voltage controller of bi-directional converter connected to a battery system
T_v^B	Integral gain of voltage controller of bi-directional converter connected to a battery system
R_L^B	Designed load resistance considering battery system power. (worst case scenario while battery alone supplies load)
R_i^B	Internal equivalent resistance of tidal, wind and solar energy sources
R_{eq}^B	Equivalent resistance of R_L^B and R_i^B in parallel.
i_{cs}^B	Total current delivered by wind, solar and tidal generators
\hat{v}_{CB}^{nom}	Nominal voltage of the DC-collection bus
\hat{v}_{CB}	Measured voltage of the DC-collection bus

List of Abbreviations

CCM	Continuous Conduction Mode
DOD	Depth of Discharging
ESS	Energy Storage System
IACS	Instantaneous Average Current Sharing
LCOE	Levelized Cost of Energy
Linprog	Linear Programing
LPSP	Loss of Power Supply Probability
LVDC	Low-Voltage Direct Current
MPPT	Maximum Power Point Tracking
MSC	Master-Slave Current
MUP	Multi-use Platform
NASA	National Aeronautics and Space Administration
PI	Proportional Integral
PV	Photovoltaic
PWM	Pulse Width Modulation
PMSG	Magnet Synchronous Generator
RES	Renewable Energy Sources
SDM	Steepest Descent Method
SOC	State of Charge
VAWTs	Vertical Axis Wind Turbines
WEC	Wave Energy Converter
3C	Circular Chain Control

List of Tables and Figures

List of Tables

Table 1.1 Classification of offshore sites [5]	2
Table 3.1 Electrical power demand of green and blue island concept [94]	50
Table 3.2 Optimization results based on the cost-reliability method.....	60
Table 3.3 Optimisation results comparison (proposed method vs Matlab/Linprog) .	63
Table 3.4 Economic impact due to using one converter versus the optimal number of converters connected to wind and tidal turbine	68
Table 4.1 System parameters at different operating conditions for circulating current investigation	97
Table 4.2 Current measurements and circulating current calculation.....	104
Table 4.3 Converters power calculations	106
Table 5.1 Boost converter and system parameters list.....	127
Table 5.2 Performance results of conventional versus proposed control schemes..	132
Table A1. Ocean of tomorrow and Horizon 2020 projects.....	199
Table B1. Specifications of wind turbine model V112-3.3 from Vestas [160]	201
Table B2. Specifications of tidal turbine model SR 2000 from Scotrenewables [161]	201
Table B3. Solar panel specifications	202
Table B4. Battery module specifications	202
Table B5. Costs of semiconductor and magnetic devices for nine scenarios of DC- DC conversion system connected to a 3.2 MW wind turbine.....	203
Table B6. Costs of semiconductor and magnetic devices for 15 proposed scenarios of DC-DC conversion system connected to a 1 MW tidal turbine.....	204
Table C1. Parameters list of wind and tidal Turbines	216
Table C2. Parameters list of a solar PV module and array	217
Table C3. Parameters list of a bi-directional buck-boost converter	217

List of Figures

Figure 1.1 Global energy consumption from 2001 to 2019 [1].	1
Figure 1.2 Schematic diagram of a potential multi-use platform [6].	3
Figure 1.3 Classification of MUPs structures [6].	3
Figure 1.4 Types of failures in a wind turbine with electrical failure breakdown [12].	6
Figure 1.5 Microgrid power quality problems.	6
Figure 2.1 Type 1 fixed speed wind turbine.	15
Figure 2.2 Type 2 limited speed wind turbine.	16
Figure 2.3 Type 3 larger speed band based DFIG.	16
Figure 2.4 Type 4 variable speed wind turbine.	17
Figure 2.5 Real PV cell: (a) single-diode equivalent circuit and its (b) $I-V$ characteristic curve.	19
Figure 2.6 PV array (a) Norton equivalent circuit and its (b) $P-V$ relationship curve.	20
Figure 2.7 Co-located independent wind and wave arrays.	24
Figure 2.8 Hybrid system: (a) Fixed bottom (b) Floating [45].	24
Figure 2.9 Satellite unit proposed under green and blue concept [55].	25
Figure 2.10 Configuration of the industrial complex concept [6].	26
Figure 2.11 Configuration of green and blue platform [6].	27
Figure 2.12 Configuration of leisure island [6].	29
Figure 2.13 Offshore platform design phases [62].	30
Figure 2.14 Configuration of hybrid marine energy farm supplies an MUP's microgrid.	32
Figure 2.15 Single line diagram for an MUP's microgrid.	33
Figure 2.16 Microgrid hierarchical control [67].	34
Figure 3.1 Hybrid power system optimization steps [77].	43
Figure 3.2 Configuration of hybrid power plant supplies loads of MUP's microgrid.	44
Figure 3.3 Wind/tidal turbine power curve [92].	46
Figure 3.4 Proposed location for the MUP in the North Sea (red sign).	49
Figure 3.5 Annual load profile hourly-averaged.	51

Figure 3.6 Annual wind and tidal speed profile hourly-averaged.....	52
Figure 3.7 Annual global solar irradiation hourly-averaged.....	53
Figure 3.8 Optimization model.	57
Figure 3.9 Power management algorithm for LPSP evaluation.....	58
Figure 3.10 Optimal sizing of energy resources based on the cost-reliability curve.	59
Figure 3.11 Efficiency curve of phase shift DC-DC converter.....	64
Figure 3.12 Optimal number of parallel converters connected to wind turbine based on the cost-efficiency curve.	66
Figure 3.13 Optimal number of parallel converters connected to tidal turbine based on the cost-efficiency curve.	67
Figure 4.1 The simplest configurable switching storage structures: (a) Switching- inductor cell and (b) Switching-capacitor cell.	71
Figure 4.2 Various possible converters configurations of inductor-cell and capacitor- cell: (a) voltage buck, (b) voltage boost, (c) voltage buck-boost, (d) current buck, (e) current boost and (f) current buck-boost converters with conversion ratio provided for all configurations.	72
Figure 4.3 Boost converter analysis circuit.....	73
Figure 4.4 Boost circuit when the switch is at position 1.	73
Figure 4.5 Boost circuit when the switch is at position 2.	74
Figure 4.6 Boost converter inductor voltage waveform.....	75
Figure 4.7 Boost converter capacitor current waveform.....	75
Figure 4.8 Voltage conversion ratio of a boost converter.....	76
Figure 4.9 Boost converter inductor (a) voltage and (b) current waveforms.....	77
Figure 4.10 Boost converter capacitor (a) current and (b) voltage waveforms.	79
Figure 4.11 Two nodes DC system with droop resistance.....	81
Figure 4.12 DC microgrid droop curve with different droop resistance.....	82
Figure 4.13 Droop curve with unequal load sharing due to nominal voltage sensing error [134].	83
Figure 4.14 Master-slave control scheme.	85
Figure 4.15 Centralized control scheme.....	86
Figure 4.16 Circular chain control (3C) scheme.....	87
Figure 4.17 Average current sharing control scheme.	88

Figure 4.18 Equivalent circuit of two parallel converters connected to DC load.....	90
Figure 4.19 Equivalent circuit of three parallel converters connected to a DC load.	92
Figure 4.20 Simulation model of three parallel converters.....	96
Figure 4.21 Simulation results of test 1.	98
Figure 4.22 Simulation results of test 2.	99
Figure 4.23 Simulation results of test 3.	99
Figure 4.24 Simulation results of test 4.	100
Figure 4.25 Simulation results of test 5.	101
Figure 4.26 Simulation results of test 6.	102
Figure 4.27 Simulation results of test 7.	102
Figure 4.28 Simulation results of test 8.	103
Figure 4.29 Simulation results of test 9.	103
Figure 5.1 Two parallel DC-DC converters connected between RES and DC-load.	110
Figure 5.2 IACS controller with the proposed section added.	112
Figure 5.3 Functional diagram of DC-DC converter.	117
Figure 5.4 Canonical model for ideal DC-DC converter in CCM [152].	117
Figure 5.5 Output impedance of DC-DC boost converter.	118
Figure 5.6 Small signal AC linearized model of DC-DC boost converter [152].	119
Figure 5.7 Boost converter model with capacitor current feedback.	120
Figure 5.8 Boost converter model with IACS controller.	120
Figure 5.9 IACS controller model with n -parallel DC-DC converters.	122
Figure 5.10 Root locus plot of (84).	128
Figure 5.11 Root locus plot of GvdGC.	128
Figure 5.12 Root locus plot of (91) at $k_{pv}=23$	128
Figure 5.13 Root locus plot of G/Z_e	129
Figure 5.14 Zero-pole map of (103) at different values of λ	130
Figure 5.15 Load voltage waveform at different values of λ	130
Figure 5.16 Simulation results of the conventional versus proposed IACS controllers (a) converters output and load currents, (b) circulating current.	131
Figure 5.17 Output load voltage considering conventional and proposed controllers.	132

Figure 5.18 Converters output and load voltages for (a) droop controller based on study [19] and (b) proposed IACS controller.....	133
Figure 5.19 Simulation results of (a) converters output currents with/without noise (b) Converters output voltages with/without noise (c) Load current and circulating current (d) load voltage.....	134
Figure 6.1 Configuration of n -parallel floating energy units.....	139
Figure 6.2 Operation modes of an islanded microgrid.....	141
Figure 6.3 Proposed coordinated controller-based IACS.....	142
Figure 6.4 Wind turbine connected to a DC microgrid [155].....	143
Figure 6.5 Block diagram of speed control of PMSG connected to wind/Tidal turbine.....	145
Figure 6.6 Linearized small-signal model of a current programmed DC-DC converter [152].....	147
Figure 6.7 Linearized small-signal model: (a) detailed block diagram of a wind turbine, PMSG and boost converter with speed control and (b) simplified block diagram.....	149
Figure 6.8 Block diagram of PV solar array, boost converter and PI controller.....	153
Figure 6.9 Current programmed boost converter model used with a solar PV system.....	153
Figure 6.10 DC-DC bi-directional converter (a) full configuration, (b) configuration during discharging mode and (c) configuration during charging mode.....	156
Figure 6.11 DC-DC bi-directional converter analysis during charging mode when: (a) Q2 is ON state, (b) Q2 is OFF state.....	158
Figure 6.12 Current programmed bi-directional model with a two-cascaded loops controller.....	160
Figure 6.13 Overall model of a floating energy unit comprises tidal, wind and solar energy resources with storage unit.....	163
Figure 6.14 Case-a: performance of a single floating energy unit at surplus energy condition.....	168
Figure 6.15 Case-b: performance of single floating energy unit at deficit energy supplied from RES.....	169

Figure 6.16 Case-c: performance of single floating energy unit at load shedding condition due to RES supply zero energy.....	170
Figure 6.17 Case-d: performance of single floating energy unit at fault condition results in tidal turbine-2 outage.....	173
Figure 6.18 Simulation results of two floating energy units connected in parallel with a single energy storage unit.....	174
Figure 6.19 Simulation results of two floating energy units with and without the IACS controller.....	176
Figure 6.20 Subpart-1, three floating energy units connected in parallel to supply a resistive load at surplus energy condition.....	177
Figure 6.21 Subpart-2, three floating energy units connected in parallel to supply a resistive load at load shedding condition.....	178
Figure 6.22 Subpart-3, three floating energy units connected in parallel to supply a resistive load at fault condition.....	179
Figure 6.23 Subpart-4, three floating energy units connected in parallel to supply a resistive load while communication is lost with the floating energy unit-3. ...	180
Figure 6.24 Subpart-5, three floating energy units connected in parallel to supply a resistive load while the communication system is completely lost.....	181

Chapter 1 Introduction

This chapter explores the concept, prominence and applications of Multi-Use Platform (MUP). Additionally, it addresses the challenges and research gaps of MUP's microgrid. Research motivation and objectives are highlighted in this chapter. Furthermore, a summary for upcoming chapters as well as research outputs is presented.

1.1 Renewable energy current situation

To limit and reduce greenhouse gas emissions, the Kyoto Protocol was adopted by the UN in December 1997 and entered into force in February 2005. This protocol binds industrialized and developed countries, which are mainly responsible for the world's high levels of greenhouse gases emissions. Addressing renewable energies as a way to reduce greenhouse gases began before the Kyoto protocol, but investments in renewables have subsequently been increasing on a continual basis after the Kyoto protocol. Although the Covid-19 crisis marked the first annual decline for the global growth in renewable power capacity in 20 years, growth is projected to resume next year, even in the most delayed forecasts.

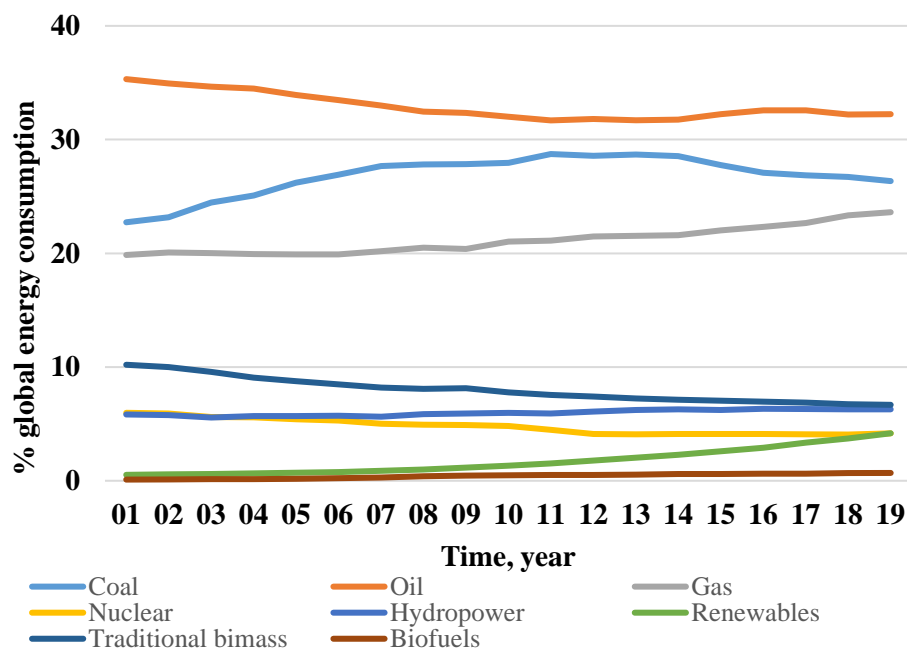


Figure 1.1 Global energy consumption from 2001 to 2019 [1].

This decline accounts for about 13% of the net additions of renewables capacity compared to the 2019 statistics as per the International Energy Agency forecast. Figure 1.1 shows the global energy consumption over the past two decades from 2001 to 2019. Although renewables show a steady increase over this period, non-renewable energy resources (oil, coal and natural gas) continue to hold the largest share of the energy sector with over 82%, while renewable energy sources contribute with under 5% of global consumption [1].

The gradual increase of global warming emissions and populations all over the world necessitates increasing contribution from renewable energy sources to mitigate these problems. In this regard, there is a high tendency to exploit oceans that cover 68.5% of the surface of the Earth [2]. Oceans, as an alternative, have a lot of opportunities for the energy and food sectors, which could be used in more sustainable activities to cut greenhouse gasses emissions and sustainably provide seafood. Offshore multi-use platforms appeared on the horizon as a way of exploiting our oceans.

1.2 Offshore multi-use platform

There are two terms to define here: offshore area and multi-use platforms. An offshore area can be defined based on different criteria such as distance from shore, water depth, jurisdictional boundaries, and wave exposure [3]. The offshore area is far from shore, in areas where there is a lack of topographical features such as capes, headlands or islands [4]. Some studies [4, 5] have provided a classification for marine sites based on sea state or wave energy spectra as shown in Table 1.1.

Table 1.1 Classification of offshore sites [5]

Location class	Wave height	Exposure degree to wave
5	Higher than 3 m	Extreme (offshore area)
1	Below 0.5 m	Insignificant (nearshore area)

In this table, Class 1 refers to marine areas that are exposed to wave heights of less than 0.5 m, so the degree of exposure to strong waves is insignificant; these are normally the nearshore areas. The site class increases as it moves further from the shore where it is more exposed to higher waves and more open ocean. When wave

height goes above 3 m, these are the offshore areas that are classified as extreme at site class 5. In between class 1 and class 5, there are various classes which used for the classification of aquaculture cages techniques.

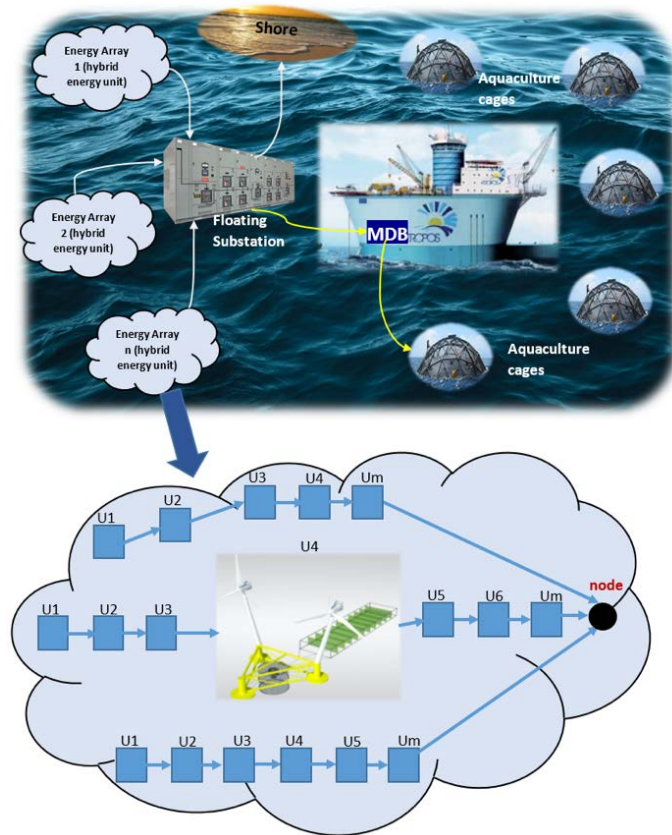


Figure 1.2 Schematic diagram of a potential multi-use platform [6].

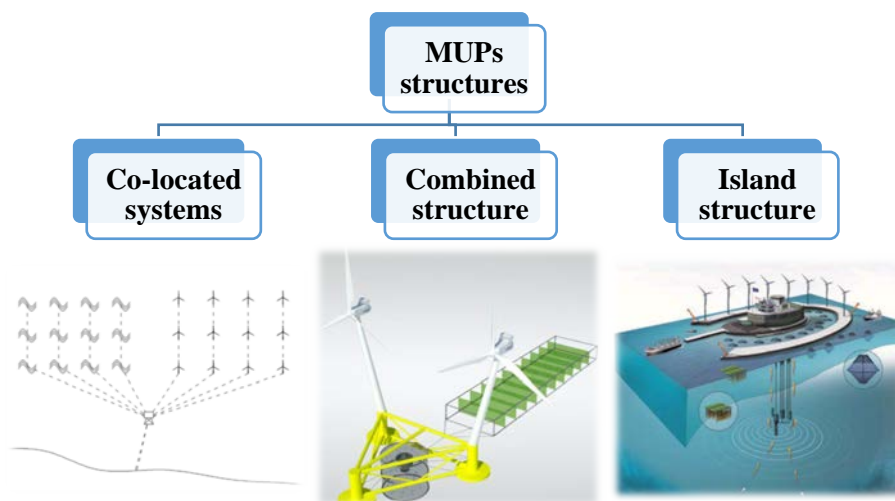


Figure 1.3 Classification of MUPs structures [6].

The other term to define is the multi-use platform, which is an area of sea or ocean that combines different activities such as aquaculture, tourism, transportation, oil production, and energy farms as shown in Figure 1.2. The combination of these activities could be completely integrated into one platform sharing the same structure such as combined or island platforms. Alternatively, they may simply share a marine space such as co-located platforms as per Figure 1.3; more focus on MUP structures comes later in Chapter 2 [7].

1.3 Prominence and potential impact of MUPs

The European Union oversees two big programs to back the concept of offshore MUPs: The Ocean of Tomorrow and Horizon 2020. The main goal of these projects is to develop MUPs to extract energy from marine resources, though they also have the potential to be used for other activities such as aquaculture. Horizon 2020 is the biggest funded program by the European Union for research and innovation, ultimately costing around 80 billion euros over seven years from 2014 to 2020. Some of the Horizon 2020 projects are provided in Table A1, Appendix A. The Ocean of Tomorrow project focused strongly on technologies and innovation issues for marine activities with considering the marine ecosystem. The Ocean of Tomorrow program comprises 31 projects under the Framework Program (FP7), as per Table A1, Appendix A [8, 9].

Bringing different activities together could potentially benefit each other by lowering installation and maintenance costs, increasing resource utilization, reducing the environmental impact, etc. [10]. Aquaculture, as a most promising sector for MUP, is expected to receive several benefits by going offshore, such as enough space for farms extensions, safe from human sources of pollution, better environment for growing a wide variety of marine species, greater ease to develop organic production, better salinity stability than coastal farms and convenient environment for some European species such as seabass and seabream.

Additionally, integrating aquaculture with other activities such as aquatic sports centres, angling centres, and tourism facilities is a great potential business opportunity. Furthermore, MUP would be very good academic centres for studying energy and aquatic animal lives. Moreover, planned fishing guarantees better social stability in

coastal communities and achieves progress in job creation especially when integrated with other activities such as renewable energy, tourism, and conservation [11]. A detailed discussion about the advantages of MUP is provided in the next chapter.

1.4 Challenges and research gaps of MUPs

MUPs, being located offshore, face challenges such as space limitation, high costs of system components, high costs of installations, no backup option available as the platform is far offshore and there are critical loads such as aquaculture or isolated community. MUP's microgrid would experience other challenges such as turbine failure, power quality issues and circulating current among parallel-connected converters [12-14].

1.4.1 Wind/tidal turbine failure

The main energy resources considered for MUP's microgrid are wind and tidal turbines as will be highlighted in the next chapter. These turbines exist in a tough operating environment that makes the accessibility to them for scheduled maintenance or repairs is more expensive, additionally, increasing the turbines' downtime. Some papers have reported different types of failures in wind turbines as summarized in Figure 1.4 [12]. These failures could be categorised as electrical, auxiliary, structural, mechanical and generator failure. The failure in the generator is considered individually and it is not included in the electrical category which comprises the power converter and the control unit.

The electrical failures could be broken down to a failure in the control unit, semiconductors, cooling system, passive filter and auxiliary supply as shown in Figure 1.4. The auxiliary category includes a yaw system, hydraulic system and sensors. The structural category comprises the rotor and tower structure. And lastly, the mechanical category includes the gearbox, drive train and mechanical brake. Study [12] estimated the annual failure probability due to each category. The category with the highest percentage of failures is found to be electrical failures with around 45 % of all failures, which is approximately equal to the percentage of failures due to all other categories (mechanical, structural and generator).

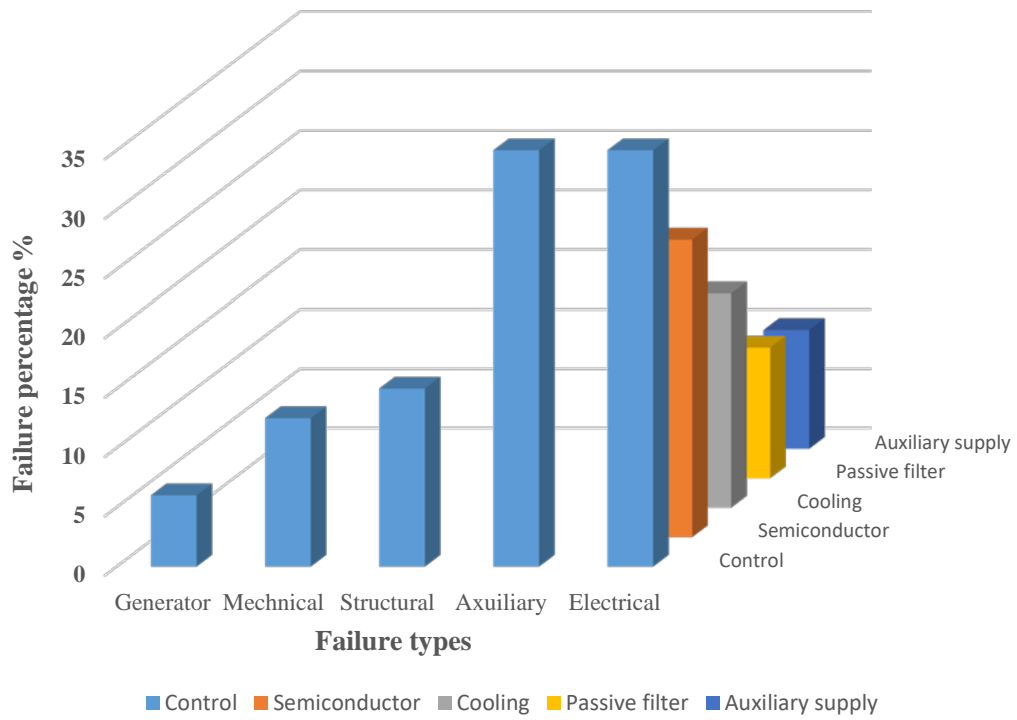


Figure 1.4 Types of failures in a wind turbine with electrical failure breakdown [12].

1.4.2 Power quality issues

MUP’s microgrid depends on many micro-sources to supply its fluctuating power and this is different from a utility power grid that depends on very large generator capacities that make it stable even when big disturbances occur. So, one of the challenges MUP’s microgrid could face is power quality problems such as voltage sag, voltage swell, voltage flicker, current and voltage harmonics and under/over voltage [13]. The authors of the paper [15] identified the microgrid power quality problems as shown in Figure 1.5.

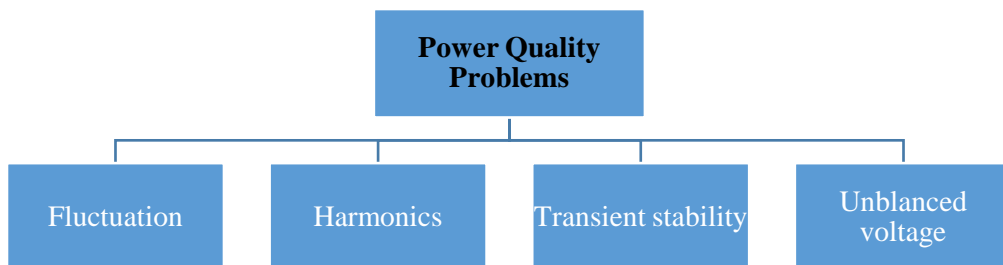


Figure 1.5 Micogrid power quality problems.

An offshore grid depends mainly on renewable sources of energy, such as solar or wind, that already have a low degree of controllability (non-dispatchable) due to their output depending on the availability of resources. This could result in the output power of renewable energy systems being unsmoothed. To avoid this, study [15] proposed a fuzzy logic controller as a way for mitigating the fluctuation of the output power of the wind turbine.

Harmonics problems could arise due to electronic interfacing and nonlinear loads [15]. Harmonic frequencies have a negative impact on grid components, and this leads to reducing a system's lifetime, efficiency and reliability [16]. The harmonic current problem can be solved via a series active power filter [17], a unified power quality conditioner [18] or dividing the turbine's power converter into smaller parallel-connected converters as considered under this research.

MUP's microgrid would experience transient stability issue, as it depends on small inertia generators that could suffer from even small disturbances. For this issue, energy storage has been used to support microgrids during transient conditions, and this strategy has shown better performance. Additionally, the MUP's microgrid could suffer from an unbalanced phase voltage problem due to single-phase loads that are unbalanced in nature. To address this issue, study [15] presented various control schemes for voltage balancing in a microgrid.

1.4.3 Circulating current problem

Circulating current is another common challenge that arises due to unequal output voltage of parallel-connected converters [14, 19]. Unless controlled, it can lead to higher losses and overloading of energy source, thereby causing source failure and system instability. The following chapters tackle the problem of circulating current in detail and proposing a new control technique for suppressing this current among parallel-connected converters in a Low Voltage Direct Current (LVDC) microgrid.

1.4.4 The complexity of the system controller

MUP's microgrid depends mainly on power electronic converters as interfacing units between the renewable energy sources and its grid. This results in a complex control

system, especially, with considering the coordination among the parallel-connected energy resources [20]. Additionally, there is a lack of technical experience for addressing operational issues such as plug-and-play micro-sources connected to the MUP's microgrid.

1.5 Research question

The previous section highlighted the challenges of the MUP in general, however, this research addressed certain questions. The problem of wind/turbine failure is addressed by many studies in the literature [21-26] as explained later in Section 3.1.2. These studies proposed a parallel converter unit instead of a single unit. In this, the rated converter of the turbine is broken down into a certain number of smaller converters in parallel for the sake of increasing the conversion system efficiency and the turbine availability. But these studies tackled the problem from a control point of view without addressing what is the optimal number of the converters to be connected in parallel. This question is addressed under this research in Section 3.8.

The problem of circulating current minimization is common in microgrids and so it is tackled by many studies in the literature [14, 19, 27-30]. Droop control was the researchers' favour for achieving circulating current minimization and system voltage regulation in DC microgrid. On the other hand, active load sharing techniques such as Instantaneous Average Current Sharing (IACS) has, to the best of authors' knowledge, not been used in DC systems for circulating current minimization. This research studies the feasibility of using the IACS control scheme to achieve the above-mentioned control goals in a DC system. Additionally, only Alternating Current (AC) systems are considered, in the literature, for the MUP's microgrid that results in stability challenges due to limited control capability and capacity capabilities.

1.6 Motivation and objectives

Many projects tackled the grid of the MUPs under the European Union funded programs but all of them considered the MUP with an AC system. Although the AC system is a proven technology over decades ago, AC would not be the best candidate for offshore platforms, especially considering the limited space on the MUP and the high costs of system installation. So, using a DC system for the local grid would bring

some advantages such as reduced distribution losses by reducing AC-DC conversion stages, improved power transfer capability and increased system efficiency due to only one conversion level used, facilitates the connection of appliances, improved power supply reliability, wires can handle more power using DC circuit and lastly no skin effect. Evidently, DC systems demonstrated their benefits in marine ships, electric buses, aeroplanes and electric cars applications.

The research in this thesis aims to investigate the feasibility of using DC systems as a promising alternative approach to improve the MUP electric infrastructure. Additionally, this research addresses the problem of wind/tidal turbines failures due to converter failure. Moreover, the problem of circulating current among parallel DC-DC converters is investigated and a new controller is proposed to minimise it. The main contributions of this thesis are:

- Proposing a new graphical concept for the optimal sizing of a hybrid DC power plant based on renewable energy resources.
- Proposing a new methodology for maximizing the DC conversion efficiency of wind/tidal turbine by defining the optimal number of parallel DC-DC converters connected to the turbine.
- Proposing a new adaptive control technique based on instantaneous average current sharing technique for suppressing the circulating current among parallel-connected converters in an LVDC microgrid.
- Proposing a new floating DC energy unit that comprises wind, tidal and solar energy resources with a storage unit.
- Demonstrate deterministically the limits of stability of the proposed control system.

1.7 Research output

1.7.1 Contribution to conference

- W. M. Nassar and O. Anaya-Lara, "Offshore multi-purpose platform: local electrical network design," All energy 2019 - SEC exhibition centre, Glasgow, United Kingdom.

- W. M. Nassar and O. Anaya-Lara "Modelling and Stability Analysis of a Variable Speed DC Tidal/Wind Turbines with MPPT in Low Voltage DC Microgrid" *2021 IEEE International Conference on Advanced Electrical Equipment and Reliable Operation*, accepted.

1.7.2 Contribution to journal

- Nassar, Walid M.; Anaya-Lara, Olimpo; Ahmed, Khaled H.; Campos-Gaona, David; Elgenedy, Mohamed. 2020. "Assessment of Multi-use Offshore Platforms: Structure Classification and Design Challenges" *Sustainability* 12, no. 5: 1860. <https://doi.org/10.3390/su12051860>.
- Nassar, Walid; Anaya-Lara, Olimpo; Ahmed, Khaled. 2021. "Coordinating Control of an Offshore LVDC Microgrid Based Renewable Energy Resources for Voltage Regulation and Circulating Current Minimization" *Energies* 14, no. 12: 3384. <https://doi.org/10.3390/en14123384>.
- W. M. Nassar and O. Anaya-Lara "A New Graphical Technique for Optimal Sizing of Renewable Energy Resources and Optimal Number of Parallel Converters for Maximizing DC Conversion Efficiency of a Microgrid - Case Study at the North Sea" *Sustainable Energy Grids and Networks-Elsevier*. Submitted (05 Feb 2021).
- Nassar, W. M., Anaya-Lara, O., & Ahmed, K. H. (2022). A new adaptive instantaneous average current sharing technique for circulating current minimization among parallel converters in a LV DC-microgrid. *International Journal of Electrical Power & Energy Systems*, 136, [107562]. <https://doi.org/10.1016/j.ijepes.2021.107562>

1.8 Thesis structure

The research under this thesis is divided into seven chapters. A summary for each chapter is given as follows

- **Chapter one**

Chapter one introduces the thesis with a brief information about the MUPs. This chapter highlights the prominence of the MUPs and the challenges it

would face. Motivation and objectives of the research are presented under this chapter as well as the research output.

➤ **Chapter two**

Chapter two provides an assessment for the MUPs. It overviews potential energy technologies which could be involved in offshore platforms with addressing similar applications all over the world. Additionally, it presents the state of the art of MUPs' structures and design methodology of offshore MUPs. Furthermore, electrical MUPs' grid configuration and control are introduced in this chapter. A floating energy unit is proposed which comprises two wind turbines, a solar array and two floating tidal turbines with energy storage.

➤ **Chapter three**

Chapter three divided, technically, into two parts. The first part, about renewable energy optimal sizing, is presented to show the size of an offshore power plant to meet the demand load of offshore loads such as aquaculture while the second part of the chapter aims to maximise the DC conversion efficiency of wind/tidal turbine. A new sizing method is proposed to estimate the shares of energy resources. The chapter is introduced with a background about optimization methods and sizing methodology. Matlab optimisation tool "Linprog" is used to verify the results of the proposed new graphical concept. A new methodology is proposed to estimate the optimal number of parallel converters to be connected to a wind/tidal turbine, for example, for maximizing the conversion efficiency. A case study for an MUP at the North Sea is provided to demonstrate the validity of the proposed optimal sizing concept and the proposed methodology for efficiency maximisation.

➤ **Chapter four**

This chapter tackle DC-DC power converters from different aspects. First, the topologies of these converters are presented. Secondly, a discussion about control techniques, recorded in the open literature, for a parallel-connected converter is provided. Lastly, a definition for the circulating current among parallel converters, in a DC microgrid, is presented. This circulating current

phenomenon is investigated using Matlab/Simulink models at various operating conditions.

➤ **Chapter five**

This chapter proposes a new adaptive instantaneous average current sharing technique for minimizing circulating current among parallel converters in a DC microgrid. A mathematical model is derived for n -parallel converters with the proposed controller. Additionally, stability analysis of the closed-loop control system is carried out by analysing the locations of the closed-loop poles using root locus analysis. Matlab/Simulink model is implemented to verify the proposed controller performance under different operating conditions.

➤ **Chapter six**

In this chapter, a new coordinated controller is proposed for controlling parallel floating energy units within offshore LVDC microgrid. Configuration of the proposed offshore LVDC microgrid is presented. Mathematical modelling of tidal, solar, wind and battery systems with Maximum Power Point Tracking (MPPT) strategies are derived for stability analysis purposes. Additionally, an overall model for a single floating energy unit is presented with stability analysis. The performance of the proposed controller is analysed, under various operation scenarios, using Matlab/Simulink model.

➤ **Chapter seven**

This chapter provides a summary of the thesis, the author's contribution and suggestions for future research.

Chapter 2 Multi-use Platforms (MUPs)

This chapter provides background and an assessment for the MUPs while addressing other similar applications all over the world. It presents the state of MUP structures and a design methodology for offshore MUPs. A floating energy unit comprising wind, solar and floating tidal systems with energy storage is proposed and selected for further performance and stability analysis described in Chapter 6. The reason for choosing this floating energy unit includes a consideration of the various energy resources that it integrates to improve the power system reliability and mitigate the power fluctuation problem introduced in Section 1.4.2.

2.1 Background

An offshore platform is not a new concept—it existed as early as the 19th century. The first offshore platform was for oil production which was constructed for the first offshore well drilled in California by 1897. The first design for an offshore platform was in 1869 by Thomas Rowland, but it was never built because it was an unrealistic idea at that time [3]. Oil and gas are the only mature sectors that have experience in constructing platforms further offshore. Thus, platform studies of oil and gas represent a large base for other sectors such as energy and aquaculture in terms of floating platforms and subsea engineering.

This chapter is structured as follows: subsections 1, 2, and 3 give a general idea about MUPs and highlight their main components such as potential energy resources. Subsection 4 explores various structures of MUPs. Subsection 5 explains the design methodology for offshore platforms. Subsection 6 examines the electrical issues of MUPs' grid such as network configuration challenges. Subsection 7 highlights the control of MUPs' grid, while the last subsection concludes this chapter.

2.2 Potential offshore energy resources

The main ocean energy technologies are a wave, tidal stream, tidal range and ocean thermal energy conversion. Wind and solar energies are not marine-based technologies, but they could be implemented offshore at different scales. Today, ocean energy from various marine energy resources is developed to a commercial scale with

a generation capacity of 0.5–17 GW under construction. Tidal range energy predominates all forms of ocean energy with around 99% of total installed capacity [31].

Some studies have proposed the combining of marine energies as a better alternative instead of using a single source of energy [32-34]. They claim that many advantages could be achieved such as better reliability systems, increased energy yields, smooth output power, and shared grid infrastructure. In addition, this option is environmentally friendly when compared with the independent installation of energies [34]. The costs of construction and maintenance could be significantly reduced via the use of shared resources such as foundations, logistics, operations, and maintenance. For example, the MWh generated from individually constructed wave converters is still more expensive than their counterparts from other renewable and conventional sources of energy [35]. So, consider integrating the wave energy with different energy resources such as wind or tidal would reduce the costs of wave converter. The following subsections explore the potential renewable sources of energy such as wind, wave, solar, tidal, ocean thermal energy conversion, and biomass that could be integrated on offshore platforms.

2.2.1 Wind and tidal energy

- **Wind energy**

There are two main categories of wind turbines: horizontal and vertical axis turbines. The three-bladed horizontal axis wind turbine is the most common turbine that is used offshore and onshore at a commercial level [36]. On the other hand, Vertical Axis Wind Turbines (VAWTs) have the advantages of simpler structures that make them a better option for floating turbines and cut costs of foundations and quicker response for changing wind direction. Moreover, VAWTs offer lower noise levels, which makes them suitable for MUPs with accommodation. They have a simpler control system as there is no need for pitch control, and their simple structure means that any required maintenance is easier to perform [36]. Many recent studies have developed VAWTs [37-39]. The authors of [39] proposed a new unusual design for a wind turbine that could reduce the cost by 65%.

However, for the purpose of this research, horizontal axis wind turbine is considered because this type of turbines is proven as a mature technology and the proposed floating energy unit has horizontal axis wind turbine-type turbines. Horizontal axis wind turbine can be classified according to the controllability level on its generator speed as follows

➤ **Type 1, turbine with fixed speed**

Wind turbine with fixed rotor resistance of Induction Generator (IG) is directly connected to the grid as shown in Figure 2.1. Type 1 turbines usually equipped with a capacitor bank to compensate for the consumed reactive power by IG. For protection, a Circuit Breaker (CB) is used to disconnect the turbine in case of faults. A Step-up transformer is used for the connection of the turbine to the grid. IG operates at a speed close to the synchronous speed imposed by the grid frequency, and so wind variation has no significant effect on the generator speed [40].

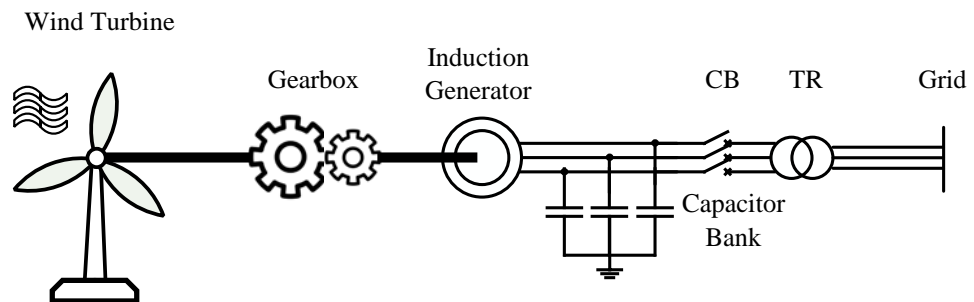


Figure 2.1 Type 1 fixed speed wind turbine.

➤ **Type 2, turbine with limited speed band control**

Type 2 turbines are similar to type 1 but with adjustable IG rotor resistance as shown in Figure 2.2. With help of power electronics, the total resistance of the IG rotor could be adjusted. By adjusting the rotor resistance of IG, the slip of IG can be controlled up to 10% over synchronous speed based on the rotor resistance variation [40].

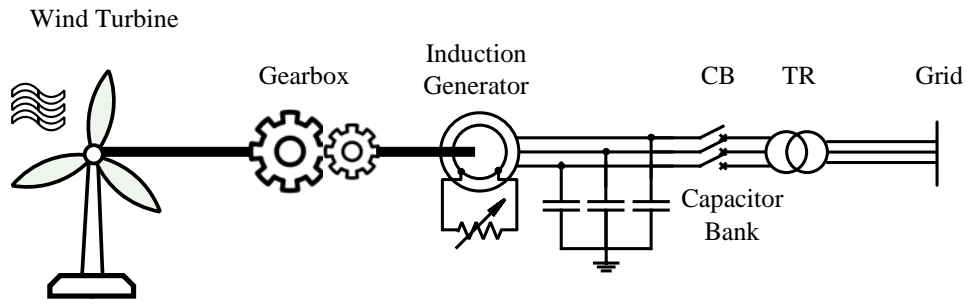


Figure 2.2 Type 2 limited speed wind turbine.

➤ **Type 3, turbine with larger speed band control**

Type 3 turbines based mainly on Doubly Fed Induction Generator (DFIG) which partially control the IG as per Figure 2.3. In DFIG, stator windings are directly connected to the grid while the rotor windings are connected to the grid too but via back-to-back voltage source converters. The rotor side converter in charge of controlling the active and reactive power, while the grid side converter in charge of maintaining the dc link, between the back-to-back converters, stable. In this topology, the stator always feeds power into the grid, while the rotor could feed or absorb energy to/from the grid based on the operation of IG over/below the synchronous speed [40].

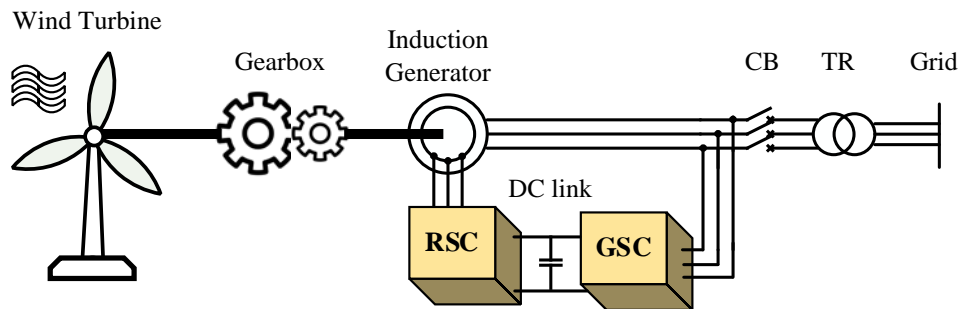


Figure 2.3 Type 3 larger speed band based DFIG.

➤ **Type 4, turbine with full speed control**

Type 4 wind turbine is fully connected to the grid via power converters. So, it could be controllable over the full band of wind speed as shown in Figure 2.4. For this type of turbines, IG or Synchronous Generators (SG) could be used. Both types of SG: wound rotor SG or permanent magnet SG (PMSG) could be

equipped for type 4 topology. PMSG due to its self-excitation gives a high power factor and higher efficiency. Additionally, the gearbox could be eliminated by using low-speed salient pole PMSG and this is a big advantage as the gearbox requires regular maintenance [40].

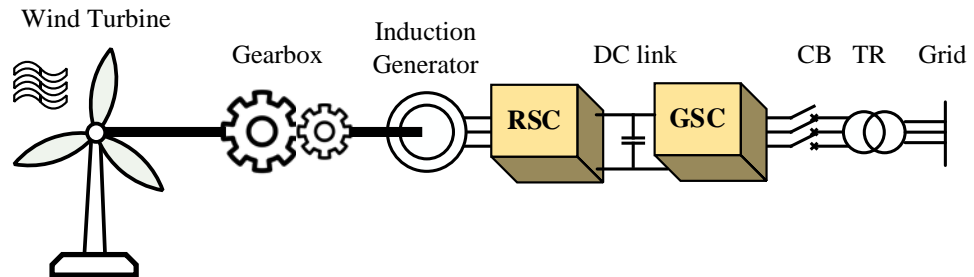


Figure 2.4 Type 4 variable speed wind turbine.

- **Tidal energy**

Tidal turbines have a similar dynamic as the HAWTs with the only difference between them is the water and air densities used for power calculations of each of them. There are many ways to classify tidal turbines. The most common category is based on conversion technology. Study [41] explored the most popular types of tidal turbines based on conversion technology and for more interested readers, studies [42-44] have classified hydrokinetic turbines in more detail.

There are many real tidal projects such as the Skerries Tidal Energy Array with 10 MW in Wales, which has been in operation since 2015, and the Irish Open Hydro Tidal Energy Array project, which is a bigger farm with 100 MW and it is expected to be in commercial operation by 2020. Additionally, the first open sea testing facility on Orkney Island in Scotland has a tidal testing site with a 5 MW power capacity [45]. It is located near Eday at water depths of 12 m and 50 m on an area of 2×3.5 km. Tidal energy is included in this chapter with expectations that the floating version of the tidal turbine (SR2000) will be developed for offshore installation in the future as the available version so far is limited to a water depth of 25 m only.

2.2.2 Floating solar photovoltaic farms

Floating solar Photovoltaic (PV) panels have been proposed under the Modular Multi-use Deep Water Offshore Platform Harnessing and Servicing Mediterranean, Subtropical and Tropical Marine and Maritime Resources (TROPOS) project as a potential offshore energy resource. Floating solar PV panels have proven themselves as an available technology that is already used in onshore lakes, reservoirs and ponds.

In the real world, there are few projects of floating solar PV farms such as that at Far Niente Winery, the USA and the other project, under construction, in Ichihara city in Japan with a power capacity of 13.4 MW [46]. However, the use of solar PV panels in a sea environment is still very limited and should be qualified to withstand humidity, salinity, sea spray, corrosion, and fouling in the open seas. So far, floating solar PV panels have only been used on boats or as a hybrid with a wind turbine in a pilot project [47]. Solar energy based floating PV panels is considered for offshore installation under this research as the satellite structure, which comes later in this chapter, has a solar PV farm.

A solar PV array consists of many PV modules connected in series and parallel as per the required design. PV cell is the basic unit of the PV module which includes electrically connected series and parallel cells. One cell can produce electrical power around 1 to 2 W according to the available irradiance.

The PV cell is modelled, in the literature, with various equivalent circuits according to the number of the considered diodes: single-diode circuit, double-diodes circuit and triple-diodes circuit. The single-diode model has the advantages of simplicity and reasonable accuracy which make it the most used model for simulation studies. Figure 2.5(a) shows the equivalent circuit of a real PV cell considering the dynamic resistances R_s^{PV} which represents the structural resistances of the PV cell, and R_p^{PV} for modelling the leakage current of the $p-n$ junction. i_g^{PV} refers to the current generated by the light as per (1).

$$i_g^{PV}(G, T) = \frac{G^{PV}}{G_r^{PV}} \{I_{sc}^{PV} + K_{sc}^{PV} (T^{PV} - T_r^{PV})\} \quad (1)$$

Where G^{PV} and G_r^{PV} are solar irradiance and the standard irradiance at the standard test condition. T^{PV} and T_r^{PV} are real cell temperature and the temperature at standard test condition. I_{sc}^{PV} and K_{sc}^{PV} are the short circuit current at standard test condition and the short circuit current temperature coefficient which are provided by the manufacturer.

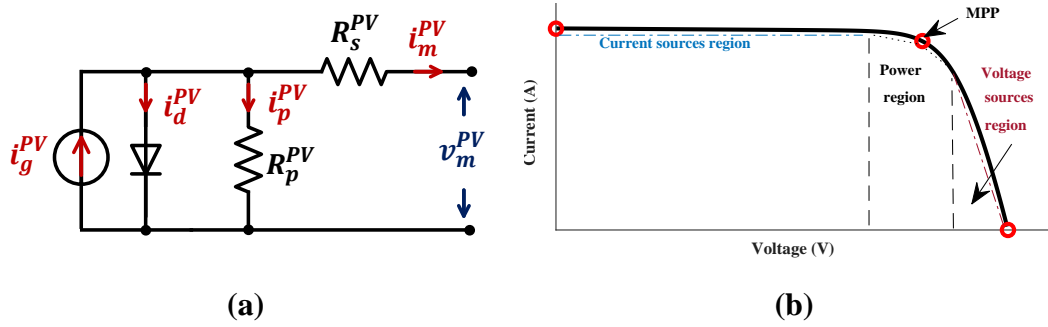


Figure 2.5 Real PV cell: (a) single-diode equivalent circuit and its (b) I - V characteristic curve.

Figure 2.5(b) shows the nonlinear relationship between the output current and voltage of a single PV cell which is described by (2) with ignoring M_s in this equation. M_s is the number of the PV cells connected in series within a module.

$$i_m^{PV} = i_g^{PV} - i_d^{PV} - i_p^{PV}$$

where

$$i_d^{PV} = I_0 \left(e^{\frac{q(v_m^{PV} + R_s^{PV} i_m^{PV})}{M_s k T^{PV} a}} - 1 \right) \quad \text{and} \quad i_p^{PV} = \frac{(v_m^{PV} + R_s^{PV} i_m^{PV})}{R_p^{PV}} \quad (2)$$

With adding M_s to (2), the equation can be used to represent the nonlinear relationship between the output current i_m^{PV} and voltage v_m^{PV} of a PV module. Where q is the electron charge (1.602e-19 C), k is the Boltzmann's constant (1.38e-23 J/K), T^{PV} is the temperature of the p - n junction and a is the diode ideality factor. I_0 is the diode reverse current saturation which is a function of T^{PV} .

Using a single PV module in a power system is unrealistic for its low output power. So, normally many modules are electrically connected in parallel and series as per the

designed output power and voltage, respectively. A model of a PV system based multi-modules is derived in the study [48] using Norton equivalent circuit. At first, the Norton theorem is applied to get the equivalent circuit of a single PV module without the section of the current source and diode to avoid the nonlinearity of the diode as per Figure 2.5(a). Then, the Norton theorem is applied again to obtain the equivalent circuit of the PV system (PV array) which consists of N_s , series-connected modules and N_p , parallel-connected modules, as shown in Figure 2.6.

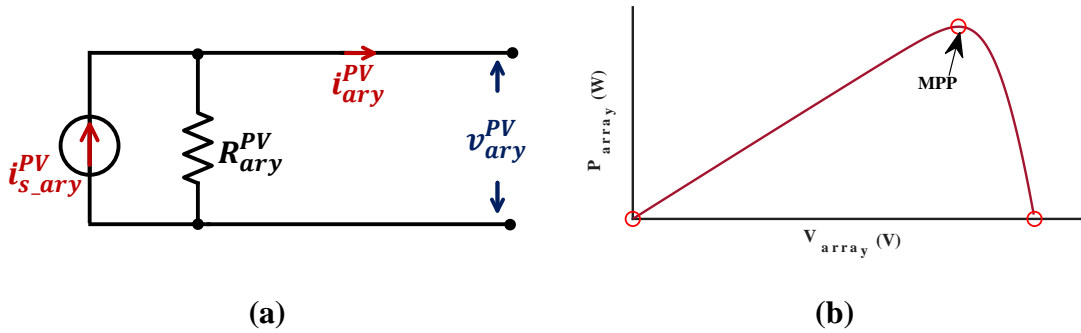


Figure 2.6 PV array (a) Norton equivalent circuit and its (b) P - V relationship curve.

The equivalent current source and resistance are given as follows

$$i_{s_ary}^{PV} = N_p \frac{R_p^{PV}}{R_p^{PV} + R_s^{PV}} [i_g^{PV} - i_d^{PV}] \quad (3)$$

$$R_{ary}^{PV} = \frac{N_s}{N_p} [R_p^{PV} + R_s^{PV}]$$

Equation (3) is valid for the PV array that has the same type of PV modules and is exposed to the same environmental conditions. The relationship between the output current i_{ary}^{PV} and voltage v_{ary}^{PV} of a PV array is obtained based on Figure 2.6(a) as follows

$$i_{ary}^{PV} = N_p \frac{R_p^{PV}}{R_p^{PV} + R_s^{PV}} [i_g^{PV} - i_{d_ary}^{PV}] - \frac{v_{ary}^{PV}}{R_{ary}^{PV}} \quad (4)$$

where $i_{d_ary}^{PV} = \left[I_0 \left(e^{\frac{q}{M_s k T^{PV}} \left(\frac{v_{ary}^{PV}}{N_s} \right)} - 1 \right) \right]$ and $v_{ary}^{PV} = N_s v_m^{PV}$ with considering the assumption of modules similarity which made above.

2.2.3 Other marine energies

- **Wave energy**

The existing wave energy converters can be divided into two main groups: direct action converters that directly convert hydrodynamic energy into electrical energy and an indirect group that does the same function indirectly. The first group of converters has a simpler structure and, as such, is more reliable and less costly [39].

In the real world, the first open sea testing facility at Orkney Island in Scotland (in operation since 2003) has a wave testing site that comprises five berths of 2.2 MW power capacity. Another grid-connected wave hub in South West England includes four separate berths, each with a capacity of 4–5 MW [45]. Recently, the NEMOS team developed a wave energy converter to be installed offshore. This converter has an 8×2 m-sized floater and a structure that is 16 m long. The standalone floating design of this converter makes it ideal for offshore installation with MUPs [49].

- **Ocean thermal energy**

The extraction of energy by using an ocean thermal energy converter is based on the thermodynamic Rankine cycle which is used in steam power plant [50]. For an ocean thermal energy conversion to be a feasible source of energy, a minimum temperature difference between the warm water and the water at 1000 m deep should be at least 20 °C [51]. For this reason, harvesting this energy is specifically available in tropical areas.

An ocean thermal energy conversion can be classified based on the location of the plant or the thermodynamic cycle used. For location-based units, there are three kinds of plants: floating, self-mounted and land-based. In terms of the thermodynamic cycle, there are three main types: open-cycle, closed-cycle, and hybrid-cycle. For more interested readers, details about all types have been provided in the handbook of ocean engineering [50].

Electricity and fresh water are the main outputs of a large ocean thermal energy conversion plant, but various by-products could be harvested such as air-conditioning and aquaculture [50]. A 50 MW hybrid cycle plant could provide the daily water needs for a small community with 300,000 people. Additionally, deep water is 28 times richer in inorganic nutrients such as nitrates, silicates, and phosphates, which could be used in a commercial way for sea farming.

- **Marine biomass energy**

Conventional technologies that are used for extracting biofuels are based on animal oils, vegetables, starch, and sugar, but these methods have been widely criticized because they consume food resources. For this reason, marine algae have appeared on the horizon as a more environmentally sustainable and friendly feedstock because they do not compete with food resources, they save freshwater, and they could be grown by wastewater.

Algal feedstock could be used to obtain energy and non-energy products. Algae could be used as biomass to harvest energy products such as biodiesel, biogas, bioethanol, and bio-jet fuels and non-energy products such as carbohydrates, pigments, proteins, biomaterials, and bioproducts [52]. Bharathiraja et al. [53] concluded that biofuels from marine algae are still not economically feasible due to the high costs of the operation, cultivation, processing, and separation of biofuels. Depending on algae, biofuels that are used as potential storage can provide better reliability for an offshore microgrid and avoid the use of large capacities of batteries.

2.3 Offshore MUP structures

Combining marine energies such as wind, wave, tidal, floating solar farms, algae biomass, and ocean thermal energy conversion with other marine activities such as aquaculture and tourism could be fulfilled in very different ways and concepts. Various structures have been proposed under the funded projects of the European Union, specifically, innovative multi-purpose offshore platforms: planning, design and operation (MERMAID), Development of a wind-wave power open-sea platform equipped for hydrogen generation with support for multiple users of energy (H2Ocean) and TROPOS projects.

Offshore wind energy appears strongly in all structures because it is a developed and mature technology. Various wave converters share these structures to promote wave energy, which still at an early stage of development. The combination of wave and offshore wind energy to generate electricity is a recent topic, and few studies have tackled this issue. Khrisanov et al. [39] highlighted the advantages of using the hybrid wave/wind power system and they concluded that hybridize floating wind and wave power systems is a promising direction for more harnessing ocean energies.

There are two main concepts for hybridizing wind and wave resources: mechanical or electrical combination. The first is combining wind and wave turbines in a mechanical complex system, and the resulting rotation moment of both turbines is used to drive the generator's rotor. Unfortunately, this kind of system suffers from less reliability and increased costs [39]. Thus, this kind of system has not been used, and an electric hybrid system has been proposed. The electrical system depends on the electrical combination between the wind and wave converters, i.e., each converter has its generator and the output power of both are combined via a power electronic converter.

There is a general classification for the offshore structures in terms of foundation type as a function of water depth: fixed structures that are constructed in shallow water with water depth less than 50 m, and floating structures exist in water at a depth of larger than 50 m [45]. Alternatively, MUPs could be classified based on a technological basis, relative location to the shoreline, or water depth. However, MUPs could be categorized, differently, based on the connectivity among activities to co-located systems, combined structures, and island structures.

2.3.1 Co-located systems

In such systems, different kinds of energy farms such as wind and wave, for example, would share the same marine area, maintenance, operation equipment, activities, grid connections, etc., although they do not share the foundations as per Figure 2.7. This kind of combination is proposed at the early stage of development.

2.3.2 Combined structures

The idea of this structure is highlighted under the MERMAID project. In such structures, different energy converters share the same foundation and connections, and

everything is shared as a unit as shown in Figure 2.8 and Figure 2.9 as an example while there are many other structures as explored in study [54]. Some loads such as aquaculture and algae farms could be attached to those structures, as proposed in the TROPOS project for the Satellite Unit as shown in Figure 2.9. The foundation of the structures could be bottom-fixed or floating as per Figure 2.8 (a) and Figure 2.8 (b), respectively [34].

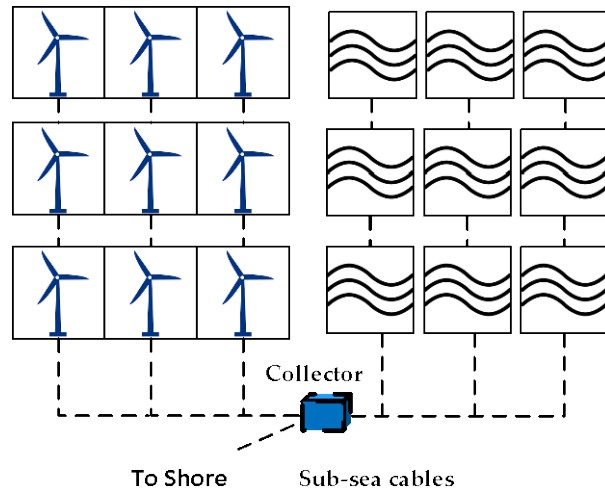


Figure 2.7 Co-located independent wind and wave arrays.



(a)

(b)

Figure 2.8 Hybrid system: (a) Fixed bottom (b) Floating [45].

- **Satellite unit structure**

The TROPOS project proposed what is called a floating satellite unit as shown in Figure 2.9, which combines wind turbines, PV solar panels, and an aquaculture breeding fish facility with an algae farm attached to it [55].



Figure 2.9 Satellite unit proposed under green and blue concept [55].

2.3.3 Island structure

The concept of an island structure became very clear under the TROPOS project via the three proposed island configurations, which are the sustainable service hub island, the green and blue island, and the leisure island. TROPOS project has aimed to develop floating multi-use platforms to adapt to deep waters with a focus on Mediterranean, tropical and sub-tropical areas [56]. Four main sectors are proposed to be integrated into floating islands which are transport, energy, aquaculture and leisure. For more information on artificial and floating islands, interested readers can look at [34]. The following subsections highlight different kinds of floating islands with general information that is useful as a background.

- **Sustainable service hub island**

This is a floating offshore platform with an industrial nature as it includes a lot of cranes and workshops. This concept focuses mainly on energy and transport issues, though it still has leisure activities and aquaculture as per Figure 2.10. It includes a large floating offshore port with repair and maintenance facilities for large ships. Lifting capabilities have been proposed for workshop activities and material storage and handling. The deliverable D4.3 “Complete Design Specification of 3 References TROPOS systems” explored all required elements on this platform [55].



Figure 2.10 Configuration of the industrial complex concept [6].

Aquaculture in this platform is limited because it conflicts with the other considered facilities, such as workshops and material handling. Thus, when possible floating cages could be used for aquaculture in different locations, such as areas between wind turbines and areas that are close to the platform. In this case, feeding operation could be managed via the platform itself or from independent floating silos among the cages [6].

Within this configuration, energy production is comprised of huge renewable sources of a large wave and wind farms. The idea of this configuration is that the generated energy supplies all facilities at the platform, while the excess energy is used to produce gases and liquid fuels that are stored as energy storage to be used as a fuel for fuel cells or even internal combustion engines. It is worth mentioning that this configuration and the green and blue configuration are designed to be grid-connected. However, grid-connected offshore floating wind turbines and arrays have yet to be developed due to a lack of experience. A report prepared by Edinburgh University [57] suggested that a mobile floating offshore substation could be used until a floating substation is proved.

The concept of this island has big influences on the transport, energy and aquaculture sectors in terms of reducing the operation and maintenance costs that are related to these sectors. The implementation of other energy sources such as solar (photovoltaic or thermal), OTECs, and marine energies within the same platform can all act to reduce related costs and increase the reliability of the power system. This platform could serve

the transport and mining industries by providing them with fuel, electrical energy, food and fresh water.

There have been few case studies for this concept, which are used to perform maintenance operations for the existing offshore wind farms. Horns Rev2 was established in the Danish North Sea to provide service for a 209 MW wind farm. Nordsee Ost, Dan Tysk and MittlePlate are three other case studies that were constructed in the German North Sea for the same reason [58].

- **Green and blue island**

This concept is mainly focused on physical and biological ocean resources to extract food and energy [55]. An offshore wind farm, a wave energy farm, aquaculture and an ocean thermal energy conversion, if applicable, are considered to be the main components of this configuration as shown in Figure 2.11. Other than the previous island configuration, this concept completely avoids industrial activities that might jeopardize the aquaculture sector.

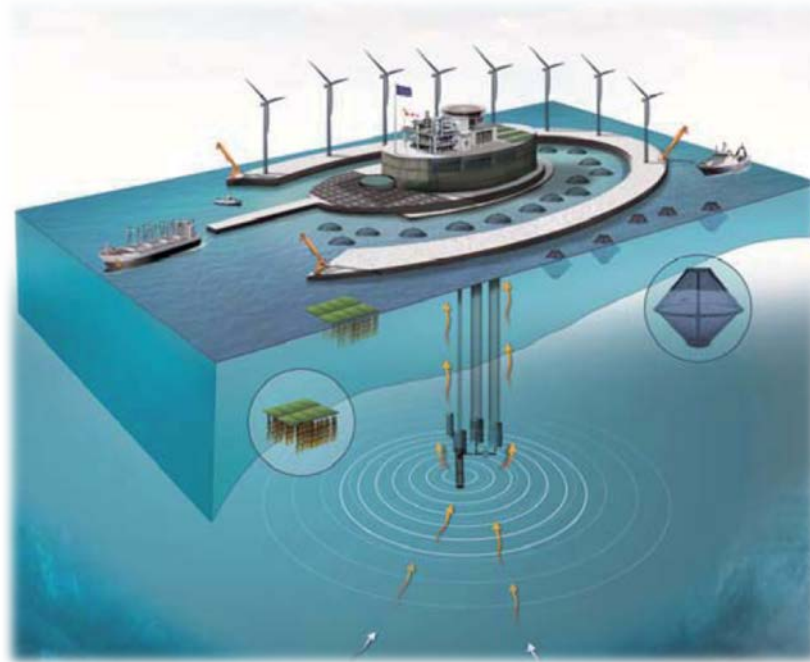


Figure 2.11 Configuration of green and blue platform [6].

The concept of green and blue focuses on algae as a source of energy by converting biomass to energy as explained earlier. Algae farm is attached to a satellite unit as per

Figure 2.9 [55].

Green and blue configuration comprises two main structures: the central unit and the floating module. The central unit involves various sections such as the crew's accommodation, a rescue system, communication, electrical units, a fish processing plant, a unit for exporting aquaculture and laboratories for aquaculture facilities. On the other hand, the floating unit has areas for a twenty-foot equivalent unit of storage and satellite spare parts as well as berthing capability for an offshore supply vessel.

There are two main sub-concepts for this configuration: One is wind and wave plus aquaculture, and the other is aquaculture with an ocean thermal energy conversion [6]. Configuration details about the above two sub-concepts and other configurations are available in [6, 59] and the energy island website [60].

- **Leisure island**

This island platform is in relatively shallow water near the coast compared to the other previous island configurations. It includes different modules: a diving centre, an aquaculture structure, a water sports centre, and an underwater observatory to watch the marine environment and aquaculture around the site as per Figure 2.12.

The floating module in this configuration is a bit different from other island configurations because it has a PV plant with storage and a substation to provide electricity to the central module when required [55]. The island is supposed to be self-sufficient in terms of all kinds of energy demands: electrical power, hot water, and air conditioning inside the buildings. For this purpose, solar energy—either PV or thermal with storage—is extensively integrated into this island's architecture with wind turbines. In other words, the energy demand for this configuration is met by wind and solar energy [6].



Figure 2.12 Configuration of leisure island [6].

2.4 Evaluation of offshore multi-use platforms

Although the MUPs can provide sustainable and economical solutions for the problem of a lack of seafood and higher prices of offshore energy, it should be designed in a way to avoid or reduce negative environmental and ecological impacts. There are some concerns about living marine environments and habitats that could be affected by the foundations of MUPs and cages [7]. Additionally, MUPs might conflict with other marine activities such as transport, tourism, fishing, entrance to marine ports, wildlife and birds area protection.

Marine litter is another problem that could be increased with commercialized MUPs. Plastic alone (around 60–80% of marine litter) was estimated to exist as 275 million metric tons (mt) in 2010, and this quantity could be increased by increasing the number of MUPs. Marine litter has a negative impact on human health, marine environments, marine ecosystems, marine industries, and marine species, and this leads to negative economic impacts. Additionally, the power system of MUPs should use 100% renewable energy resources to avoid releasing CO₂ which leads to ocean acidification that would harm the marine ecosystems [61].

2.5 Offshore MUP design methodology

Designing an offshore MUP requires the assessment of the project site from different sides: technical, economic, social and environmental. Thus, involving all relevant stakeholders at an early stage of development is required because the design of such installations depends on experts' judgement from different sectors. Barbara et al. [62]

proposed a methodology consisting of four phases for the design of an offshore platform: the pre-screening phase, the preliminary design of the single-use platform, the ranking phase and the preliminary design for the selected MUP as shown in Figure 2.13.

The pre-screening phase examines the platform components (energy sources, aquaculture, marine service hub, and leisure island) based on the site conditions in terms of wind speed, yearly wave power, tidal range, and potential fish production. The outcome of this phase is to define the various uses that are integrated onto the offshore platform at a specific site.

The preliminary design phase chooses the most suitable energy converters and applicable fish farms based on the site assessment that was accomplished in the first phase with taking legal constraints into account [62].

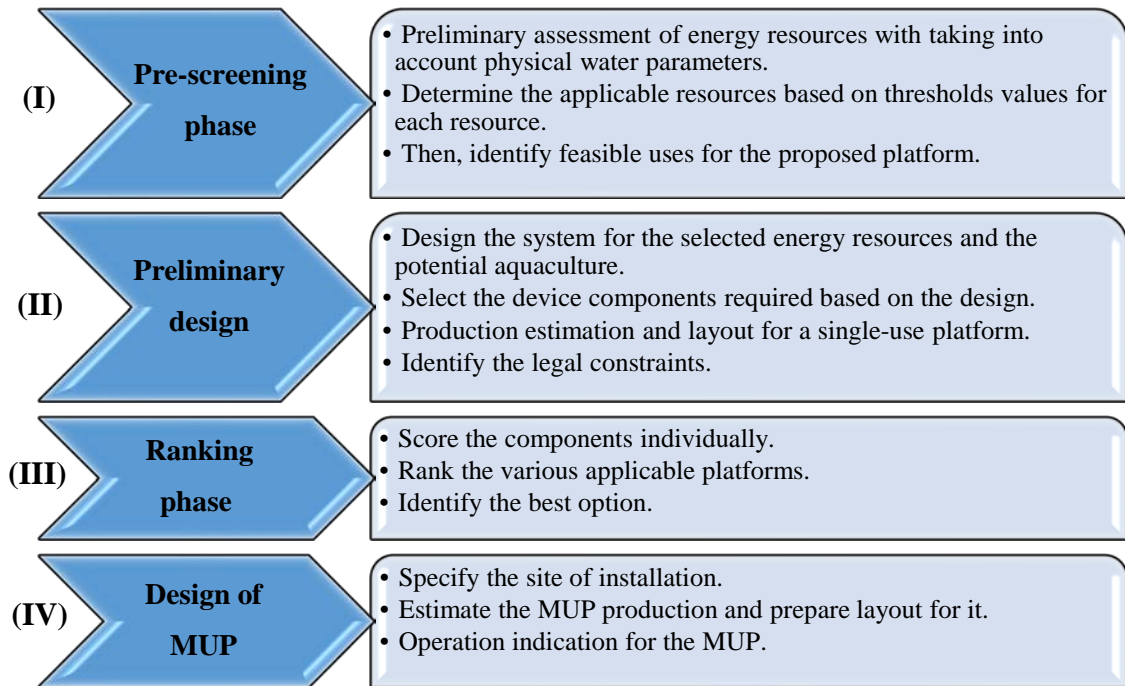


Figure 2.13 Offshore platform design phases [62].

The third phase is a ranking step where a score is given for each component in the platform based on technological and potential risks aspects. For the development level of the technology, many factors are taken into account such as reliability, performance, installation and maintenance costs as a function of system mechanical complexity and water depth. For the potential risks, factors such as pollution, power take-off failure,

geotechnical failure, and structure modularity should be considered. Then, the assigned scores for each module are combined and alternatives are weighted based on the score of each combined module. The outcome of this phase is to determine the best scheme for an offshore platform at a specific site.

The last phase is to design the selected scheme with taking the interaction and the conflict between different components on the platform into account, in addition to the optimization of spatial planning [62]. For example, the proposed sustainable service hub platform under the TROPOS project has a conflict between the aquaculture cages and the service activities that make the surrounding water not pure enough for growing fish as per Figure 2.10.

2.6 Offshore MUP grid configuration

This section highlights the electrical connection between different components of an offshore platform. It is important to differentiate between two different electrical layouts: the hybrid energy resources layout and the MUP's microgrid layout. Hybrid energy resources represent the generation power plant or the supply to the MUP's microgrid. This supply depends on different marine energies, as presented in Section 2.4.2 of the combined structures.

The electrical connection between such structures has not been reported in the literature of the MUP, to the most of author's knowledge. For this reason, this chapter proposes the layout of wind energy farms to be applied for hybrid energy resources as shown in Figure 2.14. A cluster within the wind farm could include k wind turbines, but here it combines k structures where a structure could have different renewable energy resources. Figure 2.14 shows different connection levels, starting from the structure level, through the cluster and array level, to the node level, and ending with the substation level. A substation could supply the offshore platform or export energy, after adding extra equipment, to the shore in the case of large-scale energy farms.

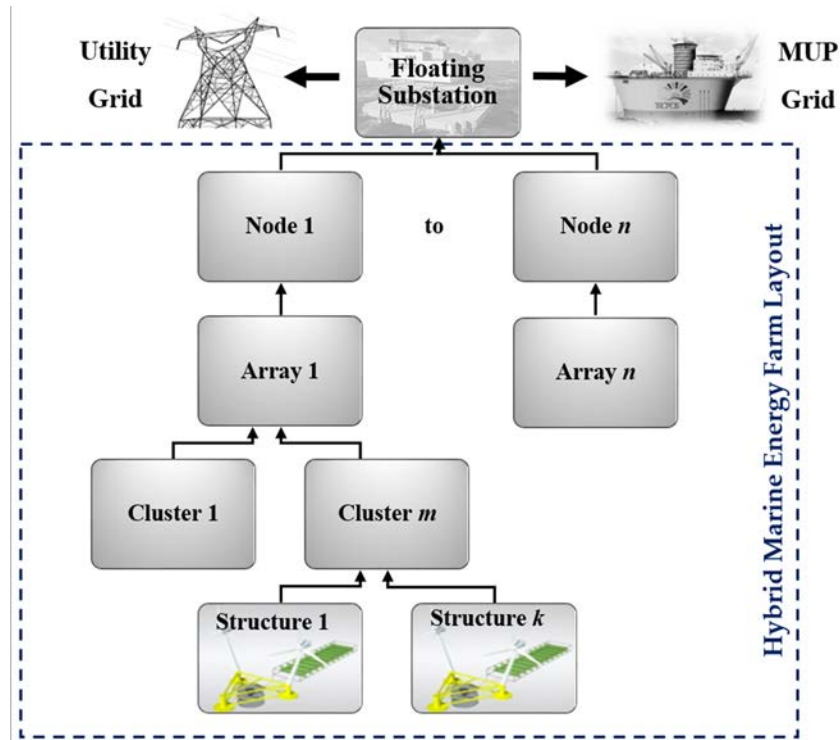


Figure 2.14 Configuration of hybrid marine energy farm supplies an MUP's microgrid.

A node is a single collection point within an array [63]. An array connection could be a proper alternative when multiple devices are connected in an array. Different array schemes are chosen based on geotechnical conditions and resource characteristics. The size of an array is limited by the acceptable voltage drop along cables and the array's maximum capacity [45].

An offshore MUP's microgrid has been explored under the TROPOS project for the three different island configurations presented in Section 2.3.3. Two AC low voltage levels have been introduced 400 and 230 VAC and 24 VDC for DC loads as shown in Figure 2.15. The 400 VAC voltage level considered for loads such as acclimatization, a refrigeration system, a lubricant system, a sewage system and a rescue system. The 230 VAC voltage level considered for loads such as aquaculture and algae systems, illumination, restaurant, hotel, and battery charger. The daily load profile of the three island scenarios is provided in [55].

However, as this research consider the analysis of MUP's DC microgrid, it is important to highlight that 1500 V is the upper limit voltage of LVDC systems which set by IEC60038 [64]. Due to the lack of standardization, there are various voltage levels (12,

48, 120, 230, 325, 380-400 and over 565 V) used in the LVDC distribution system in different applications [64]. Study [65] proposed a 3-wire system of 700 VDC (+350 VDC, 0 V, -350 VDC) that would be beneficial for use in mixed networks with industrial and residential loads. Using ± 350 VDC provide availability for connecting residential devices via +350 VDC safely and efficiently. Also, enables optimal use of copper. Besides, it is easy to scale it to a high voltage level (± 700 VDC). However, study [64] proposed a bipolar topology with different voltage levels (± 750 VDC) as the second voltage level can be extracted (± 375 VDC).

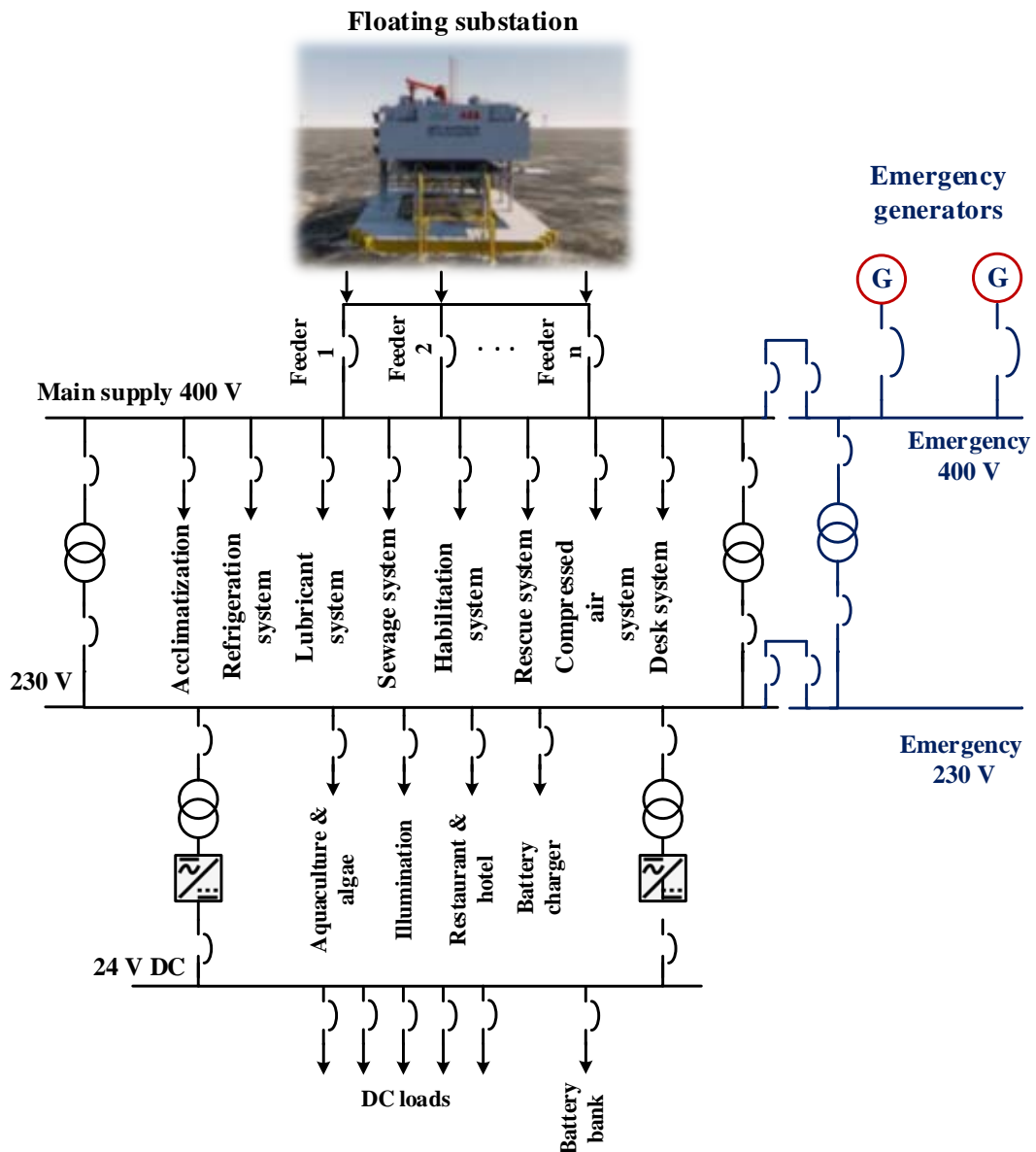


Figure 2.15 Single line diagram for an MUP's microgrid.

2.7 Offshore MUP grid control

Conventional grid depends on large synchronous generators that make its control system is simpler than that of isolated grids [66]. MUP's microgrid has a completely different nature from that of a conventional grid, as the former depends on a group of inverters, synchronous generators, and asynchronous generators [45].

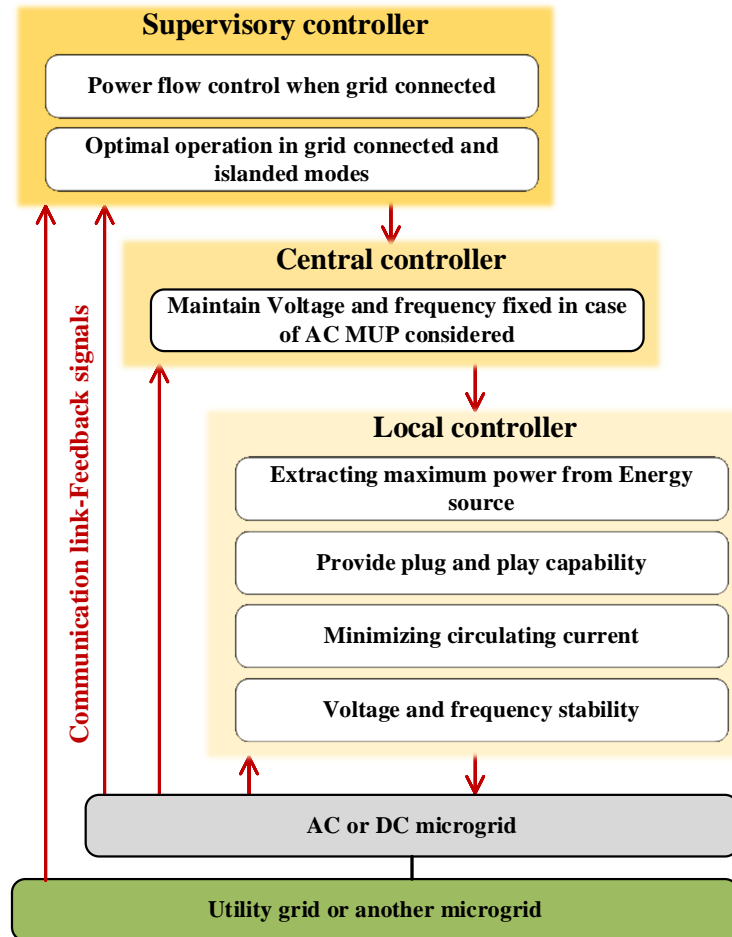


Figure 2.16 Microgrid hierarchical control [67].

Studies [66-69] have proposed a hierarchical control strategy with three control levels for controlling a microgrid considering various operation modes: islanded, grid-connected and connections with other microgrids as shown in Figure 2.16. This hierarchical control includes three control levels: a local controller, a central controller, and a supervisory controller from the lower to higher levels, respectively.

There are two types of local controllers: micro-source controller and a load controller. A micro-source controller performs some local functions, such as controlling the

voltage and frequency of microgrid in transient conditions, and it follows a central controller when connected to the grid. Both micro-source controller and central controller are used to optimize the active and reactive power of the microsource and track the load after the islanding operation. An load controller is installed at the load side to manipulate the load via a central controller for load management [68]. There are various strategies for implementing local controllers, and these were well-presented in [67].

Frequency and voltage changes could occur with a local controller even during a steady-state. Thus, a central controller is used to compensate for this deviation. However, controllers at this level are designed with a slower response time than local controllers. Lastly, the supervisory controller is the slowest control level which manages the flow of power among microgrid and utility grid to achieve optimal economic operation [67].

2.8 Summary

This chapter presented a background about the MUP, its applications and classification. A brief knowledge was given about the two big projects: the Ocean of Tomorrow and Horizon 2020 that were funded by the European Union to develop ocean technologies for energy and food harvesting. The potential offshore energy resources to be integrated with the MUP were discussed in this chapter as well. The design methodology of the MUP was explored by highlighting the different phases required for the design. The chapter proposed the classification for the offshore structures based on connectivity among different energy converters and activities to co-located systems, combined structure and island structure. The main points to be concluded from this chapter are:

- Due to the limited literature about the electrical grid configuration of MUP's microgrid, this chapter considered the layout of offshore wind energy farms for MUP's microgrid.
- From various reviews it was observed that the DC system is never been considered for offshore platforms even though this could be a better alternative for its advantages. For this reason, this research investigates the feasibility of using a DC system to improve the infrastructure of the MUP.

- The satellite structure is selected and improved by adding a floating tidal turbine. By this, a new floating structure that comprises wind, tidal and solar power sources with a storage unit, is proposed under this research as an energy unit for the offshore DC microgrid. The reason behind this choice is to integrate tidal energy, as a predictable energy resource, with the satellite unit for improving the reliability of the electric system.
- Algae biofuels would play a vital role as a potential energy storage that gives better reliability for the offshore power system and avoid using large capacities of batteries, however, it is not considered under this research.

Chapter 3 Optimal Sizing of Renewable Energy Resources

This chapter aims to improve the electric infrastructure of the MUP's micorgird by maximizing the efficiency of the DC conversion of wind/tidal turbines via determining the optimal number of parallel converters connected to a turbine. To work out the size of an offshore power plant that meets the MUP's demand load, this chapter proposes a new graphical concept to determine the share of the renewable energy resources considering the floating energy structure opted for in Chapter 2. Furthermore, a case study is considered for a site at the North Sea to show the effectiveness of the proposed techniques. This case study is based on the concept of Green and Blue island which was introduced earlier in the previous chapter under Section 2.3.3.

3.1 Background

Numerous hybrid power systems in the literature are comprised of wind and solar energy resources due to the complementary nature between them [70]. Tidal energy is not a common element of hybrid power systems and few studies have tackled it with wind energy as a hybrid shared structure [71-75]. This research considers integrating three energy resources (tidal, wind and solar) as a promising alternative to improve the reliability of power systems.

3.1.1 Optimal sizing of hybrid power systems

An optimal sizing of a hybrid power system should consider economic and technical factors to guarantee the lowest investment with higher reliability of the hybrid system [76]. Normally, in the sizing of hybrid power systems, a multi-objective function is considered, as the system costs are the main objective while the other objectives could be constraints such as system reliability, system environmental impact or system failure [77]. This multi-objective function is a complex problem due to the contradiction among different objectives, however, it is a more realistic choice as the system oversizing will increase the capital cost while system undersizing would lead to power system failure [78].

- *Objectives of an optimisation problem*

Defining the objectives of the optimization problem is an important step to be considered during sizing process of the hybrid power system. In the open literature, these can be categorized into economic, technical, and environmental objectives. There are various measures which reported for each objective and can be summarized as follows

- a) Economic objectives can be evaluated using net present cost, life cycle cost of energy, the annualized cost of the system or Levelized Cost of Energy (LCOE) could be used [67]. Study [75] considered the system costs are comprised of the net present cost of investment, operational, maintenance and replacement costs, as well as load interruption costs over the project lifetime.
- b) Technical objectives can be assessed by indicators such as Loss of Power Supply Probability (LPSP), loss of load probability, unmet load, system performance level [79]. Equivalent loss factor index considers the outages of the system components, which make it more reliable for robust system design [80].
- c) For environmental impact assessment, life cycle emissions can be used.

In this regard, numerous sizing power studies have considered three objectives to be met for assuring optimal system configuration: The net present cost of the system over the lifespan, green gas house emissions and unmet load or system reliability [77, 81-84]. However, Study [81] used embodied energy as a constraint. Cradle-to-grave approach is used to estimate this energy which associated with the fabrication and manufacturing process of a product and this includes the energy used for extracting raw material, manufacturing, transportation, distribution and all other energy required for the product until the end of product life [85]. Perera et al. [82] based their optimisation study on four objectives and constraints: unmet load, levelized cost of energy, wasted renewable energy and fuel consumption. Study [83] included the operational performance in their optimisation problem by adding real and reactive power loss as a constraint. Arabali et al. [84] considered the cost and efficiency of the system as the main objectives.

Studies [80, 86, 87] highlighted that the effect of randomness and uncertainty of the system components, such as failure or outages, could not be assessed by any of the

objectives mentioned above and so stochastic analysis is recommended to guarantee a robust and more reliable system. For this, Shi et al. [86] reported that the stochastic of the system performance can be measured by the mean value and the standard deviation of the deterministic objectives such as system cost and unmet load, autonomy level etc.

- *Optimisation techniques*

Optimisation techniques, in the open literature, can be classified into conventional, non-conventional and hybrid techniques. Identifying a suitable technique to solve the optimisation problem is a critical issue and should be done based on the nature of the system. Sinha et al. [79] in their review study, concluded that the optimization methods in the literature are quite different in terms of the level of accuracy, performance efficiency, convergence speed and computation speed. So, the selection of the convenient technique should be based on the user requirements, type of application, etc. The next section explores briefly the positive and negative sides of each category of optimization techniques.

Conventional techniques appeared at an early stage to find the optimal configuration of the hybrid system. These methods have the advantage of simplicity, ease to use and they could be applied for different applications [77]. However, Singh et al. [77] highlighted that these techniques suffer from some limitations as they are trapped in local optima when used with a large number of variables or applied to the non-linear objective function.

Non-conventional methods based on swarm behaviour or biological evolution have drawn the attention of researchers due to the complexity of the multi-objective problems and to alleviate the drawbacks of conventional methods. Although these methods have improved the optimization process by tackling complex and multi-objective problems, it has the problem of premature convergence as it takes a long time to come out from local maxima or minima.

To solve the problem of time-consuming of non-conventional methods, researchers in their recent studies, found that hybridization between different methods would lead to powerful methods that alleviate the drawbacks of the non-conventional techniques.

Genetic algorithm has a good reputation among researchers for its successful results in both single and multi-objective optimization problems on various engineering applications. It is a robust technique in solving multi-model multi-objective problems for finding the globally optimal solutions of system configuration. A large number of hybrid wind-solar studies have used genetic algorithms for finding the optimal system configuration [77]. Genetic algorithm was a common element in the hybrid algorithms other than it used as an individual technique in a large scale of studies. For example, it was used with another non-conventional technique such as artificial neural network to optimize a standalone solar system [88, 89]. It was applied with one of the conventional techniques, iterative approach, for optimization of the hybrid wind-solar system [90].

3.1.2 Optimal number of parallel converters for efficiency maximization

Although power converters help in improving power production from wind turbines via facilitating variable speed operation, DC-DC converters are suffering from lower efficiency at low power levels, specifically, wind turbines operate below the rated power most of the time [91]. Additionally, the power converter has the highest failure rate among other components of the turbine, as explained in Section 1.4.1, which result in loss of energy production [12]. Moreover, using Pulse Width Modulation (PWM) for driving the converter switches introduces harmonics to the grid [26].

Many studies in the open literature addressed these issues [21-26]. For example, to improve the overall efficiency of Input Parallel Output Parallel DC-DC converter system, study [21] proposed a control strategy based on proportional current distribution to ensure that the converter system is working efficiently at all load conditions and to facilitate alternating between current sharing mode and current distribution mode. For the same reason, study [22] proposed an on-off control technique with optimized switching points to minimize the power losses of the DC converter system via enabling a certain number of converter modules according to the load current. Study [23] proposed an efficiency-based current distribution scheme to improve the efficiency of a DC converter system connected to a PV array. Study [24] proposed an efficiency enhanced coordination control scheme to improve the efficiency of modularized parallel DC-DC converters via controlling the power flow

in each converter. The study presented this converter system for interfacing battery storage to a microgrid and the results showed that the current distribution control scheme achieves better efficiency over current sharing control scheme at light loads reaches to 90% efficiency.

The concept of using parallel converter modules instead of one rated converter module is known in the industry as well. For example, G10x 4.5 MW wind turbine from Gamesa uses a converter system consists of six identical converter modules with a power rating of 770 kW/950 kVA each [25]. Consider the idea of using parallel converter modules brings some advantages such as improving the DC-DC conversion efficiency as the above-mentioned studies presented. Also, it increases the power availability and the turbine reliability. This is because the faulty converter in a parallel converter system can be isolated without compromising the whole production of the system. Additionally, it reduces or eliminates the grid harmonics by phase-shifting PWM pulses of the activated parallel converters [26]. Moreover, it increases the lifetime of the components such as Insulated Gate Bipolar Transistor , main fan and control-card that have higher failures in time rates, as only a certain number of converter modules are activated at a time based on the available power from the turbine.

The above mentioned studies presented various control techniques for improving the overall efficiency of the conversion system. All of them focused on the operation stage of the system, i.e. the system is already designed and the converter system has a defined number of parallel converter modules. None of those studies considered the optimal number of parallel converters modules required to maximise the overall conversion system efficiency. So, the second part of this chapter addresses this issue and proposes a solution for determining the optimal number of parallel converters to be connected to a wind/tidal turbine for efficiency maximisation.

The rest of this chapter is organised as follows: after background, Section 3.2 introduces the sizing methodology. Section 3.3 and 3.4 describe the system configuration and optimisation modelling of energy resources, respectively. Section 3.5 presents the data profiles of wind, tidal and solar energy resources. Section 3.6 highlights the objectives and constraints to be fulfilled by the optimisation model.

Section 3.7 explores the optimisation model and results. Section 3.8 explains the new methodology for determining the optimal number of parallel converters connected to wind or tidal turbines. Lastly, a summary is provided in the last section.

3.2 Optimal sizing methodology

Figure 3.1 shows a flowchart for the sizing process of a hybrid system. Prior sizing process, an assessment for the renewable energy resources available at a specific site must be done. Then, technical data for the site location such as temperature, solar irradiation, wind speed or tidal current speed are required at the first step for the considered renewable energy resources. These data could be measured, real-time, on-site data, predicted data or tabulated or graphical data from different metrological websites. In addition to economic data about component costs and maintenance and operational costs [77].

The next step to consider, in the optimisation process, is the overall optimisation model for the whole system which comprises an individual model for each energy component [76]. The following step is to identify the design variables. The design variables are the parameters that have a direct impact on the energy output of the hybrid system, i.e. by changing them, a significant change in the system output will be observed. These variables are vary based on the nature of the energy component, for example, a solar component has design variables such as tilt angle and the number of PV modules, while wind energy component may have design variables such as hub height and the number of wind turbines [76]. Afterwards, the main objective and constraints are identified.

All the previous steps contribute to shaping the optimisation problem, which could be a single-objective or complex multi-objective problem as discussed in the previous section. Next, an optimisation technique should be chosen based on the type of optimisation problem. Using the opted technique with the initial values of the design variables, the cost function is evaluated then checked to ensure it satisfies the identified objective and constraints.

Then, the design variables are modified in a loop until they satisfy the objective and the constraints of the optimisation problem, at which the optimal size of the hybrid

system is obtained. The accuracy of the optimization results depends on the accuracy of the component model, the choice of the objectives and criteria of the optimization problem and the choice of the suitable optimization technique for the complexity of the system.

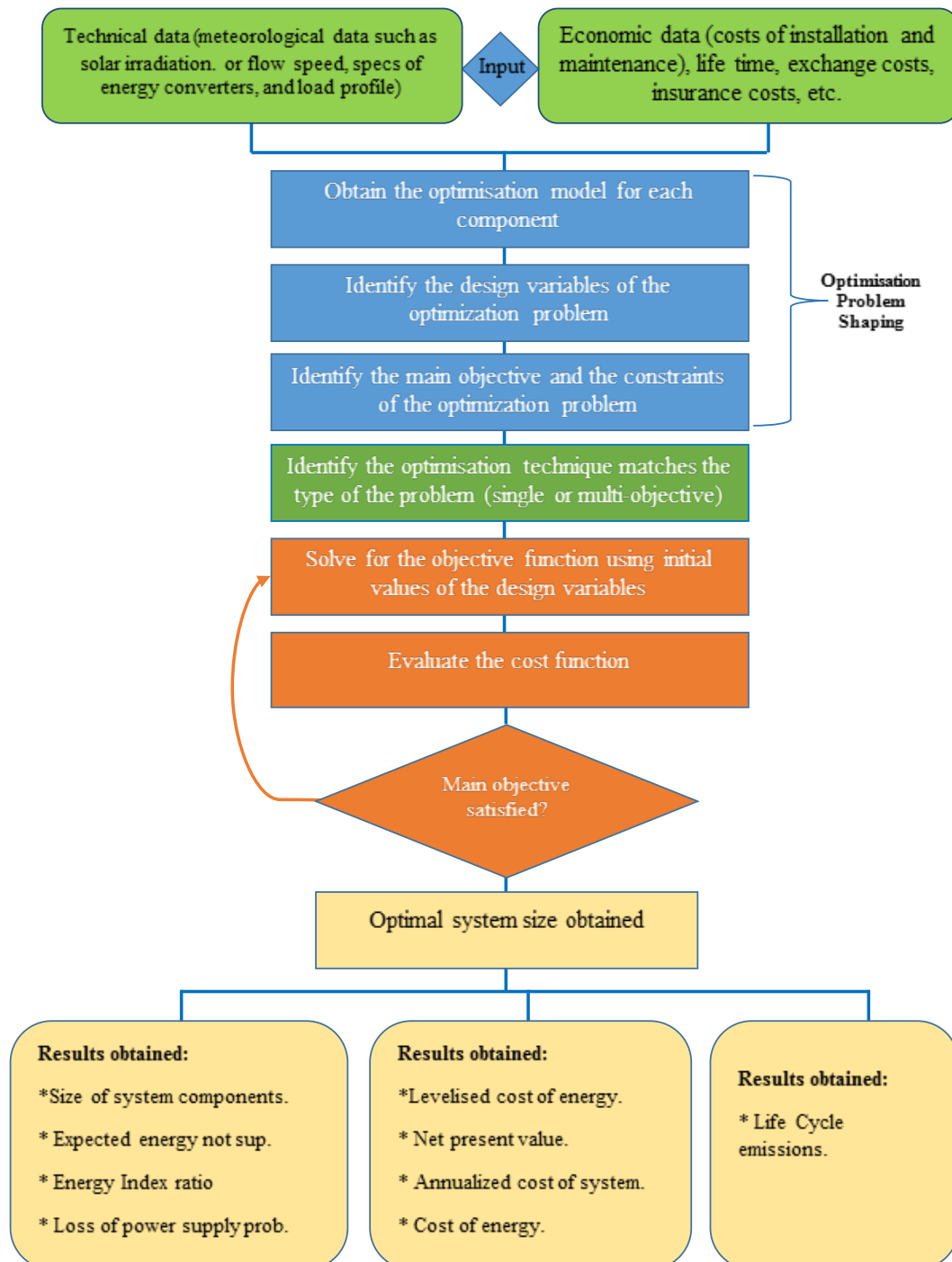


Figure 3.1 Hybrid power system optimization steps [77].

3.3 Proposed system description

An islanded hybrid power plant is proposed for supplying the MUP's microgrid as per Figure 3.2. The system consists of n -floating energy units where every unit includes wind, tidal and solar energies with a storage system. These components connected to a local bus via AC-DC and/or DC-DC converters which supply local loads or deliver energy to a central/collection bus. The MUP's microgrid is supplied from this central bus.

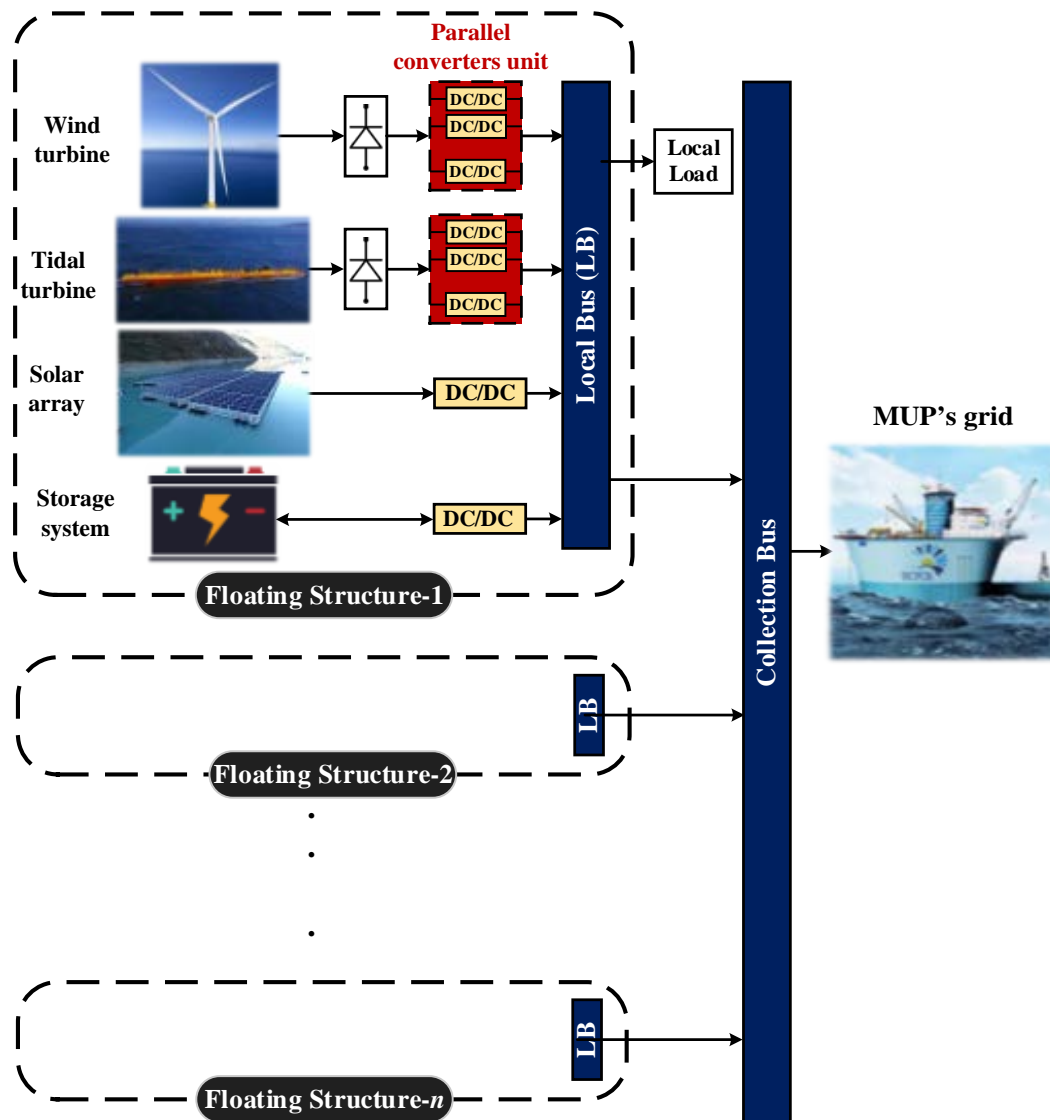


Figure 3.2 Configuration of hybrid power plant supplies loads of MUP's microgrid.

Figure 3.2 shows that tidal/wind turbines are connected to parallel converters unit instead of one rated converter for conversion efficiency maximisation as explained in Section 3.1.2.

3.4 Optimisation modelling of energy resources

Optimisation models of system components (tidal, wind, solar and battery) are presented under this section.

3.4.1 Optimization model of wind/tidal turbine

Consider horizontal axis turbines, conversion system of wind or tidal turbine is quite similar as both turbines have mechanical parts such as blades, pitch angle control mechanism and gearbox. Additionally, both turbines have the same electrical parts such as generators and power converters. Moreover, wind and tidal turbines share the same fluid dynamics except wind turbines work in air surroundings while tidal ones work underwater. So, to estimate energy production of wind and tidal turbines, air and water densities are considered, respectively as per (5) and (6) [73]. However, for safety and efficiency purposes, turbines are designed to work only between cut-in and cut-off speeds as Figure 3.3 shows.

$$P_w = 0.5\rho_w \cdot A_w \cdot C_p(\lambda, \beta) \cdot V_w^3 \quad (5)$$

$$P_t = 0.5\rho_t \cdot A_t \cdot C_p(\lambda, \beta) \cdot V_t^3 \quad (6)$$

Where P_w , P_t , V_w , V_t , ρ_w , ρ_t , A_w and A_t are the output power (w), velocity (m/s), density (kg/ m³) and rotor swept area (m²) of wind and tidal turbine, respectively. C_p , λ and β are the performance coefficient, tip speed ratio and pitch angle (degree °), respectively.

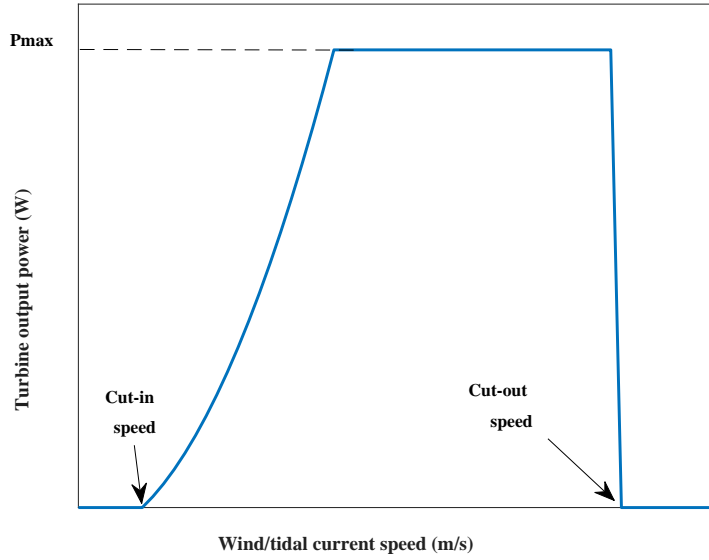


Figure 3.3 Wind/tidal turbine power curve [92].

Based on Figure 3.3, optimisation models of (5) and (6) can be refined to, accurately, estimate the energy production of wind and tidal turbines as per (7) and (8), respectively [73, 92].

$$P_w = \begin{cases} \frac{V_w^2 - V_{Cin_w}^2}{V_{rated_w}^2 - V_{Cin_w}^2} \times P_{rated_w} & ; V_{Cin_w} \leq V_w \leq V_{rated_w} \\ P_{rated_w} & ; V_{rated_w} \leq V_w \leq V_{Cout_w} \\ 0 & ; V_w \leq V_{Cin_w} \text{ and } V_w \geq V_{Cout_w} \end{cases} \quad (7)$$

$$P_t = \begin{cases} \frac{V_t^2 - V_{Cin_t}^2}{V_{rated_t}^2 - V_{Cin_t}^2} \times P_{rated_t} & ; V_{Cin_t} \leq V_t \leq V_{rated_t} \\ P_{rated_t} & ; V_{rated_t} \leq V_t \leq V_{Cout_t} \\ 0 & ; V_t \leq V_{Cin_t} \text{ and } V_t \geq V_{Cout_t} \end{cases} \quad (8)$$

Where P_w , P_t , V_w , V_t are the output power (w) and velocity (m/s) of wind and tidal turbines, respectively. P_{rated_w} and P_{rated_t} are the rated wind and tidal powers. V_{rated_w} and V_{rated_t} are the rated wind and tidal speeds. V_{Cin_w} and V_{Cin_t} are the cut-in

speeds of the wind and tidal turbines. V_{Cout_W} and V_{Cout_t} are the cut-out speeds of the wind and tidal turbines.

3.4.2 Optimization model of a solar module

A single PV cell has very low power and voltage outputs, so a solar panel comprises several cells connected in series to produce reasonable voltage and power outputs. Equation (9) is used to estimate the output power (P_{pv}) of a solar module [93].

$$P_{pv} = \eta_{mod} A_{pv} G_{tit} [1 - 0.0045(T_C - 25)] \quad (9)$$

where A_{pv} , η_{mod} , G_{tit} , T_C are the panel service area (m^2), electrical efficiency at standard test condition, slope irradiation and solar cell temperature ($^{\circ}C$), respectively.

3.4.3 Storage unit optimization model

Battery lifespan is shorter than other renewable energy resources and should be replaced during the project lifetime. Therefore, deriving a battery lifetime model is important for more accurate system cost estimation and for maximizing battery lifespan during the optimisation process. For maximising the battery lifetime, the battery maximum SOC and DOD must be considered.

There are various models for charging and discharging the battery system depending on various scenarios of the available and deficit energy. Two charging scenarios are identified, when the generated power is higher than the demand load and the whole energy surplus can be charged to the battery as per the first equation of (10). In this equation, $SOC(t - 1)$ represents the previous state of charge of the battery while the difference between the available power from the renewable sources and the load power ($P_{gen}(t) - P_{load}(t)$) shows the surplus energy to be charged to the battery. The second term of this equation represents the increased SOC due to charging the surplus energy.

The second charging scenario occurs when the energy surplus is higher than the battery capacity and this is modelled by the second equation of (10). In this equation, the difference between the assumed battery capacity and the current battery charge ($C_b - C_b(t)$) represents the amount of charge which can be accepted by the battery

not to exceed the maximum limit of SOC. The energy that exceeds this difference is considered as a dumped energy as shown in Figure 3.10.

$$SOC(t) = SOC(t - 1) + 100 \left(P_{gen}(t) - P_{load}(t) \right) \eta_{ch} \frac{t_{ss}}{C_b} \quad (10)$$

$$SOC(t) = SOC(t - 1) + 100 (C_b - C_b(t)) \eta_{ch} \frac{t_{ss}}{C_b}$$

where $SOC(t)$ refers to the annual hourly-averaged state of the charge of the battery system, $P_{gen}(t)$ is the hourly-averaged energy production from solar, wind and tidal resources in total, η_{ch} is the charging efficiency of the battery, $C_b(t)$ is the hourly-averaged battery capacity charge, t_{ss} is the step size (hour), C_b is the considered battery capacity (kWh) for the system and $P_{load}(t)$ is the hourly-averaged load power.

On the other hand, there are two different scenarios for battery discharging, both scenarios apply when the demand load is higher than the energy production. During the first scenario, the battery storage is able to cover the demand load, while it cannot do with the second scenario as per the first and second models in (11), respectively.

$$SOC(t) = SOC(t - 1) - 100 \left(P_{load}(t) - P_{gen}(t) \right) \eta_{disch} \frac{t_{ss}}{C_b} \quad (11)$$

$$SOC(t) = SOC(t - 1) - 100 (C_b(t) - C_b^{min}) \eta_{disch} \frac{t_{ss}}{C_b}$$

where C_b^{min} is the minimum battery capacity at which the battery system cannot deliver energy. η_{disch} is the discharging efficiency of the battery. In the first line of (11), the battery is able to cover the power deficit which is represented by the difference $(P_{load}(t) - P_{gen}(t))$. The second term of this equation shows the amount of SOC that will be taken out from the previous SOC. The second line of (11) implies that the battery cannot cover the load as the SOC will reach the minimum value. In this equation, the difference between the battery capacity charge and the minimum battery capacity $(C_b(t) - C_b^{min})$ represents the amount of the last energy that can be

delivered from the battery and the required energy after this limit is considered deficit energy as indicated in Figure 3.10.

3.5 Data description, a case study at the North Sea

The location of the MUP is chosen to be in the North Sea at Latitude $51^{\circ} 37' 33.5''$ (51.626), and Longitude $1^{\circ} 29' 45.5''$ (1.496) as per Figure 3.4 at a distance of 22 Km from shore.

The opted location of the MUP is close to a site of a large wind farm (630MW). So implementing the concept of Green and Blue (B&G) island, as an example of offshore application, close to this wind farm have many benefits such as 1- reduces wind farm maintenance costs and shut downtime of wind turbines, as this platform is supposed to have workshops to fix wind turbines. 2- helping to improve undeveloped technologies such as wave technology, 3- encouraging the implementation of solar panels offshore, 4- harvesting marine food with reduced costs via aquaculture due to shared operation costs. 5- This site is expected to have good current rates for tidal energy as it is in the link between the North Sea and the English Channel.



Figure 3.4 Proposed location for the MUP in the North Sea (red sign).

3.5.1 Electrical load data profile

The B&G concept is focused on the use of physical and biological ocean resources, i.e. mainly energy and food. This concept combines aquaculture facilities (producing both fish and algae) with an offshore wind farm and other devices for harnessing energy from the sea (waves, currents, solar, etc.) as described in Section 2.3.3 [94]. B&G has different kinds of loads such as operation and feeding pumps, lighting, cold storage, laundry and workshops.

Table 3.1 shows the average daily power demand of the green and blue island concept. The total annual demand load is equal to approximately 20454600 kWh (20.5 GWh/year) which is estimated from an excel spreadsheet based on the daily load profile in Table 3.1 [94].

Table 3.1 Electrical power demand of green and blue island concept [94]

Green and Blue	Condition 1 (day)			Condition 1 (night)			Mean Load			Emergency		
	kW	kVAr	kVA	kW	kVAr	kVA	kW	kVAr	kVA	kW	kVAr	kVA
	P	Q	S	P	Q	S	P	Q	S	P	Q	S
Total power	3146	2359	3932	1524	1143	1905	2176	1632	2720	467	350	583

Randomness is added to the load profile to make it more realistic. Two types of random variabilities are added to the load data: first, time-step-to-time-step variability is applied to the load profile with 10% random variability of the load power. Then to make the load profile more realistic 10% day-to-day random variability of the load power is also applied to the load profile obtained in the first step [95]. The load profile after adding this randomness is shown in Figure 3.5 for 7 days.

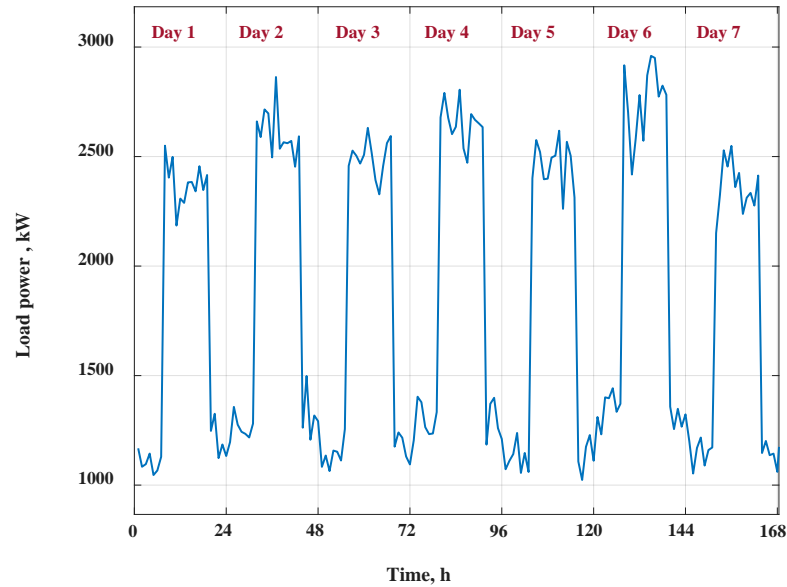


Figure 3.5 Annual load profile hourly-averaged.

3.5.2 Wind/tidal speed data profile

The National Aeronautics and Space Administration (NASA) website provides meteorological data for any part of the world based on the coordinates (Latitude, Longitude) of the location. The monthly averaged wind speed data are gathered from the NASA website for the location of the MUP considered under this case study [96]. This monthly average wind speed data is processed in a five-step process in Homer to get the annual hourly averaged wind speed data as explained in Homer documentation [97].

Tidal data are obtained from [98] with predictions for 8 samples of tidal speed per day over the year 2021. This data is interpolated using Spline interpolation in Matlab. The annual hourly-averaged wind and tidal speed profiles are shown in Figure 3.6 and Figure 3.7, respectively. The figure shows higher wind speeds are expected during winter while low speeds for the summer season. Also, it shows the neap (low speed) and spring (high speed) tides for every month.

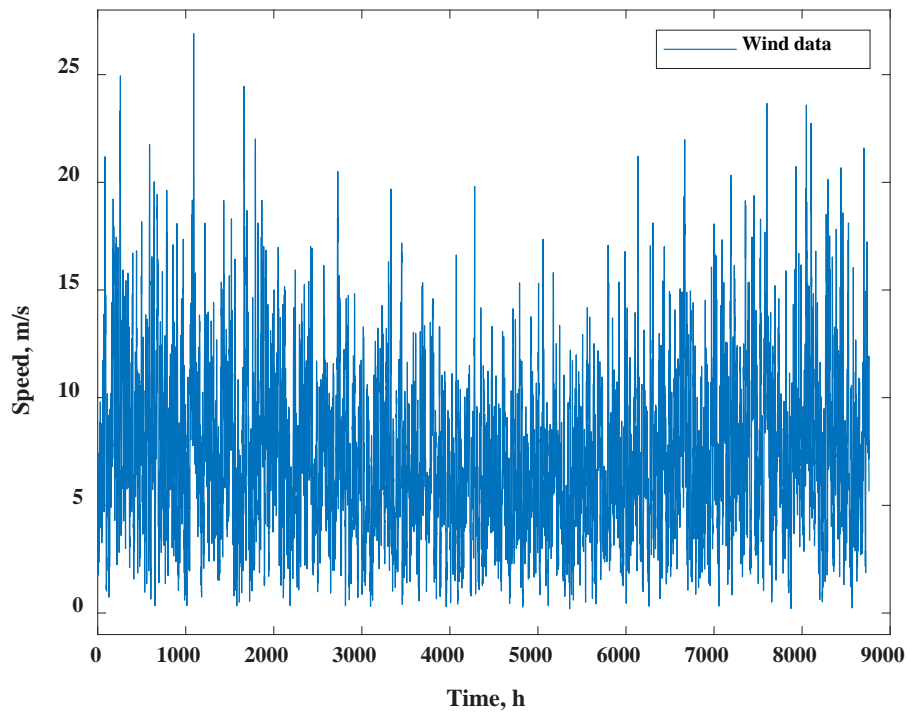


Figure 3.6 Annual wind speed profile hourly-averaged.

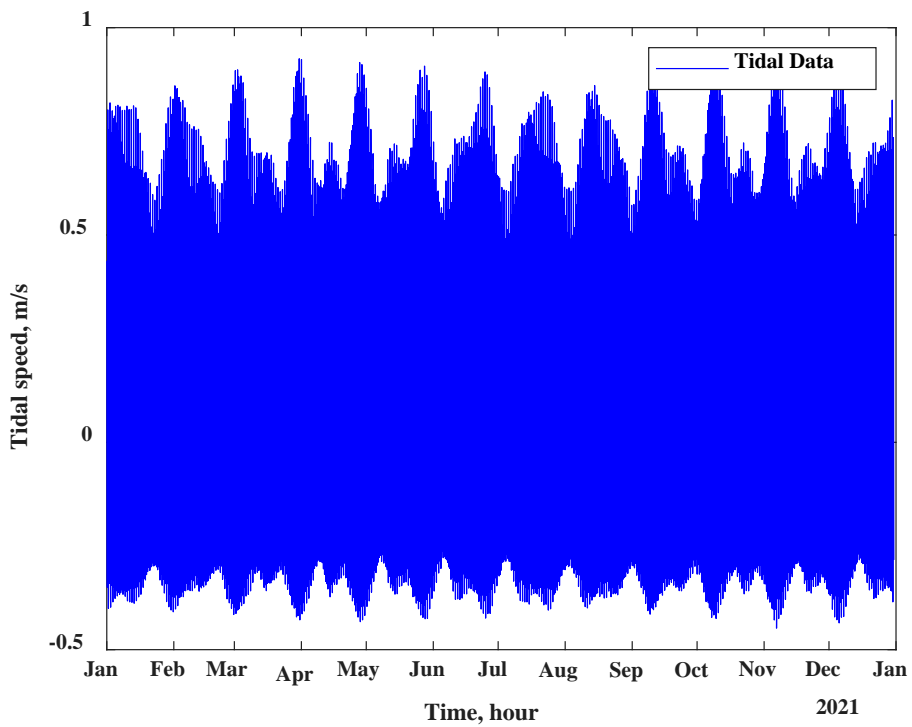


Figure 3.7 Annual tidal speed profile hourly-averaged.

3.5.3 Solar irradiation data profile

NASA surface meteorology and solar energy, Release 6.0 Data Set (Jan 2008), provides monthly averaged diffuse and global irradiation data on a horizontal surface over 22-years from July 1983 to June 2005. Also, the monthly average temperature, which is required for estimating the cell temperature, is provided by NASA website [96]. The monthly averaged solar data is processed in Homer [99], based on an algorithm presented in the study [100], to obtain hourly averaged solar data which are used for estimating the energy production of a solar array as per (9). Homer documentation highlighted that the difference in the annual PV array production is about 5% when real and synthetic data are considered. It is, also, mentioned that the difference in the economic variables such as the Levelized Cost of Energy (LCOE) is only 2% [99]. Figure 3.8 shows the annual hourly-averaged global solar irradiation (kW/m^2) at the location considered under this case study.

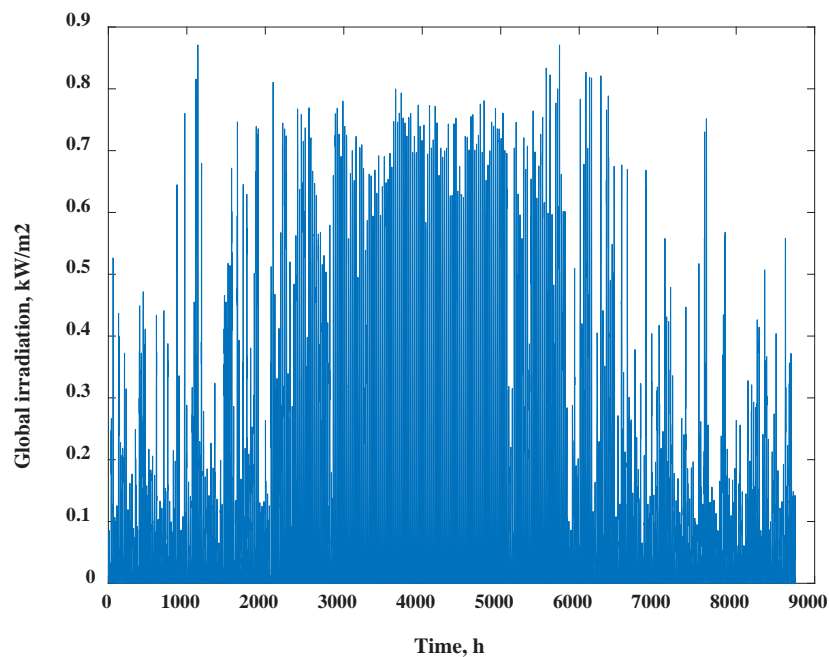


Figure 3.8 Annual global solar irradiation hourly-averaged.

3.5.4 Energy and storage systems considered for the case study

A wind turbine model V112-3.3 MW from Vestas is proposed by the study [101] for offshore MUP. The turbine specification is provided in Table B1, Appendix B. For

tidal energy, floating tidal turbine model SR2000 from Scot Renewables, with turbine specifications provided in Table B2, Appendix B, is proposed to be integrated with the floating satellite energy unit. A solar panel model CS6X-310P from Quartech, with specifications as per Table B3, Appendix B, is proposed for offshore use by the study [102].

Lead-Acid battery, as a cheaper alternative, is the most common option for large scale applications. However, due to its lower energy density, Li-ion battery module from Mitsubishi model MLiX with specifications as per Table B4, Appendix B, is considered under this case study for its higher energy density due to space limitation on the MUP.

3.6 Optimization objectives and constraints

To obtain the optimal sizing for a hybrid system with a multi-objective optimization problem, one of the objectives is considered as a final objective and the rest are considered as constraints.

3.6.1 Optimization objectives

The final objective, assumed under this case study, is the total costs of energy resources over their lifetime. Estimating the costs of the system is not an easy part as it is sensitive to site and system properties. The cost of a resource could be divided into two parts: Capital Expenditure and LCOE. Capital Expenditure is the total costs of an energy resource before actual energy production. LCOE is the total running cost of a resource during operation divided by the total energy production and this include maintenance, insurance, etc. The Capital Expenditure and LOCE for the system under this case study can be estimated as follows

$$CAPEX = C_w + C_t + C_s + C_b \quad (12)$$

$$LCOE = LCOE_w + LCOE_t + LCOE_s \quad (13)$$

where C_w , C_t , C_s and C_b are the capital expenditure of the wind and tidal turbines, solar farm and battery system, respectively. While $LCOE_w$, $LCOE_t$ and $LCOE_s$ are the

levelized cost of energy of wind, tidal and solar resources, respectively. For the battery system, replacement costs and maintenance costs are applied as running costs. To achieve the goal of optimal sizing, it is required to get the minimum *CAPEX* and *LOCE* for all considered resources in total. So, the final optimization objective can be written as follows

$$\min: \sum CAPEX + LOCE \quad (14)$$

3.6.2 Optimisation constraints and design variables

The constraints considered for the optimisation problem under this case study are LPSP, DC-DC converter efficiency and battery charging/discharging limits. LPSP is considered as an index for system reliability. LPSP equals the sum of the deficit energy over a year divided by the annual energy demand. LPSP is assumed to equal 0.02, i.e. 2% of the load are expected to be not covered during the year.

The design variables of the optimization problem are swept area of wind and tidal turbines in m^2 , area of a solar array in m^2 and the battery installed capacity in kWh. Converter size is another variable proposed for improving the DC-DC conversion efficiency. The boundaries of these design variables are set as follows

$$\begin{aligned} 0 < \text{Solar array area} < 8000 \text{ m}^2 \\ 0 < \text{Wind rotor swept area} < 75000 \text{ m}^2 \\ 0 < \text{Tidal rotor swept area} < 2000 \text{ m}^2 \\ 1 < \text{DC-DC converters number of a wind turbine} < 44 \\ 11.2 \text{ MWh} < \text{Battery size} < 20 \text{ MWh} \end{aligned} \quad (15)$$

The maximum limit of the solar array area is limited by the available area on the floating satellite structure proposed under this research. Choosing the maximum limit of the wind resource is based on covering the annual demand load (20.5GWh) with the assumed reliability index (LPSP=0.02), while other resources set to zero shares. Based on this assumption, the maximum wind share is not practically viable and the wind energy cannot cover the demand load with LPSP =0.02. So, it is assumed that the

maximum wind share equals 75000 m² of wind rotor swept area and this area match 8 of the wind turbines considered under this chapter. Applying the same conception, it is assumed that the maximum tidal share is 2000 m² of tidal rotor swept area.

For the maximum number of parallel DC-DC converters connected to a wind turbine, it is estimated to be 44 converters with a converter size equal to approximately 73 kW and this matches the minimum output power that could be delivered by a 3.2 MW wind turbine.

The minimum battery share is assumed to match the emergency load (467 kW) as per Table 3.1, i.e., the minimum battery share for one day, without other resources, is 11.2 MWh. One autonomous day is considered for sizing the battery system, as tidal energy is a predictable resource and it is expected to help in supplying the load in case there is no wind or sun. The maximum battery share is opted to achieve the required LPSP index.

3.7 Optimization model and results

The main goal of the optimization model in Figure 3.9 is to define the energy resources shares such that the optimization objective and constraints, identified in the previous sections, are satisfied.

The inputs to the model are annual hourly-averaged technical data for solar irradiation, wind speed and tidal speed as well as battery initial conditions and battery specifications. Additionally, economic data such as capital costs of solar energy per m², capital costs of wind energy per m² of wind rotor swept area, capital costs of tidal energy per m² of tidal rotor swept area and capital costs of battery storage system per kWh are fed to the model as inputs.

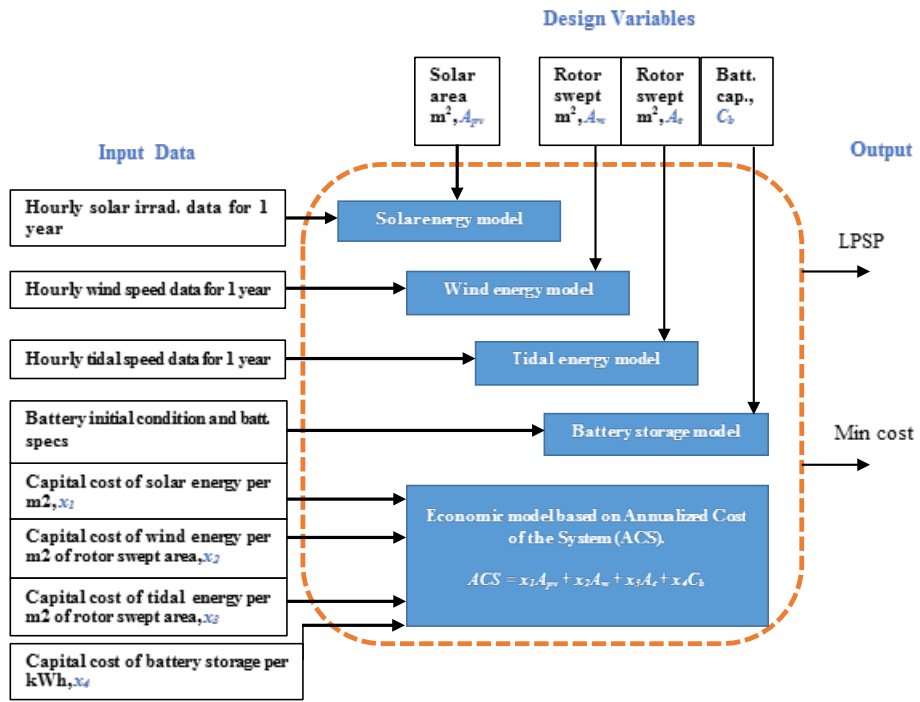


Figure 3.9 Optimization model.

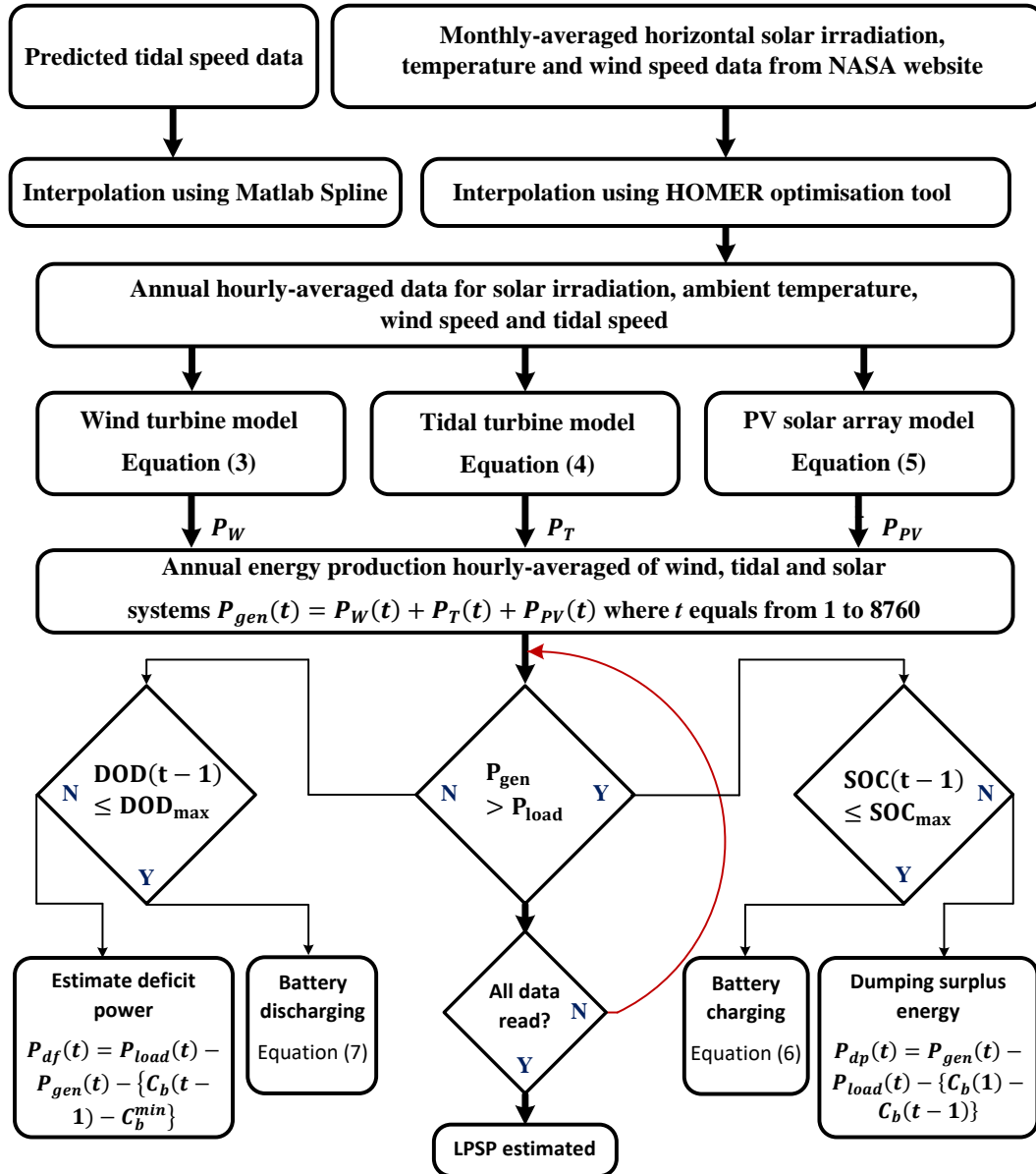


Figure 3.10 Power management algorithm for LPSP evaluation.

As mentioned earlier, there are four design variables considered which are the solar area A_{PV} , wind rotor swept area A_w , tidal rotor swept area A_t and the battery storage capacity C_b . The outputs of this model are the minimum system costs and the LPSP. Matlab code/m-file is prepared to estimate the LPSP as per the flowchart of Figure 3.10. In this figure, the available power from all renewable energy sources P_{gen} is estimated in a loop for every hour during the year. This available power is compared with the load demand P_{load} at every hour. If the $P_{gen} > P_{load}$ then charging mode of the battery is activated to absorb the surplus energy as long as the battery SOC is lower

than the maximum limit, otherwise, energy exceeds the maximum SOC will be dumped. On the other hand, If the $P_{gen} < P_{load}$ then discharging mode of the battery is activated to supply the load as long as the battery DOD is lower than the maximum limit, otherwise, the battery stops discharging and deficit energy is estimated at that hour. Once all data are read, the LPSP is estimated by dividing the sum of all deficit energy by the total load demand during the year.

3.7.1 Cost-reliability method proposed for optimal sizing of energy resources

To define the share of each energy resource, a graphical concept is proposed based on cost-reliability curve as per Figure 3.11. Using this method, one can choose the desired system reliability based on LPSP introduced in the previous sections. Then, draw a vertical line until it intersects with the costs line and this is the total hybrid system costs at the chosen reliability index as shown in Figure 3.11. The shares of energy resources are obtained by extending the same vertical line down to intersect with the resources lines. The intersection points with these lines are the optimal values of the design variables that are used in Table 3.2 to obtain the shares of all energy resources.

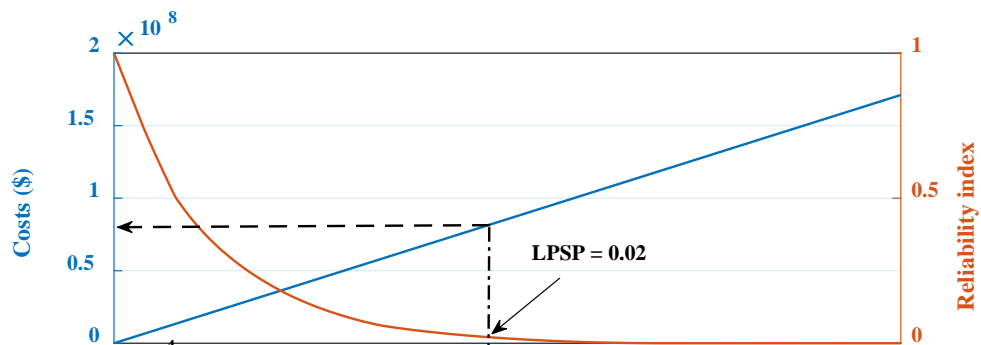


Figure 3.11 Optimal sizing of energy resources based on the cost-reliability curve.

Although the point of intersection at variable step 424 is the optimal point as per the optimization curve in Figure 3.11, this point does not satisfy the assumed LPSP = 0.02. However, the optimization results which fulfil the objectives and constraints introduced in Section 3.6 are obtained based on the intersection at step 952 at which the LPSP equals 0.02.

Table 3.2 Optimization results based on the cost-reliability method

Design variables	Optimisation results	Units of energy systems considered	No. of energy resources units	Energy resources shares
Solar, A_{PV} (m ² of solar area)	3808	1.9 m ²	2004 solar panels	2004 x 310 W = 0.62 MW
Wind, A_w (m ² of wind rotor swept area)	35700	9,852.0 m ²	4 wind turbines	4 x 3.2 MW = 12.8 MW
Tidal, A_t (m ² of wind rotor swept area)	952	401m ²	3 floating SR2000 with 6 tidal turbines included	3 x 2 MW = 6 MW
Battery, C_b (kWh)	7140	Nominal energy per module = 1.48kWh	No. of modules = 7140 / 1.48 = 4824	7.1 MWh
Total installed power capacity =				19.42 MW
Total system costs = \$ 81.4m				

These results are summarized in Table 3.2. In this table, the unit of an energy system is used to estimate the number of components for that system. For example, Figure 3.11 implies that the required solar share is 3808 m² and the solar panel selected under this case study with an area of 1.9 m² and so the number of the solar panels required is the division of these two numbers which give 2004 panels. For wind energy, Figure 3.11 implies that the required wind share is 35700 m² of rotor swept area while the rotor swept area of the turbine selected under this case study is 9852 m² and so the

number of the wind turbine is the division of these two numbers which gives 4 wind turbines. The same conception is applied to estimate the number of tidal turbines and the capacity of the battery system. It is worth mentioning that the wind share line in Figure 3.11 is divided by 3 for better scaling with other resources lines.

To verify that the assumed one autonomous day for a battery system is sufficient, the annual tidal energy production is estimated, then the daily production is obtained as the tidal is a predictable energy resource. From the Matlab algorithm, the annual tidal production is expected to be 2.22 GWh based on the installed capacity of tidal power as per Table 3.2. In other words, the tidal daily energy production is 6.1 MWh and this around half of the emergency load, which equals 11.2 MWh, as described in Section 3.5.1. So, considering a battery system with an energy size of 6.4 MWh, one autonomous day, is sufficient as the tidal energy will supply half of the emergency load during the day. The next section presents a verification, using a Matlab optimization tool, for the optimization results obtained in Table 3.2.

3.7.2 Verification of cost-reliability method using Matlab tool (Linprog)

At first, modelling of the optimization problem is required to choose the most appropriate Matlab tool to solve this problem. It is assumed that the annual hourly-averaged energy from the energy resources (tidal, wind and solar) and the battery storage must be greater than or equal to the hourly-averaged load power as per (16).

$$P_{pv-n} + P_{w-n} + P_{t-n} + C_{batt-n} > P_{load-n} \quad (16)$$

where P_{pv-n} , P_{w-n} , P_{t-n} and C_{batt-n} are the hourly-averaged energy that can be delivered from solar, wind, tidal and battery systems, respectively, to cover the hourly-averaged load power P_{load-n} at an hour n and this must be achieved for all hours during the year from 1 to 8760 hours. Equation (16) can be expanded in a matrix form for all hours during the year as follows

$$\begin{bmatrix} P_{pv1} & P_{w1} & P_{t1} & C_{batt1} \\ P_{pv2} & P_{w2} & P_{t2} & C_{batt2} \\ \cdot & \cdot & \cdot & \cdot \\ \cdot & \cdot & \cdot & \cdot \\ P_{pv8760} & P_{w8760} & P_{t8760} & C_{batt8760} \end{bmatrix} \begin{bmatrix} x_1 \\ x_2 \\ x_3 \\ x_4 \end{bmatrix} > \begin{bmatrix} P_{load1} \\ P_{load2} \\ \cdot \\ \cdot \\ P_{load8760} \end{bmatrix} \quad (17)$$

The vector x represents the variables of the optimization problem as per Section 3.6.2 where x_1 , x_2 , x_3 and x_4 are the area of a solar array in m^2 , the swept area of the wind turbines in m^2 , the swept area of the tidal turbines in m^2 and the battery installed capacity in kWh, respectively. P_{pv1} to P_{pv8760} are the hourly-averaged solar production per m^2 unit of a solar panel. P_{w1} to P_{w8760} and P_{t1} to P_{t8760} are the hourly-averaged wind and tidal production per m^2 of rotor swept area from wind and tidal turbines, respectively. Lastly, C_{batt1} to $C_{batt8760}$ represents the annual hourly-averaged SOC of the battery system considering the maximum SOC and the maximum DOD. Equation (17) represents the constraints of the optimisation problem while the objective is the cost function which is

$$\min f = U_{PV}^{m^2} \cdot x_1 + U_{win}^{m^2} \cdot x_2 + U_{tid}^{m^2} \cdot x_3 + U_{batt}^{kWh} \cdot x_4 \quad (18)$$

where $U_{PV}^{m^2}$ is the total costs of one squared meter of the solar system. $U_{win}^{m^2}$ and $U_{tid}^{m^2}$ are the total costs of one squared meter of rotor swept area of wind and tidal systems, respectively. U_{batt}^{kWh} is the total costs of one kWh of battery storage.

Matlab provides a decision table to choose the most appropriate approach to solve the optimisation problem based on the type of the equations of the constraints and objectives [103]. Equations (16) and (17) implies that both the constraint and the objective have linear equations, so the optimisation decision table suggests Linear Programing (Linprog) as a solver for this optimisation problem. Linprog solver can find the minimum value of a problem which is described as follows

$$\min f^T x \text{ such that } \begin{cases} A \cdot x \leq b, \\ A_{eq} \cdot x = b_{eq}, \\ lb \leq x \leq ub. \end{cases} \quad (19)$$

As per the problem model in (16) and (17) there are no equality constraints, i.e. A_{eq} and b_{eq} equal to zero. Vector f is the cost vector which is

$$f = [U_{PV}^{m^2}, U_{win}^{m^2}, U_{tid}^{m^2}, U_{batt}^{kWh}] \quad (20)$$

While the inequality constraints can be represented by

$$A = - \begin{bmatrix} P_{pv1} & P_{w1} & P_{t1} & C_{batt1} \\ P_{pv2} & P_{w2} & P_{t2} & C_{batt2} \\ \vdots & \vdots & \vdots & \vdots \\ P_{pv8760} & P_{w8760} & P_{t8760} & C_{batt8760} \end{bmatrix} \quad \text{and} \quad b = - \begin{bmatrix} P_{load1} \\ P_{load2} \\ \vdots \\ P_{load8760} \end{bmatrix} \quad (21)$$

Using Matlab/Linprog tool, one can get the optimal values of the variables vector x which satisfies the objective and the constraints of the optimisation problem as shown in the second column of Table 3.3. The table compares the results obtained by the proposed graphical concept and Matlab /Linprog optimisation tool.

Table 3.3 Optimisation results comparison (proposed method vs Matlab/Linprog)

Design variables, costs and reliability index	Optimisation results	
	Matlab/Linprog method	Proposed cost-reliability method
Solar share (m ² of solar area)	8000	5588
Wind share (m ² of wind rotor swept area)	59141	52388
Tidal share (m ² of wind rotor swept area)	1041	1397
Battery storage (kWh)	10500	10478
Reliability index (LPSP)	4.2304e-05	1.5365e-04
Cost (\$)	1.1985e+08	1.1956e+08

By analyzing the optimization results of both methods in Table 3.3, the energy resources shares are different for wind, tidal and solar energies and almost the same

for battery storage. However, both methods achieved the optimization constraint ($LPSP = 0$) with the same minimum total system costs around \$119 m. This means that there are various scenarios for renewable energy shares which could be used to achieve the objectives and constraints of the optimization problem.

It is important to clarify that the optimization output results in Table 3.2 are based on the system assumptions under the case study which requires $LPSP$ to equal 0.02, while the comparison results in Table 3.3 are based on $LPSP$ equals zero. The reason for this assumption is for simplifying the optimization problem model (17), as the comparison is accomplished only to verify the proposed cost-reliability method.

3.8 DC conversion efficiency maximisation

This section addresses the wind turbine failure challenge presented in Section 1.4.1 which was detailed earlier in this chapter under Section 3.1.2. The goal of this section is to determine the optimal number of parallel DC-DC converters that are connected between the wind/tidal turbines and the local bus as shown in Figure 3.2 for conversion efficiency maximisation.

Study [91] compared six topologies of DC-DC converters for offshore wind energy applications. The switching/conducting losses are estimated for these topologies, which show high overall power losses at low output power. The efficiency curve for phase shift converter topology, as an example, is plotted based on the power losses data given in [91] as per Figure 3.12.

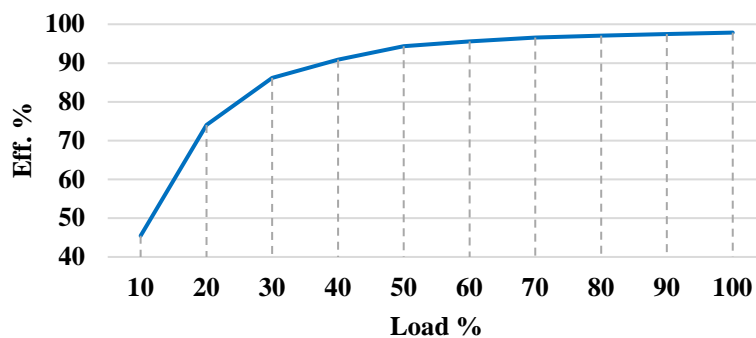


Figure 3.12 Efficiency curve of phase shift DC-DC converter.

As mentioned earlier, the DC power conversion efficiency can be improved by splitting the single DC converter into smaller converters connected in parallel to the turbine as illustrated in Figure 3.2.

- **Cost-efficiency method for the optimal number of parallel converters**

The idea to determine the optimal number of converters depends on estimating the yearly average efficiency of a wind turbine, for example, at different scenarios of DC-DC converter sizes. At the same time, the cost of the DC conversion system is estimated for each scenario as per the next subsection. For instance, in scenario 1, the DC conversion system is a single converter that matches the turbine rated power while the second scenario considers two converters in parallel with a size equals to half of the turbine rated power each and so on until scenario 44. The number 44 represents the maximum number of converters to be connected in parallel to a wind turbine which is defined based on the discussion in Section 3.6.2. The procedure to determine the optimal number of converters is summarized in the following section.

First, the annual average efficiency is determined at each scenario using the turbine output power that is estimated by the algorithm of Figure 3.10. Based on the turbine average power level at each hour, the hourly DC-DC conversion efficiency is estimated using Figure 3.12. Then the annual average efficiency of the wind turbine is estimated for each scenario as per Figure 3.13 using the Matlab code as indicated in Appendix B2.

- **Economic calculations**

Economic evaluation for each scenario is established by considering the cost of two main parts of the DC-DC converter: magnetic devices and the semiconductor switches, as those are the most expensive parts in the converter. For the cost of semiconductor switches, study [104] introduced an estimation for the costs of semiconductors, cabinets, wiring and control to be 3.79 USD per kVA of the installed switching power. Based on this costs figure, the switching power for each scenario is defined using the available power rating of the switches in the market and then the costs of semiconductors are estimated in an excel spreadsheet.

On the other hand, the costs of the magnetic devices are estimated for each scenario using equation (22) which correlates the area product and the costs of the magnetic devices [104].

$$C_{mag} = A_p \cdot 782094.4\$ / m^4 + n_{mag} \cdot 4326.9\$ \quad (22)$$

where C_{mag} is the total cost of the magnetic devices. A_p and n_{mag} are the window area product and the number of magnetic devices in each scenario. The area product is determined for different converter sizes using the Matlab algorithm presented in [105], then the costs of magnetic devices are determined as per Table B5 in Appendix B which also shows the costs of the semiconductors and the total costs of the DC conversion system for each scenario.

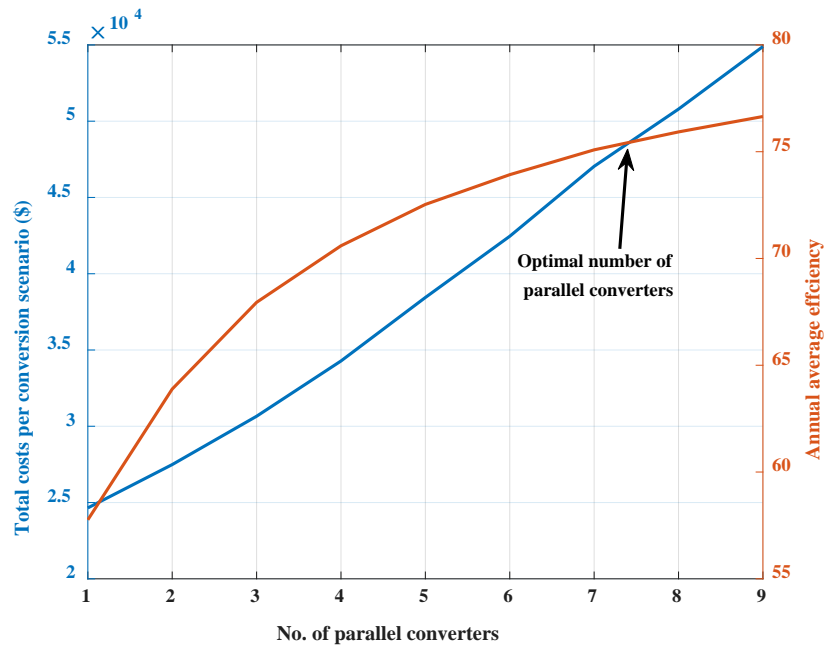


Figure 3.13 Optimal number of parallel converters connected to wind turbine based on the cost-efficiency curve.

The total costs and the annual average efficiency curves are plotted against the number of DC-DC converters as shown in Figure 3.13. The point of intersection is the optimal number of the parallel DC-DC converters which should be connected to a 3.2MW wind turbine. Figure 3.13 shows that design the DC conversion system of the wind turbine with 8 converters in parallel (i.e. 400 kW per converter) instead of one

converter, results in increasing the annual average efficiency of the conversion system from around 57% to over 75%. This approach not only has a positive economic impact on the whole system but also increases the reliability and availability of the wind turbine.

- **The optimal number of converters connected to tidal turbine**

The same procedure that is used with the wind turbine is used to determine the optimal number of DC converters that should be connected in parallel to a 1 MW tidal turbine. Based on the minimum tidal turbine output power, up to 31 converters could be connected in parallel to improve the conversion system efficiency. Table B6 in Appendix B shows the costs of the DC conversion system connected to a tidal turbine for different 15 conversion scenarios.

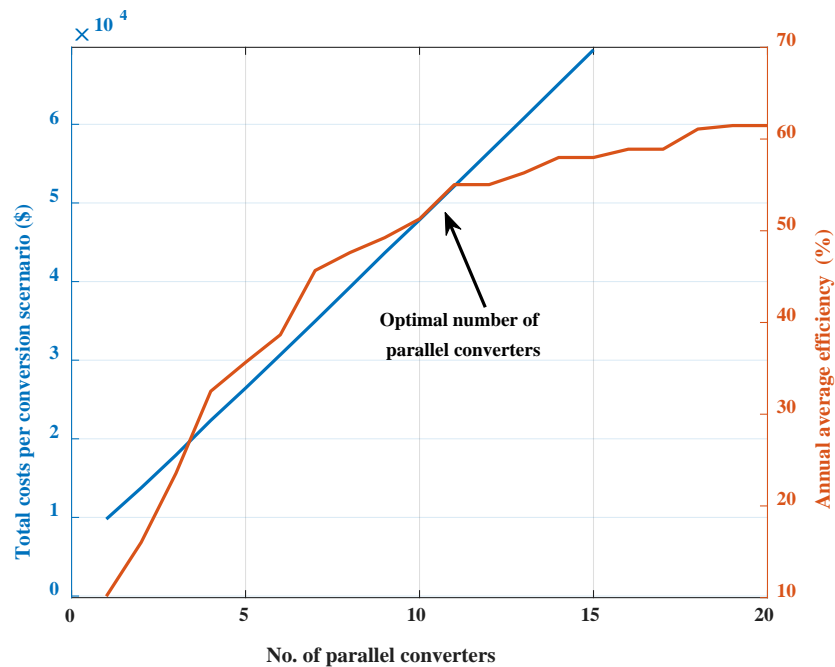


Figure 3.14 Optimal number of parallel converters connected to tidal turbine based on the cost-efficiency curve.

The cost-efficiency curve in Figure 3.14 illustrates that the optimal number of the parallel converters connected to a 1 MW tidal turbine is 10 converters (with a converter size of 100 kW each). The figure shows that the design of the DC-DC conversion system of the tidal turbine with 10 converters in parallel, instead of one converter with a size 1 MW, results in increasing the annual average efficiency of the conversion

system drastically from 10% to over 50%. Table 3.4 shows the economic impact due to using the optimal number of converters to be connected in parallel to tidal and wind turbines.

It is important to highlight that the annual return due to the improved efficiency is achieved in Table 3.4 for the wind turbines as an example. As per Table 3.4, using the optimal number of DC converters with the wind turbines under the case study results in an annual return of over 440 k\$.

Table 3.4 Economic impact due to using one converter versus the optimal number of converters connected to wind and tidal turbine

	Wind turbine		Tidal turbine	
	1 converter (3.2 MW)	8 converters (400 MW)	1 converter (sized 1 MW)	10 converters (sized 100 kW)
Annual average eff. of DC conversion (%)	57	75	10.2	52
Annual production per turbine (GWh)	11.3	11.3	1.05	1.05
Annual production per turbine after the DC conversion stage (GWh)	11.3 x .57 = 6.44	11.3 x .75= 8.5	1.02 x .12 = .122	1.05 x .52 = .546
Number of turbines	4	4	6	6
Annual production from all turbines (GWh)	6.44 x 4 = 25.8	8.5 x 4 = 34	.122 x 6 = 0.73	0.546 x 6 = 3.28
DC conversion system costs per a turbine (\$)	24647.6	50793.5	9789.6	47844.8
Annual return due to improved efficiency of wind turbines (\$), for example.	$= (\text{An. prod. with 8 cons.} - \text{An. prod. with 1 con.}) \times \text{LCOE}^*$ $- (\text{DC conv. costs with 8 cons.} - \text{DC conv. costs with 1 con.})$ $= (34 - 25.8) \times 57 \times 10^3 - (50793.5 - 24647.6) =$ <p style="text-align: center;">441254 \$</p>			

An. prod. for 8 cons. = Annual production with 8 converters in

An. prod. with 1 con. = Annual production with 1 converter

DC conv. costs with 8 cons. = DC conversion costs with 8 converters

DC conv. costs with 1 con. = DC conversion costs with 1 converter

*LCOE= Levelized Cost Of Energy based 2018 prices [106]

3.9 Summary

This chapter proposed a new design concept based on a cost-reliability curve for optimal sizing of MUP's energy resources that gives better flexibility for the system designer. Also, a new methodology is proposed to determine, at the design stage, the optimal number of DC-DC converters to be connected in parallel with wind or tidal turbine - as an example, for maximizing the overall DC conversion efficiency. To demonstrate these new techniques, a case study is presented based on an offshore microgrid, located at the North Sea, to supply aquaculture loads. The sizing of the hybrid power system considers the floating energy unit that was proposed in Chapter 2. This floating energy unit comprises tidal, wind and solar energy resources with battery storage. An optimisation model is presented showing the inputs, outputs and design variables of the optimisation problem. Matlab optimisation tool "Linprog" is used to verify the results of the proposed new sizing concept. The main points to be concluded from this chapter are:

- The proposed concept accurately determined the optimal shares of tidal, wind, solar energies and battery storage with power installed capacities of 6 MW, 12.2 MW, 0.6 MW and 6.4 MWh, respectively, to meet the demand load (20.5 GWh) of the green and blue island.
- By applying the proposed methodology to determine the optimal number of the parallel DC converters connected to wind and tidal turbines, it was found that the DC conversion efficiencies of the wind and tidal converters were increased from 57% to 75% and from 10% to 55%, respectively, considering the location under the case study.
- Although the DC conversion efficiency was improved by using parallel converters, connecting converters in parallel raises the problem of circulating current which will be discussed in Chapters 4 and 5.

Chapter 4 Parallel DC-DC Power Converters

The previous chapter proposed a new concept for maximizing the DC conversion efficiency of a wind/tidal turbine via determining the optimal number of parallel DC converters connected to the turbine. This new concept raised the issue of circulating current among parallel-connected converters. Additionally, a DC-DC power converter is an essential part of a DC microgrid that performs different goals as explained later.

So, this chapter focuses on DC-DC power converters from different dimensions. First, the topology of the converter is examined. Secondly, a discussion about control techniques, recorded in the open literature, for parallel-connected converters is then provided. Lastly, the definition for the circulating current among parallel-connected converters, in a DC microgrid, is presented. The circulating current phenomenon is investigated using Matlab/Simulink models at various operating conditions.

4.1 DC-DC power converter topology

DC-DC power converters or switched-mode power supplies were widely in use in industrial and domestic applications as early as the 1970s. They were used in different applications from small to large power scales such as PV systems, lighting and household appliances, electric vehicles, telecommunication power supply, wind turbines, fuel cell power supply, medium and high voltages applications [107-110] etc. DC-DC power converters use semiconductor switches and passive elements to perform different goals such as output voltage and current control. The design and control of DC-DC power converters are important issues as they are an essential part of systems such as electric vehicles, renewable energy systems (solar, wind, etc.) that require higher system efficiency while complying with strict power quality regulations.

In general, DC-DC converters can be classified as voltage sourced converters (converting the input voltage level to another level at the output) and current sourced converters (converting the input current level to another level). The basic principle of operation for these converters depends on connecting and disconnecting the voltage source or current source rapidly to a storage element (inductor or capacitor) in a

controlled manner using power electronic switches such as Insulated Gate Bipolar Transistor, Metal Oxide Semiconductor Field-Effect Transistor, etc. Configuration of such converters must avoid the direct connection of a capacitor to a voltage source or an inductor to a current source. Based on this, there are two basic structures for the voltage and current converters. These are the star-connected two-switch inductor cell and the delta-connected two-switch capacitor cell, shown respectively in Figure 4.1 (a) and (b). The inductor cell consists of three elements connected in a star-connection structure (two switches and the inductor as a storage element). While the capacitor cell comprises two switches with the capacitor as a storage element connected in a delta-connection structure.

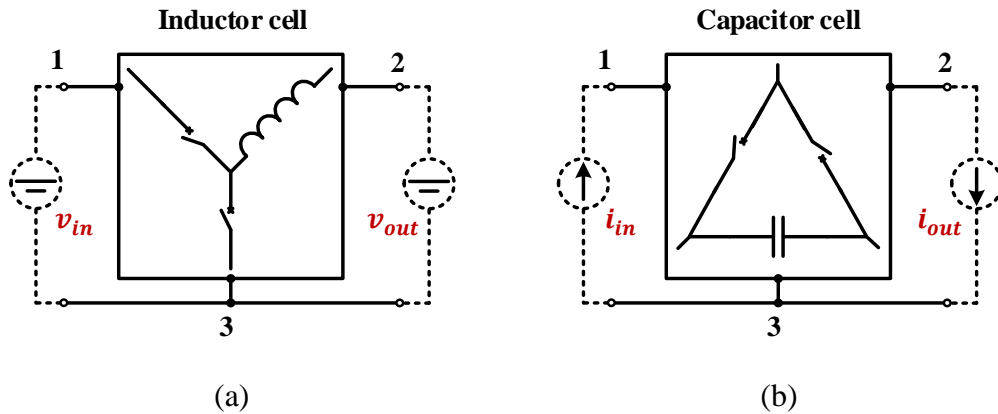


Figure 4.1 The simplest configurable switching storage structures: (a) Switching-inductor cell and (b) Switching-capacitor cell.

Rotating the switching-inductor cell in Figure 4.1 (a) between points 1, 2 and 3 results in three different voltage converters that are well-known in the literature by voltage buck, boost and buck-boost converters as shown in Figure 4.2 (a) to (c). Similarly, rotating the switching-capacitor cell in Figure 4.1 (b) generates three current converters: buck, boost and buck-boost as shown in Figure 4.2 (d) to (f).

For voltage converters, two important issues must be taken into account for proper converter operation: first, it is important to ensure that both switches are not simultaneously turned on to avoid short circuit on the source (as shown in Figure 4.2 (a)), on the load (as shown in Figure 4.2 (b)) or the source with the load (as in Figure 4.2 (c)). Secondly, ensure that there is always a path for the current passing in the

inductor, i.e. both switches must not be concurrently turned off while there is a current flowing in the inductor. On the other hand, for proper operation of current converters, both switches should not be concurrently turned off to avoid sudden open circuit cases on the source or the load, and they should not be simultaneously turned on to avoid the capacitor short circuit.

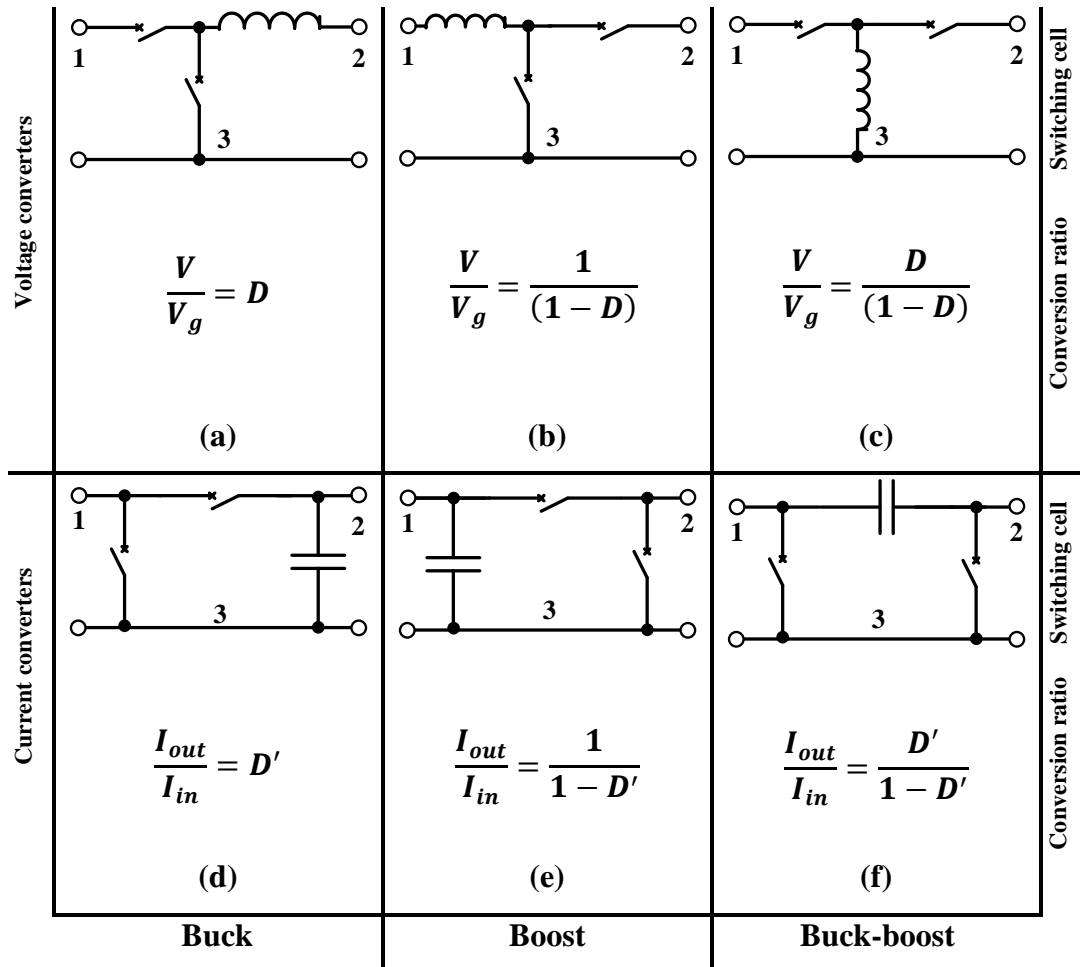


Figure 4.2 Various possible converters configurations of inductor-cell and capacitor-cell: (a) voltage buck, (b) voltage boost, (c) voltage buck-boost, (d) current buck, (e) current boost and (f) current buck-boost converters with conversion ratio provided for all configurations.

The following subsections provide the steady-state analysis for the buck and boost converters-based star-switching inductor cell and for a buck-boost converter-based delta-switching capacitor cell as examples. Additionally, deriving the expressions for the passive components of a voltage boost converter for the design of boost converters that used later in this research.

4.1.1 Boost converter steady-state analysis

The goals of this analysis are to determine the boost converter voltage ratio and estimate the inductor and capacitor values that achieve the desired inductor current ripple and output voltage ripple, respectively. To achieve these goals, volt-second balance, capacitor charge balance and small ripple approximation principles are used with considering Figure 4.3 of a boost converter. The derived equations of the inductance (L) and capacitance (C) will be used in the coming chapters for designing boost converters.

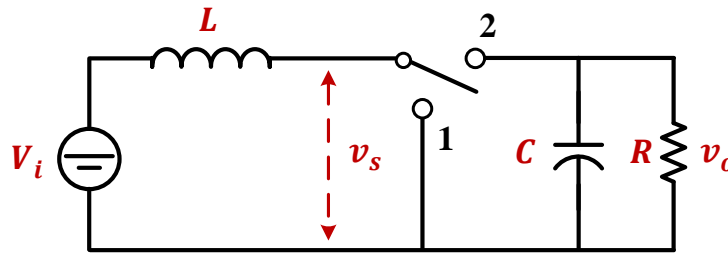


Figure 4.3 Boost converter analysis circuit.

When the switch is at position 1 as per Figure 4.4, the capacitor is partially discharged by supplying the load current. Apply Kirchoff's Voltage Law,

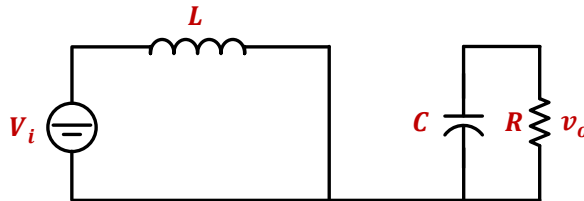


Figure 4.4 Boost circuit when the switch is at position 1.

$$V_i - v_L = 0 \quad \Rightarrow \quad v_L = V_i$$

$$i_c = \frac{-v_o}{R} \tag{23}$$

By applying small ripple approximation, i.e $v_o(t) = [V_0 + v_{ripple}(t)] \approx V_0$ which yields

$$v_L = V_i \quad \text{and} \quad i_c = \frac{-V_o}{R} \quad (24)$$

When the switch is at position 2 as shown in Figure 4.5, the inductor current supplies the load and recharging the capacitor. Apply Kirchoff's Voltage Law gives the following equations

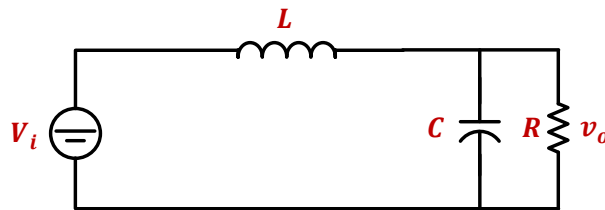


Figure 4.5 Boost circuit when the switch is at position 2.

$$V_i - v_o - v_L = 0 \quad \Rightarrow \quad v_L = V_i - v_o \quad (25)$$

$$i_c(t) = i_L(t) - \frac{v_o(t)}{R}$$

Applying linear ripple approximation, leads to $v_o(t) = V_o$ and $i_L(t) = I_L$ then

$$v_L = V_i - V_o \quad (26)$$

$$i_c(t) = I_L - \frac{V_o}{R}$$

Now using the derived equations during the first and second subintervals, one can sketch the inductor voltage and capacitor currents waveforms as shown in Figure 4.6 and Figure 4.7.

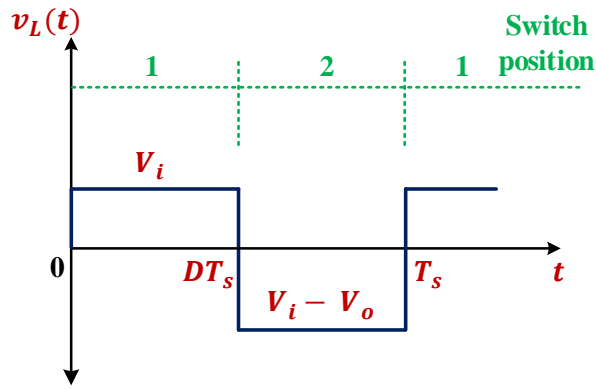


Figure 4.6 Boost converter inductor voltage waveform.

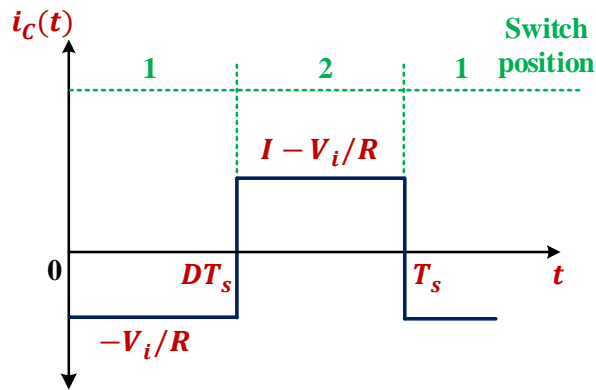


Figure 4.7 Boost converter capacitor current waveform.

To obtain the conversion ratio of a boost converter, inductor volt-second balance is applied. Over one switching period, the total volt-second applied to the inductor could be estimated as follows [111]:

$$\int_0^{T_s} v_L(t) dt = (V_i)DT_s + (V_i - V_o)D'T_s \quad (27)$$

Based on the volt-second balance principle, inductor voltage over one complete cycle equals zero, so:

$$\begin{aligned} (V_i)DT_s + (V_i - V_o)D'T_s &= 0 \\ V_iDT_s + V_iD'T_s - V_oD'T_s &= 0 \\ (D + D')V_iT_s - V_oD'T_s &= 0 \end{aligned} \quad (28)$$

but $(D' + D) = 1$, i.e $D' = 1 - D$. By substitution in the equation above

$$(1)V_i T_s - V_o(1 - D)T_s = 0 \quad (29)$$

Solution for the conversion ratio $\left(\frac{V_o}{V_i}\right)$ yields

$$M(D) = \frac{V_o}{V_i} = \frac{1}{1 - D} \quad (30)$$

$M(D)$ is the voltage conversion ratio and this gives the ratio of output voltage to the input voltage of a boost converter. Figure 4.8 shows the relationship between the conversion ratio and the duty cycle. By obtaining the voltage conversion ratio, the first goal of this analysis is achieved and the following subsections derive the capacitance and inductance expressions used for boost converter design.

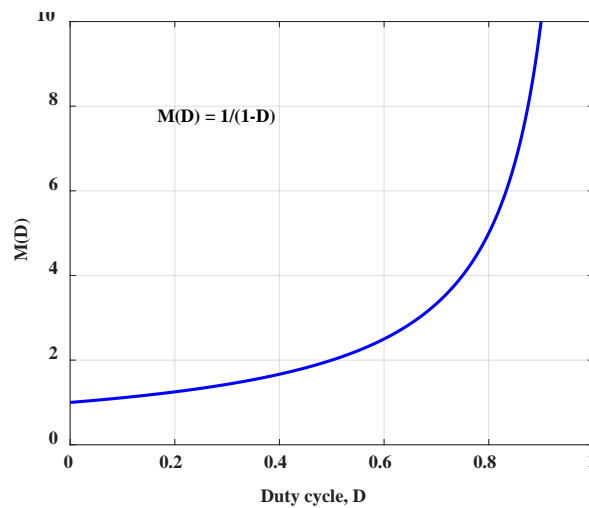


Figure 4.8 Voltage conversion ratio of a boost converter.

a) *Boost converter inductor design*

The design of the inductor is performed based on the desired value of the inductor current ripple due to its relation to the peak current as explained in the previous section for the buck converter. The first step in this design process is to plot the boost converter inductor current waveform from the obtained inductor voltage waveform in Figure 4.6 which is copied in Figure 4.9. From

the inductor current waveform, one can get the relationship between the inductor current ripple and the inductance (L) as follows

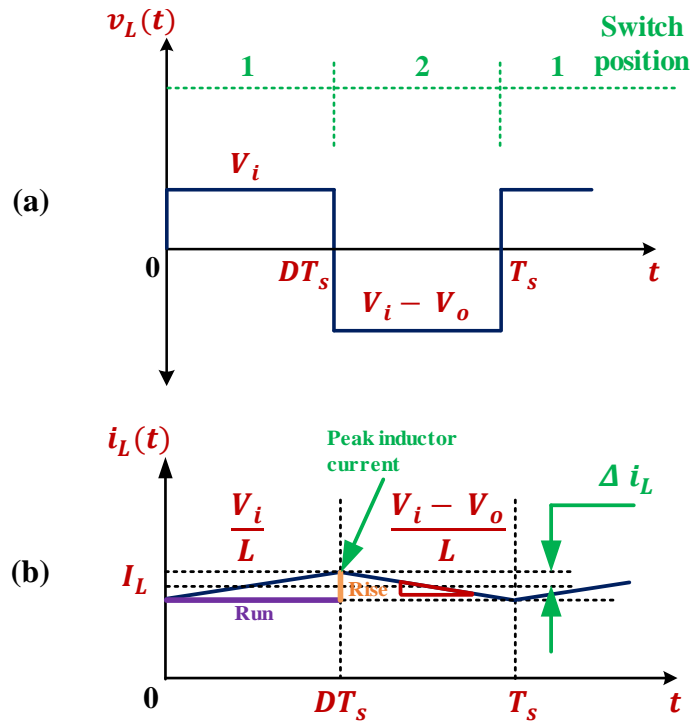


Figure 4.9 Boost converter inductor (a) voltage and (b) current waveforms.

$$\text{Slope} = \frac{\text{rise}}{\text{run}} \Rightarrow \left(\frac{V_i}{L}\right) = \frac{2\Delta i_L}{DT_s} \quad (31)$$

Solution for L yields

$$L = \frac{DT_s}{2\Delta i_L} V_i \quad (32)$$

b) Boost converter capacitor design

Inversely to the previous case of designing the inductor according to the desired inductor current ripple, in this case, the capacitor is chosen according to the desired output voltage ripple. First, the capacitor voltage waveform is plotted from the capacitor current waveform using the well-known relationship between them. Then the output or the capacitor voltage ripple will be determined from the voltage

waveform as shown in Figure 4.10 (a) and (b). The capacitor current during the first and second subinterval of a boost converter is obtained earlier as follows

$$i_c(t) = \begin{cases} -\frac{V_o}{R}, & \text{during the first subinterval} \\ I_L - \frac{V_o}{R}, & \text{during the second subinterval} \end{cases} \quad (33)$$

Using the relationship between capacitor voltage and current ($i_c(t) = C \frac{dv_c}{dt}$), the slope of the capacitor voltage ($\frac{dv_c}{dt} = \frac{i_c(t)}{C}$) could be obtained using (33) during the first and second subinterval that used to sketch the capacitor voltage waveform as per Figure 4.10 (b).

$$\frac{dv_c}{dt} = \begin{cases} -\frac{V_o}{RC}, & \text{slope during the first subinterval} \\ \frac{I_L}{C} - \frac{V_o}{RC}, & \text{slope during the second subinterval} \end{cases} \quad (34)$$

The voltage ripple magnitude can be calculated from Figure 4.10 (b) during the first subinterval as the voltage falls by $2\Delta v_c$ over time period DT_s with slope $\left(\frac{-V_o}{RC}\right)$ as follows

$$\text{Slope} = \frac{\text{fall}}{\text{run}} \Rightarrow \left(\frac{-V_o}{RC}\right) = \frac{-2\Delta v_c}{DT_s} \quad (35)$$

Solution for Δv_c yields

$$\Delta v_c = \frac{V_o DT_s}{2RC} \quad \text{hence} \quad C = \frac{V_o DT_s}{2R\Delta v_c} \quad (36)$$

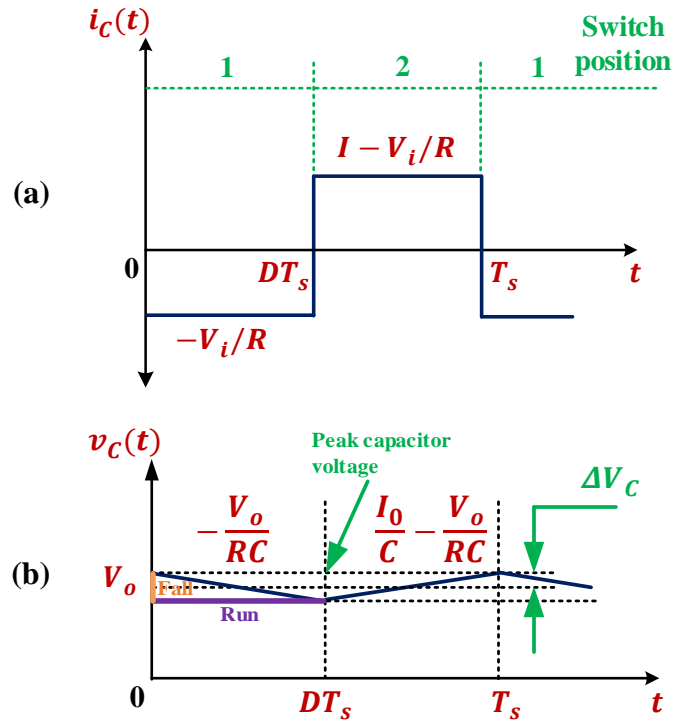


Figure 4.10 Boost converter capacitor (a) current and (b) voltage waveforms.

It is important to highlight that the switching frequency f_s has an impact on the output voltage ripple as same as the situation with inductor current ripple.

To study the impact of the capacitance and inductance on the inductor current ripple and output voltage ripple, respectively, one can solve the ripple equations of Δv_c and Δi_L for DT_s

$$DT_s = \frac{2RC\Delta v_c}{V_o} = \frac{2L\Delta i_L}{V_i} \quad (37)$$

Then solve for Δv_c and Δi_L which yields

$$\Delta i_L = \frac{RCV_i\Delta v_c}{V_oL} \quad (38)$$

$$\Delta v_c = \frac{LV_o\Delta i_L}{V_iRC}$$

Referring to (38), it is obvious that increasing the capacitance leads to increasing the inductor current ripple and reducing the output voltage ripple at the same time. On the contrary, increasing the inductance results in reducing the inductor current ripple and rising the output voltage ripple.

4.2 Parallel converters control in an islanded DC microgrid

In an isolated DC microgrid, the main objectives of converter control are to regulate the microgrid voltage at the nominal value by ensuring supply-load balance at different operating conditions. Besides, sharing the load current properly among parallel-connected converters. Lastly, minimizing the circulating current which arises due to output voltage mismatch among parallel converters.

In the open literature, there are two groups of control techniques used with parallel-connected converters: passive load-sharing techniques such as droop control [19, 112-125] and active load sharing techniques such as master-slave [126, 127], circular chain current programming [128], average current programming [129] and central limit control technique [130, 131]. The next subsections explore each technique briefly.

4.2.1 Droop control

Among dc grid control approaches, droop control is widely used for current sharing among parallel-connected converters for its simplicity and higher reliability. However, conventional droop control suffers from limitations that vitiate the accuracy of current sharing and voltage deviation. Study [13] emphasized that droop control suffers from a conflict between enhancing current sharing and DC voltage regulation. In other words, increasing the droop resistance results in accurate load sharing but increases the voltage deviation and vice versa. Additionally, droop control is suffering from voltage deviation due to load varying. Furthermore, it suffers from current sharing problems due to the propagation of voltage error along resistive transmission lines. Besides, basic droop control cannot do coordinated control functions among multiple components with different characteristics [132].

In DC systems, droop control can be achieved by linearly reducing the voltage reference while increasing the output current. The problem of accuracy of current

sharing in droop control is due to that the output voltages of parallel converters are different when line resistances are taken into account. To explain this, a DC system with two nodes is considered as per Figure 4.11.

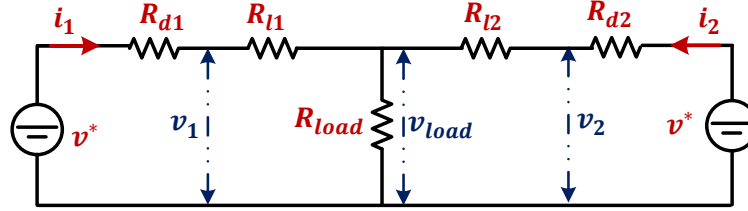


Figure 4.11 Two nodes DC system with droop resistance.

Droop control can be expressed by

$$v_i = v^* - i_i R_{di} \quad (39)$$

Where v_i is the output voltages of parallel-connected voltage sources, v^* is the reference value of the DC output voltage, i_i is the output current and R_{di} is the virtual resistance where $i = 1, 2$. The virtual resistance here is not a real resistance as one would misunderstand this from Figure 4.11 and it is just a gain used in the droop controller to estimate the reference voltage for the converter output voltage as per (39). Taking into account the interconnecting cable resistance, the load voltage can be determined as per Figure 4.11 as follows

$$\begin{aligned} v_{load} &= v^* - i_1 (R_{d1} + R_{l1}) \\ v_{load} &= v^* - i_2 (R_{d2} + R_{l2}) \end{aligned} \quad (40)$$

From the equations of (40), the relationship between the currents from both sources can be derived as follows

$$\frac{i_1}{i_2} = \frac{R_{d2}}{R_{d1}} + \frac{(R_{l2} - \frac{R_{d2}}{R_{d1}} \cdot R_{l1})}{(R_{d1} + R_{l1})} \quad (41)$$

For conventional droop control in the DC microgrid, the current of each source is inversely proportional to its virtual resistance. From (41), the current sharing error could be eliminated only when the following relationship is satisfied

$$\frac{R_{d1}}{R_{d2}} = \frac{R_{l1}}{R_{l2}} \quad (42)$$

For a small DC system, large virtual resistance could be selected which results in the line resistance is neglected with respect to the virtual resistance, i.e. the current relationship of the two sources becomes $\frac{i_1}{i_2} = \frac{R_{d2}}{R_{d1}}$. However, this assumption is not valid for the large DC system as selecting large virtual resistance put the system stability in jeopardy [133, 134].

Voltage deviation is another problem of droop control that arise from droop theory itself. This problem could be explained as follows

$$\Delta v_i = R_{di} i_i \quad \text{for } i = 1, 2 \quad (43)$$

Where Δv_i is the voltage deviation of i converter.

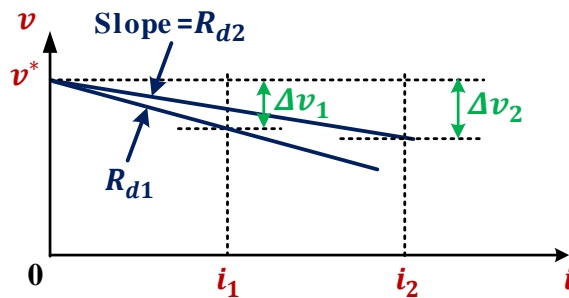


Figure 4.12 DC microgrid droop curve with different droop resistance.

Plotting the two linear equations of (43) gives Figure 4.12. The figure shows that the DC voltage deviation is zero when the converter is at open circuit condition (i.e. DC output current is zero), otherwise, the voltage deviation existed and its value varies with the DC output current value. As a solution for this problem, the virtual resistance

must be limited to a certain value as per (44) to guarantee that the maximum limit of the voltage deviation (Δv_{max}) lies within the acceptable limits.

$$R_{d1} = \frac{\Delta v_{max}}{i_{fc1}} \quad \text{and} \quad R_{d2} = \frac{\Delta v_{max}}{i_{fc2}} \quad (44)$$

where i_{fc1} and i_{fc2} are the maximum output currents of converters 1 and 2, respectively [133].

However, study [134] added another limitation for conventional droop control when it is used without communications. The study claims that unequal nominal voltages of parallel-connected converters due to an error in voltage sensing for the closed-loop operation would result in a significant deviation of source current from their required values.

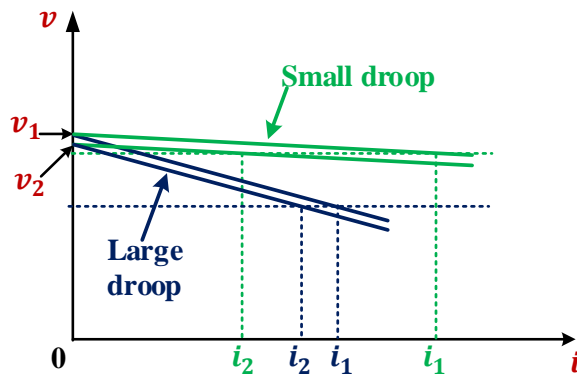


Figure 4.13 Droop curve with unequal load sharing due to nominal voltage sensing error [134].

Figure 4.13 shows a large deviation in source current is recorded with a small droop resistance while voltage deviation is small. This current deviation can be reduced by using large droop resistance, but the voltage deviation is getting larger which would not be acceptable for certain loads. For more interested readers, there are many studies, in the open literature, that addressed the limitations of the droop controller by proposing various techniques to overcome these limitations [133, 134].

4.2.2 Active load sharing control techniques

Other than passive load-sharing techniques, the active sharing schemes are used on a smaller scale. They are proposed in the literature for achieving proper current load sharing among parallel-connected converters. The reported active control techniques can be classified into: master-slave control [135-138], centralized control [139], circular chain current programming control [140], central limit control techniques [141, 142] and average current sharing approach [129].

a) Master-slave control scheme

In master-slave control, one converter acts as a master to regulate the DC grid voltage, while others act as slaves as shown in Figure 4.14. In this control technique, the load current is shared properly among parallel converters in a stable manner.

This technique can be further categorized depending on the choice of the master converter to: a dedicated master unit that serves as a master at all operating conditions. Alternatively, the unit with the highest current supply serves as a master. Lastly, the master unit could be chosen arbitrarily in a rotating scheme.

Dependency on the central controller to provide the reference current to the slave converters is the main drawback of this technique as the whole system will be at risk in the case of central controller failure.

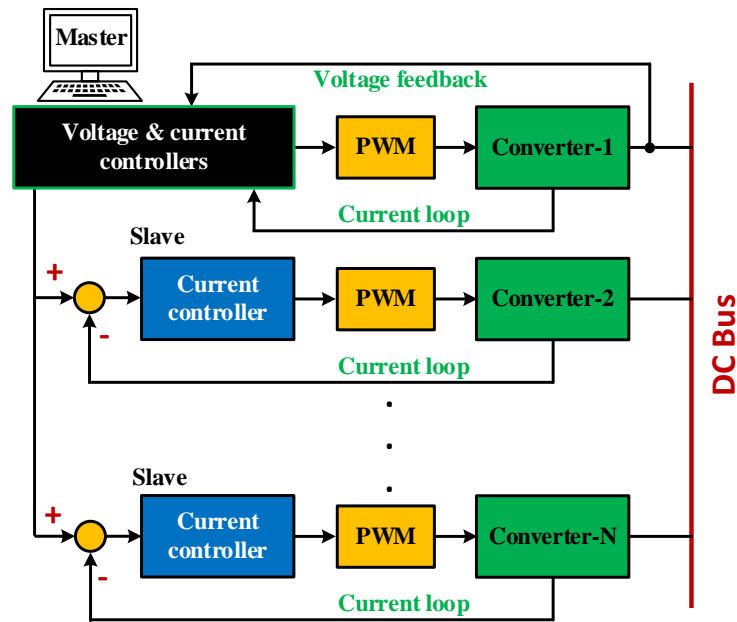


Figure 4.14 Master-slave control scheme.

Study [136] proposed an autonomous Master-Slave Current-sharing (MSC) control scheme to achieve proper current sharing among parallel-connected converters. In this scheme, the master converter with the lowest voltage loop gain becomes, while other converters become slaves. In this study, the configuration of master and slave converters is performed automatically without the need for communication that increases the system reliability.

Study [137] proposed a master-slave control scheme with inner current loop control to achieve equal current sharing among parallel-connected converters. Current distribution error is proposed as a criterion to judge the system performance. The results show that this error can be reduced greatly even with non-identical modules in the system. The proposed controller has a master-reassignment feature which is useful in selecting any converter to be a new master in case of failure of the previous master without the need for a shutdown to fix the failed master.

Another control feature, called circular queue operation or First-Activated First-Deactivated, is added to equalize the operation time among connected converters, i.e. first activated converter should be deactivated first when the load drops below a specified limit. With these two control features, master-reassignment and First-Activated First-Deactivated, the system reliability would be improved considerably.

b) Centralized control technique

This control scheme comprises a single outer voltage loop and multi-inner current loops as shown in Figure 4.15. The outer control loop exists at the central controller level for regulating the load voltage, while each converter has a single local current control loop. The reference current is supplied by the central controller to each current loop. This current reference is varying depending on the load current and voltage and it is determined by adding the output of the voltage controller and the average current (load current divided by the number of converters). This control technique suffers from a lack of reliability and redundancy although it provides tremendous controllability over current sharing and voltage regulation. The need to measure the load current makes this technique limited to small-scale applications such as electric ships, vehicles, aeroplanes, etc.

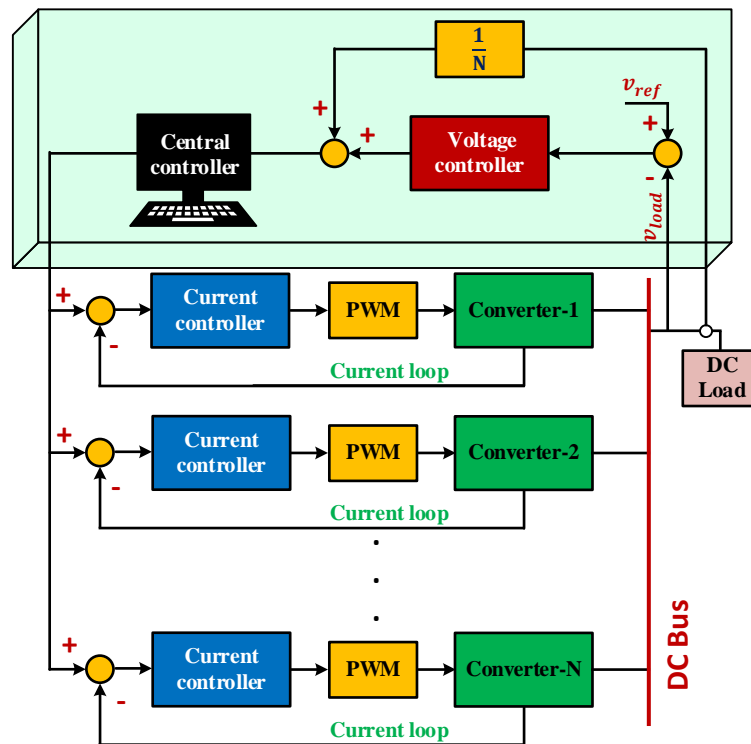


Figure 4.15 Centralized control scheme.

c) Circular chain control

In Circular Chain Control (3C) technique, there are voltage and current control loops with each converter. The voltage loop regulates the converter output voltage according

to a common reference voltage. The current loop controls the converter output current according to a reference current measured from the previous converter constituting a control ring (i.e. the first converter tracks the current of the last converter and so on).

The bi-directional communication employed with this control technique increases the system reliability. However, a failure of one converter in the chain might put the whole system in jeopardy if it is not detected and isolated quickly. Study [140] used 3C for load current sharing among parallel inverters. The results show that equal current distribution, tight output regulation and fast dynamic response can be achieved with the proposed 3C controller. The study concluded that better performance can be obtained with the 3C scheme compared with the master-slave technique.

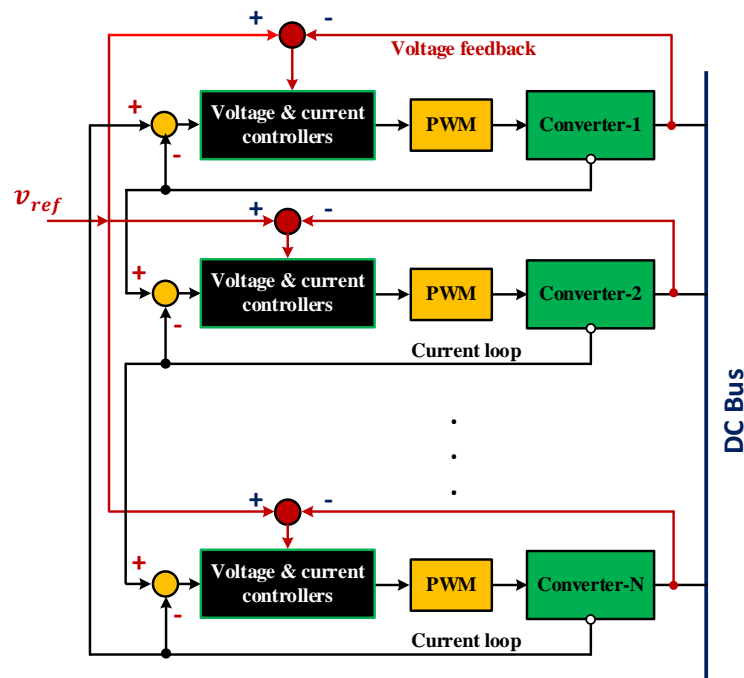


Figure 4.16 Circular chain control (3C) scheme.

d) Central limit control

This control technique is a hybrid of master-slave and circular chain control techniques. In central limit control, multi-loop controls are used to regulate the DC bus voltage and equalize the output current of each converter via tracking the central weighted current not tracking the master controller as in the master-slave scheme. Study [141] proposed a central-limit control technique to improve the transient output

current response (overshoot) in the master-slave control scheme of study [137]. A comparison is held between master-slave and central limit control techniques which concluded that central limit control avoided the current overshoot during transient which is the problem in the master-slave technique. Besides, plug and play or fault-tolerant control is easier to design and maintain in central limit control than master-slave due to symmetrical structure in central limit control technique [141].

e) *Average current sharing control*

In the Average Current Sharing Control technique, all the converters in the system take part in the load voltage regulation and converter current control. The control signal of each converter is the sum of the outputs of the voltage and current controllers as shown in Figure 4.17. The average current (i.e. total converters currents divided by the number of converters) is the reference for all converters.

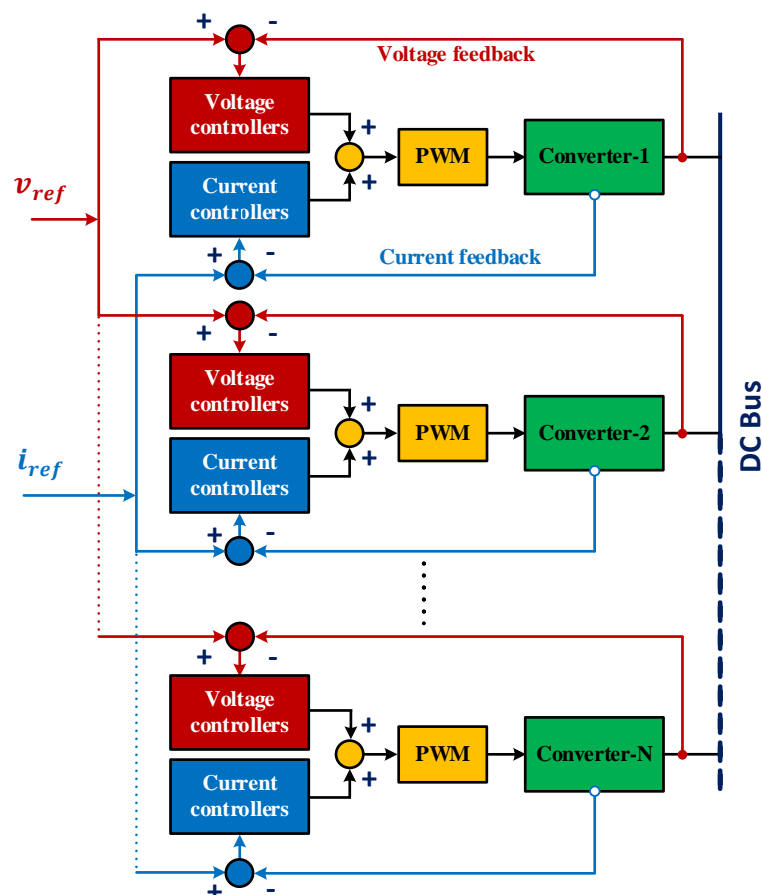


Figure 4.17 Average current sharing control scheme.

This average current can be estimated using a central controller before being transmitted to the converters via a common current bus. The voltage and current controllers in Figure 4.17 could be a traditional Proportional Integral (PI) controller, however, some studies used Proportional Resonant (PR) controller for its good dynamic response and less steady-state error [129].

Comparing Average Current Sharing Control with the master-slave scheme, Average Current Sharing Control is more reliable, expandable and highly modular. Study [129] proposed Average Current Sharing Control based adaptive gain scheduler to improve current sharing accuracy among parallel-connected inverters with considering line impedances mismatch. The study results showed a decent sharing performance. This technique is, to the best of the author's knowledge, not reported in the literature for controlling parallel DC-DC converters.

To sum up, the droop controller, as a communicationless technique, assures system stability and reliability. However, it has several drawbacks such as inaccurate load power-sharing and poor DC bus voltage regulation [19, 112]. On the other hand, the advantages of active load sharing techniques guarantee accurate power-sharing and good dynamic performance. However, due to their high dependency on high-speed communications, the system redundancy and expandability is reduced, the system costs are increased and system stability is not guaranteed [113].

4.3 Circulating current among parallel-connected converters

This part of the chapter discusses the circulating current phenomenon and load sharing among parallel-connected DC-DC converters in a Low Voltage Direct Current (LVDC) microgrid. Connecting power converters in parallel has increasing interest for reasons relating to increasing the output power capacity and system reliability, system modularity, facilitating system maintenance and reducing system design costs. Additionally, parallel converters can be applied for systems that require high current levels at a low voltage within a microgrid [143]. However, the elimination of the circulating current that arises among the parallel converters is a challenge. This current is due to an unequal output voltage of connected converters [14, 19]. Unless controlled, it can lead to higher losses and overloading of the energy sources, thereby causing

source failure and system instability. The following subsections derive expressions for the circulating current among two, three and n -parallel converters.

4.3.1 Circulating current between two parallel converters

This subsection derives an expression for the circulating current between two converters. Assume the DC-DC converters have a large capacitance at the output side. So, at a steady-state, converter output can be represented as a voltage source connected in series with the line resistance as per the equivalent circuit in Figure 4.18 [144]. R_1 , R_2 , I_1 , I_2 , V_{DC1} and V_{DC2} represent the line impedances, output currents and output voltages of converters 1 and 2, respectively. R_{Load} , V_{Load} and I_{Load} represent the resistance, voltage and current of the load. I_{C12} represents the circulating current passing from converter 1 to converter 2 while I_{C21} refers the circulating current passing in the opposite direction with the same magnitude as I_{C12} . From Figure 4.18, circulating current can be estimated directly by applying Kirchoff's Voltage Law which gives

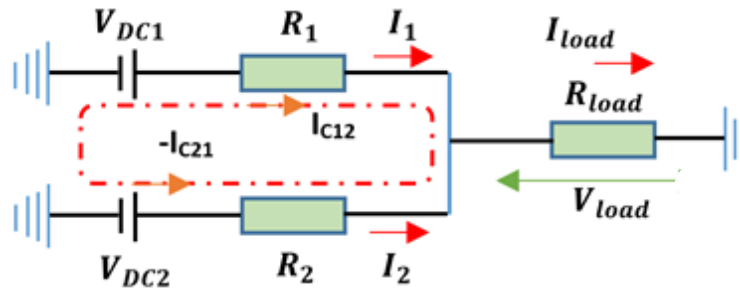


Figure 4.18 Equivalent circuit of two parallel converters connected to DC load.

$$V_{DC1} - R_1 I_{C12} - R_2 I_{C12} - V_{DC2} = 0 \quad (45)$$

$$I_{C12} = -I_{C21} = \frac{V_{DC1} - V_{DC2}}{R_1 + R_2} \quad (46)$$

To determine the current shares of the two converters (I_1 and I_2), apply Kirchoff's Voltage Law to the equivalent circuit in Figure 4.18. One can get the following equations

$$V_{DC1} - I_1 R_1 - I_{load} R_{Load} = 0 \quad (47)$$

$$V_{DC2} - I_2 R_2 - I_{load} R_{Load} = 0 \quad (48)$$

From equations (47) and (48), the output currents of the converters I_1 and I_2 can be estimated as follows

$$I_1 = \frac{(R_2 + R_{Load})V_{DC1} - R_{Load}V_{DC2}}{R_1 R_2 + R_1 R_{Load} + R_2 R_{Load}} \quad (49)$$

$$I_2 = \frac{(R_1 + R_{Load})V_{DC2} - R_{Load}V_{DC1}}{R_1 R_2 + R_1 R_{Load} + R_2 R_{Load}} \quad (50)$$

The output currents of converters 1 and 2 in (49) and (50) can be separated into two parts: load current share part and circulating current part as shown in (51) and (52), respectively.

$$I_1 = \frac{R_2 V_{DC1}}{R_1 R_{Load} + R_2 R_{Load}} + \frac{V_{DC1} - V_{DC2}}{R_1 + R_2} \quad (51)$$

$$I_2 = \frac{R_1 V_{DC2}}{R_1 R_{Load} + R_2 R_{Load}} - \frac{V_{DC2} - V_{DC1}}{R_1 + R_2} \quad (52)$$

The second term of (51) and (52) represents the circulating current I_{C12} and I_{C21} which comply with the obtained expression of (46), while the first term is the load current share of each converter. Referring to equation (46), the circulating current between two parallel converters depends mainly on the difference between the output voltages of the converters (V_{DC1} and V_{DC2}).

4.3.2 Circulating current among three parallel converters

This section derives the circulating currents among three parallel DC-DC converters for the purpose of circulating current investigation in the next subsection.

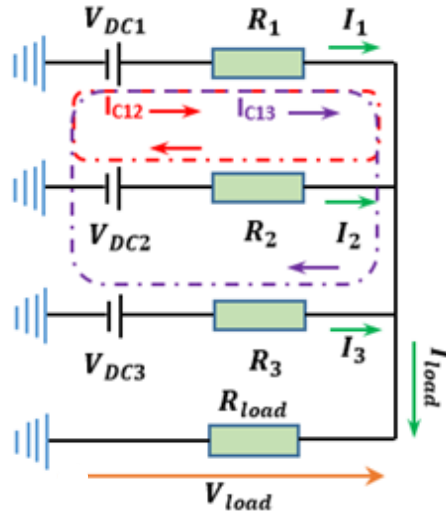


Figure 4.19 Equivalent circuit of three parallel converters connected to a DC load.

Figure 4.19 shows three parallel converters connected to a DC load. As the three branches are connected in parallel, the voltage of all branches is equal to the load voltage as follows

$$\begin{aligned}
 V_{DC1} - I_1 R_1 &= I_{load} R_{Load} & \Rightarrow & \quad I_1 = \frac{V_{DC1} - I_{load} R_{Load}}{R_1} \\
 V_{DC2} - I_2 R_2 &= I_{load} R_{Load} & \Rightarrow & \quad I_2 = \frac{V_{DC2} - I_{load} R_{Load}}{R_2} \\
 V_{DC3} - I_3 R_3 &= I_{load} R_{Load} & \Rightarrow & \quad I_3 = \frac{V_{DC3} - I_{load} R_{Load}}{R_3}
 \end{aligned} \tag{53}$$

However, the sum of the converters output currents equals the load current by applying Kirchoff's Current Law (KCL). Using (53) the load current can be estimated as follows

$$\begin{aligned}
 I_{load} &= I_1 + I_2 + I_3 \\
 I_{load} &= \frac{V_{DC1} - I_{load} R_{Load}}{R_1} + \frac{V_{DC2} - I_{load} R_{Load}}{R_2} + \frac{V_{DC3} - I_{load} R_{Load}}{R_3}
 \end{aligned} \tag{54}$$

Solve (54) for I_{load} yields

$$I_{load} = \frac{R_2 R_3 V_{DC1} + R_1 R_3 V_{DC2} + R_1 R_2 V_{DC3}}{R_1 R_2 R_3 + R_{load} R_2 R_3 + R_{load} R_1 R_3 + R_{load} R_1 R_2} \quad (55)$$

By replacing I_{load} in (53) with its value in (55), one can get the output currents I_1 , I_2 and I_3 of the three converters as follows

$$I_1 = \frac{V_{DC1}}{R_1} - \frac{R_{Load}}{R_1} \left\{ \frac{R_2 R_3 V_{DC1} + R_1 R_3 V_{DC2} + R_1 R_2 V_{DC3}}{R_1 R_2 R_3 + R_{load} R_2 R_3 + R_{load} R_1 R_3 + R_{load} R_1 R_2} \right\}$$

$$I_2 = \frac{V_{DC2}}{R_2} - \frac{R_{Load}}{R_2} \left\{ \frac{R_2 R_3 V_{DC1} + R_1 R_3 V_{DC2} + R_1 R_2 V_{DC3}}{R_1 R_2 R_3 + R_{load} R_2 R_3 + R_{load} R_1 R_3 + R_{load} R_1 R_2} \right\} \quad (56)$$

$$I_3 = \frac{V_{DC3}}{R_3} - \frac{R_{Load}}{R_3} \left\{ \frac{R_2 R_3 V_{DC1} + R_1 R_3 V_{DC2} + R_1 R_2 V_{DC3}}{R_1 R_2 R_3 + R_{load} R_2 R_3 + R_{load} R_1 R_3 + R_{load} R_1 R_2} \right\}$$

By simplifying (56), the converters output currents can be obtained as follows

$$I_1 = \frac{V_{DC1} \left(\frac{R_1 R_2 R_3}{R_{load}} \right)}{\left(\frac{R_1^2 R_2 R_3}{R_{load}} \right) + R_1 R_2 R_3 + R_1^2 R_3 + R_1^2 R_2}$$

$$+ \frac{R_1 R_3 (V_{DC1} - V_{DC2})}{\left(\frac{R_1^2 R_2 R_3}{R_{load}} \right) + R_1 R_2 R_3 + R_1^2 R_3 + R_1^2 R_2} \quad (57)$$

$$+ \frac{R_1 R_2 (V_{DC1} - V_{DC3})}{\left(\frac{R_1^2 R_2 R_3}{R_{load}} \right) + R_1 R_2 R_3 + R_1^2 R_3 + R_1^2 R_2}$$

$$I_2 = \frac{V_{DC2} \left(\frac{R_1 R_2 R_3}{R_{load}} \right)}{\left(\frac{R_2^2 R_1 R_3}{R_{load}} \right) + R_1 R_2 R_3 + R_2^2 R_3 + R_2^2 R_1}$$

$$+ \frac{R_2 R_3 (V_{DC2} - V_{DC1})}{\left(\frac{R_2^2 R_1 R_3}{R_{load}} \right) + R_1 R_2 R_3 + R_2^2 R_3 + R_2^2 R_1} \quad (58)$$

$$+ \frac{R_1 R_2 (V_{DC2} - V_{DC3})}{\left(\frac{R_2^2 R_1 R_3}{R_{load}} \right) + R_1 R_2 R_3 + R_2^2 R_3 + R_2^2 R_1}$$

$$\begin{aligned}
 I_3 = & \frac{V_{DC3} \left(\frac{R_1 R_2 R_3}{R_{load}} \right)}{\left(\frac{R_3^2 R_2 R_1}{R_{load}} \right) + R_1 R_2 R_3 + R_3^2 R_1 + R_3^2 R_2} \\
 & + \frac{R_2 R_3 (V_{DC3} - V_{DC1})}{\left(\frac{R_3^2 R_2 R_1}{R_{load}} \right) + R_1 R_2 R_3 + R_3^2 R_1 + R_3^2 R_2} \\
 & + \frac{R_1 R_3 (V_{DC3} - V_{DC2})}{\left(\frac{R_3^2 R_2 R_1}{R_{load}} \right) + R_1 R_2 R_3 + R_3^2 R_1 + R_3^2 R_2}
 \end{aligned} \tag{59}$$

Equation (57) shows the output current of converter 1 which consists of 3 terms. The first term represents the load current share of the converter 1. The second term represents the circulating currents between the converters 1 and 2. The third term represents the circulating current between the converters 1 and 3. Similarly, the output currents of the converters 2 and 3 in (58) and (59), respectively, have similar terms as explained for converter 1.

4.3.3 Circulating current among n -parallel converters

After deriving the circulating current for 2 and 3 parallel converters as per the last two subsections, this subsection derives the generalized form of the output current (converter load current share + circulating current) of the s^{th} branch that is one of the n -parallel-connected branches. The output currents of n -parallel branches could be determined using Kirchoff's Voltage Law similar to the equation (53) as follows

$$\begin{aligned}
 V_{DC1} - I_1 R_1 &= I_{load} R_{Load} & \Rightarrow & I_1 = \frac{V_{DC1} - I_{load} R_{Load}}{R_1} \\
 V_{DC2} - I_2 R_2 &= I_{load} R_{Load} & \Rightarrow & I_2 = \frac{V_{DC2} - I_{load} R_{Load}}{R_2} \\
 & \cdot & & \\
 & \cdot & & \\
 V_{DCs} - I_s R_s &= I_{load} R_{Load} & \Rightarrow & I_s = \frac{V_{DCs} - I_{load} R_{Load}}{R_s} \\
 & \cdot & & \\
 & \cdot & &
 \end{aligned} \tag{60}$$

$$V_{DCn} - I_n R_n = I_{load} R_{Load} \quad \Rightarrow \quad I_n = \frac{V_{DCn} - I_{load} R_{Load}}{R_n}$$

by applying KCL, the load current is the sum of the output currents I_1 to I_n .

$$I_{load} = I_1 + I_2 + \dots + I_s + \dots + I_n$$

$$I_{load} = \frac{V_{DC1} - I_{load} R_{Load}}{R_1} + \frac{V_{DC2} - I_{load} R_{Load}}{R_2} + \dots + \frac{V_{DCs} - I_{load} R_{Load}}{R_s} + \dots + \dots + \frac{V_{DCn} - I_{load} R_{Load}}{R_n} \quad (61)$$

$$I_{load} (R_1 R_2 R_3 \dots R_s \dots R_n) = (V_{DC1} - I_{load} R_{Load}) (R_1 R_2 R_3 \dots R_s \dots R_n) + (V_{DC2} - I_{load} R_{Load}) (R_1 R_2 R_3 \dots R_s \dots R_n) + \dots + (V_{DCs} - I_{load} R_{Load}) (R_1 R_2 R_3 \dots R_s \dots R_n) + \dots + (V_{DCn} - I_{load} R_{Load}) (R_1 R_2 R_3 \dots R_s \dots R_n)$$

Solution of (61) for I_{load} yields

$$I_{load} = \frac{\sum_{p=1}^n V_p \prod_{\substack{k=1 \\ k \neq p}}^n R_k}{\prod_{k=1}^n R_k + R_{load} \sum_{p=1}^n V_p \prod_{\substack{k=1 \\ k \neq p}}^n R_k} \quad (62)$$

By replacing the value of I_{load} in (60) with its value in (62), one can get the output currents of the n -parallel connected converters. The general form of the output current of the s^{th} converter is obtained as follows

$$I_s = \frac{\overbrace{\frac{V_s}{R_{load}} \prod_{k=1}^n R_k}^{\text{Load current share of } s \text{ converter}}}{R_s \left[\frac{\prod_{k=1}^n R_k}{R_{load}} + \sum_{\substack{p=1 \\ p \neq s}}^n \prod_{\substack{k=1 \\ k \neq p}}^n R_k \right]} + \frac{\overbrace{\sum_{p=1}^n (V_s - V_p) \prod_{\substack{k=1 \\ k \neq p}}^n R_k}^{\text{Circulating current seen by } s \text{ converter}}}{R_s \left[\frac{\prod_{k=1}^n R_k}{R_{load}} + \sum_{\substack{p=1 \\ p \neq s}}^n \prod_{\substack{k=1 \\ k \neq p}}^n R_k \right]} \quad (63)$$

where V_s , R_s are the output voltage and the line resistance of the s^{th} converter.

4.4 Investigation of circulating current among parallel-connected converters

This part of the chapter investigates the problem of the circulating current that arises among parallel-connected DC-DC converters using a Matlab/Simulink model. Three parallel DC-DC converters connected to the DC load are considered to investigate the circulating current among them as shown in Figure 4.20. Ideal voltage sources are assumed to represent the output voltages of the DC-DC converters for simplicity reasons.

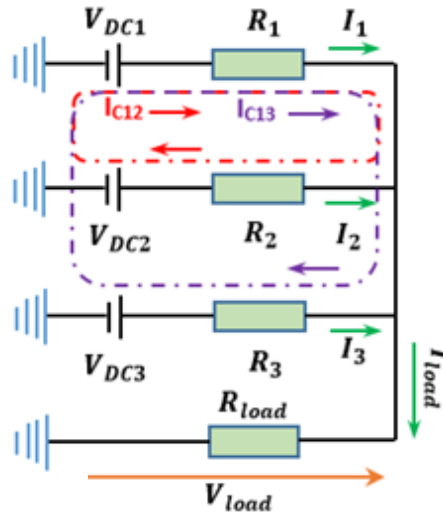


Figure 4.20 Simulation model of three parallel converters.

The circulating current seen by the voltage sources 1, 2, and 3 are I_{cc1} , I_{cc2} and I_{cc3} . Referring to Figure 4.20, I_{cc1} represents the sum of the circulating current between the voltage sources 2 and 3, i.e. $I_{cc1} = I_{c12} + I_{c13}$ and this applies to I_{cc2} and I_{cc3} . The voltage sources 1, 2 and 3 supply currents I_1 , I_2 and I_3 to the load, respectively. The three converters are assumed to have the same power rating (1/3 MVA) with a total conversion power system of 1 MVA. The rated output voltage is assumed to be 700 VDC. The parameters of the system are tabulated in Table 4.1, for nine different tests. The investigation of the circulating current is achieved considering three cases:

a) **Equal output voltages and equal line impedances case**

In this case, three simulation tests are conducted. The system parameters are given for every test as per Table 4.1. In all three tests, the output voltages of the converters are identical and the line impedances are equal. The only

difference between these tests is the loading condition as tests 1, 2 and 3 consider full load, half load and no-load condition, respectively.

b) Unequal output voltages and equal line impedances case

Tests 4, 5 and 6 investigate the circulating current among the parallel DC-DC converters at different output voltages of the converters. Similar to the previous case the tests are conducted at full load, half load and no-load conditions.

c) Unequal output voltages and unequal line impedances case

The impact of different output voltages and different line impedances on the circulating current among parallel-connected converters is investigated under this case at full load, partial load and no-load as per test 7, test 8 and test 9, respectively.

Table 4.1 System parameters at different operating conditions for circulating current investigation

Cases		Ideal case			Unequal converters output voltages			Practical case (unequal line impedances and output voltages)		
		Test1	Test2	Test3	Test4	Test5	Test6	Test7	Test8	Test9
		Full load	Half load	No-load	Full load	half load	No-load	Full load	half load	No-load
Converter 1	$V_{DC1}(V)$	700	700	700	699	699	699	699	699	699
	$R_1(\Omega)$	0.028	0.028	0.028	0.028	0.028	0.028	0.022	0.022	0.022
Converter 2	$V_{DC2}(V)$	700	700	700	701	701	701	701	701	701
	$R_2(\Omega)$	0.028	0.028	0.028	0.028	0.028	0.028	0.028	0.028	0.028
Converter 3	$V_{DC3}(V)$	700	700	700	702	702	702	702	702	702
	$R_3(\Omega)$	0.028	0.028	0.028	0.028	0.0283	0.0283	0.035	0.035	0.035
Load impedance	$R_{load}(\Omega)$	0.49	0.98	1e6	0.49	0.98	1e6	0.49	0.98	1e6

4.4.1 Simulation results

The simulation results for the three cases mentioned above are presented under this subsection. For each test, the output currents and voltages of the converters, load voltage and the circulating currents seen by every converter are plotted. The simulation model is run for 1s for every test.

a) Simulation results of tests 1, 2 and 3

Figure 4.21 shows the simulation results when the system parameters of test 1 are applied as per Table 4.1. This figure shows that the load current is shared equally among the three parallel converters (467.2 A per converter). Also, it shows that the circulating currents I_{cc1} , I_{cc2} and I_{cc3} that seen by all converters is zero. The reason behind these figures is that all converters have the same output voltage and line impedance.

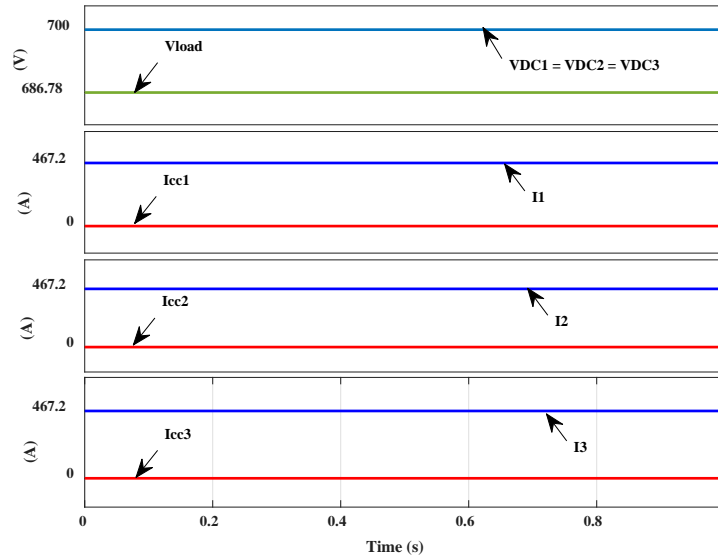


Figure 4.21 Simulation results of test 1.

Figure 4.22 shows the simulation results when the system parameters of test 2 are applied as per Table 4.1. The system parameters of tests 1 and 2 are similar except for the partial load applied in test 2 instead of the full load. The load voltage increased comparing with the figures of test 1 due to partial load is applied. However, the load current is divided evenly between the parallel converters and still no circulating current passing in the system.

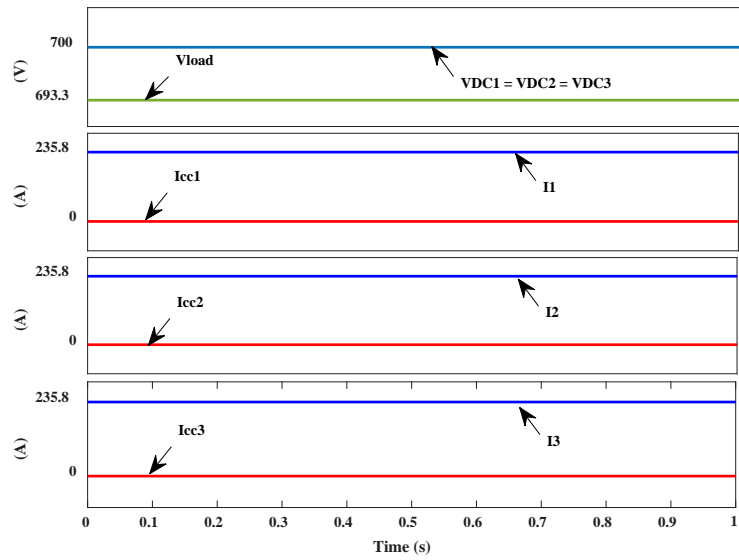


Figure 4.22 Simulation results of test 2.

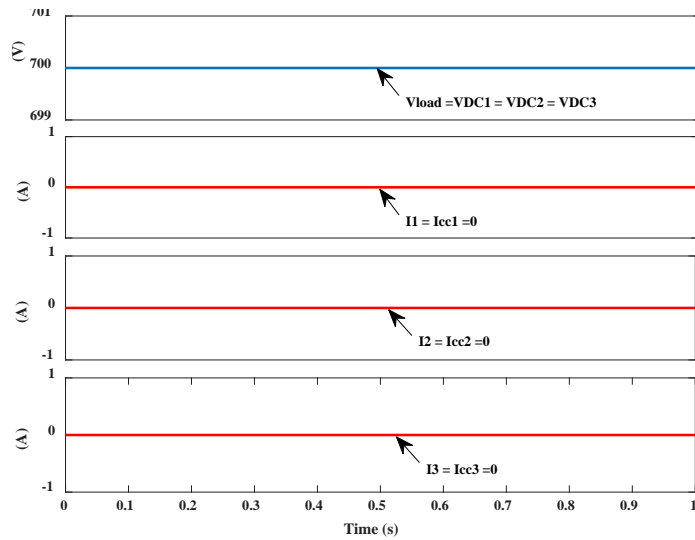


Figure 4.23 Simulation results of test 3.

Figure 4.23 shows the simulation results when the system parameters of test 3 are applied as per Table 4.1. When the no-load condition is applied, the load voltage equals the rated voltage (700 V) as no current is passing in the system. Also, no circulating current is recorded for this case.

b) Simulation results of tests 4, 5 and 6

The tests under this case are conducted to analyse the impact of different output voltages of parallel converters on the circulating current with considering the same line impedances for all converters.

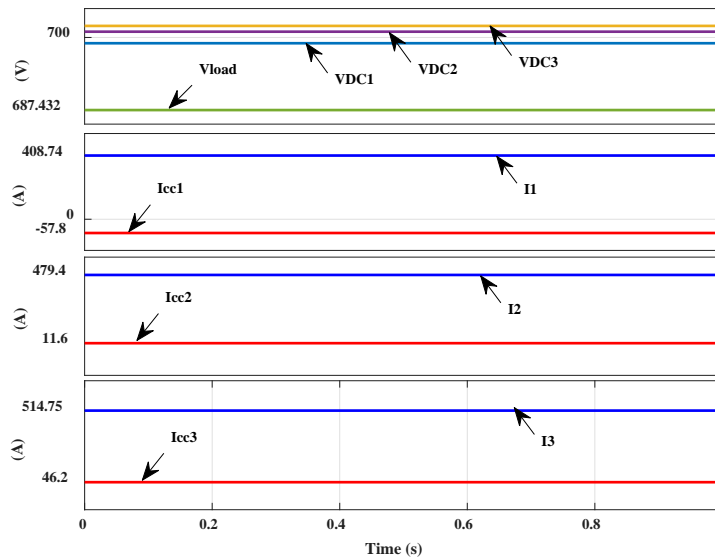


Figure 4.24 Simulation results of test 4.

Figure 4.24 shows the simulation results when the system parameters of test 4 are applied as per Table 4.1. The figure illustrates that the converters with output voltages above the average voltage are supplying circulating current to those having lower output voltages than the average voltage. For example, converter-1 with output voltage equals (699 V) that is below the average voltage (700.66 V) is receiving circulating current from converters-2 (702 V) and converter-3 (701 V). This confirms the derived equations of circulating current among 3-parallel connected converters as per (57), (58) and (59). The load current is shared unequally among the converters due to the output voltages of the converters are different.

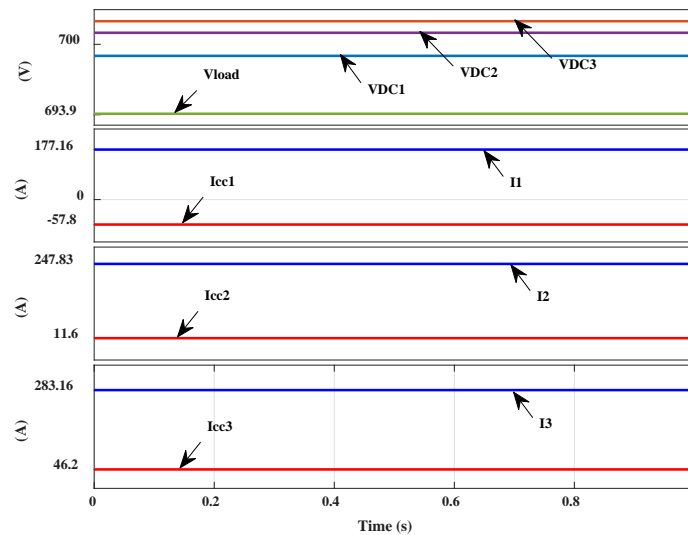


Figure 4.25 Simulation results of test 5.

Figure 4.25 and Figure 4.26 shows the simulation results when the system parameters of test 5 and test 6 are applied as per Table 4.1, respectively. By comparing the simulation results of test 4 (Figure 4.24), test 5 (Figure 4.25) and test 6 (Figure 4.26), one can notice that the circulating currents seen by all converters are almost the same with applying full load, partial load and no-load, respectively. This implies that the load impedance has a slight impact on the circulating current which is confirmed by equations (57), (58) and (59). In those equations, a higher circulating current is expected with a high load impedance (R_{Load}), i.e. no load condition, and this comply with the results of test 6. The more interesting results for test 6, although there is no load applied, there is a circulating current passing among the converters which lead to extra losses in the system.

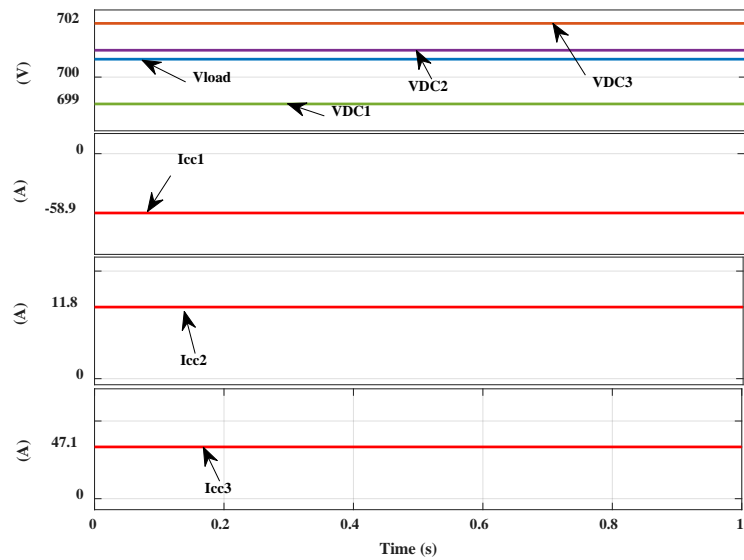


Figure 4.26 Simulation results of test 6.

c) *Simulation results of tests 7, 8 and 9*

In this case, tests 7, 8 and 9 are conducted to investigate the circulating current among the parallel converters considering unequal converters output voltages and unequal line impedances. Different loading conditions are considered for test 7 (full load), test 8 (partial load) and test 9 (no-load). The system parameters used for these tests are recorded in Table 4.1.

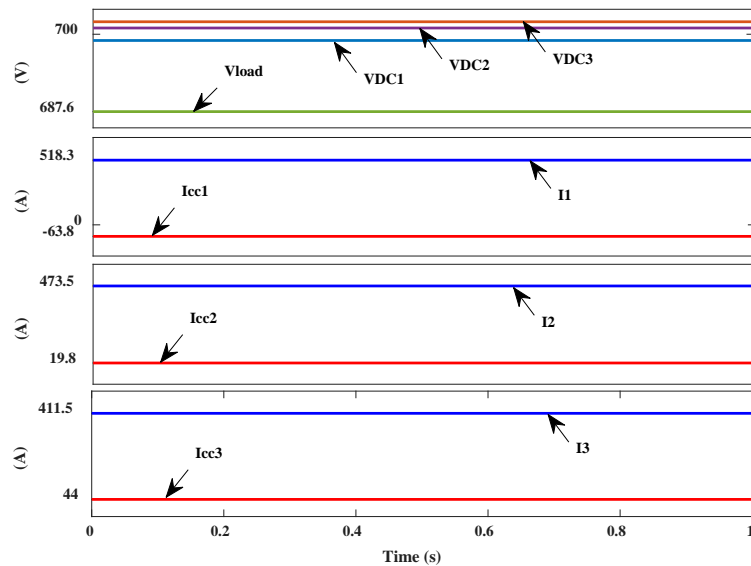


Figure 4.27 Simulation results of test 7.

Figure 4.27 shows the simulation results when the system parameters of test 7 are applied as per Table 4.1. Due to unequal output voltages of the converters, the load current is not shared evenly and the circulating current passing among the converters. Comparing the results of test 4 (unequal output voltages) and test 7 (unequal output voltages and line impedances), the latter has a higher circulating current than the former with approximately 63.8 and 57.8 Amps, respectively as per Table 4.2.

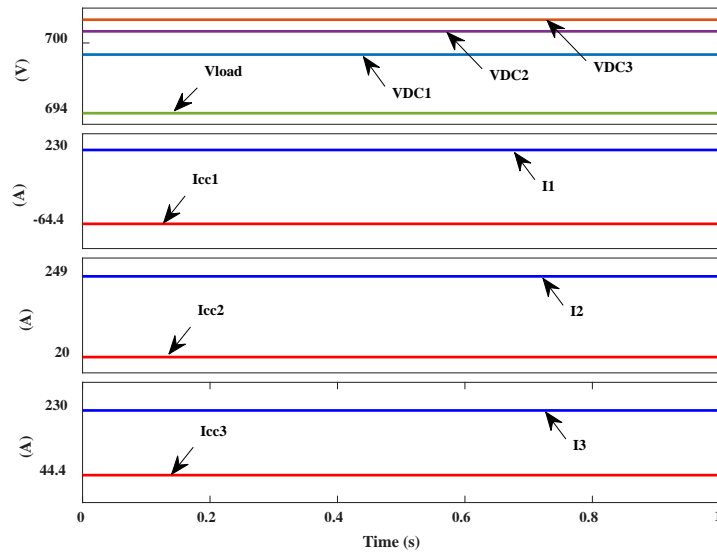


Figure 4.28 Simulation results of test 8.

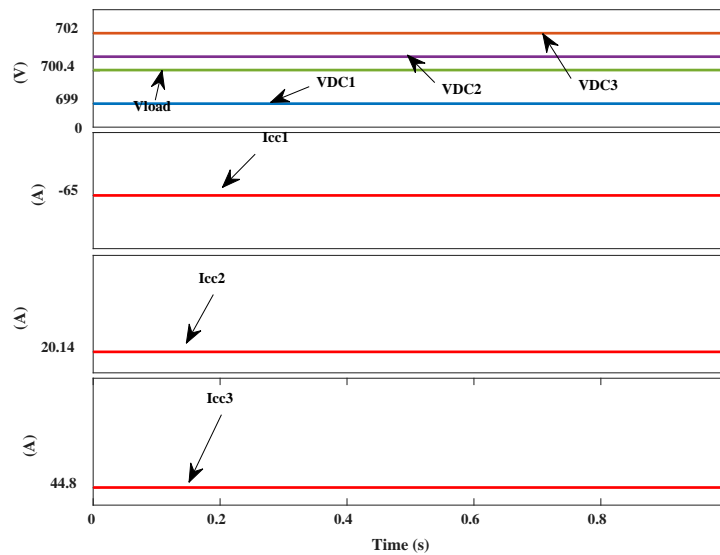


Figure 4.29 Simulation results of test 9.

Figure 4.28 and Figure 4.29 shows the simulation results when the system parameters of test 8 and test 9 are applied as per Table 4.1, respectively. The simulation results in these figures show that higher circulating currents are passing in the system comparing to the figures of tests 5 and 6 of the case-b.

Table 4.2 illustrates the output currents of all converters and the circulating currents seen by all converters in all the tests. Other than Case-a, the table shows that parallel converters are suffering from circulating current which adds extra losses to the system.

Considering unequal output voltages and unequal line impedances results in the highest-circulating current in the system as per Case-c. Additionally, line impedances mismatch has a huge impact on the load current sharing among the parallel converters as illustrated in tests 7 and 8. For example, test 7 with line impedance mismatch shows over 200 A difference between the converter with the lowest and the highest line impedances as per the highlighted cells in white in Table 4.2 comparing with only 2 A difference for test 4 where line impedances are equal.

Table 4.2 Current measurements and circulating current calculation

Cases		Case-a equal output voltages and line impedances			Case-b Unequal output voltages and equal line impedances			Case-c Unequal output voltages and line impedance		
		Test1	Test2	Test3	Test4	Test5	Test6	Test 7	Test8	Test9
		Full load	half load	No-load	Full load	half load	No-load	Full load	half load	No-load
Output currents (A)	I1	467.2	235.8	0.0	466.5	235.5	0.0	582.1	293.7	0.0
	I2	467.2	235.8	0.0	467.9	236.2	0.0	453.8	229.0	0.0
	I3	467.2	235.8	0.0	468.5	236.5	0.0	367.4	185.4	0.0
Sum (Icon)		1401.6	707.5	0.0	1402.9	708.1	0.0	1403.3	708.1	0.0
Circulating currents (A)	Icc1	0.0	0.0	0.0	-57.8	-58.3	-58.9	-63.8	-64.4	-65.0
	Icc2	0.0	0.0	0.0	11.6	11.7	11.8	19.8	20.0	20.1
	Icc3	0.0	0.0	0.0	46.2	46.7	47.1	44.0	44.4	44.9
Load current, A		1401.6	707.5	0.0	1402.9	708.1	0.0	1403.3	708.4	0.0
Load voltage, V		686.7	693.3	700	687.43	693.9	700.6	687.59	693.9	700.4
Circulating current in the system		0.0	0.0	0.0	57.8	58.3	58.9	63.8	64.1	65.0

It is important to clarify that the converters output currents (I_1 , I_2 and I_3) shown in Table 4.2 represent the first terms of equations (57), (58) and (59), respectively. Also, the circulating currents (I_{cc1} , I_{cc2} and I_{cc3}) in the same table represent the summation of the second and the third terms of equations (57), (58) and (59), respectively. However, the measured output currents of the converters 1, 2 and 3 from the Simulink model are $(I_1 + I_{cc1})$, $(I_2 + I_{cc2})$ and $(I_3 + I_{cc3})$, respectively.

Table 4.3 shows the calculated output powers (P_{con1} , P_{con2} and P_{con3}) of the converters 1, 2 and 3, respectively. Also, it shows the power losses in the line impedances due to the load current (P_{los1} , P_{los2} and P_{los3}). Additionally, it shows the power losses in the line impedances due to the circulating current (P_{lcc1} , P_{lcc2} and P_{lcc3}). And lastly, the load power P_{load} and the circulating powers (P_{c1} , P_{c2} and P_{c3}) of the three converters.

The power results in Table 4.3 show that some converters absorb power even at no load, while others are delivering it. The results for tests 1 and 2 show zero circulating power and zero power losses due to the circulating current as there is no circulating current recorded, however, there are normal power losses in the line impedance due to the converters load currents. Test 3 (at no-load) shows zero for all powers, as there is no load current nor circulating current.

To sum up, due to the difference in the converters output voltages as per the case-b and c, the circulating current is passing in the system that leads to circulating power and power losses due to this circulating current even with no load applied as per the tests 6 and 9. Comparing the listed results of tests 4 and 7, the load power is shared equally in test 4 while unequal power-sharing occurred in test 7 and this is due to unequal line impedances which leads to unequal load current sharing as explained in Table 4.2 earlier.

Table 4.3 Converters power calculations

Cases		Ideal case			Unequal converter output voltage			Practical case (unequal line impedance and output voltages)		
		Test1	Test2	Test3	Test4	Test5	Test6	Test 7	Test 8	Test 9
		Full load	half load	No- load	Full load	half load	No- load	Full load	half load	No- load
Converters output Powers (W)	Pcon1	3.3E+5	1.7E+5	0.0	3.3E+5	1.6E+5	0.0	4.1E+5	2.1E+5	0.0
	Pcon2	3.3E+5	1.7E+5	0.0	3.3E+5	1.7E+5	0.0	3.2E+5	1.6E+5	0.0
	Pcon3	3.3E+5	1.7E+5	0.0	3.3E+5	1.7E+5	0.0	2.6E+5	1.3E+5	0.0
	Sum (Pcon)	9.8E+5	5.0E+5	0.0	9.8E+5	5.0E+5	0.0	9.8E+5	5.0E+5	0.0
Load power		9.6E+5	4.9E+5	0.0	9.6E+5	4.9E+5	0.0	9.6E+5	4.9E+5	0.0
Line power losses due to converters' load current (W)	Plos1	6.2E+3	1.6E+3	0.0	5.4E+3	1.2E+3	0.0	6.6E+3	1.5E+3	0.0
	Plos2	6.2E+3	1.6E+3	0.0	6.3E+3	1.7E+3	0.0	6.1E+3	1.6E+3	0.0
	Plos3	6.2E+3	1.6E+3	0.0	6.8E+3	1.9E+3	0.0	5.3E+3	1.5E+3	0.0
	Sum (Plos)	1.9E+4	4.7E+3	0.0	1.9E+4	4.7E+3	0.0	1.8E+4	4.6E+3	0.0
Circulating powers (W)	Pc1	0.0	0.0	0.0	-4E+4	-4.1E+4	-4.1E+4	-4.5E+4	-4.5E+4	-4.5E+4
	Pc2	0.0	0.0	0.0	8.1E+3	8.2E+3	8.3E+3	1.4E+4	1.4E+4	1.4E+4
	Pc3	0.0	0.0	0.0	3.2E+4	3.3E+4	3.3E+4	3.1E+4	3.1E+4	3.1E+4
	Sum (Pc)	0.0	0.0	0.0	1.6E+2	1.6E+2	1.6E+2	1.7E+2	1.7E+2	1.7E+2
Line power losses due to circulating current (W)	Plcc1	0.0	0.0	0.0	-6.7E+2	-2.9E+2	9.8E+1	-7.3E+2	-3.2E+2	9.3E+1
	Plcc2	0.0	0.0	0.0	1.3E+2	5.8E+1	-2E+1	2.3E+2	1.0E+2	-2.9E+1
	Plcc3	0.0	0.0	0.0	5.3E+2	2.3E+2	-7.8E+1	5.0E+2	2.2E+2	-6.4E+1

4.5 Summary

In the first part of this chapter, classification of DC-DC converters was presented showing different possible converter configurations. Steady-state analysis for the buck, boost and buck-boost converters were held to obtain the voltage conversion ratio of these converters. Additionally, voltage and current ripples analyses were performed to obtain the inductor and capacitor values that achieve the desired current ripple and voltage ripple, respectively.

The second part of the chapter reviewed various control approaches for parallel-connected DC-DC converters in an islanded DC microgrid. These control techniques are divided into two categories: active load sharing techniques and passive load-sharing techniques (known as droop control). Flexibility is the main advantage of the latter due to lack of communication that makes it favoured research option based on research trends. However, the former has the potential to be improved and expanded due to the advancements in the communication infrastructure. Based on this and considering the advantages of active load sharing techniques such as good voltage regulation and current sharing performance, the instantaneous average current sharing technique is proposed and improved for minimizing the circulating current among parallel DC-DC converters later in Chapter 5.

The third part of this chapter investigated the circulating current among multiple parallel converters connected to a resistive load. Mathematical derivations were performed to obtain the converter load current share and the circulating current seen by each converter. These derivations were performed based on two converters, three converters and a general case with n -parallel converters. Simulation analyses were held for 3-parallel converters sharing the same load to visualize the circulating current phenomenon among them due to line impedance mismatch and unequal output voltages. From these simulations, it could be concluded that circulating current exists in the system regardless of the load applied and it occurs, mainly, when there is a difference in the output voltages of the parallel converters. Additionally, at no-load condition, power exchange among parallel converters occurs due to the circulating current. This power exchange can affect the control system and even damage the converters. Furthermore, line impedances mismatch has a huge impact on the load

current sharing among the parallel converters with a current difference reaching around 37% between the converters with the lowest and the highest line impedances.

Chapter 5 A New Adaptive IACS Controller for Circulating Current Minimization

This chapter addresses the MUP's challenge of the circulating current, as presented in Section 1.4.3 of Chapter 1, by proposing a new adaptive Instantaneous Average Current Sharing (IACS) technique. The objective of this chapter is to investigate the possibility of using IACS with parallel converters in DC systems for proper voltage regulation and for circulating current minimisation. Modelling of a single boost converter and the generalized model of n -parallel converters with IACS are derived with stability analysis provided for both models.

Matlab/Simulink study is held to show the advantages and performance of the proposed technique against the droop control technique of another study in the literature. It is important to confirm that this chapter focuses mainly on studying the feasibility of using IACS to control parallel DC-DC converters within a DC system. So, more attention is paid to analysing the stability of the controller itself within a simple DC system (parallel solar PV arrays) without considering all energy components of the MUP's microgrid.

5.1 Background

As presented in Section 4.3 of Chapter 4, circulating current and load sharing are affected by the line impedance mismatch and unequal output voltages of the parallel converters. Section 4.2 of Chapter 4 explored various control schemes, which proposed in the open literature for controlling parallel-connected converters. Few researchers have considered circulating current minimization in their control schemes. For example, study [114] proposed a proportional droop index algorithm with droop shifting for improving the load voltage deviation and load sharing in a DC-microgrid. The controller, in that study, successfully achieved proportional power-sharing among the converters, however, the study does not take into account the impact of the circulating current among the parallel converters. Also, the load voltage is not accurately regulated as it is varying with the input voltage and load current variations.

Studies [126, 145] proposed a master-slave control based on two layers controller to coordinate the operation of multiple wind turbines in an isolated DC microgrid. Although the results show that the controller successfully achieved power balance, the controller dependency on the communications and upper layer for providing power references to lower layer controllers degrades the system reliability in case of failure of the upper layer or there is communication loss.

Few studies [129, 146-149] proposed IACS control scheme to achieve proper voltage regulation and load sharing among parallel inverters in AC systems which showed good performance in achieving those objectives and in minimizing the circulating current. However, IACS controller has, to the best of the author's knowledge, not been proposed for parallel DC-DC converters in the literature before. For this reason, this chapter investigates the feasibility of using IACS technique to achieve proper voltage regulation and circulating current minimization among parallel DC-DC converters within a DC system.

5.2 System configuration

Figure 5.1 shows two input-parallel output-parallel DC-DC connected converters. The input to these converters is the output of the rectifier which connected to the energy system (tidal or wind) as presented earlier in Figure 3.2 of Chapter 3. V_{i1} and V_{i2} represent the input voltages from the diode rectifier. v_{conv-1} , v_{conv-2} , i_1 , i_2 , R_1 and R_2 refer to output voltages, output currents and line impedances of converter-1 and converter-2, respectively. I_{c12} represents the circulating current passing from converter-1 to converter-2 and R_{load} is the load resistance.

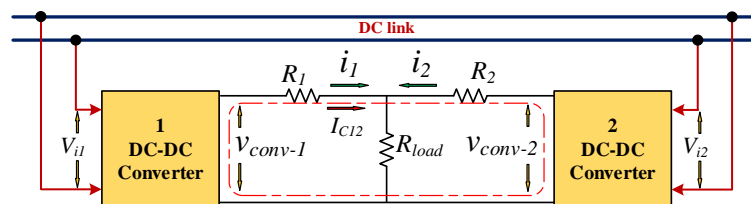


Figure 5.1 Two parallel DC-DC converters connected between RES and DC-load.

The circulating current between two parallel converters is derived in Chapter 4, Section 4.3.1 which is copied below

$$I_{C12} = -I_{C21} = \frac{v_{conv-1} - v_{conv-2}}{R_1 + R_2} \quad (64)$$

Referring to (64), the magnitude of the circulating current I_{C12} depends on the difference between the output voltages of the parallel converters v_{conv-1} and v_{conv-2} . To minimise this circulating current, a control strategy is required to ensure the output voltages of both converters (v_{conv-1} and v_{conv-2}) are equal in case there is line impedances mismatch or converters parameters deviation.

5.3 The proposed control scheme

Figure 5.2 shows the conventional IACS controller associated with the parallel DC-DC converters. IACS controller includes four control loops (three feedback loops and one feedforward loop). The three feedback control loops are: voltage feedback loop for converter output voltage regulation, outer current sharing loop for proper current sharing among parallel converters [129], and inner current feedback loop which provide a fast dynamic response for the system during steady-state and transient. Lastly, the feedforward loop is included for the high tracking accuracy of the reference voltage [129]. Two Proportional Integral (PI) controllers are used for current sharing and voltage regulation control loops.

The left part of Figure 5.2 shows the proposed IACS with the adaptive reference voltage. v_{conv-i} refers to the output voltage of the i converter which is one of the parallel converters in a DC system. v_{load} and v_{avg} are the load voltage and average output voltages of parallel converters, respectively. $v_{nominal}$ is the nominal or reference load voltage. v_{ref-i} is the reference voltage after adaptation. K_c and K refer to the gain of the inner capacitor current feedback loop and outer current loop gain, respectively. i_{ci} is the capacitor current of the i converter where i equals from 1 to n and n is the number of parallel-connected converters.

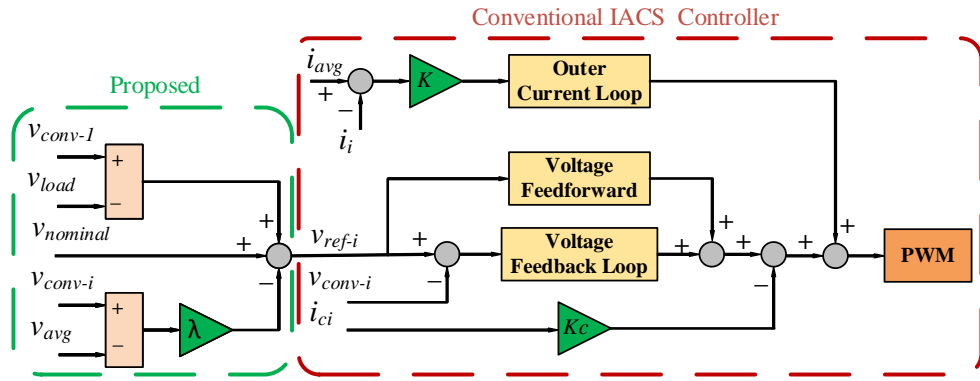


Figure 5.2 IACS controller with the proposed section added.

5.3.1 Steepest Descent Method (SDM)

SDM is an iterative method that uses the gradient of the objective function to find a search direction through design space [150]. SDM is proposed to adapt the reference voltage of individual converters such that the output voltages of all parallel converters are the same.

The idea of SDM is to select a search direction (by taking the gradient of the cost function) and then finds the minimum value of the cost function based on that direction. Then, the process is repeated by selecting a new search direction and so forth until stop criteria have been satisfied.

In order to match the output voltages of the parallel converters, it is proposed to regulate them to equal to the average voltage among them. To achieve this goal, the steady-state error which is given in (65) must be eliminated.

$$e(k) = v_{conv-i}(k) - v_{avg}(k) \quad (65)$$

where $v_{conv-i}(k)$ is the converter output voltage and $v_{avg}(k)$ is the average output voltages of parallel converters at instant k . The adaptive steepest descent algorithm is

$$v_{ref-i}(k) = v_{ref}(k-1) - \lambda \nabla f(k) \quad (66)$$

where $f(k)$, $\nabla f(k)$ are the cost function and the gradient of the cost function with respect to the converter output voltage. The negative gradient in (66) refers to the

direction of the steepest descent (minimum value). λ is the adaptive gain that controls the convergence speed of $f(k)$ and it is a positive value. The quadratic cost function equals

$$f(k) = \frac{1}{2} e^2(k) \quad (67)$$

by taking the gradient of $f(k)$ in (67)

$$\nabla f(k) = \frac{\partial f(k)}{\partial v_{conv-i}(k)} = \frac{1}{2} \frac{\partial \left(v_{conv-i}(k) - v_{avg}(k) \right)^2}{\partial v_{conv-i}(k)} = e(k) \quad (68)$$

Replacing the value of $\nabla f(k)$ in (66) with (68), the adaptive steepest descent algorithm will be

$$v_{ref-i}(k) = v_{ref}(k-1) - \lambda e(k) \quad (69)$$

replacing $e(k)$ in (69) by (65), gives

$$v_{ref-i}(k) = v_{ref}(k-1) - \lambda \left(v_{conv-i}(k) - v_{avg}(k) \right) \quad (70)$$

where $v_{ref}(k-1)$ is the nominal voltage of the microgrid. Although the algorithm in (70) gives excellent results regarding the circulating current minimization, however, there is a load voltage deviation from the nominal value. To eliminate this deviation, the difference between the converter output voltage and load voltage (v) is added to the algorithm in (70). Then, the adaptive steepest descent algorithm in its final form becomes

$$v_{ref-i}(k) = v_{ref}(k-1) - \lambda \left(v_{conv-i}(k) - v_{avg}(k) \right) + \left(v_{conv-i} - v(k) \right) \quad (71)$$

- *System stability with varying the adaptive gain*

Referring to (69), the adaptive gain λ should be selected to achieve fast convergence while maintaining the system stable as there is a trade-off between them. Lyapunov's direct method is used for analyzing the system stability while changing the adaptive gain.

According to Lyapunov's stability theorem, a system is globally asymptotically stable if the Lyapunov function $V(k)$ satisfies the following conditions: $V(k) > 0$ and $\Delta V(k) < 0$. In other words, the Lyapunov function must be always positive at any instant while the change in this function must be negative to ensure system stability. The proposed Lyapunov function is the quadratic of the error function which satisfies the first Lyapunov criteria

$$V(k) = e_i^2(k) \quad (72)$$

Change in Lyapunov function equals

$$\Delta V(k) = V(k+1) - V(k)$$

$$\Delta V(k) = e_i^2(k+1) - e_i^2(k) \quad (73)$$

$$\Delta V(k) = \Delta e_i^2(k) + 2 \Delta e_i(k)e_i(k)$$

Where $\Delta e_i(k) = e_i(k+1) - e_i(k)$. Using (65)

$$\begin{aligned} \Delta e_i(k) &= \left(v_{conv-i}(k+1) - v_{avg}(k+1) \right) \\ &\quad - \left(v_{conv-i}(k) - v_{avg}(k) \right) \\ &= v_{conv-i}(k+1) - \frac{1}{n} \sum_{j=1}^n v_{conv-j}(k+1) - v_{conv-i}(k) \\ &\quad + \frac{1}{n} \sum_{j=1}^n v_{conv-j}(k) \end{aligned} \quad (74)$$

where $v_{avg} = (\sum_{j=1}^n v_{conv-j})/n$.

As boost converters are considered for the converters of Figure 5.1, so the discrete average model of a boost converter is used for this analysis as follows

$$\begin{bmatrix} i_{li}(k+1) \\ v_{ci}(k+1) \end{bmatrix} = \begin{bmatrix} 1 & -\frac{(1-D)T_s}{L} \\ \frac{(1-D)T_s}{C} & 1 - \frac{T_s}{R_{load}C} \end{bmatrix} \begin{bmatrix} i_{li}(k) \\ v_{ci}(k) \end{bmatrix} + \begin{bmatrix} \frac{T_s}{L} \\ 0 \end{bmatrix} [V_{ii}] \quad (75)$$

Where i_{li} represents the inductor current and it is assumed to equal the converter output current. v_{ci} refers to the capacitor voltage which equals the converter output voltage v_{conv-i} . T_s , D , C and V_{ii} are the switching period, duty cycle, converter output capacitance and converter input voltage, respectively.

By replacing v_{conv-i} in (74) with its value from (75) as $v_{conv-i} = v_{ci}$, one can get

$$\begin{aligned} \Delta e_i(k) &= \frac{(1-D)T_s}{C} i_{li}(k) + \left(1 - \frac{T_s}{R_{load}C}\right) v_{ci}(k) - v_{ci}(k) \\ &\quad - \frac{1}{n} \sum_{j=1}^n \left(\frac{(1-D)T_s}{C} i_{li}(k) + \left(1 - \frac{T_s}{R_{load}C}\right) v_{ci}(k) \right) \\ &\quad + \frac{1}{n} \sum_{j=1}^n v_{conv-j}(k) \end{aligned} \quad (76)$$

The same line impedances are assumed, for simplicity. i.e. $i_{i1} = i_{i2} = \dots = i_{in} = \frac{v_{ci}}{2R_{load}}$ [19]

$$\begin{aligned} \Delta e_i(k) &= \frac{(1-D)T_s}{C} \frac{v_{ci}(k)}{2R_{load}} + \left(1 - \frac{T_s}{R_{load}C}\right) v_{ci}(k) - v_{ci}(k) \\ &\quad - \frac{1}{n} \sum_{j=1}^n \left(\frac{(1-D)T_s}{C} \frac{v_{cj}(k)}{2R_{load}} + \left(1 - \frac{T_s}{R_{load}C}\right) v_{cj}(k) \right) + \frac{1}{n} \sum_{j=1}^n v_{conv-j}(k) = \\ &\quad - \left(\frac{T_s(1+D)}{2R_{load}C} \right) e_i(k) \end{aligned} \quad (77)$$

By inserting (77) into (73), the change in Lyapunov function will be

$$\begin{aligned}\Delta V(k) &= \left[-\left(\frac{T_s(1+D)}{2R_{load}C} \right) e_i(k) \right]^2 + 2 \left[-\left(\frac{T_s(1+D)}{2R_{load}C} \right) e_i(k) \right] e_i(k) \\ &= e_i^2(k) \left(\frac{T_s(1+D)}{2R_{load}C} \right) \left[\left(\frac{T_s(1+D)}{2R_{load}C} \right) - 2 \right]\end{aligned}\quad (78)$$

As per the Lyapunov's second criterion, $\Delta V(k)$ must be negative to ensure system stability. Referring to (78), it is clear that the first term $(e_i^2(k) \left(\frac{T_s(1+D)}{2R_{load}C} \right))$ is positive definite while the change in Lyapunov function becomes negative definite if

$$\left[\left(\frac{T_s(1+D)}{2R_{load}C} \right) - 2 \right] < 0 \Rightarrow \lambda \left(\frac{T_s(1+D)}{2R_{load}C} \right) < 2 \Rightarrow \lambda < \frac{4R_{load}C}{T_s(1+D)} \quad (79)$$

The choice of the adaptive gain λ , to ensure system stability, will be decided based on the quality of the load voltage after deriving the whole system model later in this chapter.

5.4 System modelling

5.4.1 Single DC-DC converter model

The switching converter is a nonlinear system, so a small-signal AC model is required for stability analysis purposes [151]. Figure 5.3 illustrates that the output voltage $v(t)$ of the DC-DC converter depends on three independent quantities: 1) input voltage, $v_g(t)$, which could contain variations produced by a rectifier circuit or by switching neighbouring loads on and off. 2) Load current $i_{load}(t)$ is normally varying according to the applied load. 3) Duty cycle $d(t)$ is required to be variable to give fixed output voltage based on negative feedback control [152].

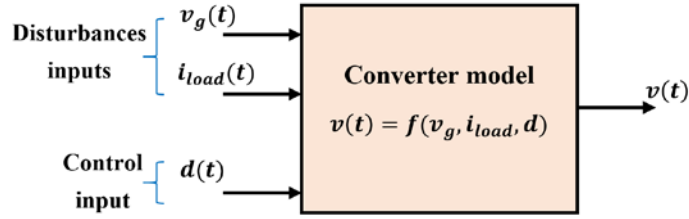


Figure 5.3 Functional diagram of DC-DC converter.

In essence, obtaining the desired output voltage cannot be achieved without using negative feedback that automatically adjusts the duty cycle to alleviate the disturbances due to the input voltage and load current variations as explained.

The following section derives the relationship or the transfer function between the converter output voltage and the three independent parameters $v_g(t)$, $i_{load}(t)$ and $d(t)$. Figure 5.4 illustrates the canonical form for an ideal DC-DC converter in a Continuous Conduction Mode (CCM).

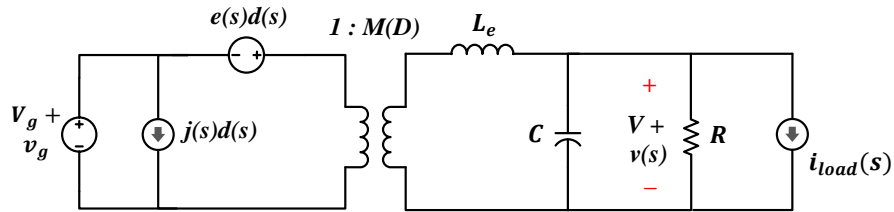


Figure 5.4 Canonical model for ideal DC-DC converter in CCM [152].

For a boost converter, $L_e = \frac{L}{(1-D)^2}$, $j(s) = \frac{V}{(1-D)^2 R}$, $M(D) = \frac{1}{(1-D)}$ and $e(s) = V \left(1 - \frac{sL}{(1-D)^2 R} \right)$ [152]. Where L , R , V and D are the converter inductance, load resistance, steady-state converter output voltage and duty cycle, respectively.

Finding the transfer functions of the boost converter can be achieved by solving the small-signal equivalent circuit model in Figure 5.4 using conventional linear circuit analysis. To obtain the transfer functions of the line-to-output voltage and the control-to-output voltage, one can set $d(s)$ and $v_g(s)$ in Figure 5.4 equal to zero, respectively. The control-to-output $G_{vd}(s)$ and the line-to-output $G_{vg}(s)$ transfer functions are given in (80) and (81), respectively [152].

$$G_{vd}(s) = G_{d0} \frac{\left(1 - \frac{s}{\omega_z}\right)}{\left(1 + \frac{s}{Q\omega_0} + \left(\frac{s}{\omega_0}\right)^2\right)} \quad (80)$$

$$G_{vg}(s) = G_{g0} \frac{1}{\left(1 + \frac{s}{Q\omega_0} + \left(\frac{s}{\omega_0}\right)^2\right)} \quad (81)$$

where $G_{d0} = \frac{V}{\dot{D}}$, $\omega_z = \frac{\dot{D}^2 R}{L}$, $\omega_0 = \frac{\dot{D}}{\sqrt{LC}}$, $Q = \dot{D} R \sqrt{\frac{C}{L}}$, $G_{g0} = \frac{1}{\dot{D}}$ and $\dot{D} = (1 - D)$. While V , D , L and C are the steady-state values of the output voltage, duty cycle, and the inductance and capacitance of the boost converter, respectively.

As per Figure 5.3, the converter output voltage variations depends on three independent quantities as mentioned in the previous section. Equations (80) and (81) illustrate the relationship between the converter output voltage and two independent quantities: the line voltage and control input. The relationship between the converter output voltage and the third independent quantity, load current, can be obtained by determining the converter output impedance which is derived in the following section.

To derive the converter output impedance, the variations in $d(s)$ and $v_g(s)$ are set to zero in Figure 5.4 which can be reduced to the circuit in Figure 5.5. From this figure, one can get Z_{out} as follows

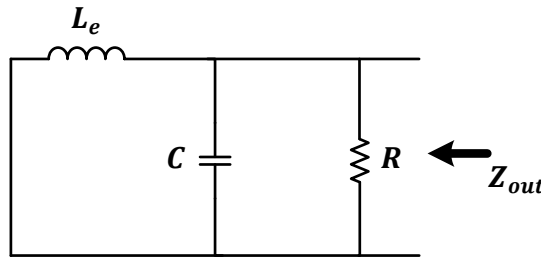


Figure 5.5 Output impedance of DC-DC boost converter.

$$Z_{out} = R \parallel sL_e \parallel \frac{1}{sC} \quad (82)$$

$$Z_{out} = \frac{sL_e}{s^2 CL_e + s\left(\frac{L_e}{R_{load}}\right) + 1}$$

Using (80), (81) and (82), the converter output voltage variation can be expressed as a linear combination of the three independent inputs as per Figure 5.6.

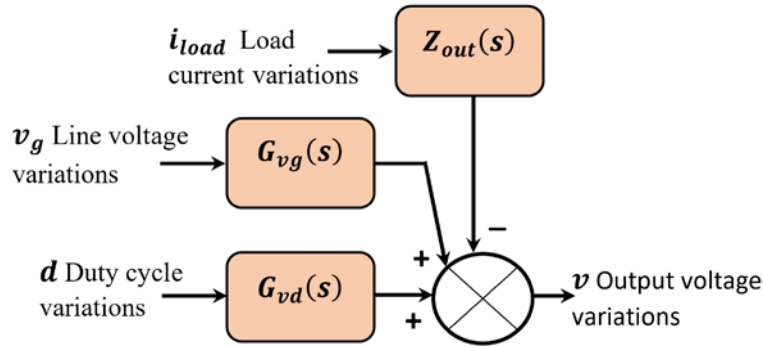


Figure 5.6 Small signal AC linearized model of DC-DC boost converter [152].

$$v(s) = G_{vd}(s)d(s) + G_{vg}(s)v_g(s) - Z_{out}(s)i_{load}(s) \quad (83)$$

Equation (83) represents the small-signal linearized model of a single boost converter.

5.4.2 Model of a boost converter with IACS

The previous section derived a small signal linearized model for a single boost converter. However, regulating the output voltage of a converter cannot be realized without a negative feedback control which changes the value of the duty cycle to alleviate the impact of the disturbances due to line voltage and load current variations as described in the previous section.

Deriving a model for a DC-DC boost converter with the IACS controller is achieved in two steps. First, obtain the control-to-output and line-to-output transfer functions of the boost converter with including the feedback from the capacitor current as per the IACS block diagram in Figure 5.2 which gives the block diagram in Figure 5.7. Then, adding the voltage feedback loop and the voltage feedforward loops to obtain the model of a boost converter with the IACS controller.

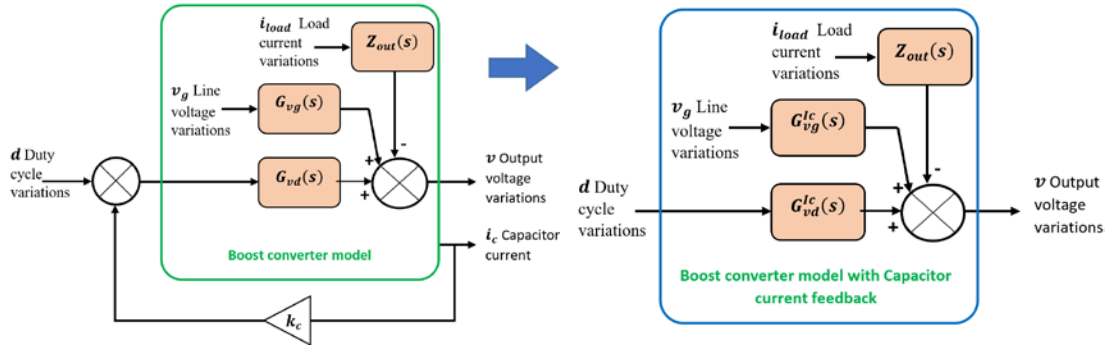


Figure 5.7 Boost converter model with capacitor current feedback.

In Figure 5.7, $G_{vd}(s)$ and $G_{vg}(s)$ represent the control-to-output and line-to-output transfer functions of the boost converter only, respectively, while $G_{vd}^{Ic}(s)$ and $G_{vg}^{Ic}(s)$ are the control-to-output and line-to-output transfer functions with adding the capacitor current feedback, respectively. The boost converter model with the IACS controller can be modelled as per Figure 5.8.

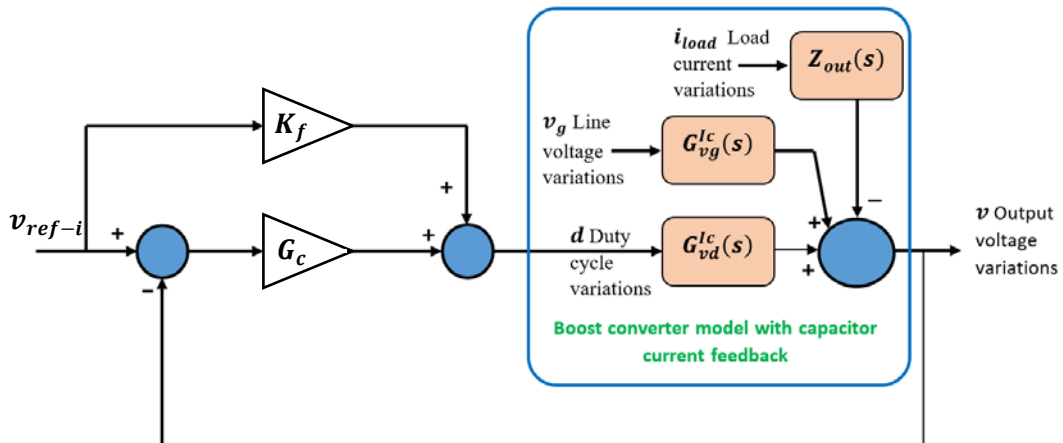


Figure 5.8 Boost converter model with IACS controller.

Where K_f and K_c refer to the gain of the voltage feedforward loop and the gain of the inner capacitor current feedback loop, respectively. v_g is the variations or the disturbance of the converter input voltage and i_{load} is the load current variations. v_{ref-i} represents the adaptive reference voltage of parallel converters. This voltage reference is different from one converter to another and it is used to regulate the output voltage of all converters to be close to the average voltage as per equation (71). G_c

refers to the transfer function of the PI controller of the voltage loop. G_c equals to $(k_{pv} + \frac{k_{iv}}{s})$ where k_{pv} and k_{iv} are the proportional and integral gains of this controller, respectively. From the block diagram of Figure 5.8, the output voltage variation of a single converter with IACS is derived as follows

$$v = \frac{G_{vd}^{Ic} [G_c + K_f]}{1 + G_{vd}^{Ic} G_c} v_{ref} + \frac{G_{vg}^{Ic}}{1 + G_{vd}^{Ic} G_c} v_g - \frac{Z_{out-i}}{1 + G_{vd}^{Ic} G_c} i_{load} \quad (84)$$

Equation (84) can be simplified to (85) as follows

$$v = G_i v_{ref-i} + P_i v_{g-i} - Z_{CL-i} i_{load-i} \quad (85)$$

where G_i , P_i and Z_{CL-i} are the closed-loop transfer functions of control-to-output, line-to-output and output impedance, respectively.

5.4.3 Model of n -parallel connected converters with IACS

To derive a model for parallel-connected converters, Thevenin theorem is used to obtain the equivalent circuit for a closed-loop converter with IACS in Figure 5.8 [149]. The closed-loop system of Figure 5.8 can be represented by an equivalent circuit as a controlled voltage source Gv_{ref} in series with the converter closed-loop output impedance Z_{CL} .

For the purpose of this chapter which analyses the impact of line impedance on the circulating current among parallel converters, the variations of the converters input voltages are assumed zero considering these converters are supplied from high capacitance DC-link. Also, it is assumed that all parallel converters are identical, i.e. it is assumed that

$$\begin{aligned} Z_{CL1} &= Z_{CL2} = Z_{CLn} = Z_{CL} \\ Z_{p1} &= Z_{p2} = Z_{pn} = Z_p \\ H_1 &= H_2 = H_n = H \\ G_1 &= G_2 = G_n = G \end{aligned} \quad (86)$$

Where Z_p is the line impedance. H is the transfer function of the current sharing PI controller. However, practically, there is no identical converter as electrical components have always tolerances. These parameter deviations make the output current of individual converters different and mismatched line impedances do the same as examined in Chapter 4. For simplicity, the impact of parameters deviations and line impedances mismatch are combined as a disturbance at the converter output current. As a result, line impedance will be the same for all converters as its impact is already included in the disturbance current i_{dis} .

At first, a model for n -parallel converters is derived without considering the adaptive section for simplicity. Based on (86), a model for n - parallel converters can be implemented as per Figure 5.9. This model can be described by a set of equations as follows

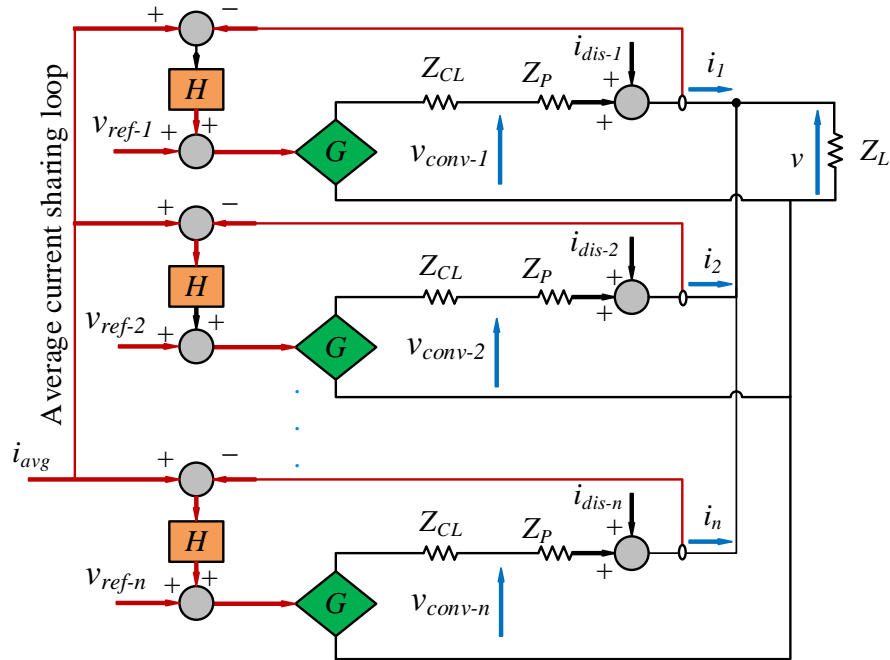


Figure 5.9 IACS controller model with n -parallel DC-DC converters.

$$(i_1 + i_2 + \dots + i_n)Z_L = Z_L \sum_{j=1}^n i_j = v \quad (87)$$

$$\begin{aligned}
 G\{v_{ref-1} + (i_{avg} - i_1)H\} - v &= (i_1 - i_{dis-1})Z_e \\
 G\{v_{ref-2} + (i_{avg} - i_2)H\} - v &= (i_2 - i_{dis-2})Z_e \\
 &\vdots \\
 &\vdots \\
 G\{v_{ref-n} + (i_{avg} - i_n)H\} - v &= (i_n - i_{dis-n})Z_e
 \end{aligned} \tag{88}$$

where $Z_e = Z_{CL} + Z_P$ and i_{avg} represents the average output currents of n -parallel converters which equals

$$i_{avg} = \frac{(i_1 + i_2 + i_n)}{n} = \frac{\sum_{j=1}^n i_j}{n} \tag{89}$$

by adding the group of equations of (88) together, one can get

$$G \sum_{j=1}^n v_{ref-j} + GH \left(ni_{avg} - \sum_{j=1}^n i_j \right) - nv = \left(\sum_{j=1}^n i_j - \sum_{j=1}^n i_{dis-j} \right) Z_e \tag{90}$$

by inserting i_{avg} from (89) and $\sum_{j=1}^n i_j$ from (87) into (90), then solve for the output voltage yields

$$v = \frac{G/n}{1 + \frac{Z_e}{nZ_L}} \sum_{j=1}^n v_{ref-j} + \frac{Z_e/n}{1 + \frac{Z_e}{nZ_L}} \sum_{j=1}^n i_{dis-j} \tag{91}$$

The output current of k^{th} converter can be obtained as follows. Referring to the equation (88), the output current of k^{th} converter can be written as follows

$$G\{v_{ref-k} + (i_{avg} - i_k)H\} - v = (i_k - i_{dis-k})Z_e \tag{92}$$

from (87) and (89), i_{avg} can be represented as

$$i_{avg} = \frac{v}{nZ_L} \quad (93)$$

by inserting v and i_{avg} from (91) and (93), respectively, into (92), the output current of the k^{th} converter can be obtained as follows

$$i_k = \frac{n_1}{d_1} v_{ref-k} + \frac{n_2}{d_2} \sum_{j=1}^n v_{ref-j} + \left(\frac{1}{n}\right) \frac{n_3}{d_2} \sum_{j=1}^n i_{dis-j} + \frac{1}{d_1} i_{dis-k} \quad (94)$$

where $n_1 = G/Z_e$, $n_2 = \left(\frac{G}{nZ_e}\right) \left(\frac{GH}{nZ_L} - 1\right)$, $n_3 = \left(\frac{GH}{nZ_L} - 1\right)$, $d_1 = \left(1 + \frac{GH}{Z_e}\right)$ and $d_2 = \left(1 + \frac{GH}{Z_e}\right) \left(1 + \frac{Z_e}{nZ_L}\right)$. It is important to confirm that output voltage and current equations in (91) and (94) are derived without considering the adaptive reference voltage for simplicity.

As the adaptive part is ignored while deriving the current and voltage equations in the previous section, the following section derives those equations with considering the adaptive part of the controller. Recall equation (71) which is rewritten for the k^{th} converter as follows

$$v_{ref-k} = v_{ref} - \lambda(v_{conv-k} - v_{avg}) + (v_{conv-k} - v) \quad (95)$$

where v_{ref} represent the nominal load voltage. From Figure 5.9, the output voltage of the k^{th} converter is

$$v_{conv-k}(s) = v(s) + (i_k - i_{dis-k})Z_p \quad (96)$$

Replace $v_{conv-k}(s)$ in (95) with (96) then rearrange which yields

$$v_{ref-k}(s) = v_{ref}(s) - \lambda v(s) + (1 - \lambda)(i_k - i_{dis-k})Z_p + \lambda v_{avg}(s) \quad (97)$$

Consider n -parallel connected converters, then n equations of (97) will be added together to give (98)

$$\begin{aligned} \sum_{j=1}^n v_{ref-j}(s) &= n v_{ref}(s) - n \lambda v(s) + (1 - \lambda) \left[\sum_{j=1}^n i_j - \sum_{j=1}^n i_{dis-j} \right] Z_p \\ &+ n \lambda v_{avg}(s) \end{aligned} \quad (98)$$

where $v_{avg}(s)$ equals

$$v_{avg}(s) = \frac{v_{c1} + v_{c2} + \dots + v_{cn}}{n} = \frac{\sum_{j=1}^n v_{cj}}{n} \quad (99)$$

replace v_{cj} in (99) with (96), where the capacitor voltage equals the converter output voltage $v_{cj} = v_{conv-k}$, one can get

$$v_{avg} = v + \frac{1}{n} \sum_{j=1}^n (i_j - i_{dis-j}) Z_p \quad (100)$$

replace v_{avg} in (98) by (100) yields

$$\sum_{j=1}^n v_{ref-j}(s) = n v_{ref}(s) + r Z_p \sum_{j=1}^n i_j - r Z_p \sum_{j=1}^n i_{dis-j} \quad (101)$$

where $r = Z_p(1 - \lambda + n)$. Recall (87) $Z_L \sum_{j=1}^n i_j = v$, i.e. $\sum_{j=1}^n i_j = \frac{v}{Z_L}$. Insert this current into (101) gives

$$\sum_{j=1}^n v_{ref-j}(s) = nv_{ref}(s) + rZ_p \left(\frac{v}{Z_L} \right) - rZ_p \sum_{j=1}^n i_{dis-j} \quad (102)$$

by inserting the value of $\sum_{j=1}^n v_{ref-j}(s)$ from (102) into (91), the load voltage of n -parallel converters with considering the adaptive IACS controller will be

$$v = \frac{G}{1 + \frac{Z_e}{nZ_L} - \frac{Z_p}{Z_L} \left(\frac{G}{n} \right) r} v_{ref} + \frac{\left(\frac{1}{n} \right) [Z_e - GZ_p r]}{1 + \frac{Z_e}{nZ_L} - \frac{Z_p}{Z_L} \left(\frac{G}{n} \right) r} \sum_{j=1}^n i_{dis-j} \quad (103)$$

The output voltage equals

$$v = \frac{G}{q_1} v_{ref} + \left(\frac{1}{n} \right) \frac{p_1}{q_1} \sum_{j=1}^n i_{dis-j} \quad (104)$$

where $p_1 = (Z_e - Gr)$, $q_1 = 1 + \frac{p_1}{nZ_L}$.

Again, by inserting v from (104) and i_{avg} from (93) into (92), the output current of k^{th} converter is obtained as follows

$$i_{k-adp} = \frac{n_1}{d_1} v_{ref-k} + \frac{nn_2}{d_1 q_1} v_{ref} + \left(\frac{1}{n} \right) \frac{n_3 w}{d_1 q_1} \sum_{j=1}^n i_{dis-j} + \frac{1}{d_1} i_{dis-k} \quad (105)$$

where $w = (1 - Gr/Z_e)$

5.5 Stability analysis

System stability analysis is achieved at different stages. Firstly, analysing the stability of a single converter with IACS as a unit base of the parallel system while the current sharing loop is open. Secondly, stability analysis of parallel converters with conventional IACS is considered without the proposed adaptive part. Lastly, analyse the stability of parallel converters with the proposed adaptive IACS controller considered. Table 5.1 shows the parameters list of the system. Matlab/ M-files are

implemented for plotting the root loci for analysing the system stability at different stages as described. For the purpose of stability analysis, the boost converter duty cycle is fixed at 0.76.

Table 5.1 Boost converter and system parameters list

Description	Value
Boost converter parameters	
Input boost inductor (L)	750 μ H
Output boost capacitor (C)	2220 μ F
Feedforward gain(K_f)	1
Capacitor current gain (K_C)	8
Load impedance(Z_L)	25 Ω
Number of converters (n)	2
System parameters	
DC load voltage (v)	100 V
Input DC voltage (v_g)	24 V
Voltage controller proportional gain (k_{pv})	23
Voltage controller integral gain (k_{iv})	50
Current controller proportional gain (k_{pc})	.2
Current controller integral gain (k_{ic})	5
Switching frequency (f_s)	10 kHz

5.5.1 Stability analysis of a single boost converter

For stability analysis of a single boost converter with IACS, stability depends on the location of the roots of the denominators of (84). If there are roots with positive real parts, the system will be unstable.

By inserting the parameters of Table 5.1 into the closed-loop transfer functions of (84), one can get the root loci of closed-loop poles as shown in Figure 5.10. This figure implies that the closed-loop converter system with IACS is stable as all poles are on the left half-plane with negative real parts.

However, increasing the proportional gain of the voltage controller threaten the system stability and k_{pv} should not exceed the critical value of 981 to guarantee a stable system. This critical value of the proportional gain is obtained from the root locus plot of the open-loop transfer function ($G_{vd}G_C$) as shown in Figure 5.11.

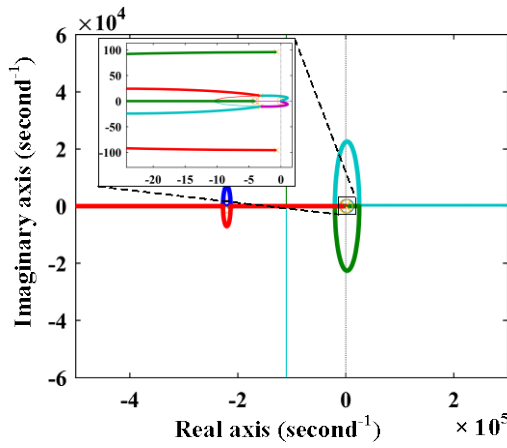


Figure 5.10 Root locus plot of (84).

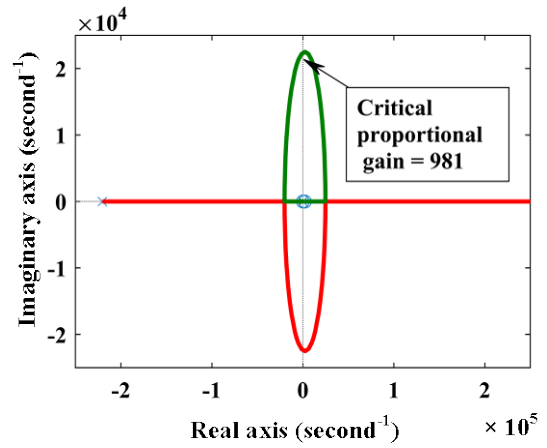


Figure 5.11 Root locus plot of $G_{vd}G_C$.

5.5.2 Stability analysis of n -parallel converters

Now, studying the stability of the load voltage under n -parallel converters connected based on (91). Equation (91) shows the relationship between the load voltage, the reference voltages and the disturbance source. Referring to (91), it can be noted that the current sharing controller H has no impact on the load voltage since (91) is free of H .

To ensure load voltage stability, all closed-loop poles of the two transfer functions of (91) must be on the left half-plane. The root locus plots of these transfer functions are shown in Figure 5.12 which illustrates that all poles are in the left half-plane.

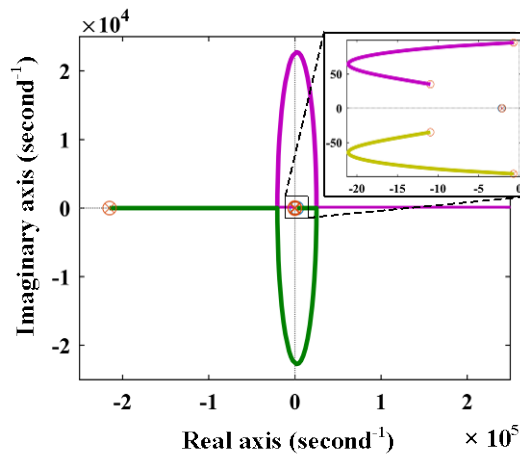


Figure 5.12 Root locus plot of (91) at $k_{pv}=23$.

It should be noted that applying proportional gain k_{pv} above the critical value ($k_{pv} = 981$) leads to an unstable load voltage. Also, by comparing (85) and (91), one can note that both equations depend on G and Z_e . In other words, stability of the load voltage with parallel converters depends on the voltage regulation capability of the individual converters.

5.5.3 Stability analysis of the current control loop in IACS

The stability of the current control loop of the k^{th} converter depends on the denominator of (94) which has two terms $(1 + Z_e/nZ_L)$ and $(1 + GH/Z_e)$. The first term is the same term of the denominator of (91) that was already analysed in the previous section. The second term depends on the current controller H . To ensure output current stability, it is required to determine the critical value of the proportional gain of H , where H is the transfer function of the PI current controller (106).

$$H = k_{pc} + \frac{k_{ic}}{s} \quad (106)$$

Insert (106) into $(1 + GH/Z_e)$ and rearrange the equation to factor k_{pc} and k_{ic} , one can get

$$1 + \frac{k_{pc}G}{Z_e} = 0 \quad \text{and} \quad 1 + \frac{k_{ic}G}{Z_e s} = 0 \quad (107)$$

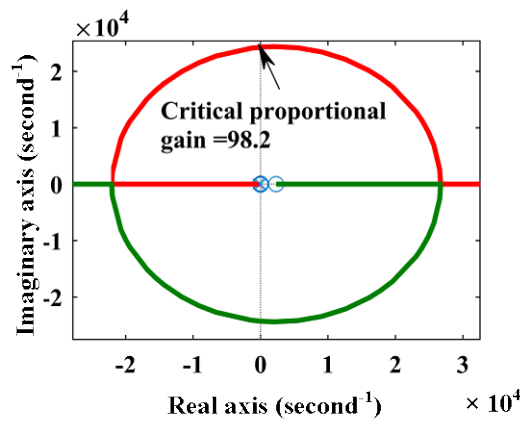


Figure 5.13 Root locus plot of G/Z_e .

From (107), using root locus to plot G/Z_e as an open loop while the current sharing loop is open which gives the critical proportional gain of the current controller. It is found that this critical value of proportional gain equals $k_{pc-critical} = 98.2$ at $k_{pv} = 1$, and $k_{iv} = 1$ as per Figure 5.13.

5.5.4 Selection of the adaptive gain λ

The choice of the adaptive gain is performed based on the load voltage quality as increasing the value of the adaptive gain λ leads to a higher voltage overshoot and a higher voltage ripple. Referring to (79), the adaptive gain must be less than 630 to ensure global stability.

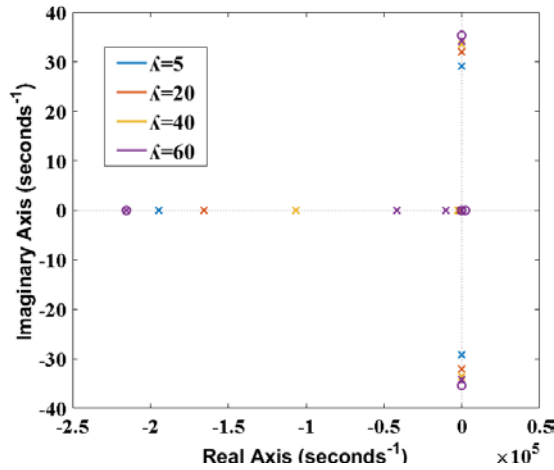


Figure 5.14 Zero-pole map of (103) at different values of λ .

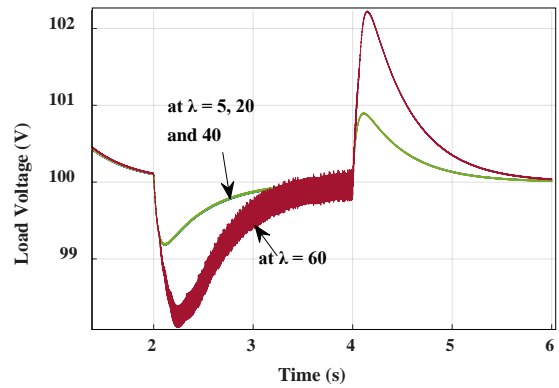


Figure 5.15 Load voltage waveform at different values of λ .

Figure 5.14 shows the zero-pole map for the closed-loop transfer function of (103) at ($\lambda = 5, 20, 40$ and 60). The figure shows that the load voltage is stable at these values of λ . However, increasing λ to 60 leads to higher overshoot and undershoot with load step change. Moreover, a higher voltage ripple appears especially at light load as Figure 5.15 shows during the period from 2 to 4 s.

5.6 Simulation results

Matlab/Simulink model is used to investigate the performance of both conventional and proposed adaptive IACS for minimizing the circulating current among parallel converters. The Simulink model is built based on 2-parallel converters as per Figure

5.1 with system parameters as per Table 5.1. This section can be divided into three parts. Part-1 compares the performance of the conventional and the proposed IACS controllers, while part-2 compares the simulation results of the proposed controller with the results of the droop controller proposed under study [19] and part-3 examines the proposed IACS with fast fluctuations applied

5.6.1 Simulation results of the conventional and proposed controllers

Two similar converters are considered with different resistive line impedances applied, 0.1Ω for converter-1 and 0.15Ω for converter-2. For analysing the impact of varying load current on the load voltage, the load current changed from 4 A to 8 A at 30 s as shown in Figure 5.17. The performance results based on Figure 5.16 and Figure 5.17 are summarized in Table 5.2.

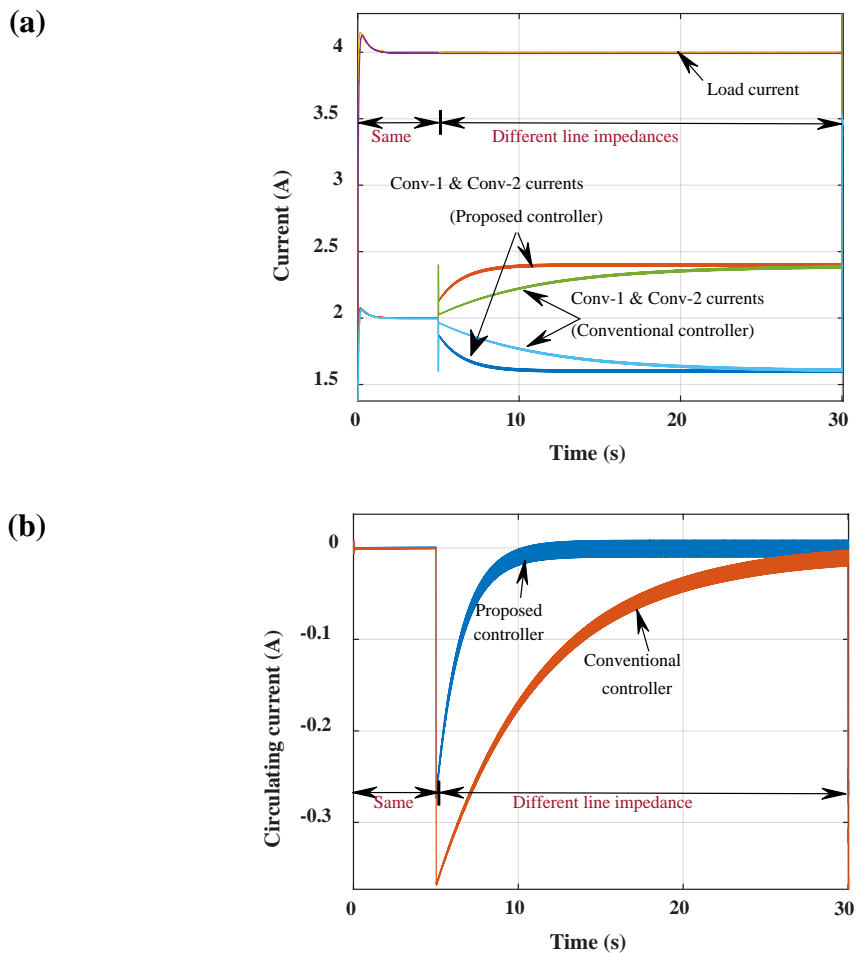


Figure 5.16 Simulation results of the conventional versus proposed IACS controllers (a) converters output and load currents, (b) circulating current.

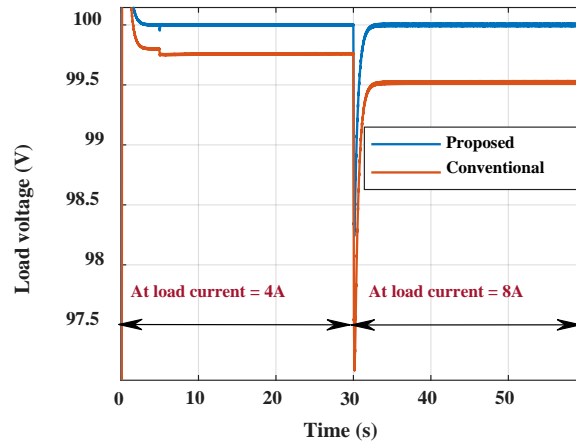


Figure 5.17 Output load voltage considering conventional and proposed controllers.

Table 5.2 Performance results of conventional versus proposed control schemes

Characteristics	Conventional IACS	Proposed IACS
Converter output current rise time (s)	9	1
Converter output current settling time (s)	24	3.6
Circulating current, mean value (mA)	-60.6	-5.6
Load voltage (V)	99.5	100

Table 5.2 shows better performance for the proposed controller scheme over the conventional in terms of fast transient response and more accurate output voltage. Figure 5.17 shows that there is a steady-state error for the load voltage when conventional IACS is applied. This steady-state error is eliminated with the proposed adaptive controller.

Also, the proposed IACS controller shows better voltage control capabilities over the conventional controller with varying load current. This is illustrated in Figure 5.17 with varying the load current from 4A to 8A. Due to this step-change, the output voltage dropped with the conventional controller scheme, while it is maintained at the desired voltage with the proposed IACS as shown in Figure 5.17.

5.6.2 Simulation results of the proposed IACS and droop controllers

The following section compares the performance of the proposed IACS controller with the droop controller based on the study [19] as both studies has the same goal of circulating current minimization among parallel-connected DC-DC converters. First,

comparing the magnitude of circulating current achieved by both methods. Second, investigate the controllers capability in regulating the load voltage at different operating points. The results of the study [19] are reproduced in Matlab/Simulink, as per Figure 5.18 (a), for the converters output voltages and load voltage.

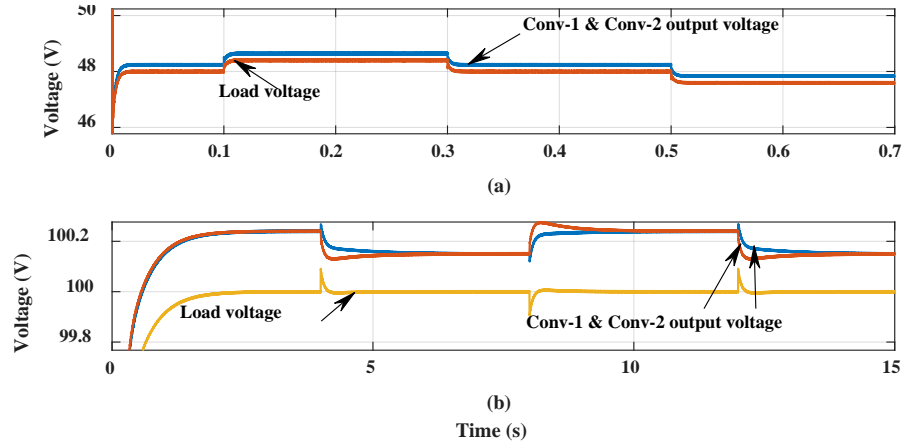


Figure 5.18 Converters output and load voltages for (a) droop controller based on study [19] and (b) proposed IACS controller.

Referring to Figure 5.18 (a), the results of the droop controller based on the study [19] show that the load voltage is changing with varying the line impedance of both converters. On the other hand, the load voltage as shown in Figure 5.18 (b), based on the proposed controller, is accurately regulated at the desired voltage while the line impedances are varying.

Although, the load voltage deviation shown in the results of the droop controller method is small and within the acceptable deviation limits, as a simplified model of a DC system is considered, however, considering real DC microgrid with many loads switched on and off, the line impedance change would be larger and higher voltage deviation is expected.

For the circulating current, study [19] based on the adaptive droop controller minimized the magnitude of the circulating current to 0.03 A, while the proposed adaptive IACS controller can reduce the magnitude of circulating current to 0.005A. Based on the above comparison, the proposed controller showed better controllability over the load voltage at different operating points and reduces the circulating current to very low values comparing the droop controller of [19].

5.6.3 Simulation results of the proposed IACS with fast fluctuations applied

To show the robustness of the adaptive IACS controller against fast fluctuations, Matlab/Simulink is used to examine this by adding noise to the measured output voltages and currents of the converters. The simulation results in Figure 5.19 show the load voltage, converters output voltages, load current and circulating current. The simulation is run for 10 s which is divided into two parts: during the first part “5 seconds” the system is operating under no noise, while the second part shows the system performance when noise is added to the measured output voltages and currents of the converters. The results show that the controller is stable under noise conditions. Additionally, it is noise rejected as the recorded error in the load voltage is very small in the range of 0.002% and similar figures are recorded for the error in circulating current.

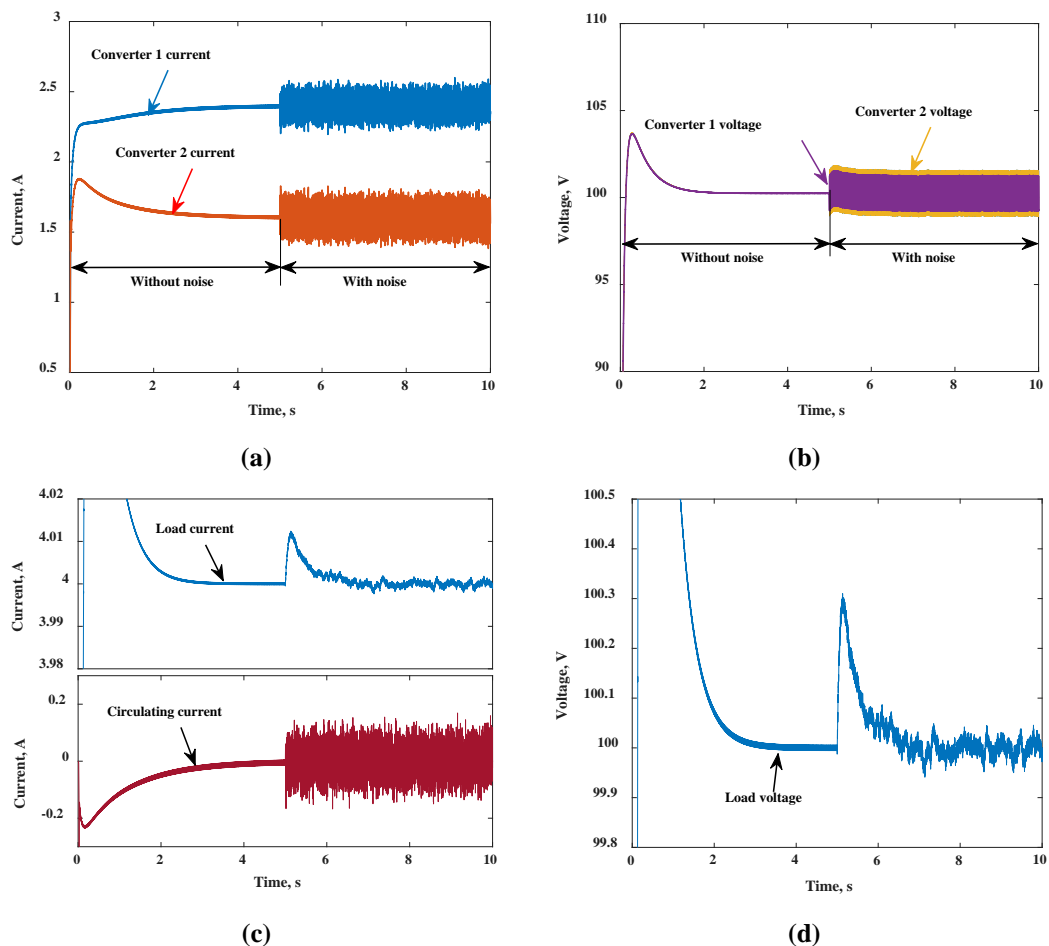


Figure 5.19 Simulation results of (a) converters output currents with/without noise (b) Converters output voltages with/without noise (c) Load current and circulating current (d) load voltage.

5.6.4 Simulation results of the proposed IACS with fast fluctuations applied

To examine the impact of controller's parameters, the simulation setup is considered where nonidentical parallel converters are used. At 11s, the adaptive gain is changed from 8 to 120. Figure 5.20 shows the impact of changing the adaptive gain on the load voltage and the circulating current minimisation. The simulation results confirm the dependency of the adaptive gain on the load resistance as obtained in equation (92). After increasing the adaptive gain to 120 at 11s, small variations in the load voltage, output currents and circulating currents are recorded which is acceptable (<1%). However, by increasing the load current from 8 A to 12 A, i.e. reducing the load resistance, these variations get higher (around 70%) which is not acceptable. So, the choice of the adaptive gain should be small to avoid such unwanted voltage overshoots when a higher load is applied.

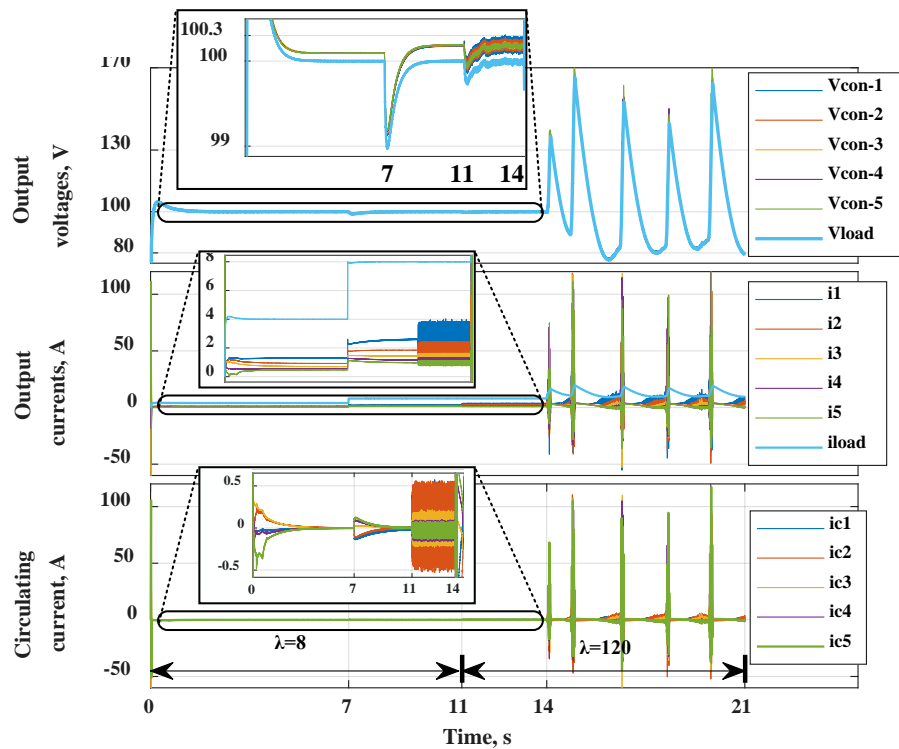


Figure 5.20 Simulation results of parallel nonidentical 5-converters which shows the impact of changing control parameters on the system performance

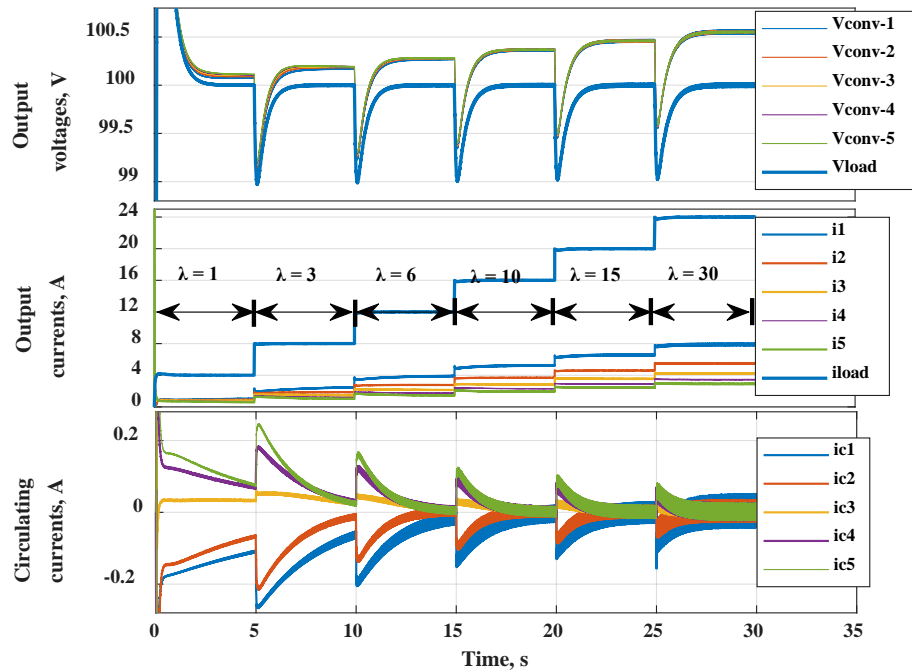


Figure 5.21 Simulation results of parallel nonidentical 5-converters which shows the impact of changing control parameters on the system performance

The adaptive gain has another impact on the time response of the controller in minimizing the circulating current. Referring to equation (83), It is expected that lower values of the adaptive gain would make a slower response in minimizing the circulating current. This is because minimizing the circulating current depends on matching the converter output voltage with the average voltage as per the second term of equation (83). To show this impact by the simulation, 5 nonidentical converters connected in parallel to resistive load in a DC system. The simulation is run for 30 s with load step change every 5s which start at load current 4 A until 24 A in 6 steps. The adaptive gain is changing with every load step change from lower to higher values as follows (1,3,6,10,15,30). The simulation results in Figure 5.21 show that the adaptive gain has no impact on the load voltage in terms of voltage undershoot and settling time due to load step change. The figure shows faster responses, as expected, in minimizing the circulating current with higher adaptive gains at every load step change.

5.7 Summary

A new adaptive IACS control scheme based on Steepest Descent Method is proposed for accurate voltage regulation and minimizing circulating current among parallel DC-DC converters connected in a DC-microgrid. N -parallel connected converters model with the proposed controller is derived assuming identical converters. Stability analysis is used for designing the PI controllers of IACS to insure stable closed loops. The main point to conclude from the stability analysis is that the stability of the load voltage with parallel DC-DC converters depends on the voltage regulation capability of the individual converters.

Matlab/Simulink is used to investigate the performance of the conventional and proposed adaptive IACS controllers based on 2-parallel DC-DC boost converters supplying a DC-load. The conventional IACS controller successfully reduced the circulating current to a very low limit, however, the controller response was slow and the load voltage is not accurately regulated to the nominal value. So, the adaptive IACS controller is proposed which overcomes the shortcomings of the conventional IACS. Also, it showed better performance compared with one of the studies in the literature reviewed in terms of accurate voltage regulation and lower circulating current levels.

The developed control technique in this chapter was considered with PIPO connected DC-DC converters which have the same input of the DC link. To show the performance of the proposed controller with considering the MUP's microgrid that proposed under this research, Chapter 6 considers the analysis of this grid which comprises n -parallel floating energy units (each unit has wind, tidal, solar and energy storage systems) connected in parallel to a DC- collection bus.

Chapter 6 A New Coordinated Controller for Offshore LVDC Microgrid Control

One of the main objectives of this research is to study the feasibility of using a DC system to improve the electric infrastructure of the MUP as discussed in Section 1.6 of Chapter 1. Considering a DC system for the MUP's microgrid addresses many of the challenges presented in Chapter 1, Section 1.4 such as space limitation, high costs of installation, the complexity of the system controller, etc. This chapter provides the design and analysis for the offshore LVDC microgrid based on the floating energy unit (Chapter 2) that comprise of tidal, wind, solar and energy storage systems.

6.1 Background

To achieve a stable bus voltage in an autonomous DC microgrid, a power balance between the demand load and the supply must occur [153]. Energy Storage System (ESS) plays an important role as an energy buffer to compensate for the unbalanced power via absorbing the surplus energy to avoid over-voltage and supply the deficit energy to avoid under-voltage [154].

The IACS controller developed in Chapter 5 is used, in this chapter, for regulating the voltage of the DC collection bus and for minimizing the circulating current among the parallel floating energy units. Models of wind/tidal turbines with boost converters, for extracting maximum power, are derived for stability analysis purposes. For the same reason, a model of a solar array is derived with a boost converter. Additionally, a model of a bi-directional DC-DC converter for battery charging/discharging is derived. An overall model of a floating energy unit including all control loops is derived for voltage stability analysis. A simulation model is performed using Matlab/Simulink for a single floating energy unit and for 3-floating energy units connected in parallel to show the grid performance at different operating conditions.

6.2 Offshore LVDC microgrid configuration

Figure 6.1 shows n -floating energy units which opted in Chapter 2 where each energy unit comprises a Solar Array (SA), Wind Turbine (WT), Tidal Turbine (TT) and ESS. Both WT and TT are connected to a local DC bus via diode bridge and boost converter while SA and ESS, as DC sources, are connected directly to the DC bus via boost converter and bi-directional buck-boost converter, respectively.

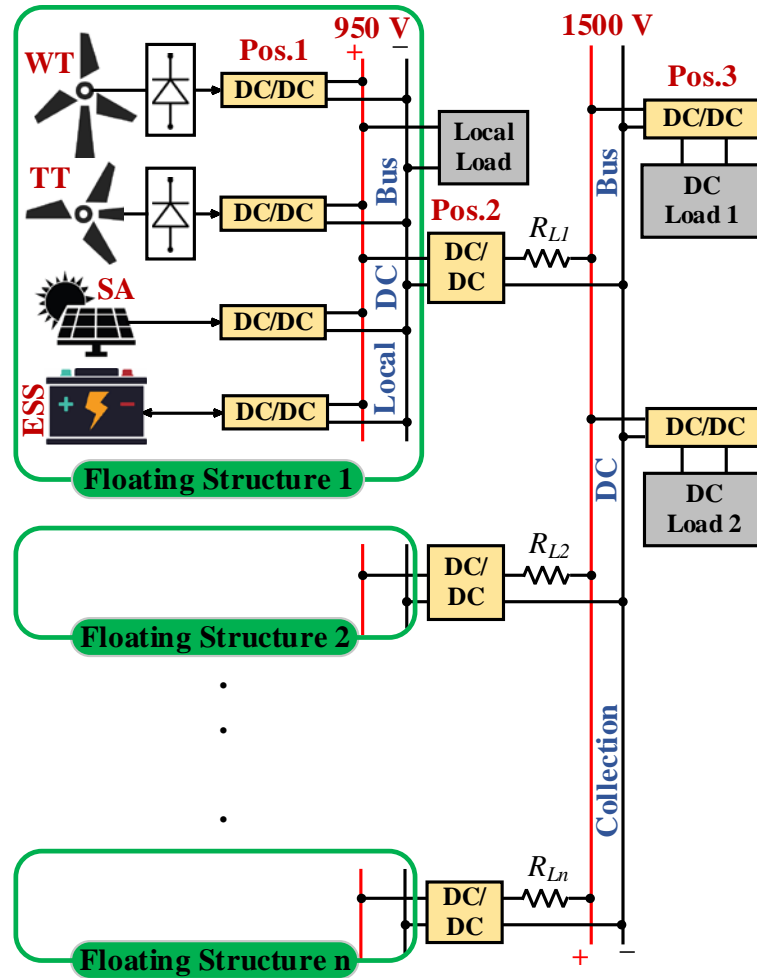


Figure 6.1 Configuration of n -parallel floating energy units.

DC-DC converters are employed in this configuration in three different positions: converters at position 1 (Pos.1) are used for MPPT purposes for renewable energy resources, while the ESS bi-directional converter is applied for battery charging/discharging control to regulate the local bus voltage. Converters at Position

2 (Pos.2) are used for boosting the output voltage of the energy floating unit from 950 V to the distribution voltage level of 1500 V. IACS controller is used to control these converters for the purpose of minimizing the circulating current and maintain the distribution voltage accurately fixed at the nominal value. Converters at position 3 (Posi.3) are buck converters that are used to decrease the distribution voltage to different operating load voltage levels.

6.3 Control of offshore LVDC microgrid

The design of the microgrid controller should consider various operation modes of renewable energy systems and ESS. For example, wind/tidal turbines have three different operation modes: Maximum Power Point Tracking (MPPT) mode at battery SOC lower than the maximum level, voltage support mode at SOC higher than the maximum charging level and lastly idle mode at maximum SOC and lower demand load required. While solar array can work in two operation modes: MPPT model at SOC lower than the maximum level and idle mode or damping mode at lower demand load applied. For ESS, there are two operation modes: voltage support mode and idle mode according to storage capacity is higher or lower than DOD, respectively [154].

However, considering the operation of the hybrid energy microgrid as a whole, three different operation modes can be identified as shown in Figure 6.2 which can be described as follows.

Mode I (surplus energy) this mode occurs in real operation when there is surplus energy from the RES and the ESS is fully charged as per (108). During this mode, RES is required to instantaneously adjust their power generation according to the demand load to maintain energy balance and this can be achieved using a pitch controller for wind/tidal turbines.

$$P_{RES} > P_{Load} \text{ and } SOC = Max. limit \quad (108)$$

$$P_{RES} < P_{Load} \text{ and } SOC > Min. limit \quad (109)$$

$$\text{while } P_{RES} + P_{ESS} \geq P_{load}$$

$$\begin{aligned}
 P_{RES} &\ll P_{Load} \text{ and } SOC > \text{Min. limit} \\
 \text{while } P_{ESS} &\geq \text{Emergency } P_{load}
 \end{aligned} \tag{110}$$

Mode II (deficit energy) occurs when the RES is not able to supply the required demand energy while the ESS has enough charge to supply, then both RES and ESS will deliver energy to balance the demand load as per (109).

Mode III (load shedding) occurs when the RES is unable to deliver energy and the ESS must cover the emergency demand load according to its SOC as per (110). During this mode, load shedding for unnecessary loads will be in operation to ensure matching the energy supplied by the ESS with the emergency load.

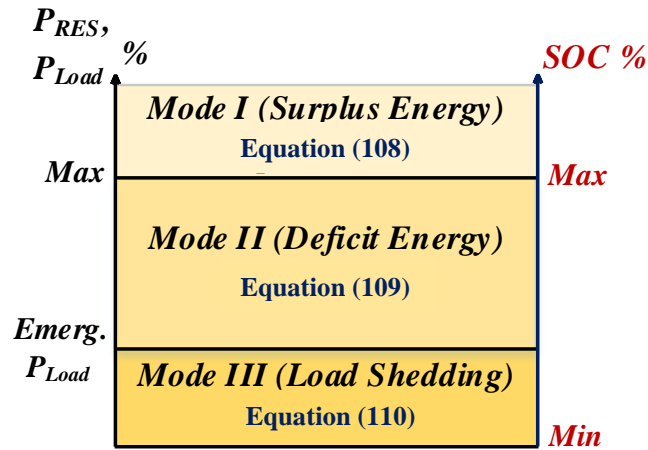


Figure 6.2 Operation modes of an islanded microgrid.

6.3.1 The proposed coordinated controller

Figure 6.3 shows the proposed coordinated controller-based IACS for controlling the MUP's microgrid. This grid comprises n -floating energy units which connected to a DC-collection bus via a boost converter and transmission line with resistance R_{li} as described in Figure 6.1. \hat{v}_{CB}^{nom} refers to the nominal voltage of the DC-collection bus, while \hat{v}_{CB} is the measured voltage of the collection bus.

Description of the IACS controller and its stability analysis with n -parallel boost converters are introduced in Chapter 5. The IACS controller is used in this chapter to control the boost converters (at position 2) for minimizing the circulating current among the parallel floating energy units. Additionally, it is used for disturbance

rejection and maintaining the voltage of the DC-collection bus fixed at the nominal value. A communication system is required as each converter send its output voltage and current to an upper control level for estimating the average current and voltage that fed to the IACS controllers of all active connected converters.

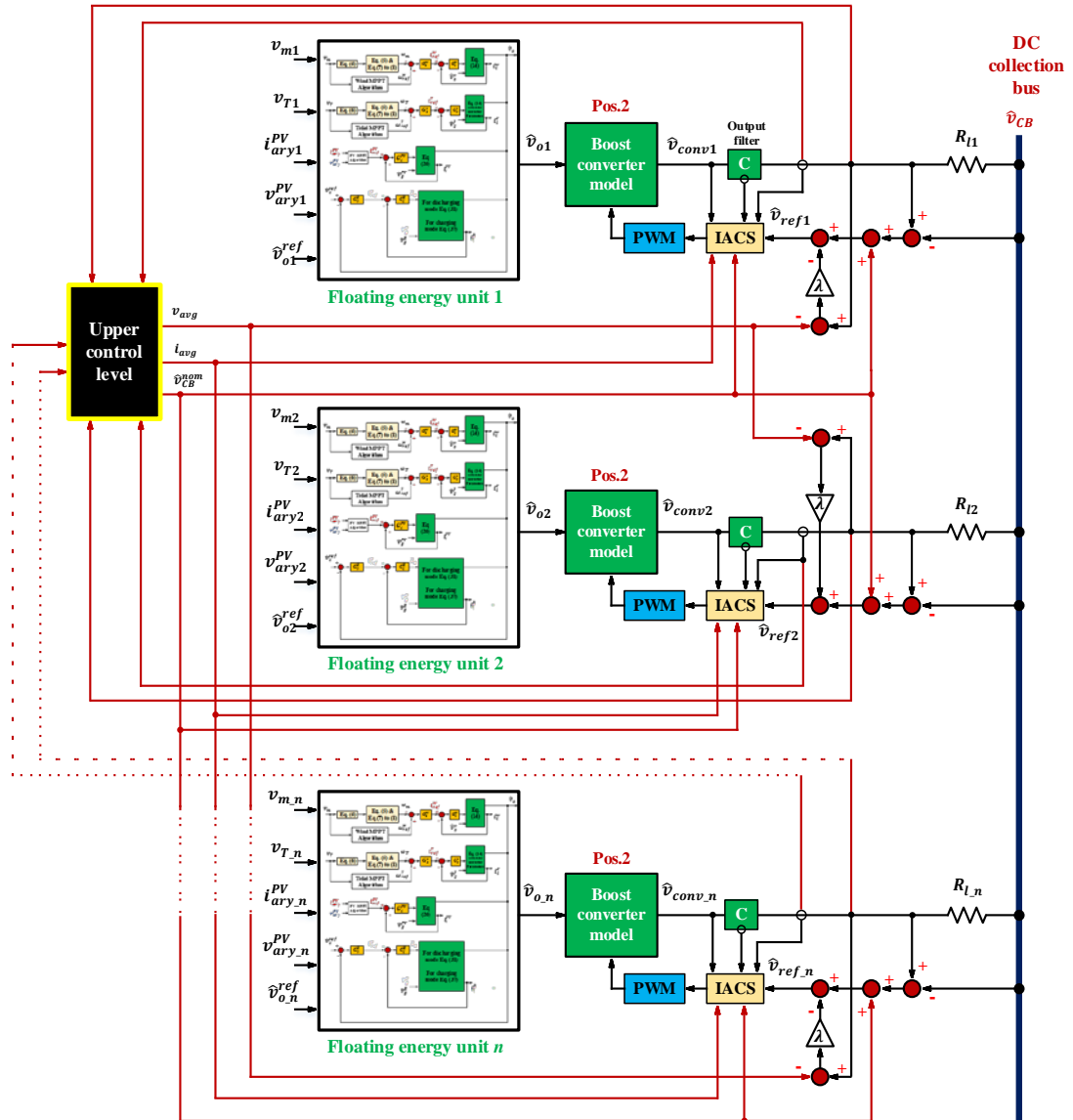


Figure 6.3 Proposed coordinated controller-based IACS.

6.4 Mathematical dynamic models and control loops of system components

This section presents mathematical modelling for the components of the floating energy unit that opted in Chapter 2 (tidal, wind, solar and storage energy systems). The

control loops associated with all components are included for stability analysis purposes.

6.4.1 Dynamic model of wind/tidal turbine with MPPT controller

Figure 6.4 shows one of the configurations available for connecting wind or tidal turbine to an LVDC microgrid via Permeant Magnet Synchronous Generator (PMSG), Diode Bridge and DC-DC converter [155]. Due to its widespread acceptance in wind turbines applications and its fast progress, PMSG is considered to be connected to wind and tidal turbines [156].

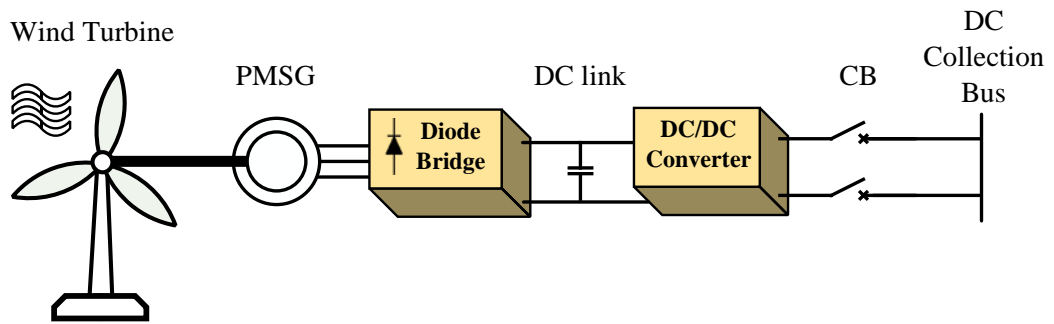


Figure 6.4 Wind turbine connected to a DC microgrid [155].

A boost converter is used to extract the maximum power from the wind turbine using two control loops. The first control loop tracks the optimal generator speed using a PI controller which provides a reference for the inductor current in the second control (current) loop.

The mechanical output power of a wind turbine P_{Wm} can be estimated from (111) as follows

$$P_{Wm} = 0.5\rho^w A^w C_p^w(\lambda^w, \beta^w)v_w^3$$

where

$$C_p^w = 0.5176 \left(\frac{116}{\lambda_i} - 0.4\beta^w - 5 \right) \exp \frac{-21}{\lambda_i} + 0.0068\lambda^w \quad (111)$$

where

$$\lambda_i = 1 / \left[\frac{1}{\lambda^w + 0.08\beta^w} - \frac{0.035}{\beta^{w^3} + 1} \right]$$

where ρ^w , A^w , C_p^w , β^w , v_w are the air density, rotor swept area of a wind turbine, power coefficient, pitch angle and wind speed, respectively. λ^w is the tip speed ratio of the wind turbine which equals to ($\lambda^w = R^w \omega_m^w / v_w$) where R^w is the rotor radius of the wind turbine.

The mechanical model of a wind turbine considering single mass modelling is given as follows

$$T_m^w = J_m^w \frac{d\omega_m^w}{dt} + B_m^w \omega_m^w + T_e^w \quad (112)$$

where, for a wind turbine, T_m^w and T_e^w are the mechanical and electromagnetic torques (N.m). J_m^w and B_m^w are the shaft inertia (kg.m^2) and viscous friction (N.m.s). ω_m^w is the rotor mechanical speed (rad/s) that equals ($\omega_m^w = \omega_r^w / P_p^w$), where ω_r^w is the rotor electrical speed (rad/s) and P_p^w is the number of pole pairs.

The relation between the mechanical output power of the wind turbine in (111) and the mechanical model in (112) is built by inserting $P_{Wm} = T_m^w \omega_m^w = T_m^w \left(\frac{\lambda^w v_w}{R^w} \right)$ into (111). Then the mechanical torque can be expressed as a function of wind speed as follows

$$T_m^w = (0.5 \rho^w A^w C_p^w (\lambda^w, \beta^w) v_w^2 R^w) / \lambda^w \quad (113)$$

Study [157] presented a detailed mathematical derivation for the PMSG model. The stator voltages of PMSG in dq -frame are given as follows

$$v_{ds}^w = R_s^w i_{ds}^w - \omega_r^w L_{qs}^w i_{qs}^w + L_{ds}^w (di_{ds}^w / dt) \quad (114)$$

$$v_{qs}^w = \omega_r^w L_{ds}^w i_{ds}^w + R_s^w i_{qs}^w + L_{qs}^w (di_{qs}^w / dt) + \omega_r^w \psi_r^w$$

where v_{ds}^w , v_{qs}^w are the stator voltages (V), i_{ds}^w , i_{qs}^w are the stator currents of PMSG in dq -frame (A). R_s^w is the stator winding resistance (Ω). ψ_r^w is the maximum flux linkage created by the permanent magnets (Wb). The generator electromagnetic torque equals

$$T_e^w = (3P_p/2)[\psi_r^w i_{qs}^w + (L_{ds}^w - L_{qs}^w) i_{qs}^w i_{ds}^w] \quad (115)$$

The large-signal model of a DC-DC boost converter can be represented, in general, as follows

$$L (di_l/dt) = d(t)v_g(t) + [1 - d(t)]\{v_g(t) - v(t)\} \quad (116)$$

$$C (dv_c/dt) = [1 - d(t)]i_l(t) - v(t)/R_L$$

where L and C are the boost converter inductance and capacitance, respectively. $v_g(t)$ and $v(t)$ are the boost converter input and output voltages, respectively. $d(t)$ represents the duty cycle and R_L refers to the load resistance. i_l is the inductor current while v_c is the capacitor voltage. It is worth mention that, through the rest of this chapter, the boost converter parameters (L , v_g , v , d and i_l) will take different symbols for various boost converters used with wind, tidal and solar systems. Figure 6.5 shows the block diagram for speed control of PMSG connected to a wind/tidal turbine.

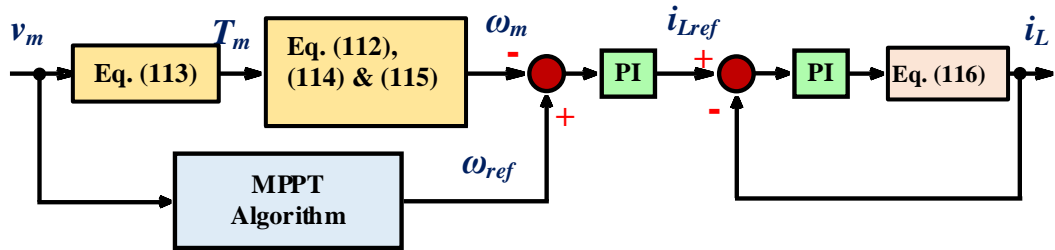


Figure 6.5 Block diagram of speed control of PMSG connected to wind/Tidal turbine.

Equations (111) to (116) represent the nonlinear large-signal model of the wind turbine, PMSG and DC-DC boost converter. Applying linear control techniques such as PI controller requires a linear system. So, the above nonlinear large-signal model is linearized using Taylor expansion to obtain the linearized small-signal model as follows.

For linearization of (113), this equation shows that the turbine torque T_m^w is a function of the wind speed v_w , turbine speed ω_m^w and the pitch angle β^w . Replacing C_p^w in (113) with its value in (111), then taking partial derivative for (113) with respect to ω_m^w , v_w and β^w with applying Taylor expansion, one can get the linearized small signal model of (113) as follows

$$\hat{T}_m^w = K_{tv}^w \hat{v}_m^w + K_{t\omega}^w \hat{\omega}_m^w + K_{t\beta}^w \hat{\beta}^w \quad (117)$$

where

$$K_{tv}^w = \left. \frac{\partial T_m^w}{\partial v_w} \right|_{v_{w0}, \omega_{m0}^w, \beta_0^w}, \quad K_{t\omega}^w = \left. \frac{\partial T_m^w}{\partial \omega_m^w} \right|_{v_{w0}, \omega_{m0}^w, \beta_0^w} \quad \text{and} \quad K_{t\beta}^w = - \left. \frac{\partial T_m^w}{\partial \beta^w} \right|_{v_{w0}, \omega_{m0}^w, \beta_0^w}$$

The gains (K_{tv}^w , $K_{t\omega}^w$ and $K_{t\beta}^w$) are varying with changing the system operating point. However, the turbine speed cannot be changed rapidly; hence the effect due to the turbine speed variation on the turbine torque is ignored, i.e., $K_{t\omega}^w = 0$. By replacing T_m^w in (112) with (117), the linearized small-signal model of a wind turbine is given as follows

$$\hat{\omega}_m^w = \frac{K_{tv}^w \hat{v}_m^w - K_{t\beta}^w \hat{\beta}^w - \hat{T}_e^w}{J_m^w s + B_m^w} \quad (118)$$

Also, the pitch control is not used for MPPT; hence the term $K_{t\beta}^w \hat{\beta}^w$ in (118) should be ignored as well [158].

Similarly, applying Taylor expansion for the nonlinear large-signal model of the PMSG (114), one can get the linearized small-signal model of (114) as follows

$$\hat{i}_{ds}^w = (\hat{v}_{ds}^w + K_{\omega d}^w \hat{\omega}_m^w + K_{i_{qd}}^w \hat{i}_{qs}^w) / (L_{ds}^w s + R_s^w) \quad (119)$$

$$\hat{i}_{qs}^w = (\hat{v}_{qs}^w - K_{\omega q}^w \hat{\omega}_m^w - K_{i_{dq}}^w \hat{i}_{ds}^w) / (L_{qs}^w s + R_s^w)$$

where $K_{\omega d}^w = P_p^w L_{qs}^w i_{qs0}^w$, $K_{\omega q}^w = P_p^w L_{ds}^w i_{ds0}^w + P_p^w \psi_r^w$, $K_{iqd}^w = P_p^w L_{qs}^w \omega_{m0}^w$ and $K_{ids}^w = P_p^w L_{ds}^w \omega_{m0}^w$.

The electromagnetic torque of PMSG in (115) can be linearized using Taylor expansion as follows

$$\hat{T}_e^w = K_{tiqs}^w \hat{i}_{qs}^w + K_{tids}^w \hat{i}_{ds}^w \quad (120)$$

where

$$K_{tiqs}^w = 1.5P_p^w [\psi_r^w + (L_{ds}^w - L_{qs}^w) i_{ds0}^w]$$

$$K_{tids}^w = 1.5P_p^w (L_{ds}^w - L_{qs}^w) i_{qs0}^w$$

As per Figure 6.5, MPPT control requires manipulating the inductor current of the boost converter to make the generator operates at the optimal speed. This can be achieved by changing the duty cycle of the boost converter as a control input with feedback from the inductor current of the converter as shown in Figure 6.6 of the linearized small-signal model of a current programmed DC-DC converter.

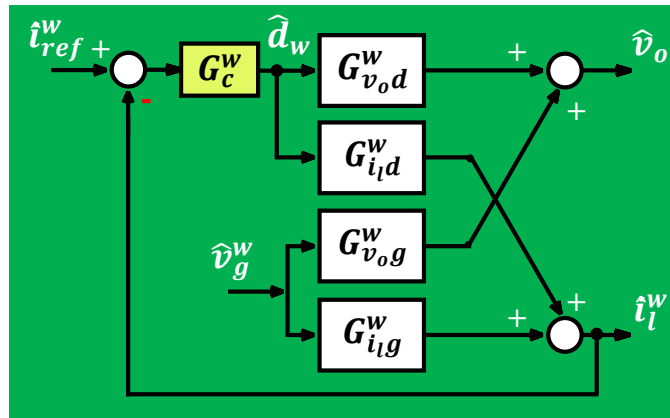


Figure 6.6 Linearized small-signal model of a current programmed DC-DC converter [152].

The block diagram of Figure 6.6 implies that the inductor current and the output voltage of the boost converter depends on the duty cycle and the input voltage as per the following equations

$$\hat{v}_o(s) = G_{v_o d}^w(s)\hat{d}_w(s) + G_{v_o g}^w(s)\hat{v}_g^w(s) \quad (121)$$

$$\hat{i}_l^w(s) = G_{i_l d}^w(s)\hat{d}_w(s) + G_{i_l g}^w(s)\hat{v}_g^w(s)$$

where \hat{v}_o represents the voltage of the local DC-bus, \hat{v}_g^w is the input voltage of the boost converter connected to the wind turbine, \hat{i}_l^w and \hat{d}_w are the inductor current and the duty cycle of the this boost converter.

The linearized model of a boost converter in (121) can be obtained by linearizing the large-signal model in (116) using Taylor expansion. The transfer functions of the boost converter in (121) are given as follows [152]

$$\begin{aligned} G_{v_o d}^w &= \frac{\hat{v}_o(s)}{\hat{d}_w(s)} = G_{d_o}^w \frac{\left(1 - \frac{s}{\omega_z^w}\right)}{den^w(s)} \\ G_{v_o g}^w &= \frac{\hat{v}_o(s)}{\hat{v}_g^w(s)} = G_{g_o}^w \frac{1}{den^w(s)} \\ G_{i_l d}^w &= \frac{\hat{i}_l^w(s)}{\hat{d}_w(s)} = \left(\frac{2V_o}{\dot{D}_w^2 R_L^w}\right) \frac{[1 + s0.5R_L^w C_w]}{den^w(s)} \\ G_{i_l g}^w &= \frac{\hat{i}_l^w(s)}{\hat{v}_g^w(s)} = \left(\frac{1}{\dot{D}_w^2 R_L^w}\right) \frac{[1 + sR_L^w C_w]}{den^w(s)} \end{aligned} \quad (122)$$

where $den^w(s) = \left(1 + \frac{s}{Q^w \omega_o^w} + \left(\frac{s}{\omega_o^w}\right)^2\right)$, $G_{d_o}^w = \frac{V_o}{(\dot{D}_w)}$, $\omega_z^w = \frac{\dot{D}_w^2 R_L^w}{L_w}$, $\omega_o^w = \frac{\dot{D}_w}{\sqrt{L_w C_w}}$, $Q^w = \dot{D}_w R_L^w \sqrt{\frac{C_w}{L_w}}$, $G_{g_o}^w = \frac{1}{\dot{D}_w}$ and $\dot{D}_w = (1 - D_w)$.

V_o , D_w , L_w and C_w are the steady-state values of the local bus voltage, duty cycle, inductance and capacitance of the boost converter connected to the wind turbine, respectively. The Equations (117) to (122) represent the mathematical linearized small-signal model of a wind turbine, PMSG and boost converter which illustrated by the block diagram in Figure 6.7.

The stability of the current closed-loop of Figure 6.6 depends on the roots of the denominator of (124) which is the characteristic equation $(1 + G_{i_{ld}}^w G_c^w = 0)$. The coefficients of this equation are all positive which means that all roots are on the left half-side of the s -plane. i.e., the closed-loop current transfer function of (124) is stable.

To analyse the stability of the local DC-bus voltage with varying the wind speed, it is required to derive the transfer function between the voltage of the local DC-bus and the wind speed as per the simplified block diagram of Figure 6.7 (b). The required transfer function comprises two transfer functions $\frac{\hat{i}_{ref}^w}{\hat{v}_m}$ and $\frac{\hat{v}_o(s)}{\hat{i}_{ref}^w}$. The transfer function from wind speed to reference current can be derived from the block diagram of Figure 6.7 (a) which yields

$$\hat{i}_{ref}^w = G_s^w (\hat{\omega}_{ref}^w - \hat{\omega}_m^w) \quad (125)$$

$$\frac{\hat{i}_{ref}^w}{\hat{v}_m} = G_s^w \left(f(P_{Wm}) - \frac{Q_c^w K_{tv}^w}{1 + Q_c^w Z^w} \right)$$

where

$$Q_c^w = \frac{1}{(J_m^w s + B_m^w)}, \quad Z^w = K_{tiqs}^w Y^w + K_{tids}^w X^w$$

$$f(P_{Wm}) = -0.5551 P_{Wm}^2 + 1.183 P_{Wm} + 0.425$$

$$X^w = \frac{a_1^w s + a_2^w}{b_1^w s^2 + b_2^w s + b_3^w}, \quad Y^w = \frac{-(a_3^w s + a_4^w)}{b_1^w s^2 + b_2^w s + b_3^w}$$

$$a_1^w = L_{qs}^w K_{\omega d}^w, \quad a_2^w = R_s^w K_{\omega d}^w - K_{iqd}^w K_{\omega q}^w, \quad a_3^w = L_{ds}^w K_{\omega q}^w, \quad a_4^w = R_s^w K_{\omega q}^w + K_{idq}^w K_{\omega d}^w,$$

$$b_1^w = L_{qs}^w L_{ds}^w, \quad b_2^w = (L_{qs}^w + L_{ds}^w) R_s^w, \quad b_3^w = R_s^{w2} + K_{idq}^w K_{iqd}^w.$$

While the transfer function between the reference current \hat{i}_{ref}^w and the local bus voltage \hat{v}_o can be obtained using Figure 6.6 and (121). From Figure 6.6, one can obtain $\hat{d}_w = G_c^w (\hat{i}_{ref}^w - \hat{i}_l^w)$. From this equation of \hat{d}_w , put the value of \hat{i}_l^w into the second line of

(121) afterwards solve for \hat{d}_w then put it in the first line of (121). One can get the local bus voltage as a function of the reference current and the input voltage as follows

$$\hat{v}_o = \frac{G_{v_{od}}^w G_c^w}{1 + G_c^w G_{i_d}^w} \hat{i}_{ref}^w + \frac{num^w(s)}{1 + G_c^w G_{i_d}^w} \hat{v}_g^w \quad (126)$$

where $num^w(s) = G_{v_{og}}^w(1 + G_c^w G_{i_d}^w) - G_c^w G_{i_g}^w$. By substituting \hat{i}_{ref}^w into (126) with its value from (125) one can obtain the overall transfer function of a wind turbine with PMSG and a boost converter as follows

$$\hat{v}_o(s) = \left(f(P_{Wm}) - \frac{Q_c^w K_{tv}^w}{1 + Q_c^w Z^w} \right) \left(\frac{G_s^w G_{v_{od}}^w G_c^w}{1 + G_c^w G_{i_d}^w} \right) \hat{v}_w + \frac{num^w(s)}{1 + G_c^w G_{i_d}^w} \hat{v}_g^w \quad (127)$$

As mentioned earlier, the tidal turbine has a similar dynamic behaviour as the wind turbine as per (111) with two differences. Instead of air density, water density is considered for tidal turbines and water speed is applied instead of wind speed. The same configuration of the wind turbine is considered for the tidal turbine; so the overall transfer function of the wind turbine is valid for the tidal turbine which can be copied from (127) with considering the mentioned differences between the wind and tidal turbines and the parameters of the tidal turbine and its PMSG and boost converter as follows

$$\hat{v}_o(s) = \left(f(P_{Tm}) - \frac{Q_c^T K_{tv}^T}{1 + Q_c^T Z^T} \right) \left(\frac{G_s^T G_{v_{od}}^T G_c^T}{1 + G_c^T G_{i_d}^T} \right) \hat{v}_T + \frac{num^T(s)}{1 + G_c^T G_{i_d}^T} \hat{v}_g^T \quad (128)$$

where

$$Q_c^T = \frac{1}{(J_m^T s + B_m^T - K_{t\omega}^T)} \quad , \quad K_{tv}^T = \left. \frac{\partial T_m^T}{\partial v_T} \right|_{v_{T0}, \omega_{m0}^T, \beta_0^T}$$

$$f(P_{Tm}) = -0.5551 P_{Tm}^2 + 1.183 P_{Tm} + 0.425 \quad ,$$

$$Z^T = K_{tiqs}^T Y^T + K_{tids}^T X^T \quad , \quad K_{t\omega}^w = \left. \frac{\partial T_m^w}{\partial \omega_m^w} \right|_{v_{w0}, \omega_{m0}^w, \beta_0^w}$$

$$\begin{aligned}
 X^T &= \frac{a_1^T s + a_2^T}{b_1^T s^2 + b_2^T s + b_3^T}, \quad Y^T = \frac{-(a_3^T s + a_4^T)}{b_1^T s^2 + b_2^T s + b_3^T} \\
 a_1^T &= L_{qs}^T K_{\omega d}^T, \quad a_2^T = R_s^T K_{\omega d}^T - K_{iqd}^T K_{\omega q}^T, \quad a_3^T = L_{ds}^T K_{\omega q}^T, \quad a_4^T = R_s^T K_{\omega q}^T + K_{idq}^T K_{\omega d}^T, \\
 b_1^T &= L_{qs}^T L_{ds}^T, \quad b_2^T = (L_{qs}^T + L_{ds}^T) R_s^T, \quad b_3^T = R_s^{T^2} + K_{idq}^T K_{iqd}^T. \\
 G_s^T &= k_s^T \left(1 + \frac{1}{s} \frac{1}{T_s^T}\right), \quad G_c^T = k_c^T \left(1 + \frac{1}{s} \frac{1}{T_c^T}\right) \\
 G_{v_{od}}^T &= \frac{\hat{v}_o(s)}{\hat{d}_T(s)} = G_{do}^T \frac{\left(1 - \frac{s}{\omega_z^T}\right)}{den^T(s)}, \quad G_{i_{id}}^T = \left(\frac{2V_o}{\hat{D}_T^2 R_L^T}\right) \frac{[1 + s0.5R_L^T C_T]}{den^T(s)} \\
 G_{v_{og}}^T &= \frac{\hat{v}_o(s)}{\hat{v}_g^T(s)} = G_{go}^T \frac{1}{den^T(s)}, \quad G_{i_{ig}}^T = \frac{\hat{i}_l^T(s)}{\hat{v}_g^T(s)} = \left(\frac{1}{\hat{D}_T^2 R_L^T}\right) \frac{[1 + sR_L^T C_T]}{den^T(s)} \\
 den^T(s) &= \left(1 + \frac{s}{Q^T \omega_o^T} + \left(\frac{s}{\omega_o^T}\right)^2\right), \quad G_{do}^T = \frac{V_o}{(\hat{D}_T)}, \quad \omega_z^T = \frac{\hat{D}_T^2 R_L^T}{L_T}, \quad \omega_o^T = \frac{\hat{D}_T}{\sqrt{L_T C_T}}, \quad Q^T = \\
 &\hat{D}_T R_L^T \sqrt{\frac{C_T}{L_T}}, \quad G_{go}^T = \frac{1}{\hat{D}_T}, \quad \hat{D}_T = (1 - D_T). \\
 num^T(s) &= G_{v_{og}}^T (1 + G_c^T G_{i_{id}}^T) - G_c^T G_{i_{ig}}^T
 \end{aligned}$$

V_o , D_T , L_T and C_T are steady-state values of the local bus voltage, duty cycle, inductance and capacitance of the boost converter connected to a tidal turbine, respectively. P_{Tm} is the mechanical output power of the tidal turbine. $f(P_{Tm})$ is the MPPT algorithm which gives the optimal rotor speed as a reference at various mechanical input powers. In this algorithm, P_{Tm} represents the mechanical tidal input power which can be obtained from (111). \hat{v}_g^T is the input voltage variations of the boost converter connected to the tidal turbine. \hat{v}_T is the tidal current speed.

6.4.2 Dynamic model of a solar array with MPPT controller

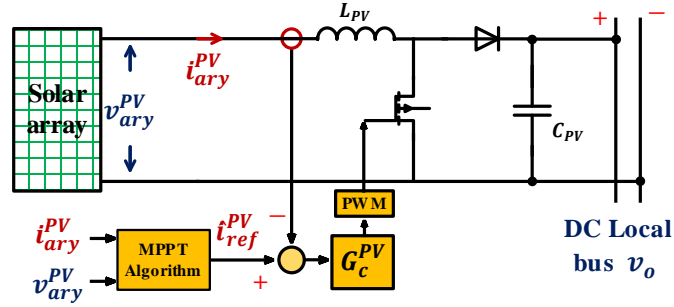


Figure 6.8 Block diagram of PV solar array, boost converter and PI controller.

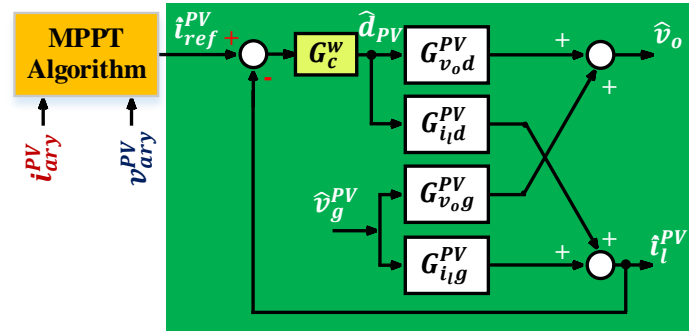


Figure 6.9 Current programmed boost converter model used with a solar PV system.

The small-signal model of a current programmed boost converter with a PI-current control loop is illustrated in Figure 6.9. The transfer functions of the current programmed boost converter are derived in Section 6.4.1 of the wind turbine and it is copied below with considering the parameters of the solar PV array.

$$\begin{aligned}
 G_{v_o,d}^{PV} &= \frac{\hat{v}_o(s)}{\hat{d}_{PV}(s)} = G_{do}^{PV} \frac{\left(1 - \frac{s}{\omega_z^{PV}}\right)}{den^{PV}(s)} \\
 G_{v_o,g}^{PV} &= \frac{\hat{v}_o(s)}{\hat{v}_g^{PV}(s)} = G_{go}^{PV} \frac{1}{den^{PV}(s)} \\
 G_{i_{l,d}}^{PV} &= \frac{\hat{i}_l^{PV}(s)}{\hat{d}_{PV}(s)} = \left(\frac{2V_o}{\hat{D}_{PV}^2 R_L^{PV}}\right) \frac{[1 + s0.5R_L^{PV} C_{PV}]}{den^{PV}(s)} \\
 G_{i_{l,g}}^{PV} &= \frac{\hat{i}_l^{PV}(s)}{\hat{v}_g^{PV}(s)} = \left(\frac{1}{\hat{D}_{PV}^2 R_L^{PV}}\right) \frac{[1 + sR_L^{PV} C_{PV}]}{den^{PV}(s)}
 \end{aligned} \tag{129}$$

where

$$\begin{aligned} den^{PV}(s) &= \left(1 + \frac{s}{Q^{PV}\omega_o^{PV}} + \left(\frac{s}{\omega_o^{PV}}\right)^2\right), G_{do}^{PV} = \frac{V_o}{(D_{PV})}, \omega_z^{PV} = \frac{\dot{D}_{PV}^2 R_L^{PV}}{L_{PV}}, \omega_o^{PV} = \frac{\dot{D}_{PV}}{\sqrt{L_{PV}C_{PV}}}, \\ Q^{PV} &= \dot{D}_{PV} R_L^{PV} \sqrt{\frac{C_{PV}}{L_{PV}}}, G_{go}^{PV} = \frac{1}{\dot{D}_{PV}} \text{ and } \dot{D}_{PV} = (1 - D_{PV}). \end{aligned}$$

V_o , D_{PV} , L_{PV} and C_{PV} are the steady-state values of the local bus voltage, duty cycle, inductance and capacitance of the boost converter connected to the PV array, respectively. Figure 6.9 shows that the local DC-bus voltage is a function of the reference current \hat{i}_{ref}^{PV} and the input voltage \hat{v}_g^{PV} of the converter as follows

$$\hat{v}_o = \frac{G_{v_o d}^{PV} G_c^{PV}}{1 + G_c^{PV} G_{i_d}^{PV}} \hat{i}_{ref}^{PV} + \frac{num^{PV}(s)}{1 + G_c^{PV} G_{i_d}^{PV}} \hat{v}_g^{PV} \quad (130)$$

where $num^{PV}(s) = G_{v_o g}^{PV}(1 + G_c^{PV} G_{i_d}^{PV}) - G_c^{PV} G_{i_l g}^{PV}$

Equation (130) represents the overall transfer function of a PV system connected to a boost converter with a current closed loop. This transfer function is used for analysing the stability of the PV array later in this chapter.

6.4.3 Dynamic model of bi-directional buck-boost converter with control loops

Many battery models are presented, in the literature, with different degrees of complexity. Study [159] classified battery models into electrochemical, experimental and electrical models. Among these categories, electrical models would be a better option to represent the electrical characteristics of the batteries. There are four types of batteries in the market: Lead Acid, Nickel-Cadmium, Nickel-Metal-Hydride and Lithium-Ion. However, modelling of the battery is out of the scope of the thesis.

To protect the batteries against rapid degradation and for controlling the local DC bus voltage, a control system with two cascaded loops is employed for controlling the charging and discharging processes of the battery via a DC-DC bi-directional converter. The outer loop regulates the DC-bus voltage using a PI-controller which provides a reference current for the inner loop. The inner loop regulates the delivered or received current by the battery via providing the converter with the duty cycle

applied to the switch Q1 (as per Figure 6.10) after a Pulse Width Modulation (PWM). The pulses applied to Q2 is the complement of that applied to the Q1. Turning the two switches (Q1 and Q2) on, simultaneously, would damage the converter, so proper dead time should be applied between the driving signals.

- *Bi-directional converter configuration*

Figure 6.10 shows the full configuration of a bi-directional buck-boost converter. It also shows the converter configurations during discharging and charging modes. During step-up (discharging mode), Q2 is off-state and only the anti-parallel diode (D2) is appeared as per Figure 6.10 (b). While Q1 is off-state during step-down (charging mode) and only (D1) is represented as per Figure 6.10 (c). To analyse the stability of the bi-directional converter, deriving the mathematical dynamic models of the converter during boosting (discharging) and bucking (charging) modes are required.

- *Modelling of the bi-directional converter during discharging mode*

During the discharging mode as per Figure 6.10 (b), the bi-directional converters is typically a boost converter with the battery system at the input (lower-voltage side) and the load at the output (higher-voltage side). So, the current programmed boost converter model derived earlier in (121) and (122) is valid for the bi-directional converter during discharging phase (boosting mode). The transfer functions of this model are copied in (131) considering the designed parameters of the bi-directional converter.

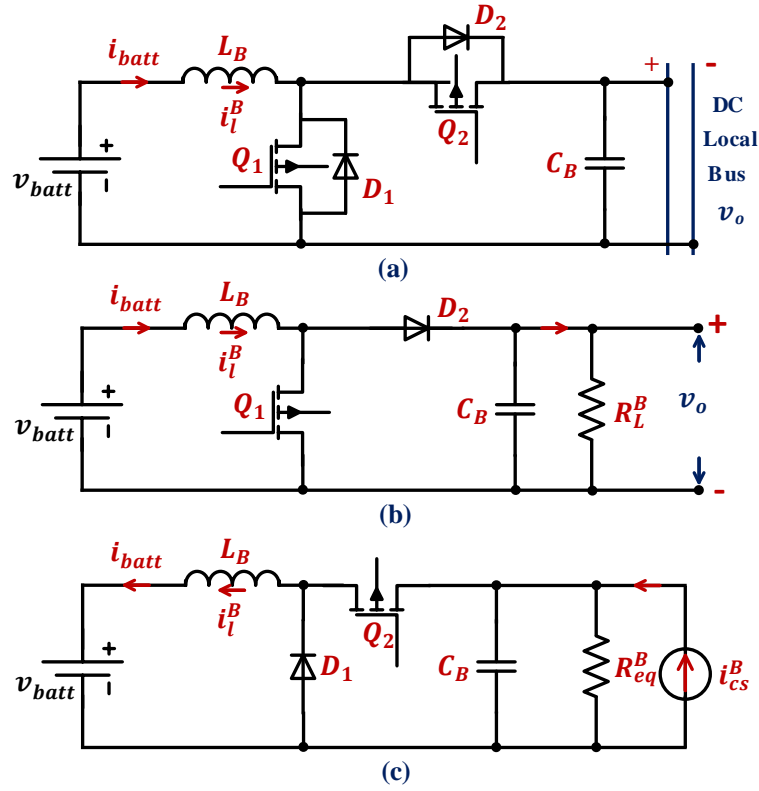


Figure 6.10 DC-DC bi-directional converter (a) full configuration, (b) configuration during discharging mode and (c) configuration during charging mode.

$$\begin{aligned}
 G_{v_{od}}^B &= \frac{\hat{v}_o(s)}{\hat{d}_B(s)} = G_{do}^B \frac{\left(1 - \frac{s}{\omega_z^B}\right)}{\text{den}^B(s)} \\
 G_{v_{og}}^B &= \frac{\hat{v}_o(s)}{\hat{v}_g^B(s)} = G_{go}^B \frac{1}{\text{den}^B(s)} \\
 G_{i_{ld}}^B &= \frac{\hat{i}_l^B(s)}{\hat{d}_B(s)} = \left(\frac{2V_o}{\dot{D}_B^2 R_L^B}\right) \frac{[1 + s0.5R_L^B C_B]}{\text{den}^B(s)} \\
 G_{i_{lg}}^B &= \frac{\hat{i}_l^B(s)}{\hat{v}_g^B(s)} = \left(\frac{1}{\dot{D}_B^2 R_L^B}\right) \frac{[1 + sR_L^B C_B]}{\text{den}^B(s)}
 \end{aligned} \tag{131}$$

where $\text{den}^B(s) = \left(1 + \frac{s}{Q^B \omega_o^B} + \left(\frac{s}{\omega_o^B}\right)^2\right)$, $G_{do}^B = \frac{V_o}{(\dot{D}_B)}$, $\omega_z^B = \frac{\dot{D}_B^2 R_L^B}{L_B}$, $\omega_o^B = \frac{\dot{D}_B}{\sqrt{L_B C_B}}$,

$Q^B = \dot{D}_B R_L^B \sqrt{\frac{C_B}{L_B}}$, $G_{go}^B = \frac{1}{\dot{D}_B}$ and $\dot{D}_B = (1 - D_B)$.

V_o , D_B , L_B and C_B represent the steady-state values of the local bus voltage, duty cycle, inductance and capacitance of the bi-directional converter connected to a battery system, respectively.

Analysing the stability of the bi-directional converter during the discharging mode depends on the denominators of the transfer functions of (131). Referring to (131), all transfer functions have the same denominator. This denominator has all poles in the left-half plane where L_B , C_B , R_L^B and D_B are positive values which implies that the converter is stable during discharging mode. The transfer function in the first line of (131) shows a zero in the right half-plane. This zero has no impact on the system at low frequencies, however, it tends to destabilize the output voltage due to phase reversal which happens at high frequencies with a duty cycle step change.

- *Modelling of the bi-directional converter during charging mode*

During charging mode, the current in the inductor is reversed to be delivered from the load side to the battery side. As described earlier, the battery system is connected to an islanded offshore microgrid supplied by renewable energy resources (wind, tidal and solar). These energy sources are current-controlled for extracting the maximum power while the battery system is in charging mode. Those energy sources can be modelled using Norton theorem as a current source i_{cs}^B in parallel with an internal resistance R_i^B . Where i_{cs}^B is the total current delivered by wind, solar and tidal systems, while R_i^B is the internal equivalent resistance of these energy sources.

Figure 6.10 (c) represents the DC-DC bi-directional converter during bucking mode where the storage system is at the output (lower-voltage side) and the current source at the input (higher-voltage side). To maintain the nomenclature of d_B , the switch Q_2 is activated while Q_1 is switched off and this could occur during the cycle period $[1 - d_B]T_s^B$.

To obtain the dynamic model of the bi-directional converter during charging mode, the circuit diagram of Figure 6.10 (c) is analysed when Q2 is turned ON and OFF as follows

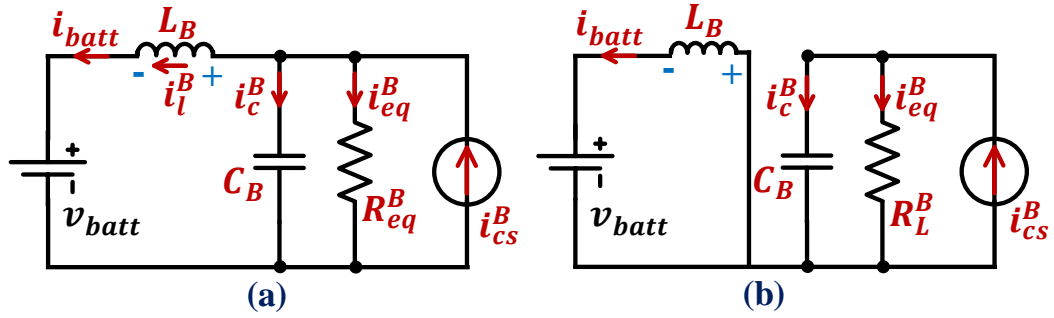


Figure 6.11 DC-DC bi-directional converter analysis during charging mode when:
 (a) Q_2 is ON state, (b) Q_2 is OFF state.

When Q_2 is in ON state, the circuit diagram of Figure 6.11 (a) is applied which gives the following system equations

$$L_B \frac{di_l^B}{dt} = v_o - v_g^B \quad , \quad C_B \frac{dv_o}{dt} = i_{cs}^B - \frac{v_o}{R_{eq}^B} - i_l^B \quad (132)$$

where R_{eq}^B is the equivalent resistance of R_L^B and R_i^B in parallel.

When Q_2 is in OFF state, the circuit diagram of Figure 6.11 (b) is applied which gives the following system equations during the cycle period $d_B T_s^B$

$$L_B \frac{di_l^B}{dt} = -v_g^B \quad , \quad C_B \frac{dv_o}{dt} = i_{cs}^B - \frac{v_o}{R_{eq}^B} \quad (133)$$

Consider the converter switching frequency is f_s^B , then the switching cycle is T_s^B . To obtain the converter equation during one switching cycle T_s^B , the average model can be obtained from the switching model in (132) and (133) as follows.

$$\begin{aligned} \frac{di_l^B}{dt} &= \frac{1}{L_B} [v_o(1 - d_B) - v_g^B] \\ \frac{dv_o}{dt} &= \frac{1}{C_B} \left[i_{cs}^B - \frac{v_o}{R_{eq}^B} - i_l^B(1 - d_B) \right] \end{aligned} \quad (134)$$

Equations (134) represents a nonlinear average model of the bi-directional DC-DC converter during charging mode. To obtain the steady-state values of the state variables (i_l^B and v_o), one can put the derivative parts in (134) equal to zero which yields

$$V_g^B = (1 - D_B)V_o, \quad I_l^B = \frac{1}{(1 - D_B)} \left(I_{cs}^B - \frac{V_o}{R_{eq}^B} \right) \quad (135)$$

Then, Taylor expansion is applied to the nonlinear model of (134) to obtain the small-signal linearized model of the bi-directional DC-DC converter during charging mode as per (136).

$$\begin{aligned} \frac{d\hat{i}_l^B}{dt} &= \frac{1}{L_B} [\hat{D}_B \hat{v}_o - V_o \hat{d}_B - \hat{v}_g^B] \\ \frac{d\hat{v}_o}{dt} &= \frac{1}{C_B} \left[\hat{i}_{cs}^B - \frac{\hat{v}_o}{R_{eq}^B} - \hat{D}_B \hat{i}_l^B - I_l^B \hat{d}_B \right] \end{aligned} \quad (136)$$

Taking Laplace transform for (136) and using superposition theorem, i.e. put \hat{i}_{cs}^B and \hat{v}_g^B equal to zero, one can get the transfer functions of control \hat{d}_B -to-output \hat{v}_o during charging mode as per the first line of (137).

$$G_{v_o d}^B(s) = \frac{\hat{v}_o}{\hat{d}_B} = \frac{\frac{V_o}{\hat{D}_B} \left[1 + \frac{1}{V_o \hat{D}_B^2} \left(I_{cs}^B - \frac{V_o}{R_{eq}^B} \right) s \right]}{den^B(s)} \quad (137)$$

$$G_{i_l d}^B = \frac{\hat{i}_l^B}{\hat{d}_B} = \frac{-G_{dc0}^B \left[1 + \left(\frac{V_o C_B}{\frac{2V_o}{R_{eq}^B} - I_{cs}^B} \right) s \right]}{den^B(s)}$$

where $G_{dc0}^B = \frac{1}{\hat{D}_B^2} \left(\frac{2V_o}{R_{eq}^B} - I_{cs}^B \right)$

Also, the small-signal model (136) can be used to drive the control-to-inductor current ($G_{i_l d}^B$) transfer function as per the second line of (137) during charging mode.

It is important to clarify that the transfer functions of the bi-directional converter during the discharging and charging phases have similar denominators as per (131)

and (137). So, the stability discussion performed earlier for (131) stands for (137). However, The transfer function in the first line of (137) shows that there is a zero which could be in the right half or the left half of the s -plane depending on the value of the total current supplied by the renewable energy sources comparing with the load current as follows

$$if \begin{cases} I_{cs}^B > \frac{V_o}{R_{eq}^B}, & \text{Zero located in the left – half plane} \\ I_{cs}^B < \frac{V_o}{R_{eq}^B}, & \text{Zero located in the right – half plane} \end{cases} \quad (138)$$

But charging mode occurs only when the current source (I_{cs}^B) is higher than the load current (V_o/R_{eq}^B) considering high internal impedance for all energy sources. In other words, this zero will be always at the left half-plane.

To regulate the local bus voltage \hat{v}_o during different operation modes, a two-cascaded loops control system is employed as described earlier in this section as shown in Figure 6.12. The converter model with the controller shows that the output voltage variations \hat{v}_o depends on two independent AC variables which are the input voltage \hat{v}_g^B and reference voltage \hat{v}_{ref}^B variations. It is worth mention that the transfer functions of Figure 6.12 must be defined as per the battery operation mode. In other words, transfer functions of (131) are considered for discharging mode while for charging mode the transfer functions of (137) are applied.

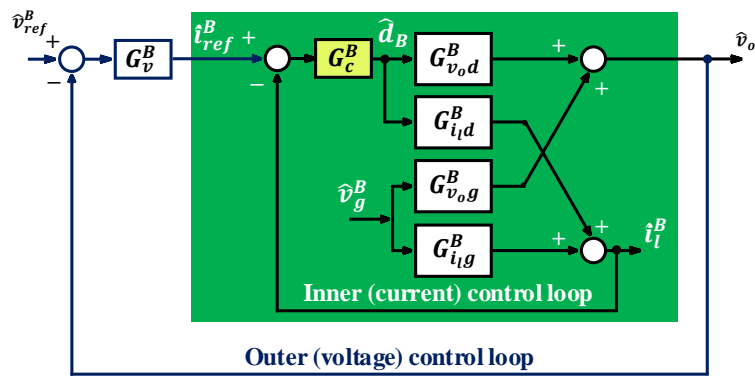


Figure 6.12 Current programmed bi-directional model with a two-cascaded loops controller.

The following section derive the mathematical equation which relates the output voltage with these inputs. First, obtain the closed-loop transfer function of the inner loop while the outer voltage loop is open. The relationship between the output voltage variation and the input variations of \hat{i}_{ref}^B and \hat{v}_g^B is derived earlier for the boost converter of the wind turbine as per equation (126). This equation is copied here with considering different operation modes of the bi-directional converter as follows

$$\hat{v}_o = \frac{G_{v_o d}^B G_c^B}{1 + G_c^B G_{i_d}^B} \hat{i}_{ref}^B + \frac{num^B(s)}{1 + G_c^B G_{i_d}^B} \hat{v}_g^B \quad (139)$$

where $num^B(s) = G_{v_o g}^B (1 + G_c^B G_{i_d}^B) - G_c^B G_{i_g}^B$

Equation (139) can be used for tuning the PI-controller of the outer loop using the inner closed-loop transfer function ($\hat{v}_o/\hat{i}_{ref}^B$) while the input voltage $\hat{v}_g^B = 0$.

To get the output voltage variation as a function of the reference voltage \hat{v}_{ref}^B , and the input voltage \hat{v}_g^B , this can be achieved by applying the superposition principle to the block diagram of Figure 6.12 which yields

$$\hat{v}_o = \frac{G_{v_o d}^B G_c^B G_v^B}{1 + G_c^B G_{i_d}^B + G_{v_o d}^B G_c^B G_v^B} \hat{v}_{ref}^B + \frac{G_{v_o g}^B (1 + G_c^B G_{i_d}^B) - G_{v_o d}^B G_{i_g}^B G_c^B}{1 + G_c^B G_{i_d}^B + G_{v_o d}^B G_c^B G_v^B} \hat{v}_g^B \quad (140)$$

simplified to

$$\hat{v}_o = G_{CL_v_{oref}}^B \hat{v}_{ref}^B + G_{CL_v_{og}}^B \hat{v}_g^B$$

where $G_v^B = k_v^B (1 + \frac{1}{s T_v^B})$ is the transfer function of the PI voltage controller. k_v^B and T_v^B are the proportional and integral gains, respectively. It is important to clarify that the output voltage equation (140) is valid for discharging and charging battery modes

and so considering certain battery mode requires choosing the transfer functions derived for that mode as per (131) and (137).

Tuning the PI-controllers (G_c^B and G_v^B) of the inner and outer control loops can be achieved using *pidtune* command in Matlab. For tuning the inner loop controller G_c^B , the open-loop transfer function $G_{i_{id}}^B$ is considered, while the open-loop transfer function ($\hat{v}_o/\hat{i}_{ref}^B$) which is the inner closed loop as per (140), is used for tuning the outer controller, G_v^B .

6.5 Overall model of floating energy unit and stability analysis

Figure 6.13 illustrates the overall model of a single floating energy unit that comprises a wind turbine, tidal turbine, solar array and battery system connected to a local DC bus. Each energy source has a current loop for MPPT, while the battery system has a cascaded voltage and current loops for controlling the voltage of the local DC bus.

Figure 6.13 implies that the DC bus voltage \hat{v}_o at a floating energy unit depends on the variations on wind speed \hat{v}_w , tidal speed \hat{v}_T , solar irradiance which represented by the current reference \hat{i}_{ref}^{PV} and the reference voltage of the DC bus \hat{v}_{ref}^B . This can be written in a mathematical form as follows

$$\begin{aligned}
 \hat{v}_o = & \left(f(P_{Wm}) - \frac{Q_c^w K_{tv}^w}{1 + Q_c^w Z^w} \right) \left(\frac{G_s^w G_{v_{od}}^w G_c^w}{1 + G_c^w G_{i_{id}}^w} \right) \hat{v}_w \\
 & + \left(f(P_{Tm}) - \frac{Q_c^T K_{tv}^T}{1 + Q_c^T Z^T} \right) \left(\frac{G_s^T G_{v_{od}}^T G_c^T}{1 + G_c^T G_{i_{id}}^T} \right) \hat{v}_T \\
 & + \frac{G_{v_{od}}^{PV} G_c^{PV}}{1 + G_c^{PV} G_{i_{id}}^{PV}} \hat{i}_{ref}^{PV} + \frac{G_{v_{od}}^B G_c^B G_v^B}{1 + G_c^B G_{i_{id}}^B + G_{v_{od}}^B G_c^B G_v^B} \hat{v}_{ref}^B \\
 & + \frac{G_{v_{og}}^B (1 + G_c^B G_{i_{id}}^B) - G_{v_{od}}^B G_{i_{lg}}^B G_c^B}{1 + G_c^B G_{i_{id}}^B + G_{v_{od}}^B G_c^B G_v^B} \hat{v}_g^B + \frac{num^T(s)}{1 + G_c^T G_{i_{id}}^T} \hat{v}_g^T \\
 & + \frac{num^w(s)}{1 + G_c^w G_{i_{id}}^w} \hat{v}_g^w + \frac{num^{PV}(s)}{1 + G_c^{PV} G_{i_{id}}^{PV}} \hat{v}_g^{PV}
 \end{aligned} \tag{141}$$

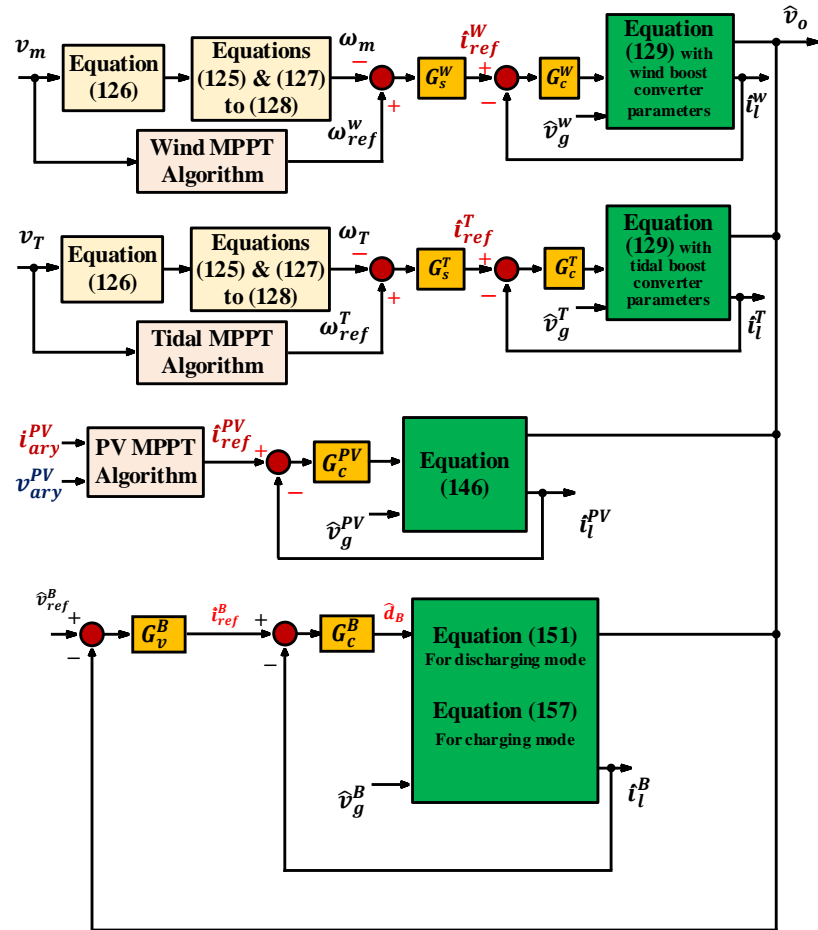


Figure 6.13 Overall model of a floating energy unit comprises tidal, wind and solar energy resources with storage unit.

Equation (141) shows that the stability of the voltage of the local bus of a single floating energy unit depends on the characteristic equations, i.e. the denominators of all the transfer functions between \hat{v}_o and \hat{v}_w , \hat{v}_T , \hat{i}_{ref}^{PV} , \hat{v}_{ref}^B , \hat{v}_g^B , \hat{v}_g^T , \hat{v}_g^w and \hat{v}_g^{PV} , which are

$$\begin{aligned}
 (1 + Q_c^w Z^w)(1 + G_c^w G_{i_d}^w) &= 0 \\
 (1 + Q_c^T Z^T)(1 + G_c^T G_{i_d}^T) &= 0 \\
 1 + G_c^B G_{i_d}^B + G_{v_o d}^B G_c^B G_v^B &= 0 \\
 1 + G_c^{PV} G_{i_d}^{PV} &= 0 \\
 1 + G_c^T G_{i_d}^T &= 0 \\
 1 + G_c^w G_{i_d}^w &= 0
 \end{aligned} \tag{142}$$

Applying Routh-Hurwitz stability criterion, for the closed-loop transfer function of a system to be stable, the characteristic equation of that system must have all zeros on the left half-plane. Regarding the characteristic equations at the first and second lines of (142), to ensure they have all zeros on the left half-plane, one should ensure that the numerators of both terms have positive coefficients. The term $(1 + G_c^w G_{id}^w)$ has positive coefficients as the transfer functions G_c^w and G_{id}^w has positive coefficients. Similarly, this analysis stands for the characteristic equations with similar terms as for those in the fourth to sixth lines of (142). The term $(1 + Q_c^w Z^w)$ is expanded to show its coefficients which yields

$$1 + Q_c^w Z^w = g_3 s^3 + g_2 s^2 + g_1 s + g_0 = 0 \quad (143)$$

where

$$g_3 = J_m^w L_{qs}^w L_{ds}^w$$

$$g_2 = J_m^w (L_{qs}^w + L_{ds}^w) R_s^w + B_m^w L_{qs}^w L_{ds}^w$$

$$\begin{aligned} g_1 = & J_m^w [R_s^{w2} + (P_p^w L_{ds}^w \omega_{m0}^w)(P_p^w L_{qs}^w \omega_{m0}^w)] + B_m^w (L_{qs}^w + L_{ds}^w) R_s^w \\ & + L_{qs}^w (P_p^w L_{qs}^w i_{qs0}^w)(1.5 P_p^w (L_{ds}^w - L_{qs}^w) i_{qs0}^w) \\ & - L_{ds}^w (P_p^w L_{ds}^w i_{ds0}^w)(1.5 P_p^w [\Psi_r^w + (L_{ds}^w - L_{qs}^w) i_{ds0}^w]) \end{aligned}$$

$$\begin{aligned} g_0 = & B_m^w [R_s^{w2} + (P_p^w L_{ds}^w \omega_{m0}^w)(P_p^w L_{qs}^w \omega_{m0}^w)] \\ & + [R_s^w P_p^w L_{qs}^w i_{qs0}^w - (P_p^w L_{qs}^w \omega_{m0}^w)(P_p^w L_{ds}^w i_{ds0}^w)](1.5 P_p^w (L_{ds}^w - L_{qs}^w) i_{qs0}^w) \\ & - [R_s^w P_p^w L_{ds}^w i_{ds0}^w + (P_p^w L_{ds}^w \omega_{m0}^w)(P_p^w L_{qs}^w i_{qs0}^w)](1.5 P_p^w [\Psi_r^w + (L_{ds}^w - L_{qs}^w) i_{ds0}^w]) \end{aligned}$$

The steady-state currents i_{qs0}^w and i_{ds0}^w are negative for PMSG. The coefficients g_3 and g_2 are positive values for both SPMSG and IPMSG. Considering SPMSG (i.e. $i_{ds0}^w = (L_{ds}^w - L_{qs}^w) = 0$) this means that g_1 is positive as the third and fourth terms of this coefficient will be zero. g_0 shows positive sign as well, as the second term goes to zero while the negative sign of the third term will turn into positive due to the negative sign of i_{qs0}^w .

If IPMSG considered (i.e. $L_{ds}^w \neq L_{qs}^w$), then the sign of the third and the fourth term of g_1 depends on the difference ($L_{ds}^w - L_{qs}^w$). Similarly, the second term of g_0 will be positive if ($P_p^w \omega_{m0}^w L_{ds}^w i_{ds0}^w > R_s^w i_{qs0}^w$ and $L_{ds}^w - L_{qs}^w < 0$) while the third term of this coefficient will be positive if ($L_{ds}^w - L_{qs}^w < 0$). The same analysis is applied to the characteristic equation of the tidal turbine in the second line of (142).

It is required to analyse the stability of the voltage of the floating energy unit during discharging and charging phases separately. To do this, the characteristic equation in the third line of (142) is considered. During the discharging phase, the transfer functions of (131) are used to extract the coefficients of this characteristic equation as follows

$$1 + G_c^B G_{i_d}^B + G_{v_o d}^B G_c^B G_v^B = 0 \quad (144)$$

$$n_4 s^4 + n_3 s^3 + n_2 s^2 + n_1 s + n_0 = 0$$

where

$$n_4 = \frac{T_c^B T_v^B}{(\omega_o^B)^2}$$

$$n_3 = \frac{T_c^B T_v^B}{Q^B \omega_o^B} + \frac{V_o T_c^B T_v^B K_c^B C_B}{\dot{D}_B^2} - \frac{V_o K_c^B K_v^B T_c^B T_v^B L_B}{\dot{D}_B^3 R_L^B}$$

$$n_2 = T_c^B T_v^B + \frac{V_o K_c^B K_v^B T_c^B T_v^B}{\dot{D}_B} + \frac{2V_o T_v^B K_c^B (T_c^B + 0.5R_L^B C_B)}{\dot{D}_B^2 R_L^B} - \frac{V_o L_B (T_c^B + T_v^B) K_c^B K_v^B}{\dot{D}_B^3 R_L^B}$$

$$n_1 = \frac{2V_o T_v^B K_c^B}{\dot{D}_B^2 R_L^B} + \frac{V_o (T_c^B + T_v^B) K_c^B K_v^B}{\dot{D}_B} - \frac{V_o L_B K_c^B K_v^B}{\dot{D}_B^3 R_L^B}$$

$$n_0 = \frac{V_o K_c^B K_v^B}{\dot{D}_B}$$

The stability of the voltage of a floating energy unit during the discharging mode requires all coefficients n_0 to n_4 to be positive. The coefficients n_0 and n_4 are positive definite while the sign of the other terms n_1 to n_3 depends on the choice of the

parameters of the PI-controllers to ensure system stability by avoiding negative signs for these coefficients.

Consider the charging mode for the characteristic equation in the third line of (142). For this, the transfer functions of (137) are used to obtain the coefficients of this characteristic equation as follows

$$1 + G_c^B G_{id}^B + G_{v_{od}}^B G_c^B G_v^B = 0 \quad (145)$$

$$m_4 s^4 + m_3 s^3 + m_2 s^2 + m_1 s + m_0 = 0$$

where

$$m_4 = \frac{T_c^B T_v^B}{(\omega_o^B)^2}$$

$$m_3 = \frac{T_c^B T_v^B}{Q^B \omega_o^B} - \frac{K_c^B T_c^B T_v^B V_o C_B}{\dot{D}_B^2} + \frac{K_c^B K_v^B T_c^B T_v^B}{\dot{D}_B^3} \left(I_{cs}^B - \frac{V_o}{R_{eq}^B} \right)$$

$$m_2 = T_c^B T_v^B + \frac{K_c^B K_v^B T_c^B T_v^B V_o}{\dot{D}_B} + \frac{K_c^B K_v^B (T_c^B + T_v^B)}{\dot{D}_B^3} \left(I_{cs}^B - \frac{V_o}{R_{eq}^B} \right) - \frac{K_c^B T_c^B T_v^B}{\dot{D}_B^2} \left(\frac{2V_o}{R_{eq}^B} - I_{cs}^B \right) - \frac{K_c^B T_v^B V_o C_B}{\dot{D}_B^2}$$

$$m_1 = \frac{K_c^B K_v^B (T_c^B + T_v^B) V_o}{\dot{D}_B} + \frac{K_c^B K_v^B}{\dot{D}_B^3} \left(I_{cs}^B - \frac{V_o}{R_{eq}^B} \right) - \frac{K_c^B K_v^B}{\dot{D}_B^2} \left(\frac{2V_o}{R_{eq}^B} - I_{cs}^B \right)$$

$$m_0 = \frac{K_c^B K_v^B V_o}{\dot{D}_B}$$

For the system to be stable during the charging phase, all coefficients m_4 to m_1 must be positive. The coefficients m_0 and m_4 are positive definite while the sign of the other terms m_1 to m_3 depends on the choice of the parameters of the PI-controllers to ensure system stability by avoiding negative signs for these coefficients.

6.6 Simulation results

This section is divided into three parts. The first part is to show the dynamic performance of a single floating energy unit that comprises a wind turbine (3MW),

two tidal turbines with an output power of 750 kW each, a solar PV array (327 kW) and a battery system. It also shows the performance of the battery controller while it regulates the output voltage of a single floating unit fixed at different operating conditions. The second part analyses the dynamic performance of two-parallel connected floating energy units with/without the IACS controller. The third part of this simulation evaluates the performance of an islanded offshore LVDC microgrid that comprises three floating energy units. The system simulation parameters are provided in Appendix C.

6.6.1 Part I: Single floating energy unit

This part evaluates the dynamic performance of a single floating energy unit at different operating conditions: a) surplus energy supply, b) deficit energy supply, c) load shedding and d) fault condition.

a) Renewable energy sources deliver surplus energy

In this case, the Renewable Energy Sources (RES) are delivering enough energy to cover the load ($R_{load} = 0.5 \Omega$, $v_o = 950 \text{ V}$) while the battery system is in charging mode. This test considers variable wind speed to show the intermittent nature of the wind energy while solar and tidal energy supplying the rated power. The simulation runs for 2.3 seconds.

Figure 6.14 shows that the load current is met by the RES while the surplus energy is fed to the storage system. The load voltage is regulated at the nominal voltage using the battery charging/discharging controller. Although there is voltage overshoot and undershoot due to wind speed step change, the figures show stable operation with load voltage regulated within the acceptable limits.

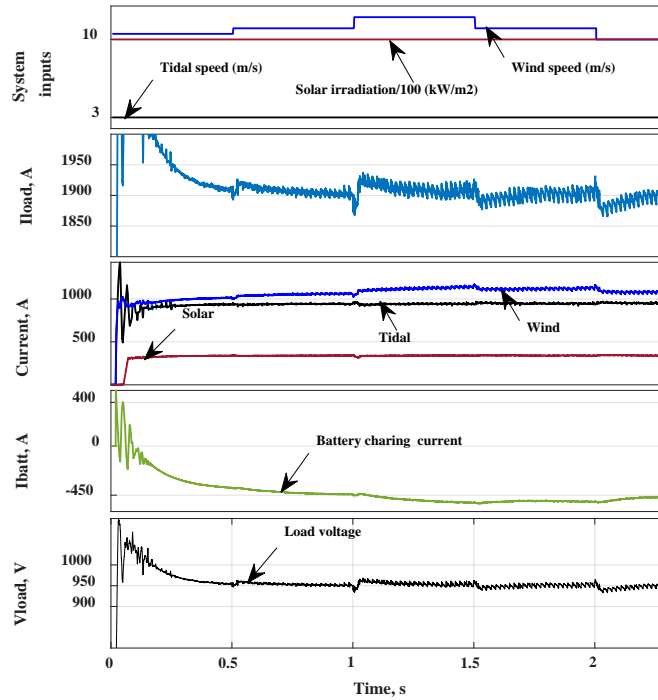


Figure 6.14 Case-a: performance of a single floating energy unit at surplus energy condition.

b) *RES deliver lower energy (deficit energy condition)*

When the RES supply lower power than the required for the demand load, then both the battery system and the RES will supply the load. The same load ($R_{load} = 0.5 \Omega$, $v_o = 950 \text{ V}$) is considered as in case-a. The wind turbine works at variable wind speeds but with a lower energy supply comparing with that of the case-a. Also, the tidal turbine and the solar array are supplying lower energy in this case.

Figure 6.15 shows that the load current is supplied by the RES and battery system due to the deficit energy of the RES. The load voltage is regulated at the nominal voltage using the battery charging/discharging controller. Similar to case-a, there is output voltage overshoot and undershoot due to wind speed step change, but the figures show stable operation with load voltage regulated within the acceptable limits. The transient overshoot at the starting which appeared in case-a is not seen in case-b due to the limited energy supplied from the RES. The battery current plot shows discharging current to support the load voltage via balancing the input supply power with the load power. However,

this mode of operation is considered for a short time before load shedding as the battery storage is designed only to meet the emergency load demand.

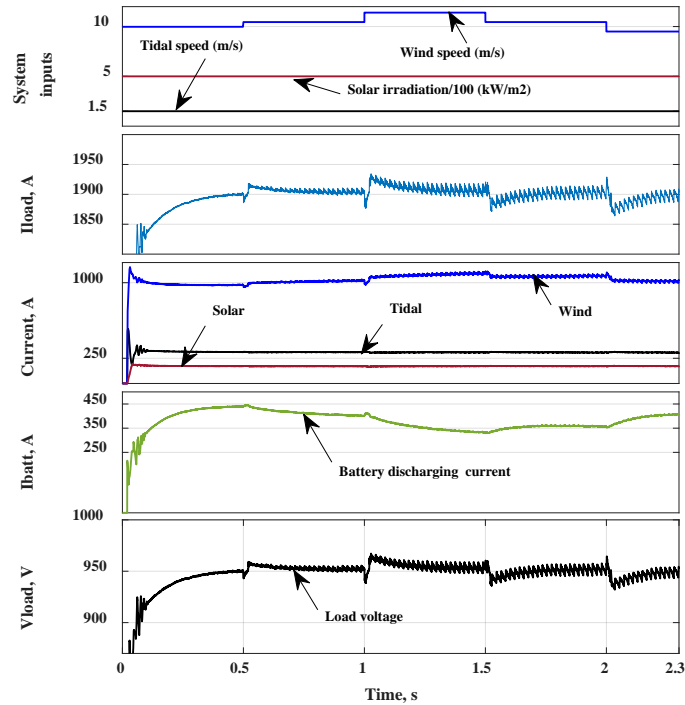


Figure 6.15 Case-b: performance of single floating energy unit at deficit energy supplied from RES.

c) *RES deliver zero energy (load shedding)*

When the RES deliver zero energy, then load shedding must be considered to allow the battery storage to supply only the emergency load to maintain the load voltage regulated at the nominal value. The emergency load is 475 kW as per the blue and green island considered in Chapter 3, Section 3.5.1 ($V_{load} = 950$ V, $I_{load} = 500$ A and $R_{load} = 1.9$ Ω).

Consider DC system, load shedding entails disconnection of unnecessary loads, to maintain source-to-load power balance, with the objective of preventing voltage degradation and hence ensure the system stability. It is assumed that the unnecessary loads are classified into 4 groups based on the priority of each load. Each load is connected to the main DC bus via cable with which has specific resistance.

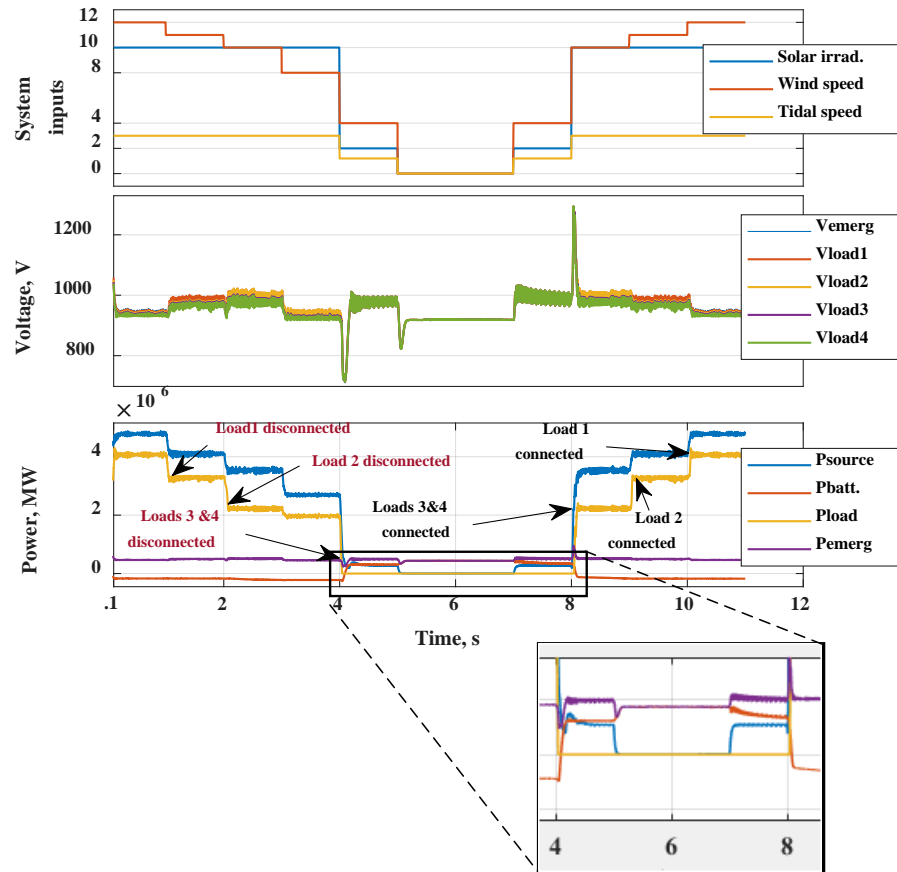


Figure 6.16 Case-c: performance of single floating energy unit at load shedding condition due to RES supply zero energy.

A timer-based load shed scheme is used, in which, non-essential loads are disconnected from the system when their voltage remains below the threshold voltage specified for each load for a predefined time. The voltage threshold is set for every load according to its priority. Load 4 with higher priority takes voltage threshold equals the nominal -4% . Load 3 has threshold voltage equals the nominal voltage -3% , loads 2 and 1 have threshold voltages equal to the nominal voltages -2% and -1% , respectively.

Figure 6.16 shows the system inputs which are the solar irradiation (kW/m^2) divided by 100 to be plotted with the wind and tidal speeds (m/s). The voltage at the terminals of all loads (4 non-essentials loads and one emergency load) are shown, as well. The available power from the renewable energy sources (P_{source}), the battery charging and discharging power (P_{batt}), the total power

of the non-essential loads (P_{load}) and the power of the emergency load (P_{emerg}) are recorded in the figure. The figure shows that the battery charging and discharging controller, successfully, controlled the loads' voltages within the acceptable voltage limit ($950\pm 5\%$) by applying load shedding for the non-essential loads according to the voltage at the load terminal with matching the load power and the available power as explained earlier.

During the period from 0.1 to 1s, the available energy from solar, wind and tidal systems are enough to cover all loads and charging the battery system, as well. At 1s, the wind turbine loses around 700 kW from its output power which results in the voltage at the terminal of load 1 goes below the threshold voltage. Additionally, the available power from renewable energy sources is not enough to cover all loads. So, the controller decision is to disconnect load 1 from the system to maintain the voltage of the system within the acceptable limits. One can notice that the system voltage increased after disconnecting load 1, this is expected as the power of the disconnected load 1 is higher than the reduced power at 1s which results in increasing the system voltage although the battery absorbing its rated power. However this voltage increases within the accepted voltage zone. The same scenario applies for shedding load 2 at 2s and loads 3 and 4 are disconnected together at 4s when the renewable energy systems start to deliver very low power.

During the periods 4 to 5s and 7 to 8s, the available energy from the renewable energy sources is very low which cannot supply the emergency load. So, the battery system is changed from the charging to the discharging mode, at 4s, to support the load voltage which is maintained at a nominal value. The emergency load is supplied during these periods from the renewable energy sources and the battery system. A voltage undershot is recorded at 4s which is expected due to the large drop in the source power at this time. The renewable energy systems deliver zero power during the period from 5 to 7s, and so the battery system alone is supplying the emergency load during this period as the figure shows.

At the 8s, a large increase in the source power leads to voltage overshoot for a short period as expected then reconnecting loads 3 and 4 in a one-step. Due to the increase in the power of the renewable energy sources at 9s and 10s, loads 2 and 1 are reconnected to the system, respectively.

d) Tidal turbine breakdown (Fault condition)

The operating condition of case-a is repeated under this case to analyse the transient stability of the floating energy unit due to tidal turbine-2 outage. Tidal turbine-2 is isolated from the system at 0.6s due to an internal fault. The battery storage compensates for the turbine energy to maintain the load voltage regulated until the turbine re-joins the grid at 1.3s.

Figure 6.17 shows a stable operation, although voltage undershoot is recorded at 0.6s due to a fault that leads to disconnecting the tidal turbine-2. By the time tidal turbine-2 is disconnected, the battery system is changed from charging to discharging mode to support the load voltage. By re-connecting the turbine, voltage overshoot is recorded at 1.3s and the battery system is back to charging mode.

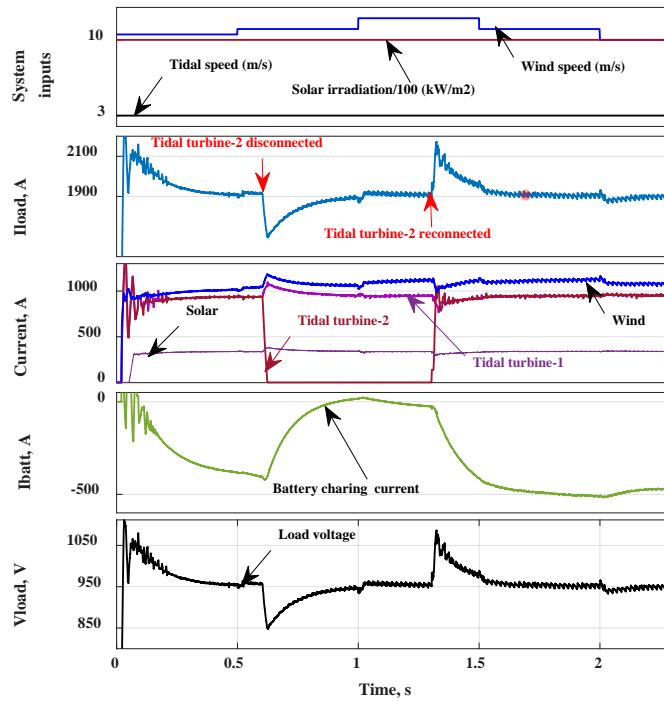


Figure 6.17 Case-d: performance of single floating energy unit at fault condition results in tidal turbine-2 outage.

The figures of part I of this simulation section confirm the stability of the local voltage of the floating unit at different operating conditions as introduced earlier in the stability analysis section.

6.6.2 Part II: Dynamic performance of 2-floating energy units

This part of the simulation section shows the performance of two parallel-connected floating energy units considering the circulating current between them. There are three different scenarios considered under this part. The first scenario considers two floating energy units which are connected in parallel with a single storage unit at the load side. The second scenario considers a storage unit connected to each floating energy unit, i.e. connected to the source side instead of the load side. The third scenario considers applying IACS for minimizing the circulating current between the parallel-connected floating energy units.

a) *Scenario-1 Single energy storage at the load side*

A single energy storage unit is connected in parallel to the load side. A resistive load is considered with $R_{load} = 0.33 \Omega$ while different line impedances are considered with $R_{l1} = 0.0283$ and $R_{l2} = 0.02 \Omega$. The inputs (tidal speed, wind speed and solar irradiation) for both energy units are different as shown in Figure 6.18.

The simulation results for the two energy units are shown in Figure 6.18. The figure shows the output voltages and currents of the two energy units, load current, load voltage and the circulating current between the two units.

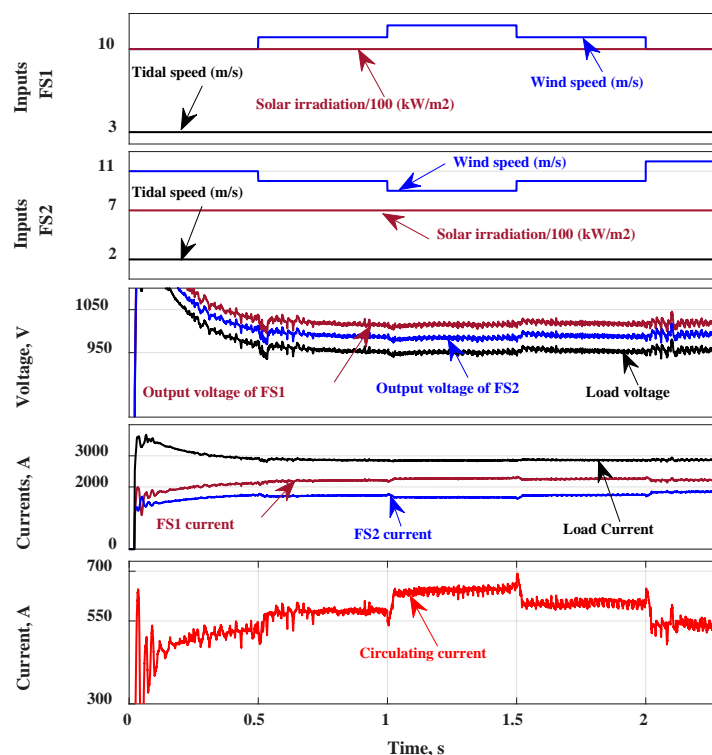


Figure 6.18 Simulation results of two floating energy units connected in parallel with a single energy storage unit.

Figure 6.18 shows that the storage controller successfully regulated the load voltage by absorbing the surplus energy delivered by the RES. However, due to line impedance mismatch and unequal output voltages of the two floating energy units, a large circulating current passes between them. To reduce this circulating current, an energy storage unit is connected to each floating energy

unit for the sake of regulating the output voltages of both floating energy units to the same value as per scenario-2.

b) Scenario-2 Energy storage unit connected to each floating energy unit

The simulation setup of scenario-1 is considered under this scenario to show the impact of using two energy storage units on the circulating current instead of a single storage unit at the load side. The idea is that the controllers of these storage units regulate the output voltages of the floating energy units to the same voltage level to minimise the circulating current.

Figure 6.19 shows that the load voltage is regulated using the controllers of the two storage units by absorbing the surplus energy delivered by the RES in each floating unit. Although the circulating current is reduced as expected, however, the figure shows a slow response for minimizing the circulating current to the lowest level. Additionally, the load voltage is not regulated properly at the nominal voltage. The next scenario considers the use of the IACS controller which was developed in Chapter 5 of this thesis for minimising the circulating current between the two parallel-connected floating energy units.

c) Scenario-3 IACS controller employed with two parallel floating energy units

The simulation setup of scenario-1 is repeated under this scenario to show the impact of employing the IACS controller on minimizing the circulating current comparing with the previous two scenarios. The simulation results are shown in Figure 6.19. The figures show the output voltages and currents of the two energy units, load current, load voltage and circulating current between the two floating units.

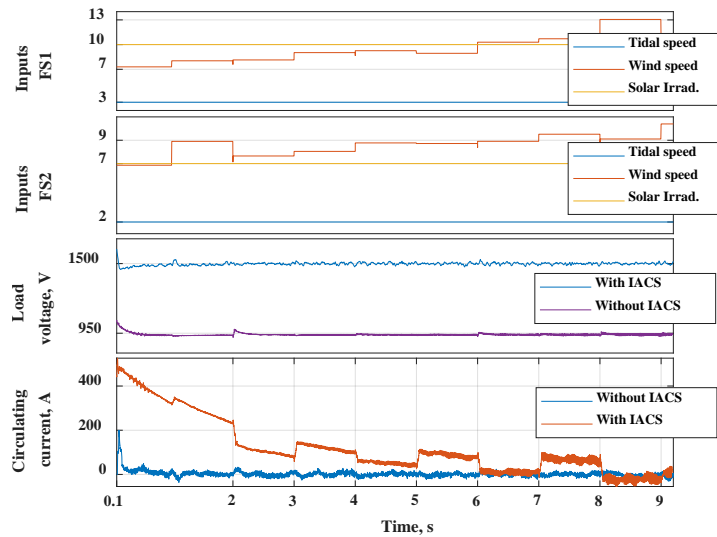


Figure 6.19 Simulation results of two floating energy units with and without the IACS controller.

As per Figure 6.19, with applying the IACS controller, a fast response for the circulating current is recorded, approximately 0.25 s comparing with over 2 s in scenario-2. Another advantage of using the IACS controller is boosting the output voltage of the floating structure to a higher voltage level (voltage of the collection bus) which has a positive impact on the system efficiency via reducing the distribution line losses. Additionally, the load voltage is regulated properly at the nominal voltage.

6.6.3 Part III: 3- parallel energy units within an islanded offshore DC microgrid

For this part, a simulation setup is performed for three floating energy units connected in parallel to a DC collection bus as per Figure 6.1. Figure 6.3 shows the IACS controllers connected to each floating structure for minimizing the circulating current and for maintaining the voltage of the DC collection bus fixed at the nominal voltage. The simulation results of this part are divided into five subparts to show the performance of the proposed coordinated controller (as per Section 6.3.1) under various operating conditions such as surplus energy, load shedding, plug and play capability and communication loss as follows

a) Subpart 1: Surplus energy delivered

This subpart shows the performance of the proposed controller under normal operation while three floating energy units are connected in parallel to the DC collection bus and all RES working in MPPT mode. Storage units are used to support the voltage of the local DC bus at each floating energy unit.

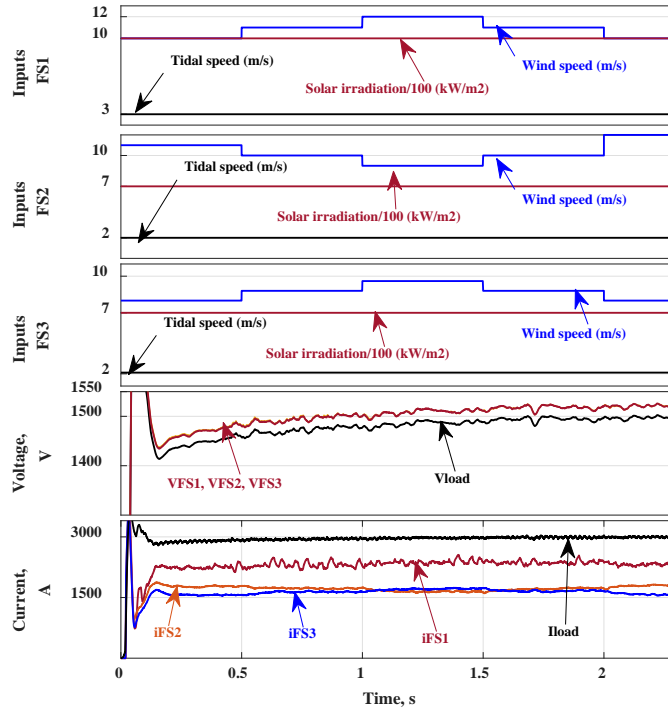


Figure 6.20 Subpart-1, three floating energy units connected in parallel to supply a resistive load at surplus energy condition.

The voltage of the DC collection bus is 1500 V, while the output voltage of each floating energy unit is 950 V. Resistive load is considered at the DC collection bus which equals 0.5 Ω . Different line impedances are considered for all energy units which equals 0.0283, 0.02 and 0.024 Ω .

Figure 6.20 shows the system inputs (wind and tidal speeds and solar irradiation) considered for the three floating energy units. It also shows the output voltages and currents of the floating energy units, the voltage of the DC-collection bus and the load current. The figure shows that the IACS controller successfully regulated the voltage of the DC-collection at the nominal value. Additionally, it regulates the output voltages of all floating units to be equal to

the average voltage and this has a direct impact on minimizing the circulating current between the floating energy units.

b) Subpart 2: Zero RES energy delivered (Load shedding)

This subpart shows the performance of the LVDC microgrid when there is no RES energy delivered. Load shedding is considered to allow the battery storage supplies the emergency load only. The emergency load is 475 kW ($V_{load} = 1500$ V, $I_{load} = 317$ A and $R_{load} = 4.74$ Ω).

Figure 6.21 shows that the load voltage is regulated at the nominal voltage using the battery charging/discharging controller. The voltage overshoot and undershoot shown in Figure 6.20 disappeared in this case as the load voltage is supported only by the battery system. The figure shows zero current delivered from each floating energy unit as RES deliver zero power.

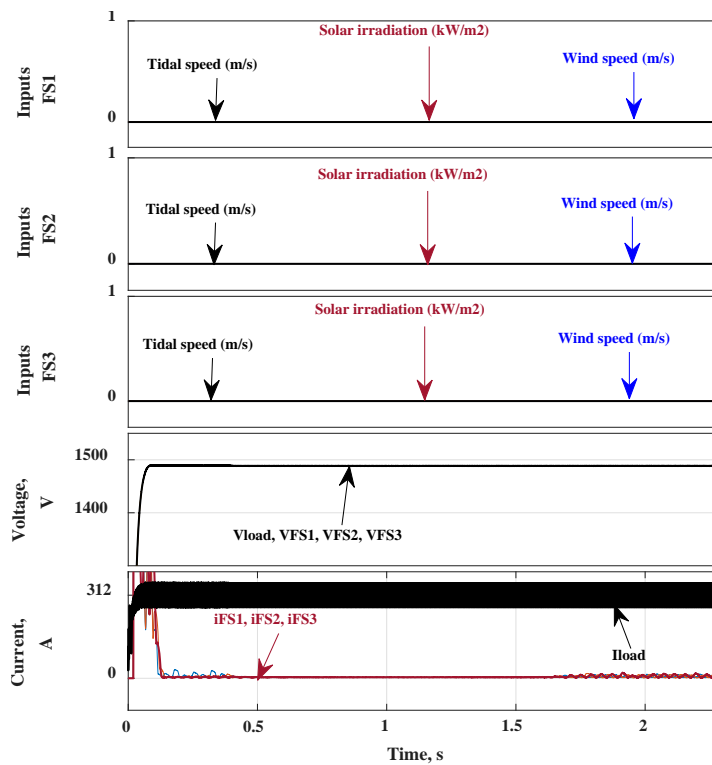


Figure 6.21 Subpart-2, three floating energy units connected in parallel to supply a resistive load at load shedding condition.

c) *Subpart 3: Fault condition (plug and play capability)*

This subpart shows the performance of the proposed controller when a fault occurs which leads to disconnecting the floating energy unit-1. The same operating condition of subpart 1 is considered under this case except at 1.4 s the floating energy unit-1 is disconnected from the system due to cable fault. The disconnected energy unit is re-joined after fault clearance at 2.8 s.

Figure 6.22 shows that the load voltage is regulated at the nominal voltage value before and after disconnecting the faulty energy unit and the load current is shared by the active energy units 2 and 3.

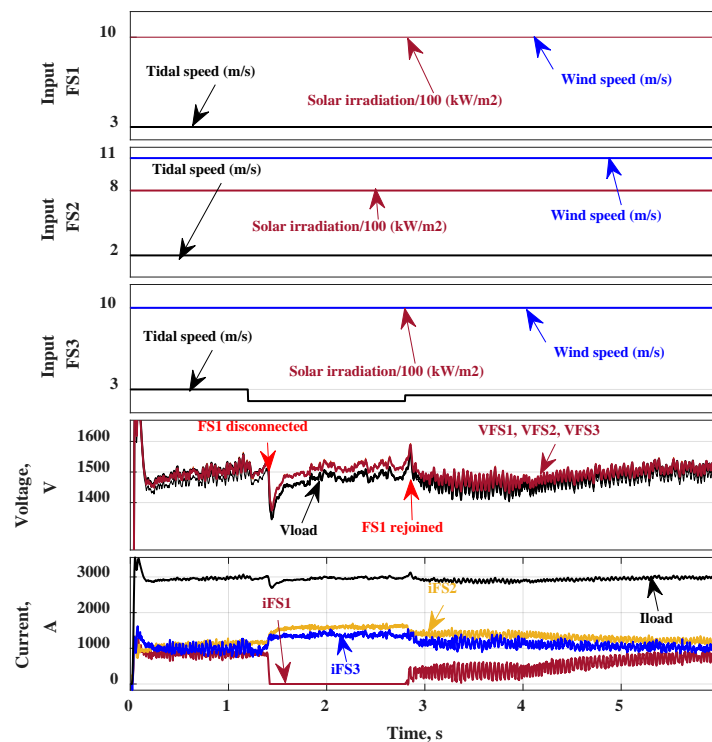


Figure 6.22 Subpart-3, three floating energy units connected in parallel to supply a resistive load at fault condition.

d) *Subpart 4: One converter lost communication with the rest of the grid*

The same operating condition of subpart-1 is considered under this subpart. This subpart examines the case when there is a single converter (at Pos.2 as per Figure 6.3) that is unable to send its output voltage and current due to communication loss with the rest of the system. Normally, all converters send their output voltages and currents to an upper control layer for estimating the

average current and voltage as per Figure 6.3. When one converter loses communication with the whole system, this results in wrong calculations of the average voltage and current.

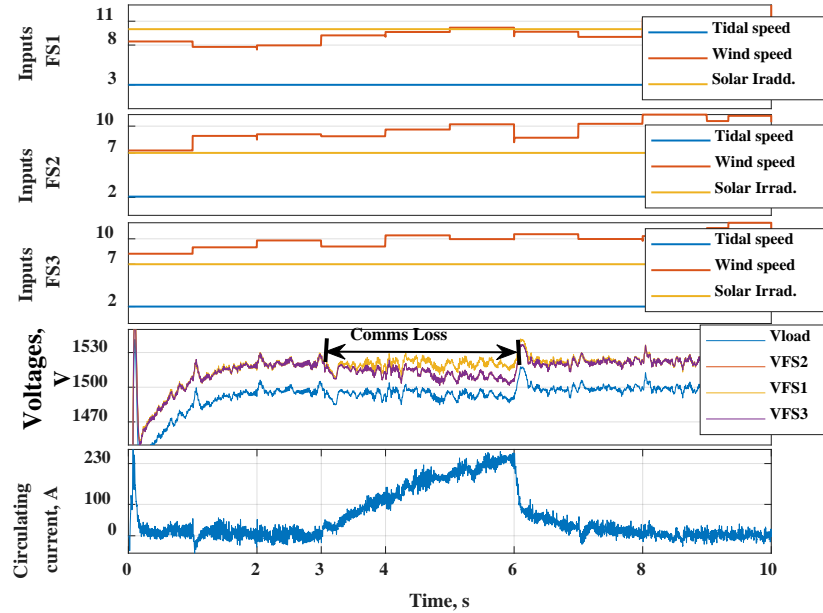


Figure 6.23 Subpart-4, three floating energy units connected in parallel to supply a resistive load while communication is lost with the floating energy unit-3.

In such cases, the average voltage and current are estimated considering only the number of the converters that actively communicated to the upper control layer. For the converter with a communication issue, its output voltage is regulated at the nominal load voltage.

Figure 6.23 shows the simulation results when the communication is lost with the floating energy unit-3. The figures show that the output voltages of all converters are equal until the communication is lost with the floating energy unit-3 at 3s. During the period from 3s to 6s, the floating energy units 1 and 2 have the same output voltage while the output voltage of the third unit is different. Circulating current is expected to pass between the floating energy units with different output voltages, i.e. between (1 and 3) and (2 and 3).

e) *Subpart 5: Loss of the whole communication system*

A similar operating condition to that of subpart-1 is considered under subpart 5. This subpart considers the case when the communication with the upper control layer is lost for all converters at Pos.2. This leads to that the average voltage and current are missing in the IACS controller. In such cases, it is proposed that the output voltages of all converters are regulated at the nominal load voltage.

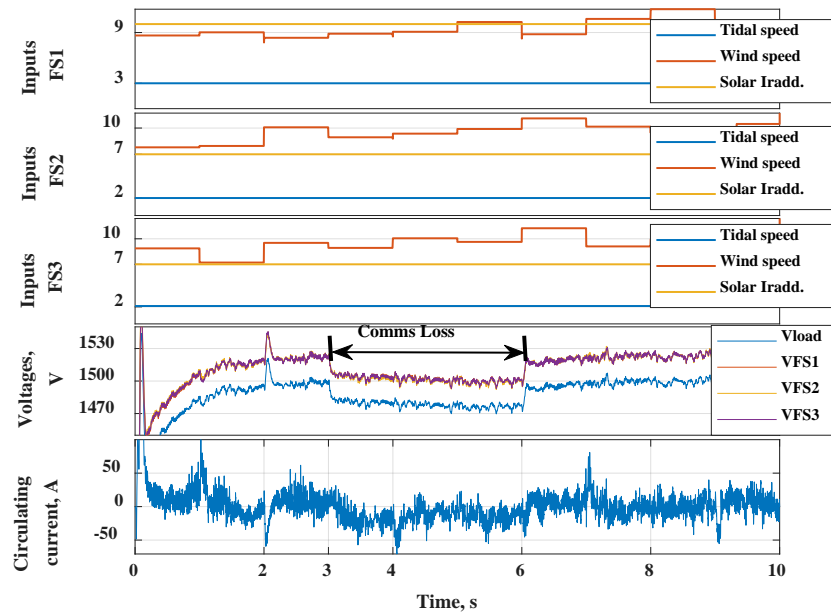


Figure 6.24 Subpart-5, three floating energy units connected in parallel to supply a resistive load while the communication system is completely lost.

Figure 6.24 shows the simulation results when the communication system is lost completely. The figure shows that the output voltages of all converters are equal until the communication with the upper control layer is lost at 3s. During the period from 3s to 6s, the figures show a drop in the output voltages of all floating energy units and the load voltage, although the load voltage remains within the accepted deviation limits. By recovering the communication system, the load voltage starts growing up again to reach the nominal value at around 6.7s.

6.7 Summary

A new control approach based on IACS is proposed for accurate voltage regulation and minimizing circulating current among parallel floating energy units connected in an islanded LVDC-microgrid. Each floating energy unit comprises tidal, wind and solar energy resources with a storage unit. Mathematical modelling is performed for all components (tidal, wind, solar) with the DC-DC boost converter for Maximum Power Point Tracking (MPPT) and a mathematical model for bi-directional buck-boost converter is derived which controls the storage unit for voltage regulation. Additionally, an overall model for a single floating energy unit and n -parallel floating energy units are derived.

Stability analysis is held for all components with the DC-DC converters, and then stability analysis is performed for the overall model of the floating energy unit. Matlab/Simulink setup is used to investigate the dynamic performance of a single floating energy unit with DC load at the different operating conditions to evaluate the stability analysis performed. Other Matlab/Simulink setups are used to investigate the performance of the proposed control scheme based on 2 and 3-parallel floating energy units supplying a DC-load.

To conclude this chapter, the simulation results showed excellent dynamic performance for the proposed control scheme in regulating the grid voltage and minimizing the circulating current among the floating energy units. Based on the stability analysis and simulation results performed under this chapter, Low Voltage Direct Current (LVDC) offshore microgrid based renewable energy sources is a viable candidate with many advantages to be considered for substituting low voltage AC microgrids for powering offshore loads such as aquaculture or isolated communities.

Chapter 7 Conclusions and Future Works

7.1 General conclusion

The idea of Multi-use Platforms (MUPs) which was supported by the European Union over two big projects attracted the attention of academic circles all over the world over the past decade. The intention is to develop offshore platforms to extract marine energy sustainably within lower costs, as well as other uses, such as aquaculture. Hence, this thesis focused on developing the electric infrastructure of the MUP's microgrid by addressing many of its challenges highlighted in Chapter 1.

From chapter 2, one can conclude that the DC system has never been proposed for the MUP's microgrid. Also, integrating different energy resources on the same floating structure has a positive economic impact and improves grid reliability. For this reason, it is proposed to add floating tidal turbines, as predictable energy resources, to the satellite unit that already has solar and wind energy resources.

Chapter 3 proposed a new graphical concept to estimate the optimal size of a hybrid energy system to meet certain load demands. Additionally, to improve the DC-DC converter efficiency and operation, a new methodology is proposed to estimate the optimal number of parallel DC-DC converters to be connected to a wind/tidal turbine. From this chapter, it can be concluded that the proposed sizing technique, verified by the Matlab optimisation tool "Linprog", accurately determined the optimal share of the energy resources considered under the case study. Also, it is found that the DC conversion efficiencies of the wind and tidal converters increased from 57% to 75% and from 10% to 55%, respectively, by applying the proposed technique to determine the optimal number of parallel converters.

Chapter 4 focused on DC-DC power converters being the main component of the DC system. From the control section of this chapter, it can be concluded that flexibility is the main advantage of the passive load sharing approaches due to the lack of communication that makes it the favour of most researchers. With active load sharing techniques, good voltage regulation and current sharing performance are guaranteed but with lower reliability due to dependency on the communication. However, active load sharing techniques have the potential to be improved and expanded due to the

advancements in the communication infrastructure. From the third part of this chapter, it can be concluded that circulating current exists in the system regardless of the load level and it occurs when there is a difference in the output voltages of the parallel converters. Additionally, at no-load condition, power exchange among parallel converters occurs due to the circulating current. This power exchange can affect the control system and even damage the converters.

Chapter 5 proposed a new adaptive IACS control scheme based on SDM for accurate voltage regulation and minimizing circulating current among parallel DC-DC converters connected in a DC-microgrid. From the stability analysis, it can be concluded that the stability of the voltage of a DC grid with parallel converters depends on the voltage regulation capability of the individual converters. Also, it can be concluded that the proposed controller overcomes the shortcomings of the conventional IACS in terms of better voltage regulation with varying line impedances and in minimizing the circulating current. The proposed control scheme showed better performance compared with adaptive droop control of one of the studies in the literature in terms of accurate voltage regulation and lower circulating current levels.

Chapter 6 proposed a new control approach based on IACS for accurate voltage regulation and minimizing circulating current among parallel floating energy units connected within an offshore LVDC-microgrid. Stability analysis is held for all components with the DC-DC converters, then stability analysis is performed for the overall model of the floating energy unit. Matlab/Simulink model is used to investigate the dynamic performance of a single floating energy unit with DC load at different operating conditions which confirm the stability analysis undertaken. The simulation results showed excellent dynamic performance for the proposed control scheme in regulating the grid voltage and minimizing the circulating current among the floating energy units. The main point to conclude from this chapter is that LVDC offshore microgrid based renewable energy sources is a viable candidate with many advantages to be considered for substituting low voltage AC microgrid for powering offshore loads such as aquaculture or isolated communities.

7.2 Suggestions for future research

For further research, the following areas could be suggested:

- This thesis analysed the LVDC microgrid of the MUPs based on a floating energy unit that comprises wind, tidal, solar with a storage unit. However, adding wave energy would improve the performance of this energy unit and reduce the costs of the wave energy. So, modelling and analysis of the whole DC system are required.
- The proposed adaptive controller in chapter 5 can be examined for integration with other control schemes such as master-slave, droop, etc.
- Investigation of the proposed coordinated control scheme in grid-connected mode.
- Defining the optimal number of parallel-connected converters to a wind turbine is achieved using the graphical concept. However, further study would be required to develop a Matlab or Excel tool to obtain the converters number directly by providing the system inputs.
- The environmental impact of the whole system is recommended for further study with comparing the impact of using DC and AC systems.
- Algae biofuels would play a vital role as potential energy storage that gives better reliability for the offshore power system and avoid using large capacities of batteries.

7.3 Author's contribution

The research carried out in this thesis focused on improving the electric infrastructure of the MUP's microgrid by addressing many of the challenges presented in Chapter one. The contribution of the thesis can be summarized as follows

- State of the art of the multi-purpose platforms is presented.
- A new circulating current definition is derived and verified by simulation model for n -parallel DC-DC converters connected in parallel to DC load.
- A new graphical concept for the optimal sizing of a hybrid DC power plant is proposed and verified by the Matlab optimisation tool "Linprog".

- A new methodology for defining the optimal number of the parallel DC-DC converters connected to a wind/tidal turbine for maximizing the DC conversion efficiency is proposed.
- A new adaptive control technique based on instantaneous average current sharing technique for suppressing the circulating current among parallel-connected DC-DC converters is proposed.
- A new floating DC energy unit (comprising wind turbines, tidal turbines and solar array with energy storage unit) is proposed with presenting modelling and stability analysis for it.
- A new coordinated controller-based IACS is proposed for controlling an islanded offshore LVDC microgrid with n -floating DC energy units.

References

- [1] H. Ritchie. "Energy." OurWorldInData. <https://ourworldindata.org/energy> (accessed 23/02, 2021).
- [2] W. S. School. "How Much Water is There on Earth?" USGS science for a changing world. (accessed 15-02-2020, 2020).
- [3] AOGHS. American Oil and Gas History Society. <https://aoghs.org/offshore-history/offshore-oil-history/> (accessed 25 Dec, 2017).
- [4] J. Ryan, D. Maguire, and G. Mills, "farming the deep blue."
- [5] M. Shainee, H. Ellingsen, B. J. Leira, and A. Fredheim, "Design theory in offshore fish cage designing," *Aquaculture*, pp. 134-141, 2013.
- [6] E. Quevedo *et al.*, "Multi-Use Offshore Platform Configurations in the Scope of the FP7 TROPOS Project," in *OCEANS - Bergen, 2013 MTS/IEEE*, Bergen, 2013.
- [7] M. Stuiver *et al.*, "The Governance of Multi-Use Platforms at Sea for Energy Production and Aquaculture: Challenges for Policy Makers in European Seas," *Sustainability* vol. 8, no. 4, 2016.
- [8] E. Commission, "The Ocean of Tomorrow Projects (2010 - 2013)," Commission, European, Brussels, 2014.
- [9] E. Commoission, "Horizon 2020 Projects," 2020.
- [10] J. Bard. "Multi-use Platform Concepts for the Oceans of Tomorrow." <https://www.icoe-conference.com/publication/multi-use-platform-concepts-for-the-oceans-of-tomorrow/>. (accessed 07 June, 2021).
- [11] R. Clarke and J. Bostock, "Regional Review on Status and Trends in Aquaculture Development in Europe – 2015," FAO, Rome, 2015.
- [12] S. Bala, J. Pan, D. Das, O. Apeldoorn, and S. Ebner, "Lowering failure rates and improving serviceability in offshore wind conversion-collection systems," in *2012 IEEE Power Electronics and Machines in Wind Applications*, 2012-07-01 2012: IEEE, doi: 10.1109/pemwa.2012.6316362.
- [13] Z. H. Jian, Z. Y. He, J. Jia, and Y. Xie, "A Review of Control Strategies for DC Micro-grid," in *Fourth International Conference on Intelligent Control and Information Processing (ICICIP)*, Beijing, 2013.
- [14] S. Augustine, M. K. Mishra, and N. Lakshminarasamma, "Circulating current minimization and current sharing control of parallel boost converters based on Droop Index," in *2013 9th IEEE International Symposium on Diagnostics for Electric Machines, Power Electronics and Drives (SDEMPED)*, 27-30 Aug. 2013 2013, pp. 454-460, doi: 10.1109/DEMPED.2013.6645755.
- [15] M.Kamel and Rashad, "New Inverter Control for Balancing Standalone Micro-Grid Phase Voltages: A Review on MG Power Quality Improvement," *Renewable and Sustainable Energy Reviews*, vol. 63, pp. 520–532, 2016.
- [16] D. I. I. P. L. President. (2017, Jan 26) Cover Story - Energy Efficiency: Role of Harmonics Standards in Reducing Power Quality Problems in the Grid. *Business Insights: Global*.

- [17] G. Xiaozhi, L. Linchuan, and C. Wenyan, "Power Quality Improvement for Microgrid in Islanded Mode," *Procedia Engineering*, vol. 23, pp. 174 – 179, 2011.
- [18] A. Rasheed and G. K. Rao, "Improvement of Power Quality for Microgrid using Fuzzy based UPQC Controller," *Indian Journal of Science and Technology*, vol. 8, no. 23, 2015.
- [19] S. Augustine, M. K. Mishra, and N. Lakshminarasamma, "Adaptive Droop Control Strategy for Load Sharing and Circulating Current Minimization in Low-Voltage Standalone DC Microgrid," *IEEE Transactions on Sustainable Energy*, vol. 6, no. 1, pp. 132-141, 2015, doi: 10.1109/TSTE.2014.2360628.
- [20] S. Chowdhury and P. Crossley, *Microgrids and Active Distribution Networks*. Institution of Engineering and Technology, 2009.
- [21] F. Lu, L. He, Q. Tan, and H. Zhou, "Efficiency Optimization of IPOP DC/DC System for HEV," *IEEE Access*, pp. 1-1, 2021-01-01 2021, doi: 10.1109/access.2021.3060018.
- [22] T. Kohama, Y. Sogawa, and S. Tsuji, "Optimized on-off control to improve efficiency of paralleled converter system," in *2014 IEEE 36th International Telecommunications Energy Conference (INTELEC)*, 2014-09-01 2014: IEEE, doi: 10.1109/intelec.2014.6972181.
- [23] J. Yan and L. Mu, "A method to improve the efficiency of asymmetric parallel converters for PV generation," in *2015 5th International Conference on Electric Utility Deregulation and Restructuring and Power Technologies (DRPT)*, 2015-11-01 2015: IEEE, doi: 10.1109/drpt.2015.7432587.
- [24] Y. L. Juan, Y. Lung Lee, C. Y. Huang, H. Mei Chang, Y. Y. Tai, and M. Hsun Lu, "Efficiency Coordinated Control for Modularized Parallel DC-DC converters," in *2019 IEEE 4th International Future Energy Electronics Conference (IFEEC)*, 2019-11-01 2019: IEEE, doi: 10.1109/ifeec47410.2019.9015064.
- [25] B. Andresen and J. Birk, "A high power density converter system for the Gamesa G10x 4,5 MW wind turbine," in *2007 European Conference on Power Electronics and Applications*, 2007-01-01 2007: IEEE, doi: 10.1109/epe.2007.4417312.
- [26] J. Birk and B. Andresen, "Parallel-connected converters for optimizing efficiency, reliability and grid harmonics in a wind turbine," in *2007 European Conference on Power Electronics and Applications*, 2007-01-01 2007: IEEE, doi: 10.1109/epe.2007.4417318. [Online]. Available: <https://ieeexplore.ieee.org/document/4417318/>
- [27] A. Nawaz, J. Wu, and C. Long, "Mitigation of circulating currents for proportional current sharing and voltage stability of isolated DC microgrid," *Electric Power Systems Research*, vol. 180, p. 106123, 2020, doi: 10.1016/j.epsr.2019.106123.
- [28] M. R. Jyothish and E. A. Jasmin, "Load Sharing Control and Circulating Current Minimization of Parallel DC-DC Converters Based on Droop Index," 2018: IEEE, doi: 10.1109/cetic4.2018.8530954. [Online]. Available: <https://dx.doi.org/10.1109/cetic4.2018.8530954>
- [29] A. Jain, S. Jain, and D. K. Palwalia, "Stability enhancement of DC-DC converters using robust droop control scheme and circulating current elimination in DC micro-grid," 2016: IEEE, doi:

- 10.1109/poweri.2016.8077192. [Online]. Available: <https://dx.doi.org/10.1109/poweri.2016.8077192>
- [30] S. Augustine, M. K. Mishra, and N. Lakshminarasamma, "An improved droop control algorithm for load sharing and circulating current control for parallel DC-DC converters in standalone DC microgrid," 2014: IEEE, doi: 10.1109/aicera.2014.6908222. [Online]. Available: <https://dx.doi.org/10.1109/aicera.2014.6908222>
- [31] W. E. Council, "World Energy Resources Marine Energy | 2016," World Energy Council, 2016.
- [32] C. Pérez and G. Iglesias, "Integration of Wave Energy Converters and Offshore Windmills," in *4th International Conference on Ocean Energy*, Dublin, 2012.
- [33] C. Perez-Collazo, M. M. Jakobsen, and H. Buckland, "Synergies for a Wave-Wind Energy Concept," in *Proceedings of the European offshore wind energy conference.*, Frankfurt, 2013.
- [34] N. Pérez-Collazo, C., D. Greaves, and G. Iglesias, "A Review of Combined Wave and Offshore Wind Energy," *Renewable and Sustainable Energy Reviews*, vol. 42, pp. 141-153, 2015.
- [35] S. Astariz and G. Iglesias, "The Economics of Wave Energy: A Review," *Renewable and Sustainable Energy Reviews*, vol. 45, pp. 397–408, 2015.
- [36] W. Tjiu, K. Sopian, M. H. Ruslan, S. Mat, and j. Marnoto, "Darrieus vertical axis wind turbine for power generation II: Challenges in HAWT and the opportunity of multi-megawatt Darrieus VAWT development," *Renewable energy*, vol. 75, pp. 560-571, 2015.
- [37] W. Tjiu, K. Sopian, M. H. Ruslan, S. Mat, and j. Marnoto, "Darrieus vertical axis wind turbine for power generation I: Assessment of Darrieus VAWT configurations," *Renewable Energy*, vol. 75, pp. 50-67, 2015.
- [38] W. Liu and Q. Xiao, "Investigation on Darrieus Type Straight Blade Vertical Axis Wind Turbine with Flexible Blade," *Elsevier*, vol. 110, p. 339–356, 2015.
- [39] V. I. Khrisanov and B. F. Dmitriev, "Marine Electrical Power Industry with Renewable Energy Carriers. Part 1. Wind and Wave Turbines of Offshore Power Plants," *Elektrotehnika*, vol. 7, pp. 49–57, 2016.
- [40] Qiuwei Wu and Y. Sun, *Modeling and Modern Control of Wind Power*. John Wiley & Sons Ltd., 2018.
- [41] K. Koca *et al.*, "Energy converters," Mermaid EU project, 2013.
- [42] M. J. Khan, G. Bhuyan, M. T. Iqbal, and J. E. Quaioco, "Hydrokinetic Energy Conversion Systems and Assessment of Horizontal and Vertical Axis Turbines for River And Tidal Applications: A Technology Status Review," *Applied Energy*, vol. 86, no. 10, pp. 1823-1835, 2009.
- [43] K. Kaygusuz and M. S. Güneş, "Hydrokinetic Energy Conversion Systems: A Technology Status Review," *Renewable and Sustainable Energy Reviews*, vol. 14, no. 9, pp. 2996-3004, 2010.
- [44] N. M. Eshra and M. E. Abdelnaby, "Study of Application of Small Hydropower for Nile River in Egypt," *Middle East Journal of Applied Sciences*, vol. 4, no. 4, pp. 1118-1129, 2014.

- [45] J. S. Martínez *et al.*, "Integration of Energy Converters in Multi-Use Offshore Platforms," Seventh Framework Programme Mermaid EU, 2015. [Online]. Available: <http://www.vliz.be/projects/mermaidproject/docmanager/public/>
- [46] P. Technology. "Kyocera Floating Solar Power Plant, Chiba Prefecture." Power Technology. (accessed 15-02, 2020).
- [47] H. C. f. M. Research, "D4.5 Aquaculture Pilot Scale Report," Tropos EU 2015.
- [48] A. Yazdani *et al.*, "Modeling Guidelines and a Benchmark for Power System Simulation Studies of Three-Phase Single-Stage Photovoltaic Systems," *IEEE Transactions on Power Delivery*, vol. 26, no. 2, pp. 1247-1264, 2011, doi: 10.1109/TPWRD.2010.2084599.
- [49] N. Team, "The NEMOS Wave Energy Converter," ed: NEMOS Company, 2020.
- [50] M. R. Dhanak and N. I. Xiros, *Handbook of Ocean Engineering*. London: Springer Nature, 2016.
- [51] U. o. Edinburgh, "D2.3 Sample locations and setups for further design," Tropos EU, Edinburgh 2013.
- [52] J. Trivedi, M. Aila, D. P. Bangwal, S. Kaul, and M. O. Garg, "Algae based biorefinery-How to make sense?," *Renewable and Sustainable Energy Reviews*, vol. 47, pp. 295–307, 2015.
- [53] B. Bharathiraja *et al.*, "Aquatic biomass (algae) as a future feedstock for bio-refineries: A review on cultivation, processing and products," *Renewable and Sustainable Energy Reviews*, vol. 47, pp. 634–653, 2015.
- [54] W. M. Nassar, O. Anaya-Lara, K. H. Ahmed, D. Campos-Gaona, and M. Elgenedy, "Assessment of Multi-Use Offshore Platforms: Structure Classification and Design Challenges," *Sustainability*, vol. 12, no. 5, p. 1860, 2020. [Online]. Available: <https://www.mdpi.com/2071-1050/12/5/1860>.
- [55] U. P. d. Madrid, "D4.3 Complete Design Specification of 3 Reference TROPOS systems," Tropos EU, Madrid, 2015.
- [56] T. P. Team, "TROPOS Project," EU.
- [57] T. U. o. Edinburgh, "D5.8 Overall Deployment Strategy for the deployment and exploitation of multi-use marine platforms," Tropos EU, Edinburgh, 2014.
- [58] T. U. o. Edinburgh, "D5.7 Technical Strategy for the deployment and exploitation of multi-use marine platforms," Tropos EU, Edinburgh, 2014.
- [59] T. p. Team, "D2.1 report on methodology, evaluation matrix setup, and overall design constraints," Tropos project EU, 2012.
- [60] U. o. S. School of Engineering Sciences, UK, "Energy Island," ed: School of Engineering Sciences, Univ. of Southampton, UK.
- [61] P. A. L. D. Nunes, L. E. Svensson, and A. Markandya, *Handbook On The Economics And Management Of Sustainable Oceans*. Edward Elgar, 2017, p. 624.
- [62] B. Zanuttigh, E. Angelelli, A. Kortenhuis, K. Koca, Y. Krontira, and P. Koundouri, "A Methodology for Multi-Criteria Design of Multi-Use Offshore Platforms for Marine Renewable Energy Harvesting," *Renewable Energy*, vol. 85, pp. 1271-1289, 2016.
- [63] F. I. IWES, "D3.5 Integrated Concept Offshore Platform System Design," Tropos EU Project, Glasgow, 2014.

- [64] E. Rodriguez-Diaz, F. Chen, J. C. Vasquez, J. M. Guerrero, R. Burgos, and D. Boroyevich, "Voltage-Level Selection of Future Two-Level LVdc Distribution Grids: A Compromise Between Grid Compatibility, Safety, and Efficiency," *IEEE Electrification Magazine*, vol. 4, no. 2, pp. 20-28, 2016, doi: 10.1109/mele.2016.2543979.
- [65] W. D. J. Aerts, Stijn ; Haeseldonckx, Dries ; van Willigenburg, Pepijn ; Woudstra, Johan ; Stokman, Harry, "Sustainable Impact and Standardization of a DC Micro Grid," *Proceedings of Ecodesign 2013 International Symposium*, 2013.
- [66] Nikos, *Microgrids Architectures and Control*. Noida,: IEEE, 2014.
- [67] A. Bidram and A. Davoudi, "Hierarchical Structure of Microgrids Control System," *TRANSACTIONS ON SMART GRID*, vol. 3, no. 4, pp. 1963- 1976, 2012.
- [68] S. Antonis, T. G., Hatziargyriou, and N. D, "Centralized Control for Optimizing Microgrids Operation," in *Power and Energy Society General Meeting, IEEE*, Detroit, MI, USA, USA, 2011.
- [69] M. Savaghebi, A. Jalilian, J. C. Vasquez, and J. M. Guerrero, "Secondary Control Scheme for Voltage Unbalance Compensation in an Islanded Droop-Controlled Microgrid," *TRANSACTIONS ON SMART GRID*, vol. 3, no. 2, pp. 797- 807, 2012.
- [70] A. Askarzadeh, "Optimisation of solar and wind energy systems: a survey," *International Journal of Ambient Energy*, vol. 38, no. 7, pp. 653-662, 2017/10/03 2017, doi: 10.1080/01430750.2016.1155493.
- [71] A. Mohanty, M. Viswavandya, P. K. Ray, and S. Mohanty, "Reactive power control and optimisation of hybrid off shore tidal turbine with system uncertainties," *Journal of Ocean Engineering and Science*, vol. 1, no. 4, pp. 256-267, 2016.
- [72] A. Mohanty, M. Viswavandya, S. Mohanty, and D. K. Mishra, "Reactive Power Compensation in a Stand-alone Wind-diesel-tidal Hybrid System by a Fuzzy Logic Based UPFC," *Procedia Computer Science*, vol. 57, pp. 1281-1288, 2015.
- [73] S. M. M. G., "An autonomous hybrid energy system of wind/tidal/microturbine/battery storage," *International Journal of Electrical Power & Energy Systems*, vol. 43, no. 1, pp. 1144-1154, 2012.
- [74] F. D. Wijaya, K. D. Pribadi, and S. Sarjiya, "Maximum power point tracking using particle swarm optimization algorithm for hybrid wind-tidal harvesting system on the south coast of Java," vol. 7, no. 2, pp. 659-666, 2017, doi: 10.11591.
- [75] R. M.L., O. S., and S. Y., "Hybrid Offshore Wind and Tidal Turbine Power System to Compensate for Fluctuation (HOTCF)," presented at the Zero-Carbon Energy Kyoto 2010, 2011.
- [76] H. Yang, W. Zhou, L. Lu, and Z. Fang, "Optimal sizing method for stand-alone hybrid solar-wind system with LPSP technology by using genetic algorithm," 2008.
- [77] S. Singh, M. Singh, and S. C. Kaushik, "A review on optimization techniques for sizing of solar-wind hybrid energy systems," *International Journal of Green Energy* vol. 13, no. 15, pp. 1564-1578, 2016.

- [78] A. Chauhan and R.P.Saini, "A review on Integrated Renewable Energy System based power generation for stand-alone applications: Configurations, storage options, sizing methodologies and control," *Renewable and Sustainable Energy Reviews* vol. 38, pp. 99-120, 2014.
- [79] S. Sinha and S. S. Chandel, "Review of recent trends in optimization techniques for solar photovoltaic–wind based hybrid energy systems," *Renewable and Sustainable Energy Reviews*, vol. 50, pp. 755-769, 2015, doi: <https://doi.org/10.1016/j.rser.2015.05.040>.
- [80] A. K. Kaviani, G. H. Riahy, and S. M. Kouhsari, "Optimal Design of a Reliable Hydrogen-based Stand-alone Wind/PV Generation System, considering component outages " *Renewable Energy*, vol. 34, no. 1, pp. 2380-2390, 2009, doi: <https://doi.org/10.1016/j.renene.2009.03.020>.
- [81] D. Abbes, A. Martinez, and G. Champenois, "Life cycle cost, embodied energy and loss of power supply probability for the optimal design of hybrid power systems," *Mathematics and Computers in Simulation*, vol. 98, pp. 46-62, 2014, doi: <https://doi.org/10.1016/j.matcom.2013.05.004>.
- [82] A. T. D. Perera, R. A. Attalage, K. K. C. K. Perera, and V. P. C. Dassanayake, "A hybrid tool to combine multi-objective optimization and multi-criterion decision making in designing standalone hybrid energy systems," *Applied Energy*, vol. 107, pp. 412-425, 2013.
- [83] W. L. Theo, J. S. Lim, W. S. Ho, H. Hashim, and C. T. Lee, "Review of distributed generation (DG) system planning and optimisation techniques: Comparison of numerical and mathematical modelling methods," *Renewable and Sustainable Energy Reviews*, vol. 67, pp. 531-573, 2017.
- [84] A. Arabali, M. Ghofrani, M. Etezadi-Amoli, M. S. Fadali, and Y. Baghzouz, "Genetic-Algorithm-Based Optimization Approach for Energy Management," *IEEE Transactions on Power Delivery*, vol. 28, no. 1, pp. 162-170, 2013, doi: 10.1109/TPWRD.2012.2219598.
- [85] R. Tuladhar and S. Yin, "Sustainability of using recycled plastic fiber in concrete," Elsevier, 2019, pp. 441-460.
- [86] J.-h. Shi, Z.-d. Zhong, X.-j. Zhu, and G.-y. Cao, "Robust design and optimization for autonomous PV-wind hybrid power systems," *Journal of Zhejiang University-SCIENCE A*, vol. 9, no. 3, pp. 401-409, 2008/03/01 2008, doi: 10.1631/jzus.A071317.
- [87] A. Mawardi and R. Pitchumani, "Effects of parameter uncertainty on the performance variability of proton exchange membrane (PEM) fuel cells," *Journal of Power Sources*, vol. 160, no. 1, pp. 232-245, 2006, doi: <https://doi.org/10.1016/j.jpowsour.2006.01.017>.
- [88] S. A. Kalogirou, "Optimization of solar systems using artificial neural networks and genetic algorithms," *Applied Energy*, vol. 77, no. 4, pp. 383-405, 2004, doi: [https://doi.org/10.1016/S0306-2619\(03\)00153-3](https://doi.org/10.1016/S0306-2619(03)00153-3).
- [89] Adel Mellita, S. A. Kalogirou, and M. Drif, "Application of neural networks and genetic algorithms for sizing of photovoltaic systems," *Renewable Energy*, vol. 35, no. 12, pp. 2881-2893, 2010.
- [90] T. Khatib, A. Mohamed, and K. Sopian, "Optimization of a PV/wind micro-grid for rural housing electrification using a hybrid iterative/genetic algorithm: Case study of Kuala Terengganu, Malaysia," *Energy and*

- Buildings*, vol. 47, pp. 321-331, 2012, doi: <https://doi.org/10.1016/j.enbuild.2011.12.006>.
- [91] Y. Zhou, D. E. Macpherson, W. Blewitt, and D. Jovicic, "Comparison of DC-DC converter topologies for offshore wind-farm application," in *6th IET International Conference on Power Electronics, Machines and Drives (PEMD 2012)*, 27-29 March 2012 2012, pp. 1-6, doi: 10.1049/cp.2012.0196.
- [92] T. E. Tawil, J. F. Charpentier, and M. Benbouzid, "Sizing and rough optimization of a hybrid renewable-based farm in a stand-alone marine context," *Renewable Energy*, vol. 115, pp. 1134-1143, 2018, doi: <https://doi.org/10.1016/j.renene.2017.08.093>.
- [93] W. Mohamadi, *Techno-economic Assessment of a Hybrid Solar-Wind Electrical System* German: LAP LAMBERT Academic Publishing, 2016.
- [94] U. P. d. Madrid. D4.3 Complete Design Specification of 3 reference TROPOS systems [Online] Available: <http://www.troposplatform.eu/Deliverables-Media>
- [95] Homer. "Generating Synthetic Load Data." https://www.homerenergy.com/products/pro/docs/latest/generating_synthetic_load_data.html (accessed 01/09, 2021).
- [96] T. N. A. a. S. Administration. Power Data Access Viewer [Online] Available: <https://power.larc.nasa.gov/data-access-viewer/>
- [97] Homer. "Generating Synthetic Wind Data." https://www.homerenergy.com/products/pro/docs/latest/generating_synthetic_wind_data.html (accessed 31/08, 2021).
- [98] N. T. CURRENTS. "Annual Prediction Tables." https://tidesandcurrents.noaa.gov/noaacurrents/Annual?id=ACT0791_1 (accessed 31/8, 2021).
- [99] Homer. "Generating Synthetic Solar Data." https://www.homerenergy.com/products/pro/docs/latest/generating_synthetic_solar_data.html (accessed 31/08, 2021).
- [100] V. A. Graham and K. G. T. Hollands, "A method to generate synthetic hourly solar radiation globally," *Solar Energy*, vol. 44, no. 6, pp. 333-341, 1990, doi: 10.1016/0038-092x(90)90137-2.
- [101] U. P. d. Madrid. Deliverable 4.2 - Final Design Specification of base platform [Online] Available: [http://www.troposplatform.eu/Deliverables-Media/\(offset\)/5](http://www.troposplatform.eu/Deliverables-Media/(offset)/5)
- [102] U. P. d. Madrid. D3.3 Technical dossier for each of the established modules including key features [Online] Available: [http://www.troposplatform.eu/Deliverables-Media/\(offset\)/25](http://www.troposplatform.eu/Deliverables-Media/(offset)/25)
- [103] Matlab. Optimization Decision Table [Online] Available: <https://uk.mathworks.com/help/optim/ug/optimization-decision-table.html>
- [104] S. P. Engel, M. Stieneker, N. Soltan, S. Rabiee, H. Stagge, and R. W. D. Doncker, "Comparison of the Modular Multilevel DC Converter and the Dual-Active Bridge Converter for Power Conversion in HVDC and MVDC Grids," *IEEE Transactions on Power Electronics*, vol. 30, no. 1, pp. 124-137, 2015, doi: 10.1109/TPEL.2014.2310656.
- [105] R. J. G. Montoya, "High-Frequency Transformer Design for Solid-State Transformers in Electric Power Distribution Systems," 2015.

- [106] T. U. Government. "Electricity Generation Costs 2020." The UK Government https://assets.publishing.service.gov.uk/government/uploads/system/uploads/attachment_data/file/911817/electricity-generation-cost-report-2020.pdf (accessed 02 Feb, 2021).
- [107] M. Z. Hossain, N. A. Rahim, and J. A. L. Selvaraj, "Recent progress and development on power DC-DC converter topology, control, design and applications: A review," *Renewable and Sustainable Energy Reviews*, vol. 81, pp. 205-230, 2018, doi: 10.1016/j.rser.2017.07.017.
- [108] W. Chen, A. Q. Huang, C. Li, G. Wang, and W. Gu, "Analysis and Comparison of Medium Voltage High Power DC/DC Converters for Offshore Wind Energy Systems," *IEEE Transactions on Power Electronics*, vol. 28, no. 4, pp. 2014-2023, 2013-04-01 2013, doi: 10.1109/tpel.2012.2215054.
- [109] S. F. Tie and C. W. Tan, "A review of energy sources and energy management system in electric vehicles," *Renewable and Sustainable Energy Reviews*, vol. 20, pp. 82-102, 2013-04-01 2013, doi: 10.1016/j.rser.2012.11.077.
- [110] W. Li and X. He, "Review of Nonisolated High-Step-Up DC/DC Converters in Photovoltaic Grid-Connected Applications," *IEEE Transactions on Industrial Electronics*, vol. 58, no. 4, pp. 1239-1250, 2011-04-01 2011, doi: 10.1109/tie.2010.2049715.
- [111] R. w. Erickson and D. Maksimovic, *Fundamentals of Power Electronics*. Colorado: Springer, 2001.
- [112] X. Lu, J. M. Guerrero, K. Sun, J. C. Vasquez, R. Teodorescu, and L. Huang, "Hierarchical Control of Parallel AC-DC Converter Interfaces for Hybrid Microgrids," *IEEE Transactions on Smart Grid*, vol. 5, no. 2, pp. 683-692, 2014, doi: 10.1109/TSG.2013.2272327.
- [113] H. Xiao, A. Luo, Z. Shuai, G. Jin, and Y. Huang, "An Improved Control Method for Multiple Bidirectional Power Converters in Hybrid AC/DC Microgrid," *IEEE Transactions on Smart Grid*, vol. 7, no. 1, pp. 340-347, 2016, doi: 10.1109/TSG.2015.2469758.
- [114] S. Augustine, N. Lakshminarasamma, and M. K. Mishra, "Control of photovoltaic-based low-voltage dc microgrid system for power sharing with modified droop algorithm," *IET Power Electronics*, vol. 9, no. 6, pp. 1132-1143, 2016, doi: 10.1049/iet-pel.2015.0325.
- [115] X. Zhao, Y. W. Li, H. Tian, and X. Wu, "Energy Management Strategy of Multiple Supercapacitors in a DC Microgrid Using Adaptive Virtual Impedance," *IEEE Journal of Emerging and Selected Topics in Power Electronics*, vol. 4, no. 4, pp. 1174-1185, 2016, doi: 10.1109/JESTPE.2016.2601097.
- [116] J. M. Guerrero, J. C. Vasquez, J. Matas, L. G. d. Vicuna, and M. Castilla, "Hierarchical Control of Droop-Controlled AC and DC Microgrids—A General Approach Toward Standardization," *IEEE Transactions on Industrial Electronics*, vol. 58, no. 1, pp. 158-172, 2011, doi: 10.1109/TIE.2010.2066534.
- [117] L. Meng, T. Dragicevic, J. C. Vasquez, and J. M. Guerrero, "Tertiary and Secondary Control Levels for Efficiency Optimization and System Damping in Droop Controlled DC–DC Converters," *IEEE Transactions on Smart Grid*, vol. 6, no. 6, pp. 2615-2626, 2015, doi: 10.1109/TSG.2015.2435055.

- [118] V. Nasirian, A. Davoudi, F. L. Lewis, and J. M. Guerrero, "Distributed Adaptive Droop Control for DC Distribution Systems," *IEEE Transactions on Energy Conversion*, vol. 29, no. 4, pp. 944-956, 2014, doi: 10.1109/TEC.2014.2350458.
- [119] P. Wang, X. Lu, X. Yang, W. Wang, and D. Xu, "An Improved Distributed Secondary Control Method for DC Microgrids With Enhanced Dynamic Current Sharing Performance," *IEEE Transactions on Power Electronics*, vol. 31, no. 9, pp. 6658-6673, 2016, doi: 10.1109/TPEL.2015.2499310.
- [120] T. R. Oliveira, W. W. A. G. Silva, and P. F. Donoso-Garcia, "Distributed Secondary Level Control for Energy Storage Management in DC Microgrids," *IEEE Transactions on Smart Grid*, vol. 8, no. 6, pp. 2597-2607, 2017, doi: 10.1109/TSG.2016.2531503.
- [121] J. Xiao, P. Wang, and L. Setyawan, "Hierarchical Control of Hybrid Energy Storage System in DC Microgrids," *IEEE Transactions on Industrial Electronics*, vol. 62, no. 8, pp. 4915-4924, 2015, doi: 10.1109/TIE.2015.2400419.
- [122] L. Meng, T. Dragicevic, J. Vasquez, J. Guerrero, and E. R. Sanseverino, "Hierarchical control with virtual resistance optimization for efficiency enhancement and State-of-Charge balancing in DC microgrids," in *2015 IEEE First International Conference on DC Microgrids (ICDCM)*, 7-10 June 2015 2015, pp. 1-6, doi: 10.1109/ICDCM.2015.7152000.
- [123] Y. Ito, Y. Zhongqing, and H. Akagi, "DC microgrid based distribution power generation system," in *The 4th International Power Electronics and Motion Control Conference, 2004. IPEMC 2004.*, 14-16 Aug. 2004 2004, vol. 3, pp. 1740-1745 Vol.3.
- [124] P. Prabhakaran, Y. Goyal, and V. Agarwal, "Novel Nonlinear Droop Control Techniques to Overcome the Load Sharing and Voltage Regulation Issues in DC Microgrid," *IEEE Transactions on Power Electronics*, vol. 33, no. 5, pp. 4477-4487, 2018, doi: 10.1109/TPEL.2017.2723045.
- [125] Y. Xia, W. Wei, Y. Peng, P. Yang, and M. Yu, "Decentralized Coordination Control for Parallel Bidirectional Power Converters in a Grid-Connected DC Microgrid," *IEEE Transactions on Smart Grid*, vol. 9, no. 6, pp. 6850-6861, 2018, doi: 10.1109/TSG.2017.2725987.
- [126] P. Kou, D. Liang, and L. Gao, "Distributed Coordination of Multiple PMSGs in an Islanded DC Microgrid for Load Sharing," *IEEE Transactions on Energy Conversion*, vol. 32, no. 2, pp. 471-485, 2017, doi: 10.1109/TEC.2017.2649526.
- [127] J. Rajagopalan, K. Xing, Y. Guo, F. C. Lee, and B. Manners, "Modeling and dynamic analysis of paralleled DC/DC converters with master-slave current sharing control," in *Proceedings of Applied Power Electronics Conference. APEC '96*, 3-7 March 1996 1996, vol. 2, pp. 678-684 vol.2, doi: 10.1109/APEC.1996.500513.
- [128] W. Tsai-Fu, C. Yu-Kai, and H. Yong-Heh, "3C strategy for inverters in parallel operation achieving an equal current distribution," *IEEE Transactions on Industrial Electronics*, vol. 47, no. 2, pp. 273-281, 2000, doi: 10.1109/41.836342.
- [129] A. M. Roslan, K. H. Ahmed, S. J. Finney, and B. W. Williams, "Improved Instantaneous Average Current-Sharing Control Scheme for Parallel-

- Connected Inverter Considering Line Impedance Impact in Microgrid Networks," *IEEE TRANSACTIONS ON POWER ELECTRONICS*, vol. 26, no. 3, pp. 702-716, 2011.
- [130] K. Siri, C. Q. Lee, and T. Wu, "Current distribution control for parallel connected converters. II," *IEEE Transactions on Aerospace and Electronic Systems*, vol. 28, no. 3, pp. 841-851, 1992, doi: 10.1109/7.256304.
- [131] I. Batarseh, K. Siri, and H. Lee, "Investigation of the output droop characteristics of parallel-connected DC-DC converters," in *Proceedings of 1994 Power Electronics Specialist Conference - PESC'94*, 20-25 June 1994 1994, vol. 2, pp. 1342-1351 vol.2, doi: 10.1109/PESC.1994.373859.
- [132] T. Dragičević, X. Lu, J. C. Vasquez, and J. M. Guerrero, "DC Microgrids—Part I: A Review of Control Strategies and Stabilization Techniques," *IEEE TRANSACTIONS ON POWER ELECTRONICS*, vol. 3, no. 7, pp. 4876-4891, 2016.
- [133] X. Lu, J. M. Guerrero, K. Sun, and J. C. Vasquez, "An Improved Droop Control Method for DC Microgrids Based on Low Bandwidth Communication With DC Bus Voltage Restoration and Enhanced Current Sharing Accuracy," *IEEE TRANSACTIONS ON POWER ELECTRONICS*, vol. 29, no. 4, pp. 1800-1812, 2014.
- [134] S. Anand, B. G. Fernandes, and J. M. Guerrero, "Distributed Control to Ensure Proportional Load Sharing and Improve Voltage Regulation in Low-Voltage DC Microgrids," *IEEE TRANSACTIONS ON POWER ELECTRONICS*, vol. 28, no. 4, pp. 1900-1913, 2013.
- [135] P. Kou, D. Liang, S. Member, and L. Gao, "Distributed Coordination of Multiple PMSGs in an Islanded DC Microgrid for Load Sharing," *IEEE TRANSACTIONS ON ENERGY CONVERSION*, vol. 32, no. 2, pp. 471 - 485, 2107.
- [136] J. Rajagopalan, K. Xing, Y. Guo, F. C. Lee, and B. Manners, "Modelling and Dynamic Analysis of Paralleled dc/dc Converters with Master-Slave Current Sharing Control," in *Proceedings of Applied Power Electronics Conference. APEC '96*, 1996.
- [137] K. SIRI, C. Q. LEE, and E.-E. WU, "Current Distribution Control For Parallel Connected Converters: Part I," *IEEE Transactions on Aerospace and Electronic Systems*, vol. 28, no. 3, pp. 829-840, 1992.
- [138] P. Kou, I. Liang, and J. Wang, "Stable and Optimal Load Sharing of Multiple PMSGs in an Islanded DC Microgrid," *IEEE TRANSACTIONS ON ENERGY CONVERSION*, vol. 33, no. 1, pp. 260-271, 2018.
- [139] C. N. Papadimitriou, E. I. Zountouridou, and N. D. Hatziargyriou, "Review of hierarchical control in DC microgrids," *Electric Power Systems Research*, vol. 122, pp. 159-167, 2015, doi: 10.1016/j.epsr.2015.01.006.
- [140] T.-F. Wu, Y.-K. Chen, and Y.-H. Huang, "3C Strategy for Inverters in Parallel Operation Achieving an Equal Current Distribution," *IEEE TRANSACTIONS ON INDUSTRIAL ELECTRONICS*, vol. 47, no. 2, pp. 273-281, 2000.
- [141] K. SIRI, C. Q. LEE, and T.-F. WU, "Current Distribution Control For parallel Connected Converters: Part II," *IEEE Transactions on Aerospace and Electronic Systems*, vol. 28, no. 3, pp. 841-851, 1992.

- [142] I. Batarseh, K. Siri, and H. Lee, "Investigation of the output droop characteristics of parallel connected DC-DC converters," in *Proceedings of 1994 Power Electronics Specialist Conference - PESC'94*, Taipei, Taiwan, 1994.
- [143] C. Liu, J. Zhao, S. Wang, W. Lu, and K. Qu, "Active Identification Method for Line Resistance in DC Microgrid Based on Single Pulse Injection," *IEEE Transactions on Power Electronics*, vol. 33, no. 7, pp. 5561-5564, 2018, doi: 10.1109/TPEL.2017.2784565.
- [144] S. Augustine, M. K. Mishra, and N. Lakshminarasamma, "Circulating Current Minimization and Current Sharing Control of Parallel Boost Converters Based on Droop Index," in *2013 9th IEEE International Symposium on Diagnostics for Electric Machines, Power Electronics and Drives (SDEMPED)*, Valencia, Spain, 2013.
- [145] P. Kou, D. Liang, J. Wang, and L. Gao, "Stable and Optimal Load Sharing of Multiple PMSGs in an Islanded DC Microgrid," *IEEE Transactions on Energy Conversion*, vol. 33, no. 1, pp. 260-271, 2018, doi: 10.1109/TEC.2017.2755461.
- [146] M. Zolfaghari, S. H. Hosseinian, S. H. Fathi, M. Abedi, and G. B. Gharehpetian, "A New Power Management Scheme for Parallel-Connected PV Systems in Microgrids," *IEEE Transactions on Sustainable Energy*, vol. 9, no. 4, pp. 1605-1617, 2018, doi: 10.1109/TSTE.2018.2799972.
- [147] S. Tolani and P. Sensarma, "Extended Bandwidth Instantaneous Current Sharing Scheme for Parallel UPS Systems," *IEEE Transactions on Power Electronics*, vol. 32, no. 6, pp. 4960-4969, 2017, doi: 10.1109/TPEL.2016.2604251.
- [148] Y. Zhang, M. Yu, F. Liu, and Y. Kang, "Instantaneous Current-Sharing Control Strategy for Parallel Operation of UPS Modules Using Virtual Impedance," *IEEE Transactions on Power Electronics*, vol. 28, no. 1, pp. 432-440, 2013, doi: 10.1109/TPEL.2012.2200108.
- [149] S. Xiao, L. Yim-Shu, and X. Dehong, "Modeling, analysis, and implementation of parallel multi-inverter systems with instantaneous average-current-sharing scheme," *IEEE Transactions on Power Electronics*, vol. 18, no. 3, pp. 844-856, 2003, doi: 10.1109/TPEL.2003.810867.
- [150] M. French, "Fundamentals of Optimization". West Lafayette, USA: : Springer 2018.
- [151] R. D. Middlebrook, "Small-signal modeling of pulse-width modulated switched-mode power converters," *Proceedings of the IEEE*, vol. 76, no. 4, pp. 343-354, 1988, doi: 10.1109/5.4421.
- [152] R. w. Erickson and D. Maksimovic, *Fundamental of Power Electronics*. Colorado: Springer, 2001.
- [153] X. He, H. Ji, Y. Song, G. Song, H. Cai, and Y. Mi, "Voltage stability control for DC microgrid with energy storage," in *2017 IEEE Conference on Energy Internet and Energy System Integration (EI2)*, 26-28 Nov. 2017 2017, pp. 1-6, doi: 10.1109/EI2.2017.8245761.
- [154] D. Wu, F. Tang, T. Dragicevic, J. M. Guerrero, and J. C. Vasquez, "Coordinated Control Based on Bus-Signaling and Virtual Inertia for Islanded DC Microgrids," *IEEE Transactions on Smart Grid*, vol. 6, no. 6, pp. 2627-2638, 2015, doi: 10.1109/TSG.2014.2387357.

- [155] D. Fujin, "Design and Control of A DC Grid for Offshore Wind Farms," Aalborg University, Aalborg, 2012.
- [156] M. Davari and Y. A. I. Mohamed, "Robust DC-Link Voltage Control of a Full-Scale PMSG Wind Turbine for Effective Integration in DC Grids," *IEEE Transactions on Power Electronics*, vol. 32, no. 5, pp. 4021-4035, 2017, doi: 10.1109/TPEL.2016.2586119.
- [157] V. Yaramasu and B. Wu, *Model Predictive Control of Wind Energy Conversion Systems*. John Wiley & Sons, 2016.
- [158] M. Nasiri, J. Milimonfared, and S. H. Fathi, "Modeling, analysis and comparison of TSR and OTC methods for MPPT and power smoothing in permanent magnet synchronous generator-based wind turbines," *Energy Conversion and Management*, vol. 86, pp. 892-900, 2014/10/01/ 2014, doi: <https://doi.org/10.1016/j.enconman.2014.06.055>.
- [159] O. Tremblay, L. Dessaint, and A. Dekkiche, "A Generic Battery Model for the Dynamic Simulation of Hybrid Electric Vehicles," in *2007 IEEE Vehicle Power and Propulsion Conference*, 9-12 Sept. 2007 2007, pp. 284-289, doi: 10.1109/VPPC.2007.4544139.
- [160] Vestas. "Vestas V112-3.3." <https://en.wind-turbine-models.com/turbines/693-vestas-v112-3.3> (accessed 30/09, 2021).
- [161] S. T. P. Ltd. "Scotrenewables - Model SR 2000 - Tidal Turbine." <https://www.energy-xprt.com/products/scotrenewables-model-sr-2000-tidal-turbine-555757> (accessed 30/09, 2021).

Appendices

Appendix A The Ocean of Tomorrow Projects

Table A1. Ocean of tomorrow and Horizon 2020 projects.

Project: The Ocean of Tomorrow	European Union Fund	Status
FP7-Ocean-2010		
Arctic Climate Change Economy and Society	€10,978,468	Done
Vector of Change in Oceans and Seas Marine Life	€12,484,835	Done
Sub-seabed CO2 Storage: Impact on Marine Ecosystems	€10,500,000	Done
FP7-Ocean-2011		
Development of a Wind-Wave Power Open-Sea Platform	€4,525,934	Done
Innovative Multi-Purpose Offshore Platforms: Planning, Design and Operation	€5,483,411	Done
Modular Multi-use Deep Water Offshore platform	€4,877,911	Done
Marine Microbial Biodiversity, Bioinformatics and Biotechnology	€8,987,491	Done
FP7-OCEAN-2012		
Priority Environmental Contaminants in Seafood: Safety Assessment, Impact and Public Perception	€3,999,874	Done
Integrated Biotechnological Solutions for Combating Marine Oil Spills	€8,996,599	Done
Suppression of underwater Noise Induced by Cavitation	€2,999,972	Done
Science and Technology Advancing Governance on Good Environmental Status	€999,733	Done
FP7-OCEAN-2013		
Marine Environmental In-Situ Assessment and Monitoring Tool	€5,434,221	Done
Real-Time Monitoring of SEA Contaminants by an Autonomous Lab-On-A-Chip Biosensor	€5,751,459	Done
Sensing Toxicants In Marine Waters Makes Sense Using Biosensors	€4,144,263	Done
Marine Sensors for the 21st Century	€5,924,945	Done
Low-Toxic, Cost-Efficient, Environment-Friendly Antifouling Materials	€7,447,584	Done
Synergistic Fouling Control Technologies	€7,995,161	Done
Logistic Efficiencies and Naval architecture for Wind Installations with Novel Developments	€9,986,231	Done
Project: Horizon 2020		
United Multi-use Offshore Platforms Demonstrators for Boosting Cost-Effective and Eco-Friendly Production in Sustainable Marine Activities	€11,399,118	End 2023
Lean Innovative Connected Vessels	€7,808,691	Done

Appendices

Functional Platform for Open Sea Farm Installations of the Blue Growth Industry	€9,854,077	End 2021
Multi-use in European Seas	€1,987,603	Done
Multiple-Uses of Space for Island Clean Autonomy	€9,834,521	End 2024
Multi-use Affordable Standardized Floating Space@Sea	€7,629,927	End 2020
Marine Investment for the Blue Economy	€1,977,951	Done

Appendix B Energy Systems Datasheets, Converters Costs and Matlab Codes of Chapter 3

Table B1. Specifications of wind turbine model V112-3.3 from Vestas [160]

Turbine specs	Data	Turbine specs	Data
Rated power:	3,200.0 kW	Power density 1:	335.0 W/m ²
Cut-in wind speed:	3.0 m/s	Power density 2:	3.0 m ² /kW
Rated wind speed:	13.0 m/s	Generator	
Cut-out wind speed:	25.0 m/s	Number:	1.0
Wind class (IEC):	Ib	Grid frequency:	50/60 Hz
Rotor data		Tower	
Diameter:	112 m	Hub height:	84/94/119/140 m
Swept area:	9,852 m ²	Type:	Steel tube
Number of blades:	3	Shape:	conical
Type:	54.7	Corrosion	painted
Material:	GFRP	Manufacturer:	Welcon

Table B2. Specifications of tidal turbine model SR 2000 from Scotrenewables [161]

Technical Specs.	Data
Rated power (1000 +1000 kW)	2000kW
Rated current speed	3 m/s
Cut-in current speed	1 m/s
Cut-out current speed	4.5 m/s
Maximum rotor speed	16 rpm
Rotor and blades	
Rotor diameter	16 m
Swept area	2 x 201 m ²
Electrical	
Power regulation	Variable speed with fixed pitch blades
Output voltage	6.6 kV / 11kV
Output frequency	50 Hz

Table B3. Solar panel specifications

Electrical data	Model: CS6X-310P	
	at STC	at NOTC
Nominal maximum power	310W	225W
Optimum operating voltage	36.4V	33.2V
Optimum operating current	8.52A	6.77
Open circuit voltage	44.9V	41.3V
Short circuit current	9.08A	7.36A
Module efficiency	16.16%	
Operating temperature	-40 to +85 °C	
Power tolerance	0 to 5W	

Standard Test Condition (STC) at (irradiance = 1000W/m² and cell temperature 25 °C)

Normal operating cell Temperature (NOCT) at (irradiance = 800W/m² and cell temperature 20 °C)

Table B4. Battery module specifications

Battery specs		Specs. for 8-cell module
Nominal capacity		50Ah
Nominal energy		1.48kWh
Nominal voltage		29.6V
Maximum current	Continuous	100A (25°C)
	Instant	300AX10sec. (25°C)
Operational temperature (charge)		0°C ~ 50°C
Operational temperature (discharge)		-20°C ~ 50°C
Weight		Approx. 15Kg
Size (W X D X H)		379mm x 137mm x 230mm

Table B5. Costs of semiconductor and magnetic devices for nine scenarios of DC-DC conversion system connected to a 3.2 MW wind turbine

No. of parallel converters	Converter size (kW)	Area product A_p (m ⁴)	Costs of magnetic devices (\$)	Switching current per a converter	Available switching current in the market	Installed switching power (kVA)	Total installed switching power (KVA) per scenario	Costs of semiconductors (\$)	Total costs per scerrio (\$)
1	3200	0.0097	11,913	2666.7	2800	3360	3360	12734.4	24647.6
2	1600	0.0039	14,754	1333.3	1400	1680	3360	12734.4	27488.5
3	1067	0.0023	18,377	888.9	900	1080	3240	12279.6	30656.8
4	800	0.0015	22,000	666.7	675	810	3240	12279.6	34279.8
5	640	0.0011	25,936	533.3	550	660	3300	12507	38443.0
6	533	8.98E-04	30,177	444.4	450	540	3240	12279.6	42456.7
7	457	7.34E-04	34,308	381.0	400	480	3360	12734.4	47042.0
8	400	6.09E-04	38,423	333.3	340	408	3264	12370.56	50793.5
9	356	5.22E-04	42,614	296.3	300	360	3240	12279.6	54893.4

Table B6. Costs of semiconductor and magnetic devices for 15 proposed scenarios of DC-DC conversion system connected to a 1 MW tidal turbine

No. of parallel converters	Converter size (kW)	Area product A_p (m4)	Costs of magnetic devices (\$)	Switching current per a converter	Available switching current in the market	Installed switching power (kVA)	Total installed switching power (KVA) per scenario	Cost for semiconductors (\$)	Total cost (\$)
1	1000	0.0021	5,969	833.3	840	1008	1008	3820.32	9789.6
2	500	8.21E-04	9,938	416.7	420	504	1008	3820.32	13758.5
3	333	4.83E-04	14,114	277.8	280	336	1008	3820.32	17934.3
4	250	3.28E-04	18,335	208.3	220	264	1056	4002.24	22337.3
5	200	2.42E-04	22,579	166.7	170	204	1020	3865.8	26444.7
6	167	1.93E-04	26,868	138.9	140	168	1008	3820.32	30688.3
7	143	1.55E-04	31,134	119.0	120	144	1008	3820.32	34954.8
8	125	1.35E-04	35,461	104.2	105	126	1008	3820.32	39281.7
9	111	1.16E-04	39,758	92.6	95	114	1026	3888.54	43646.6
10	100	9.66E-05	44,025	83.3	84	100.8	1008	3820.32	47844.8
11	91	8.69E-05	48,344	75.8	76	91.2	1003.2	3802.128	52146.0
12	83	7.73E-05	52,648	69.4	70	84	1008	3820.32	56468.4
13	77	6.76E-05	56,937	64.1	65	78	1014	3843.06	60780.3
14	71	6.76E-05	61,317	59.5	60	72	1008	3820.32	65137.3
15	67	5.80E-05	65,583	55.6	57	68.4	1026	3888.54	69472.0

B1. LPSP evaluation using Matlab/m-file as per Figure 3.10 in Chapter 3

```

function [ LPSP, Cost]= LPSPCalculation(A)
Pload = xlsread('load1.xlsx'); % Importing Load
A=[ Apv Aw At Ab]; % A= Design variables vector

                                %%%%% Solar energy data %%%%%%
%Ppv (t) = Apv * module eff. * 1m2 * G(t) *[ 1-0.0045(Tc(t)-25)]
% Ppv = Ppv (t) = Energy production from solar farm at hour t
% Apv = total area of solar farm (Variable)
% modeff = module efficiency = 0.1616
% 1m2 = one meter squared area of solar module
% G = G(t)= insolation on a horizontal module at hour t
% Tc = Tc(t)= cell temperature at hour t
Apv = A(1);
modeff = 0.1616;
filename= 'solar.xlsx';
G = xlsread(filename,'C02:C8761');
filename1 = 'cell_temp.xlsx' ;
Tc= xlsread(filename1,'J02:J8761');
Ppv = zeros(8760,1);

                                % Calculation of wind production WITHOUT considering cut in and cut out speeds %
% Vciw = cut in speed of wind turbine in m/s
% Vcow = cut out speed of wind turbine in m/s
% Vrw = rated speed of wind turbine in m/s
% Cp = power coefficient = 0.4 to 0.5
% Rohw = Air density = 1.22
% Aw = the total swept area of all turbines (variable)
Pwin= zeros(8760,1); % define or declare the size of this vector column to speed up the execution process
Vciw = 3;
Vcow = 25;
Vrw = 12;
Cp = .45;
Rohw = 1.22;
Aw = A(2);
filename2= 'wind.xlsx'; % read wind data

```

Appendices

```
Win_data = xlsread(filename2,'C02:C8761');
```

```
Pr1 = 0.5 * Cp * Roh1 * Aw * Vr1^3 * 0.001; %0.001 is a factor to convert the unit to kW
```

% Calculation of tidal production WITHOUT considering cut in and cut out speeds %

```
% Vcit = cut in speed of tidal turbine in m/s.
```

```
% Vcot = cut out speed of tidal turbine in m/s.
```

```
% Vrt = rated speed of tidal turbine in m/s.
```

```
%Cp = power coefficient = .4 to .5.
```

```
% Roht = sea water density = 1029 kg/m3.
```

```
% At = is the total swept area of all turbines (Variable)
```

```
Vcit = 1;
```

```
Vcot = 4.5;
```

```
Vrt = 3;
```

```
Cp = .45;
```

```
Roht = 1029;
```

```
At = A(3);
```

```
filename3= 'tidal.xlsx'; % read tidal data
```

```
Tid_data = xlsread(filename3,'C02:C8761');
```

```
Ptid= zeros(8760,1); % define or declare the size of this vector column to speed up the execution process
```

```
Pr2 = 0.5 * Cp * Roh2 * At * Vr2^3 * 0.001; %0.001 is a factor to convert the unit to kW
```

% Calculation of wind/tidal production WITH considering cut in and cut out speeds %

```
SOCmax = 100; % provided by the manufacturer %
```

```
DODmax = 70; % provided by the manufacturer %
```

```
Eff.ch = 1 ; % charging efficiency of battery. It is provided by the manufacturer, 1 here means 100%
```

```
Step_time = 1; % simulation step time which equals 1 hour
```

```
SOC = zeros(8760,1); %define or declare the size of this vector column to speed up the execution
```

```
DOD = zeros(8760,1);
```

```
SOC(1,1) = 100; % initial condition for the state of charge of the battery in a percentage % .
```

```
DOD(1,1) = 0; % initial condition for the depth of discharge of the battery in a percentage % .
```

```
    % where SOC + DOD = 100%
```

```
Cb = zeros(8760,1);
```

```
Cb (1,1) = A(4); %initial charge in the battery.
```

```
Cbmin = 0.3*A(4); % minimum energy level of the battery.
```

```
Pdeficit = zeros(8761,1); %define or declare the size of this vector column to speed up the execution
```

```
Pgen = zeros(8760,1);
```

```
DOD = zeros(8760,1);
```

Appendices

```
Pdump = zeros(8760,1);
```

```
for t = 1:8760
```

```
    % Solar Calculation
```

```
    Ppv(t,1) = A(1) * modeff * 1 * G(t,1) * (1-0.0045*(Tc(t,1) - 25));
```

```
    % Wind Calculation
```

```
    if Win_data(t,1) >= Vciw && Win_data(t,1) < Vrw
```

```
        Pwin(t,1) = Pr1 * ((Win_data(t,1)^3 - Vciw^3) / (Vrw^3 - Vciw^3));
```

```
    elseif Win_data(t,1) >= Vrw && Win_data(t,1) < Vcow
```

```
        Pwin(t,1) = Prw;
```

```
    elseif Win_data(t,1) >= Vcow
```

```
        Pwin(t,1) = 0;
```

```
    else
```

```
        Win_data(t,1) <= Vciw;
```

```
        Pwin(t,1) = 0;
```

```
    end
```

```
    % Tidal Calculation
```

```
    if Tid_data(t,1) >= Vcit && Tid_data(t,1) < Vrt
```

```
        Ptid(t,1) = 0.5 * Cp * Roht * A(3) * Tid_data(t,1)^3 * 0.001; %0.001 is a factor to convert the unit to kW
```

```
    elseif Tid_data(t,1) >= Vrt && Tid_data(t,1) < Vcot
```

```
        Ptid(t,1) = Prt;
```

```
    elseif Tid_data(t,1) >= Vcot
```

```
        Ptid(t,1) = 0;
```

```
    else
```

```
        Tid_data(t,1) >= 0 && Tid_data(t,1) <= Vcit;
```

```
        Ptid(t,1) = 0;
```

```
    end
```

% LPSP Evaluation %

```
Pgen(t,1) = Ppv(t,1) + Pwin(t,1) + Ptid(t,1);
```

```
    %charging cycle
```

```
if Pgen(t,1) > Pload(t,1) && SOC(t-1,1) <= SOCmax && (Pgen(t,1) - Pload(t,1)) < (Cb(1,1) - Cb(t-1,1)) % where (Cb(1,1) - Cb(t-1,1)), is the empty portion of the battery to be charged
```

```
    SOC(t,1) = SOC(t-1,1) + 100 * (Pgen(t,1) - Pload(t,1)) * Eff.ch * Step_time / (1 * A(4)); % charge the battery with surplus energy
```

```
    Pdeficit(t,1) = 0;
```

```
    Cb(t,1) = SOC(t,1) * A(4) / 100;
```

Appendices

```
DOD(t,1)= DOD(t-1,1)+(SOC(t-1,1)-SOC(t,1));  
end  
if Pgen(t,1) > Pload(t,1) && SOC(t-1,1)<=SOCmax && (Pgen(t,1)- Pload(t,1))> (Cb(1,1)-Cb(t-1,1))  
% (Cb(1,1)-Cb(t-1,1)), is the empty portion of the battery to be charged  
SOC(t,1)= SOC(t-1,1)+100*((Cb(1,1)-Cb(t-1,1)))* Eff.ch*Step_time/(1*A(4));  
Pdeficit (t,1) = 0;  
Pdump(t,1)= Pgen(t)- Pload(t,1)-(Cb(1,1)-Cb(t-1,1));  
Cb(t,1) = SOC(t,1)*A(4)/100;  
DOD(t,1)= DOD(t-1,1)+(SOC(t-1,1)-SOC(t,1));
```

end

```
if Pgen(t,1) > Pload(t,1) && SOC(t-1,1)== SOCmax  
Pdump(t,1)= Pgen(t)- Pload(t,1);  
Pdeficit (t,1) = 0;  
SOC(t,1)= SOCmax;  
Cb(t,1) = SOC(t,1)*A(4)/100;  
DOD(t,1)= DOD(t-1,1)+(SOC(t-1,1)-SOC(t,1));
```

end

%discharging cycle

```
if Pgen(t,1) < Pload(t,1) && DOD(t-1,1)< DODmax && (Pload(t,1) - Pgen(t,1))< (Cb(t-1,1)- Cbmin) % where  
(Cb(t-1,1)- Cbmin), the available energy in the battery.  
SOC(t,1)= SOC(t-1,1)-100*((Pload(t,1)-Pgen(t,1))*(Step_time/(1*A(4))));  
Pdeficit (t,1) = 0;  
Cb(t,1) = SOC(t,1)*A(4)/100;  
DOD(t,1)= DOD(t-1,1)+(SOC(t-1,1)-SOC(t,1));
```

end

```
if Pgen(t,1) < Pload(t,1) && DOD(t-1,1)< DODmax && (Pload(t,1) - Pgen(t,1))> (Cb(t-1,1)- Cbmin) % where  
(Cb(t-1,1)- Cbmin), the available energy in the battery.  
SOC(t,1)= SOC(t-1,1)-100*((Cb(t-1,1)- Cbmin)*(Step_time/(1*A(4))));  
Pdeficit (t,1) = Pload(t,1) - Pgen(t,1) - (Cb(t-1,1)- Cbmin);  
Cb(t,1) = SOC(t,1)*A(4)/100;  
DOD(t,1)= DOD(t-1,1)+(SOC(t-1,1)-SOC(t,1));
```

end

```
if Pgen(t,1) < Pload(t,1) && DOD(t-1,1)== DODmax  
SOC(t,1)= SOCmax-DODmax;  
Pdeficit (t,1) = Pload(t,1) - Pgen(t,1) ;  
Cb(t,1) = SOC(t,1)*A(4)/100;  
DOD(t,1)= DOD(t-1,1)+(SOC(t-1,1)-SOC(t,1));
```

Appendices

```
end
if SOC(t,1)<=0
    SOC(t,1)=30;
elseif SOC(t,1)>100
    SOC(t,1)=100;
end
% estimation of the deficit power Pdef
if Pload(t,1)>Pgen(t,1)+Cb(t,1)
Pdef1(t,1)= Pload(t,1)-(Pgen(t,1)+Cb(t,1));
else
    Pdef1(t,1)= 0;
end
end
LPSP(q)=sum(Pdef1)/sum(Pload);
Cost(q)= 226.5*A(1)+1417.7*A(2)+27612*A(3)+520*A(4);
end
```

% Optimisation results verification using Matlab tool (Linprog) %

% Lower bounds

```
lb=zeros(4,1);
lb(1)=0;
lb(2)=0;
lb(3)=0;
lb(4)=0;
```

% Upper bounds

```
ub(1)=8000;
ub(2)=75000;
ub(3)=2000;
ub(4)=2000;
```

%Linear inequality

```
A=zeros(8760,4);
A(1:8760,1)=-Ppv/U(1); % power available from 1 m2 of solar installed capacity
A(1:8760,2)=-Pwin/U(2); %power available from 1 m2 of wind installed capacity
A(1:8760,3)=-Ptid/U(3); % power available from 1 m2 of tidal installed capacity
A(1:8760,4)=-Cb/U(4); % power Avialble from 1kWh of battery installed capacity
```

```

b=zeros(8760,1);
b=0-Pload;

%Linear equality
Aeq=zeros(1,4);
beq=zeros(1,1);

%Objective
f=zeros(4,1);
f(1)=226.5; f(2)=1417.7; f(3)=27612; f(4)=520;
% optimal solution
x = linprog(f,A,b)

```

B2. Matlab/m-file to obtain the cost-efficiency curve of a wind turbine as per Figure 3.13 in Chapter 3

```

Vciw = 3;
Vcow = 25;
Vrw = 13;
Cp = .45;
Rohw = 1.22;
filename2= 'wind.xlsx'; % read wind data
Win_data = xlsread(filename2,'C02:C8761');
Pr1 = 0.5 * Cp * Roh1 * 9852 * Vr1^3 * 0.001; %swept area for one wind turbine=9852 m2

% Wind energy calculation
for t= 1:8760
    if Win_data(t,1) >= Vciw && Win_data(t,1) < Vrw
        Pwin(t,1) = Prw*(( Win_data(t,1)^3- Vciw^3)/(Vrw^3-Vciw^3));
    elseif Win_data(t,1) >= Vrw && Win_data(t,1) < Vcow
        Pwin (t,1) = Prw;
    elseif Win_data(t,1) >= Vcow
        Pwin(t,1) = 0;
    else
        Win_data(t,1) <= Vciw;
        Pwin(t,1) = 0;
    end
end

```

```

end
end
for n=1:9;
for t= 1:8760
    Pr(t,1)=Prw;
    if (Pwin(t,1)/Pr(t,1))*100*n>10 && (Pwin(t,1)/Pr(t,1))*100*n<20
        eff(t,1)= 2.86*(Pwin(t,1)/Pr(t,1))*100+16.8;
    elseif (Pwin(t,1)/Pr(t,1))*100*n>20 && (Pwin(t,1)/Pr(t,1))*100*n<30
        eff(t,1)= 1.214*(Pwin(t,1)/Pr(t,1))*100+49.8;
    elseif (Pwin(t,1)/Pr(t,1))*100*n>30 && (Pwin(t,1)/Pr(t,1))*100*n<40
        eff(t,1)= 0.47*(Pwin(t,1)/Pr(t,1))*100+72.11;
    elseif (Pwin(t,1)/Pr(t,1))*100*n>40 && (Pwin(t,1)/Pr(t,1))*100*n<50
        eff(t,1)= 0.343*(Pwin(t,1)/Pr(t,1))*100+77.2;
    elseif (Pwin(t,1)/Pr(t,1))*100*n>50 && (Pwin(t,1)/Pr(t,1))*100*n<70
        eff(t,1)= 0.111*(Pwin(t,1)/Pr(t,1))*100+88.79;
    elseif (Pwin(t,1)/Pr(t,1))*100*n>70 && (Pwin(t,1)/Pr(t,1))*100*n<=100
        eff(t,1)= 0.043*(Pwin(t,1)/Pr(t,1))*100+93.6;
    end
end
end
eff_mean(n,1)=mean(eff);
end

Con_cost=[24647.6 27488.5 30656.8 34279.8 38443.0 42456.7 47042.0 50793.5 54893.4]; % these
data from excel spreadsheet
figure;
yyaxis right
plot(eff_mean);
yyaxis left
plot(Con_cost);
grid on

```

B3. Matlab/m-file to obtain the cost-efficiency curve of a tidal turbine as per

Figure 3.14 in Chapter 3

```

clear all
Vcit = 1;
Vcot = 4.5;

```

Appendices

```
Vrt = 3;
Cp = .45;
Roht = 1029;
filename2= 'tidal.xlsx'; % read tidal data
Tid_data = xlsread(filename2,'C02:C8761');

% Tidal energy calculation
Prt = 0.5 * Cp * Roht * 401 * Vrt^3 * 0.001; %0.001 is a factor to convert the unit to kW
for t= 1:8760
    if Tid_data(t,1) >= Vcit && Tid_data(t,1) < Vrt
        Ptid(t,1) = 0.5 * Cp * Roht * 401 * Tid_data(t,1)^3 * 0.001; %0.001 is a factor to convert the unit
to kW
    elseif Tid_data(t,1) >= Vrt && Tid_data(t,1) < Vcot
        Ptid (t,1) = Prt;
    elseif Tid_data(t,1) >= Vcot
        Ptid(t,1) = 0;
    else
        Tid_data(t,1) >= 0 && Tid_data(t,1) <= Vci2;
        Ptid(t,1) = 0;
    end
end
for n=1:20;
for t= 1:8760
    Pr(t,1)=Prt;
    if (Ptid(t,1)/Pr(t,1))*100*n>10 && (Ptid(t,1)/Pr(t,1))*100*n<20
        eff(t,1)= 2.86*(Ptid(t,1)/Pr(t,1))*100+16.8;
    elseif (Ptid(t,1)/Pr(t,1))*100*n>20 && (Ptid(t,1)/Pr(t,1))*100*n<30
        eff(t,1)= 1.214*(Ptid(t,1)/Pr(t,1))*100+49.8;
    elseif (Ptid(t,1)/Pr(t,1))*100*n>30 && (Ptid(t,1)/Pr(t,1))*100*n<40
        eff(t,1)= 0.47*(Ptid(t,1)/Pr(t,1))*100+72.11;
    elseif (Ptid(t,1)/Pr(t,1))*100*n>40 && (Ptid(t,1)/Pr(t,1))*100*n<50
        eff(t,1)= 0.343*(Ptid(t,1)/Pr(t,1))*100+77.2;
    elseif (Ptid(t,1)/Pr(t,1))*100*n>50 && (Ptid(t,1)/Pr(t,1))*100*n<70
        eff(t,1)= 0.111*(Ptid(t,1)/Pr(t,1))*100+88.79;
    elseif (Ptid(t,1)/Pr(t,1))*100*n>70 && (Ptid(t,1)/Pr(t,1))*100*n<=100
        eff(t,1)= 0.043*(Ptid(t,1)/Pr(t,1))*100+93.6;
    end
end
```

Appendices

end

```
eff_mean(n,1)=mean(eff);
```

end

```
Con_cost=[9789.6 13758.5 17934.3 22337.3 26444.7 30688.3 34954.8 39281.7 43646.6 47844.8  
52146.0 56468.4 60780.3 65137.3 69472.0]; % these data from excel spreadsheet
```

Figure;

```
yyaxis right
```

```
plot(eff_mean);
```

```
yyaxis left
```

```
plot(Con_cost);
```

```
grid on
```

Appendix C System simulation figures and parameters of Chapter 6

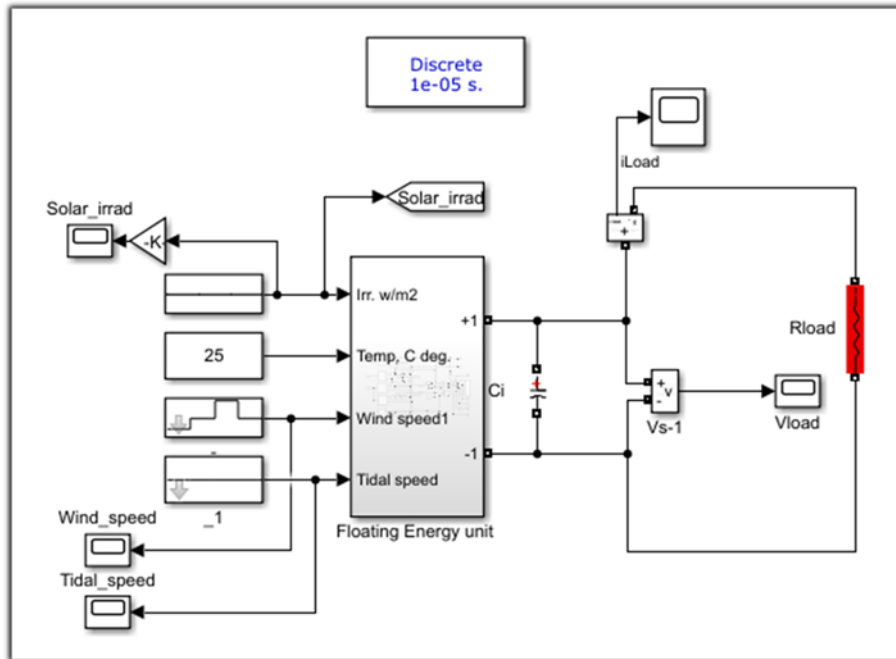


Figure C1. Single floating energy unit comprises wind, tidal and solar energy resources in one Simulink block.

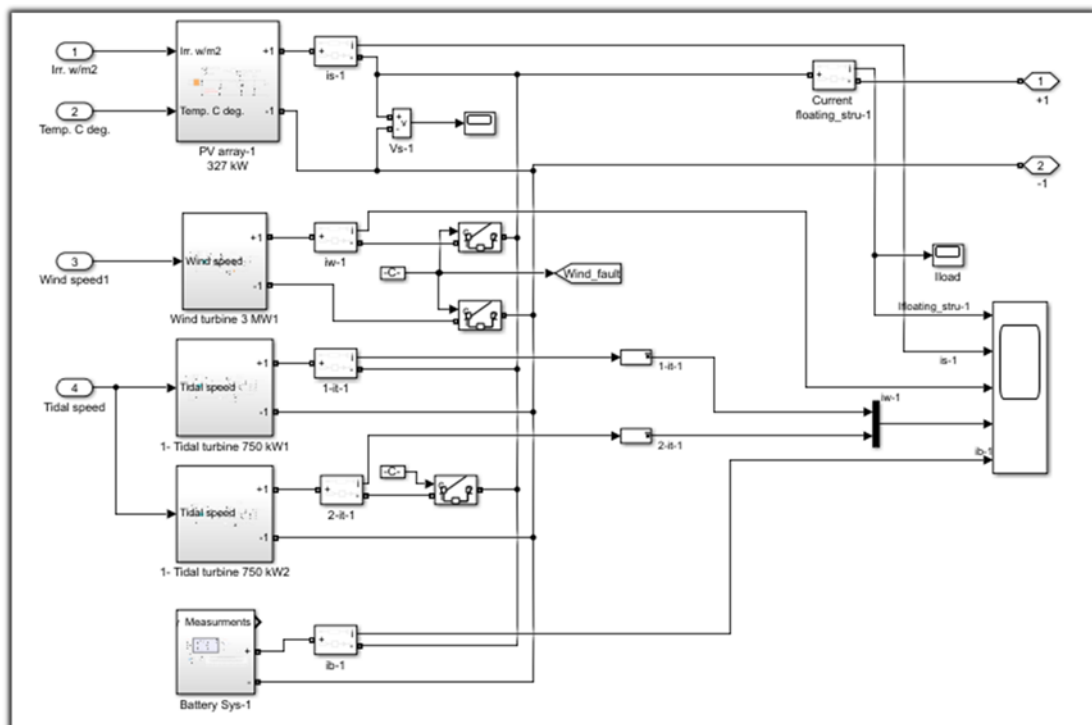


Figure C2. Single floating energy unit comprises wind, tidal and solar energy resources in blocks.

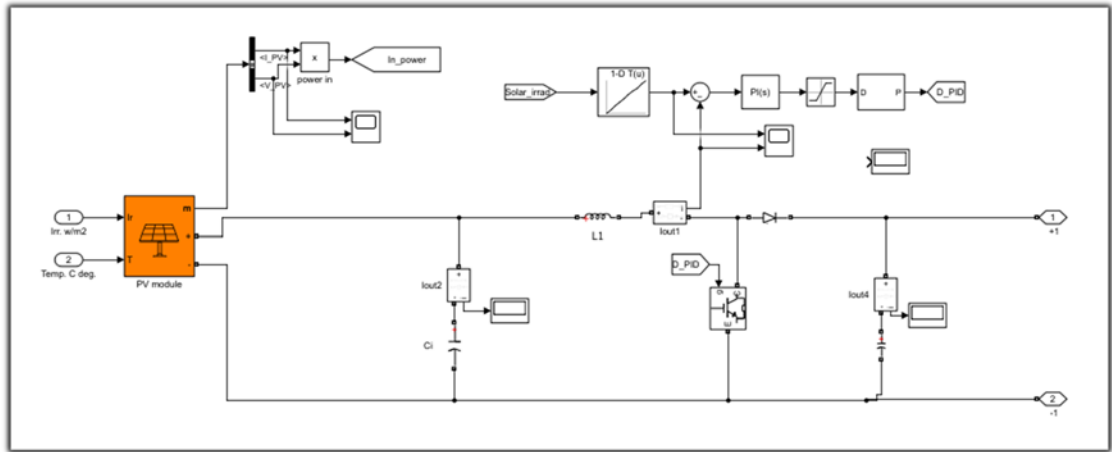


Figure C3. Solar array with boost converter.

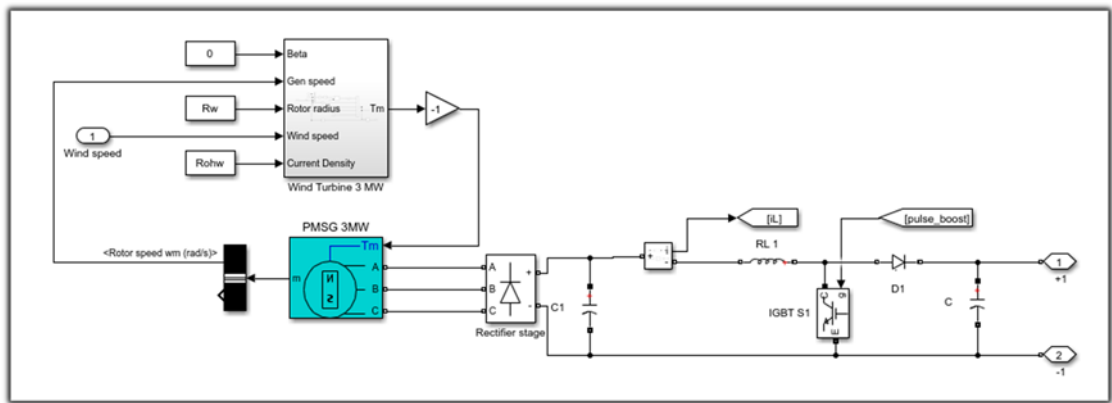


Figure C4. Wind/tidal turbine with PMSG and boost converter.

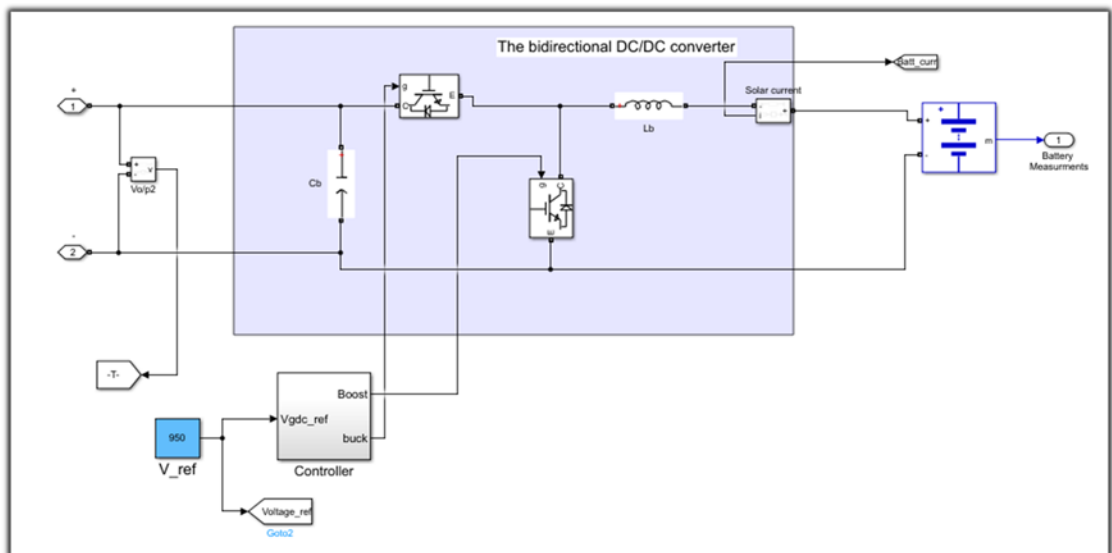


Figure C5. Battery system with bidirectional DC-DC converter.

Table C1. Parameters list of wind and tidal Turbines

Description	Wind turbine	Tidal turbine
Turbine parameters		
Rated power (kW)	3000	750
Rotor radius (m)	51	7.025
Air density/ Water density (kg/m ²)	1.225	1025
Rated wind/current speed (m/s)	12	3
Cut-in wind/current speed (m/s)	3	
Cut-out wind/current speed (m/s)	25	
PMSG parameters		
Generator pole pairs	26	26
Shaft moment of inertia (kg.m ²)	466e3	117e3
Viscous friction (N.m.s)	0.001189	0.001189
Stator phase resistance R_s (Ω)	1.63e-3	6.52e-3
Direct stator inductance (H)	0.94e-3	3.74e-3
Quadrature stator inductance (H)	1.47e-3	5.88e-3
Flux linkage (V.s)	8.295	8.295
Boost converter parameters		
Input boost inductor, L_w, L_T (H)	1.7e-3	1.2e-3
Output boost capacitor, C_w, C_T (F)	24.5e-6	3e-3
Switching frequency f_s^w, f_s^T (Hz)	50e3	50e3
Controller parameters		
Speed controller proportional gain, k_s^w, k_s^T	2000	2000
Speed controller integral gain, T_s^w, T_s^T	500	500
Current controller proportional gain, k_c^w, k_c^T	2000	2000
Current controller integral gain, T_c^w, T_c^T	50	50

Table C2. Parameters list of a solar PV module and array

Description	Solar system
Solar module (CS6X-310P)	
Nominal max. power (W)	310
Operating voltage at MPP (V)	36.4
Operating current at MPP (A)	8.52
Open circuit voltage (V)	44.9
Short circuit current (A)	9.08
Module efficiency (%)	16.16
Operating temperature (°C)	-40 to 85
Shunt resistance, R_p^{PV} (Ω)	333.67
Series resistance, R_s^{PV} (Ω)	0.35
Number of cells per module, M_s	72
Diode ideality factor, a	1.0114
The temperature of the p-n junction, T^{PV} (°C)	25
Solar array size	
Number of series connected modules per string, N_s	17
Number of parallel strings per array, N_p	62
Boost converter parameters	
Input boost inductor, L_{PV} (H)	6e-3
Output boost capacitor, C_{PV} (F)	1e-4
Switching frequency f_s^{PV} (Hz)	50e3

Table C3. Parameters list of a bi-directional buck-boost converter

Description	Solar system
Bi-directional converter	
Steady state input voltage (battery side), V_g^B (V)	600
Steady state output voltage (load side), V_o (V)	1500
Input boost inductor, L_B (H)	3.4e-3
Output boost capacitor, C_B (F)	2.2e-6
Switching frequency f_s^B (Hz)	50e3
PI-controllers gains	
Inner current controller proportional gain, k_c^B	1.28e-3
Inner current controller integral gain T_c^B	1.57e-4
Outer voltage controller proportional gain, k_v^B	2.27e-5
Outer voltage controller integral gain, T_v^B	1.32e-7